On selected numerical approaches to Cellular Tissue

Dissertation

zur Erlangung des Doktorgrades
der Naturwissenschaften

vorgelegt beim Fachbereich Physik
der Johann Wolfgang Goethe – Universität
in Frankfurt am Main

von
Gernot Schaller
aus Wismar

Frankfurt am Main 2005
(D F1)

Kurzfassung

Theoretische Modelle von in der Natur existierenden komplizierten Systemen erlauben es, Hypothesen zunächst nicht am realen System, sondern an einem Modell zu testen. Im Vergleich zur Durchführung von realen Experimenten haben diese theoretischen Experimente die Vorteile einer totalen Kontrolle von Messfehlern und verursachen oftmals um Größenordnungen geringere Kosten. Das realistische System kann nicht komplett durch theoretische *in silico* Modelle beschrieben werden, denn diese vereinfachen Systemeigenschaften, um eine theoretische Behandlung überhaupt erst zu ermöglichen. Dadurch ergibt sich jedoch die Möglichkeit, die im System relevanten Mechanismen zu identifizieren.

Viele Modelle benutzen Kontinuumsbeschreibungen von Konstituenteneigenschaften, um das System mit ordinären oder partiellen Differentialgleichungen zu beschreiben. Im Gebiet der Gewebemodelle erfreuen sich gerade im Hinblick auf einen eventuell monoklonalen Ursprung von Krankheiten wie Krebs agentenbasierte Ansätze großer Beliebtheit, denn in diesen Modellansätzen wird jede Zelle individuell im Modell repräsentiert und somit lassen sich die Nachkommen einer einzelnen Zelle individuell verfolgen. Im Hinblick auf die großen Zellzahlen in höheren Organismen werden agentenbasierte Modelle benötigt, welche mit vergleichsweise geringen numerischen Aufwand gelöst werden können. Ein bekannter Ansatz besteht darin, die räumliche Dynamik der Zellen auf einem Gitter zu modellieren, indem eine Zelle durch einen oder, für höhere gewünschte Auflösungen, auch durch mehrere Gitterpunkte approximiert wird. Der Zustand der Zellen auf dem Gitter ändert sich durch lokale Wechselwirkungsregeln. Diese Ansätze führen allerdings oft zu numerischen Gitterartefakten, welche durch stochastische Wechselwirkungsregeln reduziert werden können. Die Verbindung von Modellparametern mit messbaren Observablen wird dadurch jedoch nochmals erschwert. In Hinsicht auf die Bewertung der Ergebnisse von darauf basierenden Modellen taucht auch die Frage auf, ob die intrinsische gitterbasierte Repräsentation die Ergebnisse eventuell verfälscht. Diese Frage kann nur mit Modellen beantwortet werden, welche diese Näherung aufgeben.

Die vorliegende Arbeit führt numerische Methoden für die Konstruktion von gitterfreien Modellen zellularen Gewebes ein. Um die Anwendbarkeit zu demonstrieren, werden sie auf verschiedene biologische Modellsysteme angewandt und auch teilweise mit kontinuumsbasierten Methoden verglichen. Unter der Annahme von kontaktvermittelten Zell-Zell-Wechselwirkungen kann mit Zuhilfenahme der Nachbarschaftstopologie die Zahl der zu betrachtenden Wechselwirkungen deutlich reduziert werden. Die reguläre Delaunay-Triangulation stellt dabei eine Methode dar, solche Topologien effizient zu erstellen: Das Objekt wird durch eine Kugel repräsentiert, deren Nachbarschaft mit anderen Objekten (Kugeln) durch die Delaunay-Triangulation definiert ist. Objekte, welche in der Triangulation

nicht verbunden sind, haben auch keinen Kontakt untereinander und die entsprechenden Kontakt-wechselwirkungen müssen nicht berücksichtigt werden. Zur Delaunay-Triangulation kann, analog zur Wigner-Seitz-Zelle, geometrisch eine duale Konstruktion, die Voronoi-Zerlegung, eingeführt werden. Diese duale Konstruktion ermöglicht es auch, geometrische Korrekturen des Zellvolumens bei mehrfachen Überlapps zu berechnen. Die Modellierung von lebendem Gewebe stellt jedoch deutlich erhöhte Anforderungen an die benutzte Delaunay-Triangulation: Die Zellbewegung erfordert die Unterstützung kinetischer Punktmengen, und Prozesse wie Zellteilung und Zelltod korrespondieren mit dem Einfügen bzw. Entfernen von Kugeln aus der Triangulation. Eine Triangulation, welche dies simultan leistet, wurde im Rahmen dieser Arbeit erstmals erstellt: In dieser Implementation wird die Änderung der Nachbarschaftstopologie durch eine Folge von elementaren topologischen Transformationen repräsentiert. Gleichfalls werden in der vorliegenden Arbeit verwendete Algorithmen zum Einfügen bzw. Entfernen von Objekten diskutiert. Von besonderem Interesse ist hierbei ein neuartiges Kriterium zur Berechnung der maximalen Schrittweite, welches in den kinetischen Algorithmen Anwendung findet. Die durchschnittliche algorithmische Komplexität der Kontakt-Erkennung durch die Delaunay-Triangulation ist dominant bestimmt durch den verwendeten kinetischen Algorithmus und skaliert damit linear mit der Zahl der betrachteten Objekte für realistische Modellapplikationen.

Da die Dynamik von Zell-Zell-Kontakten nicht genau verstanden ist, wird ein für unbelebte Materie etabliertes Kontaktmodell (JKR-Modell) diskutiert und für seine Anwendbarkeit auf Gewebesimulationen modifiziert. Dies beinhaltet die Erweiterung durch dissipative und stochastische Kräfte. Im Gegensatz zur Langevin-Gleichung wird jedoch auch Zell-Zell-Reibung und Reibung mit stationären Randbedingungen mit einbezogen, so dass die Bewegungsgleichungen erheblich komplexer werden. In der überdämpften Näherung $m\ddot{x} \approx \mathbf{0}$ können diese auf die Form

$$A(t)\dot{x}(t) = \mathbf{b}(t)$$

gebracht werden, wobei der Vektor $\mathbf{b}(t)$ sowohl konservative als auch stochastische Wechselwirkungen, und die Matrix $A(t)$ die dissipativen Kräfte enthält. Da die Matrix $A(t)$ dünn besetzt und für physiologische Parameter auch positiv definit ist, können iterative Methoden wie die der konjugierten Gradienten benutzt werden, um das System nach $\dot{x}(t)$ und, nach zeitlicher Integration mit adaptiver Schrittweite, somit nach der zellularen Kinetik $x(t)$ aufzulösen.

Die Übertragung von Informationen aller Art im Gewebe wird jedoch nicht nur durch Kontaktwechselwirkungen, sondern auch durch diffundierende Substanzen bewerkstelligt. Im einfachsten Fall handelt es sich z. B. um die Diffusion von Nährstoffen. Aufgrund des riesigen Größenunterschieds zwischen einzelnen Molekülen und Zellen können diffundierende Signal- und Nährstoffe durch

Reaktions-Diffusions-Gleichungen der Form

$$\frac{\partial u}{\partial t} = \nabla\left[D(\boldsymbol{x}, t)\nabla u(\boldsymbol{x}, t)\right] + Q(\boldsymbol{x}, t)$$

hinreichend beschrieben werden. Dabei beschreibt $u(\boldsymbol{x}, t)$ die räumlich und zeitlich heterogene Dynamik des diffundierenden Faktors, $D(\boldsymbol{x}, t)$ den im Allgemeinen von den lokalen Bedingungen abhängigen effektiven Diffusionskoeffizient und $Q(\boldsymbol{r}, t)$ die lokale Aufnahme- bzw. Produktionsrate des diffundierenden Faktors. Die diskretisierte Version solcher partieller Differentialgleichungen lässt sich auf einer Rechteck-Diskretisierung durch den Übergang von Differentialquotienten zu Differenzenquotienten erhalten und führt auf die Lösung dünnbesetzter Gleichungssysteme mit spezieller band-diagonaler Struktur. Diese Arbeit diskutiert verschiedene numerische Methoden zur Lösung dieser Gleichungen, welche im Rahmen der Modellkonstruktion erstellt und verglichen wurden. Das beinhaltet sowohl Lösungen für das volle zeitabhängige System als auch die Lösung im Gleichgewicht, d. h. für $\frac{\partial u}{\partial t} \approx 0$. Um eine konsistente Verbindung mit gitterfreien agentenbasierten Modellen herzustellen, werden die lokalen Konzentrationen an den Zellzentren durch lineare Interpolation zwischen den Gitterpunkten berechnet. Dieses Vorgehen kann nur angewendet werden, wenn die Gitterkonstante des Diskretisierungsgitters auf Bereiche oberhalb der typischen Zellgröße eingeschränkt ist.

Der Zellzyklus wird im Modell durch interne diskrete Zustände der Agenten repräsentiert, d. h. in Abhängigkeit des internen Zustandes verändern die Agenten ihre Eigenschaften. Das Modell unterscheidet dabei zwischen M-Phase, G_1-Phase, S/G_2-Phase und einer G_0-Phase, über deren Dauer die Gesamtzellzykluszeit gesteuert wird. Zusätzlich können die Modellagenten nekrotisieren, was im Modell durch ein Ende der Nährstoffaufnahme und eine – verzögerte – Entfernung der Agenten aus der Simulation realisiert wird. An einzelnen biologischen Systemen wird das Modell weiter spezifiziert.

Multizelluläre Tumorsphäroide sind *in vitro* Systeme von unsterblichen Zell-Linien, welche in dreidimensionaler Kultur sphärische Zellpopulationen formen. Aufgrund des Nährstoffmangels im Inneren der Sphäroide bildet sich in der Regel eine typische, durch Schichten bestimmte Struktur heraus: Ein nekrotischer Kern ist umgeben von einer nichtproliferierenden Zellschicht, welche wiederum von einer äußeren Schicht proliferierender Zellen umgeben ist. Eine solche Struktur findet man auch in vielen avaskularen Tumoren *in vivo*, weshalb multizelluläre Tumorsphäroide ein beliebtes experimentelles Modellsystem darstellen, um z. B. den Effekt von Chemotherapeutika unter realistischeren Bedingungen zu testen. Das Wachstum der Tumorsphäroide folgt anfänglich dem erwarteten exponentiellen Verlauf, flacht dann jedoch ab und für einige Zell-Linien wird sogar eine Sättigung beobachtet. Diese Abweichung vom exponentiellen Wachstum ist jedoch nicht allein durch die Verarmung an Nährstoffen bedingt, sondern auch durch andere Faktoren. In dieser Arbeit wird gleichfalls der

Beitrag durch die Kontaktinhibition der Zellteilung untersucht. Durch Variieren der experimentell nicht oder nur schwer erreichbaren Modellparameter kann die Abweichung zwischen Modellvorhersage und experimentellen Messungen im Sinne eines χ^2-Fits minimiert werden. Die so erhaltenen Modellparameter stellen eine Modellvorhersage dar.

Um das Wachstum dieser Sphäroide im Modell zu untersuchen, werden in einem agentenbasierten und einem kontinuumsbasierten Modell die Prozesse der Nekrose und Kontaktinhibition als verlangsamende Faktoren in der Wachstumsdynamik der Sphäroide diskutiert. Dabei wird das kontinuumsbasierte Modell so analog wie möglich zum agentenbasierten Modell konstruiert. Als nekroseinduzierend werden zwei diffundierende Nährstoffe betrachtet, Sauerstoff und Glukose, was die simultane Lösung der beiden Reaktions-Diffusionsgleichungen impliziert. Mit einem einfachen Ansatz über die Abhängigkeit der Nekrose von den lokalen Nährstoffkonzentrationen gelingt es, mit ansonsten gleichen Parametern vier Wachstumskurven bei verschiedenen Nährstoffkonzentrationen modellunabhängig zu reproduzieren. Das agentenbasierte Modell hat den Vorteil der Auflösung des Zellzyklus und der besseren Beschreibung der Zellkinetik, welche im Kontinuumsmodell durch einen nichtlinearen (positiven) Diffusionsterm charakterisiert ist. Zudem liegt die betrachtete Systemgröße von $10^5 \ldots 10^6$ Zellen an der Grenze des mit agentenbasierten Modellen berechenbaren, was starke Vereinfachungen der Bewegungsgleichungen erfordert. Beide Modelle approximieren die experimentellen Wachstumskurven mit annähernd gleicher Qualität, so dass auf dieser Ebene keine Diskriminierung zwischen den Modellen möglich ist. Auf der Ebene der morphologischen Daten, d. h. der Größe des nekrotischen Kerns und der anderen Schichten, ist aber sehr wohl eine Modelldiskriminierung möglich. Das agentenbasierte Modell erlaubt zudem eine Saturation des Wachstums, was im speziellen konstruierten kontinuumsbasierten Ansatz nicht möglich ist.

Um einem realistischen Modell für das Tumorwachstum *in vivo* näherzukommen, wird das agentenbasierte Modell auf die Beschreibung der Epidermis angepasst. Diese ist ein mehrschichtiges verhornendes Plattenepithelgewebe und bildet die obere Schicht der menschlichen Haut. Die vorherrschenden Zelltypen sind Keratinozyten, Melanozyten, Merkel-Zellen und Langerhans-Zellen. Die Epidermis lässt sich histologisch in mehrere Schichten unterteilen. Das aus nur einer Zellschicht bestehende *stratum germinativum* grenzt direkt an die Basalmembran. Hier teilen sich Keratinozyten, von denen ein Teil in der Basalschicht verbleibt, der andere Teil jedoch die Basalschicht verlässt und zum *stratum corneum* aufsteigt. Während dieser Passage durchlaufen die Keratinozyten mehrere Zellteilungen und einen Differenzierungsprozess, welcher sich auch histologisch verschiedenen Schichten zuordnen lässt. Dieser Prozess besteht in einer speziellen Form des Zelltodes, der Kornifizierung (auch anoikis) genannt wird: Das Zytoplasma verliert Wasser, die Zellen verflachen sich und formen polarisierte Bindungen. Schließlich lösen sich diese Bindungen an der Oberfläche auf und die kornifizierten

Keratinozyten verlieren den Kontakt. Es ist bekannt, dass die Struktur des *stratum corneum* eine wirkungsvolle Barriere für viele diffundierende Substanzen darstellt. Die Melanozyten befinden sich im Normalfall an der Basalschicht. Krebsartig entartete Melanozyten können ein Melanom bilden.

Im Modell wird nur zwischen drei Zelltypen mit verschiedenen Eigenschaften unterschieden: Keratinozyten, deren Stammzellen in der Basalschicht und Melanozyten. Mit verschiedenen Eigenschaften der korrespondierenden Agenten können die Effekte verschiedener Parameter im Modell auf die Koexistenz von verschiedenen Zelltypen untersucht werden. Die kleinere betrachtete Systemgröße von $10^3 \ldots 10^4$ Zellen ermöglicht es indes, die Bewegungsgleichungen ohne weitere Näherungen zu behandeln. Im Modell wird eine moderierende (verlangsamende) Funktion von großen extrazellularen Wasserkonzentrationen auf die Proliferationsrate der Keratinozyten und deren Stammzellen angenommen. Da erst durch den Aufbau eines schützenden *stratum corneum* der Verlust von Wasser durch die Hautoberfläche eingedämmt wird, hat das Abtragen dieser Schicht im Modell die Folge einer proliferativen Antwort. Diese wird z. B. auch in tape-stripping Experimenten beobachtet. Allerdings können mit dem Modell keinerlei Aussagen über die Art des moderierenden Faktors gemacht werden, denn auch andere diffundierende Faktoren würden zu formal identischen Modellgleichungen führen.

In der vorliegenden Arbeit wird auch der Einfluss einer variierenden Adhäsion von Melanozyten zur Basalmembran auf das Wachstum von *in silico* Melanomen untersucht. Diese Frage ist stark verbunden mit dem Verhältnis der Proliferationsraten von Melanozyten und Keratinozyten im Modell. Es stellt sich heraus, dass in einigen Bereichen des Parameterraumes stochastische Störungen einen sehr großen Einfluss haben können, zum einen durch die Variation der Anfangsbedingungen für das Tumorwachstum, zum anderen aber auch auf das Wachstum des Melanoms selbst.

Die Übertragbarkeit der Modellresultate auf reale Systeme hängt stark von der Gültigkeit der verwendeten Näherungen und der Relevanz der untersuchten Mechanismen ab. Die Schwachpunkte der verwendeten Modelle werden daher in der Arbeit diskutiert, um eine sinnvolle Einordnung zu ermöglichen. Für weitere Untersuchungen werden Verbesserungsvorschläge gemacht und einige experimentelle Signaturen hervorgehoben, welche in Experimenten falsifiziert werden können. Diese Arbeit schließt mit einer kritischen Betrachtung der verwendeten numerischen Algorithmen, Modelle und der Philosophie. Die selbst entwickelten bzw. selbst implementierten Algorithmen wurden verschiedenen numerischen Tests unterworfen, was im Anhang ausführlicher erläutert wird.

In experimenteller Hinsicht unterstreichen die Resultate die Notwendigkeit eines klar definierten experimentellen Modellsystems, an welchem Modelle falsifiziert und unbekannte Modellparameter fixiert werden können. In theoretischer Hinsicht bergen agentenbasierte gitterfreie Methoden das Potential, Artefakte von gitter- bzw. kontinuumsbasierten Ansätzen aufzudecken.

Abstract

Different numerical approaches and algorithms arising in the context of modelling of cellular tissue evolution are discussed in this thesis. Being suited in particular to off-lattice agent-based models, the numerical tool of three-dimensional weighted kinetic and dynamic Delaunay triangulations is introduced and discussed for its applicability to adjacency detection. As there exists no implementation of a code that incorporates all necessary features for tissue modelling, algorithms for incremental insertion or deletion of points in Delaunay triangulations and the restoration of the Delaunay property for triangulations of moving point sets are introduced. In addition, the numerical solution of reaction-diffusion equations and their connection to agent-based cell tissue simulations is discussed. In order to demonstrate the applicability of the numerical algorithms, biological problems are studied for different model systems:

For multicellular tumour spheroids, the weighted Delaunay triangulation provides a great advantage for adjacency detection, but due to the large cell numbers the model used for the cell-cell interaction has to be simplified to allow for a numerical solution. The agent-based model reproduces macroscopic experimental signatures, but some parameters cannot be fixed with the data available. A much simpler, but in key properties analogous, continuum model based on reaction-diffusion equations is likewise capable of reproducing the experimental data. Both modelling approaches make differing predictions on non-quantified experimental signatures.

In the case of the epidermis, a smaller system is considered which enables a more complete treatment of the equations of motion. In particular, a control mechanism of cell proliferation is analysed. Simple assumptions suffice to explain the flow equilibrium observed in the epidermis. In addition, the effect of adhesion on the survival chances of cancerous cells is studied. For some regions in parameter space, stochastic effects may completely alter the outcome.

The findings stress the need of establishing a defined experimental model to fix the unknown model parameters and to rule out further models.

Contents

Chapter 1

Motivation

1.1 The Benefit of Theoretical Models

Models are theoretical representations of phenomena.

This infers that they are formal representations of human beliefs.

Since – in contrast to the realistic system – theoretical models can be controlled completely, they provide a favourable alternative to the realistic system for testing hypotheses.

In some parts of science one has the ability to establish experimental models: Simplified and well-understood systems that are designed to resemble more complicated systems. In contrast, this thesis will deal with theoretical models, in particular with certain mathematical models in biology.

Usually, a mathematical model is defined by a set of variables, that describe the state of the system, a set of equations, that establish relations between the variables, and a set of parameters, that allow to vary the relations between the variables in a discrete or continuous way.

There is some concensus about how mathematical models can be classified (compare subsection 2.1). These classes of models are usually not disjoint:

- **Deterministic models** always yield the same results if restarted with the same initial conditions, whereas **stochastic models** will produce a different outcome.

- **Dynamic models** do account for the full time evolution of a system, whereas **static models** only account for a single state, for example the long-time limit.

- Technically, mathematical models can as well be divided into **linear models** that use linear differential equations to describe the evolution of their variables and **nonlinear models** where nonlinear equations are applied.

In addition, models can be distinguished by the degree to which they use available information on the system. Some systems for example consist of many constituents with similar properties, where it is impossible and sometimes unnecessary to model every constituent separately. In other systems however, the properties of individual constituents may be very important and accordingly, the degree to which this is reflected in the model varies strongly. In some cases, models can be considerably simplified by averaging over individual properties. For example, in thermodynamics one is not interested in the specific momentum or position of every single particle, but rather in the evolution of average quantities. For many systems in physics this model simplification has been very successful. However, it must be said that fundamental prerequisites of this procedure – indistinguishability of the constituents and large constituent numbers – are not always given in cell tissues, where to a first approximation cells can be viewed as the smallest functional unit. In such systems, a too extensive averaging of constituent properties may lead to the destruction of important properties. In the class of agent-based models, where every constituent is represented individually, the main model simplification is the simplification of individual properties. The large amount of information that can be produced by agent-based models is paid for by strong computational requirements. However, the goal of understanding such systems is well worth the effort:

The current hypotheses on cancer evolution for example, point to a monoclonal origin of this disease [1]. Especially in the initial stages of tumour growth *in vivo*, the individual properties of the tumour cells play an important role, as in this stage the fate of a single cell may determine life or death.

In addition, models that solely represent cells by average quantities have sometimes difficulties to explain simple processes such as cell sorting or cell movement. Here, agent-based models can be used to reveal the shortcomings in the averaging approach and thereby contribute to an improvement of over-simplifying models. For example, the kinetics of the cellular distribution is often modelled by a mere diffusion approach, which is only valid in the limit of low cellular density and passive cell motion. If the cell density is large, the elastic and adhesive cell properties dominate the cellular kinetics.

A model is much easier controlled than the original experimental system. For example, in mathematical models, the experiments can be set up with much less effort and the system can be prepared to defined initial states. The experimental error is under control and in addition, usually the solution is obtained much faster than with real experiments. These advantages have led to a widespread application of mathematical modelling in nearly all fields of natural sciences. Provided, the mathematical model does not contain intrinsic logic errors or errors within its solution, significant progress can be achieved in the following way:

- The most important results can be established by using a mathematical model that fails to

predict experimental data correctly even though in its design all currently available knowledge has been included. This outcome leads to refinement of theories and finally to progress, if an improved theory is in agreement with the experiment. Thus, in this way a model can be used as a tool to find human misconceptions. In on-going iterations of comparing simulation outcomes to experimental results, a model is improved by including new underlying mechanisms. On the contrary, a model that is in full agreement with the experiment does not contribute at all to understanding the underlying mechanisms, since the knowledge that has been included in the design process has not been falsified and no new information about underlying mechanisms has been gained.

- Nevertheless, even in cases where mathematical models reproduce experimental data with sufficient accuracy, further knowledge can be gained. In this stage, models can be used to establish reasonable estimates of parameters. In addition, the model can be used as a tool to reveal errors in experimental setups.

The existence of unexpected and nontrivial behaviour arising in complex systems made of simple constituents is called **Emergence**. This term is popularly circumscribed by "the whole lot is more than just the sum of its constituents". The evolution of cellular tissues is currently hardly understood. It is not clear whether this can be attributed to the missing knowledge about its constituents or to missing effects arising from Emergence.

1.2 Goals of this study

This work is aimed at constructing and improving mathematical models to understand the evolution of cellular systems, in particular tissues:

1. Currently, to a large extent technical aspects determine the limits of modelling. Therefore, special focus should be laid on the details of the used numerical approaches. This includes the development of software for the solution of partial differential equations as well as for specific large ordinary systems.

2. In order to have the possibility of revealing shortcomings of averaged modelling approaches, agent-based models should be constructed. To go beyond the widely-used lattice approaches, an off-lattice model is favoured. This would normally increase the computational complexity by orders of magnitude. Therefore, the weighted Delaunay triangulation shall be discussed as a tool to detect cellular adjacencies. This requires the implementation of such a triangulation

as independent software that provides – unlike the present triangulation software [2] – efficient functions for cellular movement, proliferation and cell death simultaneously.

3. The numerical methods must be tested and cross-checked to exclude numerical or conceptual artifacts as far as possible.

4. For different cellular systems, mathematical models – based on established mechanisms – have to be constructed. This includes the application of agent-based modelling to tumour growth as well as a comparison to a corresponding continuum model. In addition, modelling approaches to epidermal tissue shall be discussed.

1.3   Conventions & Notation

The Einstein sum convention will be generally used in this thesis, if confusion is not possible: Indices occurring twice within a term are summed up automatically with the limits on the summation indices arising from the context. Whenever confusion is possible, indices denoting Cartesian coordinates are denoted by Greek letters, whereas indices denoting elements of other vectors will be given as Latin letters.

If referenced as a whole, vectors are denoted in bold symbols, whereas vertices – if supplemented with weights – will be denoted bold with hats. The nabla operator ∇ is understood as a vector containing the derivatives with respect to the Cartesian coordinates.

An overview of the used symbols and abbreviations can be found on page 167. Definitions in the text will be denoted in bold letters.

CPU times given refer to a 1.533 GHz AMD Athlon processor with 1 GByte of RAM. The source code has been compiled using the GNU g++ compiler (version 3.3) with compiler optimisation set.

Chapter 2

Introduction

2.1   Mathematical models in biology

Mathematical models can be classified as indicated in figure 2.1. Models where the state of the system is entirely characterized by using continuous variables are termed **continuum models**. Usually, their evolution is characterized by partial differential equations (termed **density dynamics**) or ordinary differential equations (termed **population dynamics**) that yield a continuous solution. In the other group, the internal state of the system is at least partly characterized by **discrete variables**. If some of these variables are discretised on a lattice, the model belongs to the class of **cellular automata**[1], whereas in **off-lattice models** none of the state variables is discretised on a lattice. In the context of tissue modelling, both of the latter sub-classes have representatives that base their dynamics on the boundary of a cell (see e. g. the Potts model [5] for cellular automata or [6] for an off-lattice counterpart) or on its centre (see e. g. regular cellular automata [7] or off-lattice models [8]), where the centre-based models usually use less degrees of freedom.

A quite complete review of continuum models – both based on population or on density dynamics can be found in [9, 10]. Among these, probably the study of population models has the longest history. Inspired by observations in daily life, Leonardo of Pisa (called Fibonacci later on) as early as 1202 set up a model to predict the population dynamics of rabbits. If one starts with a single immature pair of rabbits, the number of rabbit pairs in his model is given by a sequence of numbers that later became known as the Fibonacci sequence [9].

More realistic population models (incorporating the effect of growth saturation for limited resources) have been set up in the 19$^{\text{th}}$ century. For example, the logistic growth equation was set up in 1838 by

---

[1]There exist other definitions of cellular automata [3, 4].
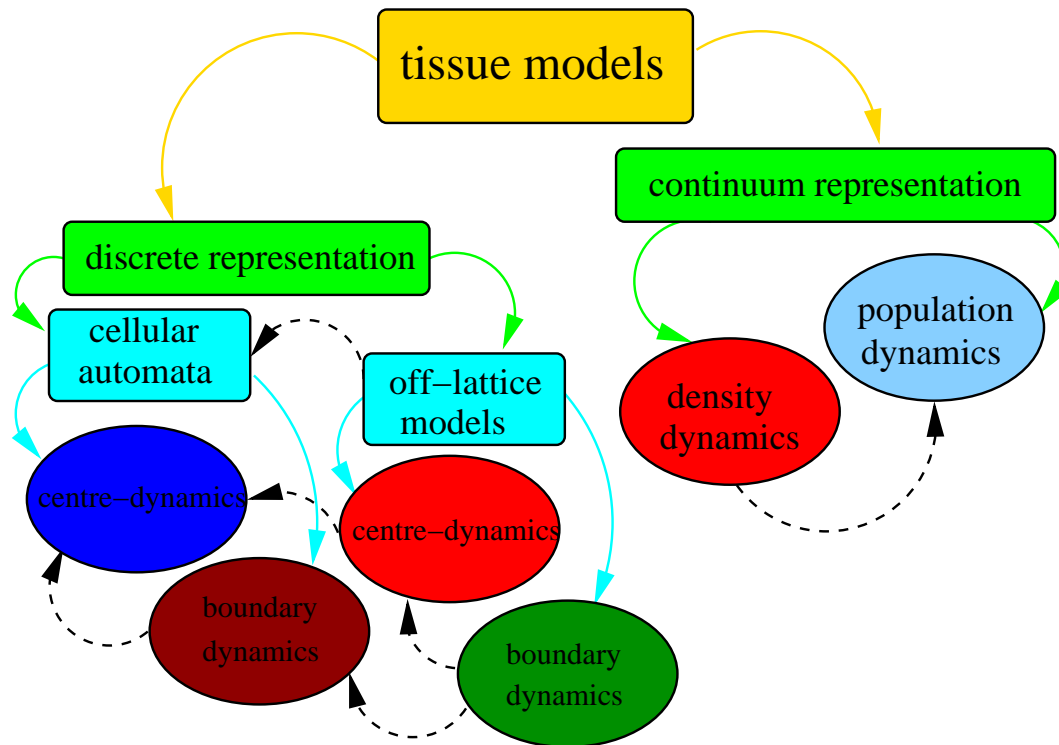
Figure 2.1: Hierarchy of mathematical models in biology. Different classification schemes can be applied and hybrid forms exist. Dashed lines indicate correspondence via simplifications, whereas solid lines indicate subsets. Relative heights indicate varying degrees of computational complexity. Representatives of the models indicated red are discussed in this thesis.

Malthus

$$\frac{dN}{dt} = rN(t)\left[1 - \frac{N(t)}{K}\right],$$ (2.1)

where $N(t)$ is the number of individuals at time t, r is their proliferation rate, and K is the carrying capacity of the particular environment. The above equation is widely used to make predictions for population numbers.

In medicine, an additional growth law has found wide-spread application. It is given by the Gompertz equation published in 1825 [11] as a demographic model

$$\frac{dN}{dt} = \alpha \exp\left(-\beta t\right) N(t) = \beta \ln\left[\frac{N^{\infty}}{N(t)}\right] N(t),$$ (2.2)

where (with $N^{\infty} = N_0 \exp\{\alpha/\beta\}$) the relative growth rate depends on time (or the population number) itself. The Gompertz equation has the solution

$$N^{\text{GOMP}}(t) = N_0 \exp\left\{\frac{\alpha}{\beta}\left[1 - e^{-\beta t}\right]\right\},$$ (2.3)

which can be derived by separation of variables. Interestingly, the Gompertz model fits the growth processes of many populations, individuals, and even the growth of many avascular tumours remarkably well [12, 13, 14, 15].

The population dynamics model (2.1) has been extended by Fisher [16] and Kolmogoroff [17] in 1937 to incorporate the spatial distribution by combining it with the diffusion equation

$$\frac{\partial n}{\partial t} = D\nabla^2 n(\boldsymbol{x}, t) + rn(\boldsymbol{x}, t)\left[1 - \frac{n(\boldsymbol{x}, t)}{K}\right],$$ (2.4)

where $n(\boldsymbol{x}, t)$ describes the population density, and D is a diffusion constant that effectively includes the mobility[2] of the individuals.

Since in the last century computational techniques have evolved significantly, nowadays more complete models are in use. In some of these models, individuals are not described in an approximate way as by continuum approaches, but as individual agents. However, in contrast to early approaches such as the one by Fibonacci, they are capable of incorporating many interacting agents. In the late 1940s John von Neumann introduced the concept of cellular automata [18].

In [19] **cellular automata** are characterized as "(discrete) models of spatiotemporal dynamical systems, namely discrete in time, space and state space". The most famous cellular automaton has been

---

[2]The term motility will be used as referring to active cell movement, whereas mobility does not result from individual action. For specific cases, random motility may as well be described by the diffusion equation.

introduced in 1970 by John Horton Conway with what was termed "Game of Life" [20]. This cellular automaton produces complicated patterns emerging from simple interaction rules. Stephen Wolfram [3] and Andreas Deutsch [4] give reviews of cellular automata. For cell tissues, the concept of cellular automata can be applied to centre-based models, where every lattice site is assigned to a single cell (see e. g. [7] for a model on tumour growth) or to boundary-based models, where a single cell can be distributed on several lattice nodes [5]. For many practical applications however, it is quite complicated to draw connections from physically measurable quantities to the parameters of cellular automata. In addition, many cellular automata have to cope with lattice artifacts and the stochastic counter-strategies often employed make this connection even more difficult. For this reason, the off-lattice models have been developed, for an overview see e. g. [21]. In these models, the cells do not reside on a lattice, but arbitrary coordinates are allowed. In addition, they do not interact by automaton rules, but via physically motivated interactions. These models can be subdivided in centre-based models (e. g. Voronoi tessellations [22, 23]) or models that describe the dynamics of the cell membrane [6, 24] as well.

2.2   Construction of an off-lattice model

For off-lattice agent-based models of cellular tissue, the calculation of cell-cell interactions will contribute significantly to the computational time. A simple problem that may arise within this context is the calculation of a measure for contact area.

A reasonable estimate of this quantity may for example be given by the circle uniquely defined by the intersection of two non-identical spheres. If one uses no means of accelerating the adjacency detection amongst a set of N spheres, the corresponding calculation time will scale quadratically with the number of spheres. If the inter-spherical adjacency topology however is already known, for every sphere only a subset of other spheres has to be tested. The Delaunay triangulation is a tool well-suited for calculating and storing the adjacency relations within a set of spheres (see figure 2.2). Here, the Delaunay triangulation will be used as a numerical tool that has the potential of aiding in decreasing the runtime of off-lattice agent-based simulations. There exist efficient libraries providing support for two-dimensional Delaunay triangulations. In addition, there are libraries constructing three-dimensional Delaunay triangulations for a given set of spheres [2]. Though these libraries support insertion and removal of spheres (also termed **dynamic**) in the system, the use of these functions for moving spheres [25] is inefficient [26] (compare appendix A.1). Within the context of collision detection [27], more efficient routines are applied to a set of moving spheres, but these algorithms do not support the removal of spheres (purely **kinetic** algorithms). This however is an essential property
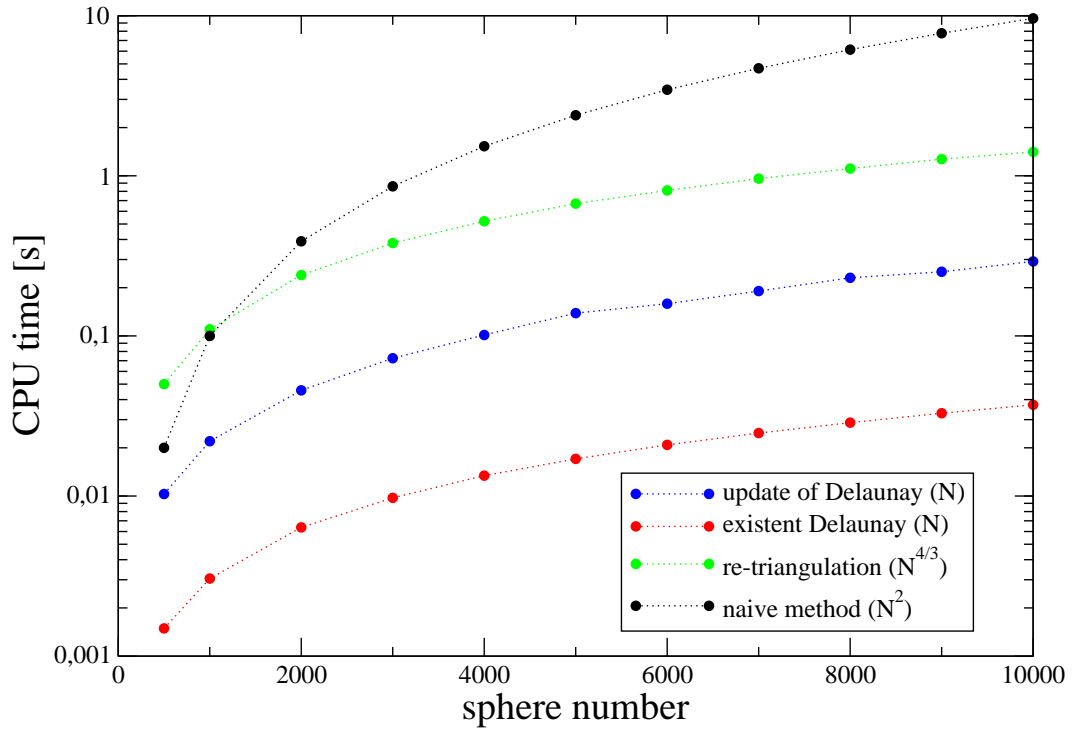
Figure 2.2: Numerical advantage of the Delaunay triangulation for the detection of adjacencies. The naive calculation time of sphere-sphere contact (black) would scale quadratically in time. If a valid Delaunay triangulation is provided, the inter-spherical contacts can be calculated in linear and substantially shorter times (red). If one considers more than $O\left(10^3\right)$ spheres, then even time necessary for Delaunay construction (green) is shorter than naive calculation of inter-spherical contact. However, as during the time-course of agent-based simulations the cell positions will change in a continuous way, the intercellular adjacencies will do likewise. The time to restore the Delaunay property in a triangulation in which the spheres have moved by 10% of their average distance is given in blue. Therefore, the calculation time to maintain a kinetic Delaunay triangulation and compute the intercellular contact surfaces (blue and red) is still orders of magnitude smaller than in the naive approach if more than $O\left(10^3\right)$ spheres are considered.

necessary for the modelling of cellular tissues. Since currently no library simultaneously supporting insertion, removal and movement of spheres is provided [25], a numerical implementation of such a triangulation that is suitable for adjacency detection [26] will be described within this thesis. In the following section it will be discussed, how to create and maintain Delaunay triangulations. In addition, further advantages of the Delaunay triangulation will be illuminated.

The remaining sections in this introducing chapter will describe further necessary ingredients of an intrinsically consistent modelling approach towards cellular tissues.

2.3 Kinetic and Dynamic Delaunay triangulations

2.3.1 Definitions

As Delaunay triangulations are – at least for their two-dimensional representation – a well covered topic in the literature, the reader is referred to textbooks such as e. g. [28] that cover all fundamental definitions and properties of Delaunay triangulations. In this chapter, only the definitions necessary for this thesis will be given.

In accordance with the notation in the literature [29, 30] the term **vertex** (or point) denotes a position in d-dimensional space. Furthermore, the term **weighted vertex** denotes a point supplemented with a weight. A n**-simplex** in $\mathbb{R}^d$ with $n \leq d$ is the convex hull of a set T of $n + 1$ affinely independent vertices, which reduces in the three-dimensional case to tetrahedra (3-simplices), triangles (2-simplices), edges (1-simplices) and vertices (0-simplices). Then, every n-simplex has a uniquely defined n-circumsphere.

These $(n < d)$-simplices σ_U – formed by the convex hull of a subset $U \subset T$ – will be called **faces** of T. Since in this section a three-dimensional realisation will be discussed, the corresponding 3-simplices will be shortly denoted by the term **simplex**.

A collection of simplices $\mathcal{K}$ is called a **simplicial complex** if [29]:

- The faces of every simplex in $\mathcal{K}$ are also in $\mathcal{K}$ (the set is closed),

- If $\sigma_T \in \mathcal{K}$ and $\sigma_{T'} \in \mathcal{K}$, then $\sigma_T \cap \sigma_{T'} = \sigma_{T \cap T'}$. (The intersection of two simplices is at most a face of both, the simplices are "disjoint".)

In numerical calculations with kinetic vertices the above criterion can be destroyed: A vertex might move inside another simplex thus yielding two n-simplices whose intersection is again an n-simplex. This situation will be referred to as an **invalid triangulation**. On the contrary, a valid triangulation is defined as follows [29]:

If S is a finite set of points in $\mathbb{R}^d$, then a simplicial complex $\mathcal{K}$ is called a **valid triangulation** of S if

- each vertex of $\mathcal{K}$ is in S,

- the underlying space of $\mathcal{K}$ is conv(S).

The number of simplices containing a particular vertex as endpoint will be denoted by the **degree** of this vertex in a triangulation. Furthermore, the terms tetrahedralization and triangulation will be used synonymously in three dimensions.

2.3.2 Elementary Topological Transformations

To an existing triangulation in $\mathbb{R}^3$ several elementary topological transformations – also called **flips** – can be applied, of which a detailed discussion can be found in e. g. [29, 31]. These transformations do not change the position of vertices. In contrast, they change the triangulation topology. They rely on Radon's theorem [29, 32] (see figure 2.3 for a three-dimensional illustration):

> Let X be a set of $d + 2$ points in $\mathbb{R}^d$. Then a partition $X = X_1 \cup X_2$ with $X_1 \cap X_2 = \emptyset$ exists such that conv(X_1) $\cap$ conv(X_2) $\neq \emptyset$.

The radon partition is unique if the set X is in **general position** – meaning that every subset of X with at most $d + 1$ elements is affinely independent. In three dimensions this simply means that

- no two points are identical,

- no three points lie on a common line,

- no four points lie on a common plane.

In this thesis however, this definition of "general position" is extended by the further property that no $d + 1$ points may lie on a common sphere [30, 33].

From the Radon partition in $\mathbb{R}^3$ one finds that there are four possible ways of triangulating five points in three dimensions, two for every partition in figure 2.3. The elementary flips transform between these possible triangulations without changing the vertex positions.

For the case of figure 2.3 left panel the two possible flips are shown in figure 2.4. The flip changing the triangulation from 1 to 4 simplices corresponds to adding a vertex to an existing triangulation. Note however, that in practice the inverse transformation may not always be applicable, since the configuration of one vertex (*E* in figure 2.4) being the endpoint of exactly four simplices (as is the

(a)   (b)
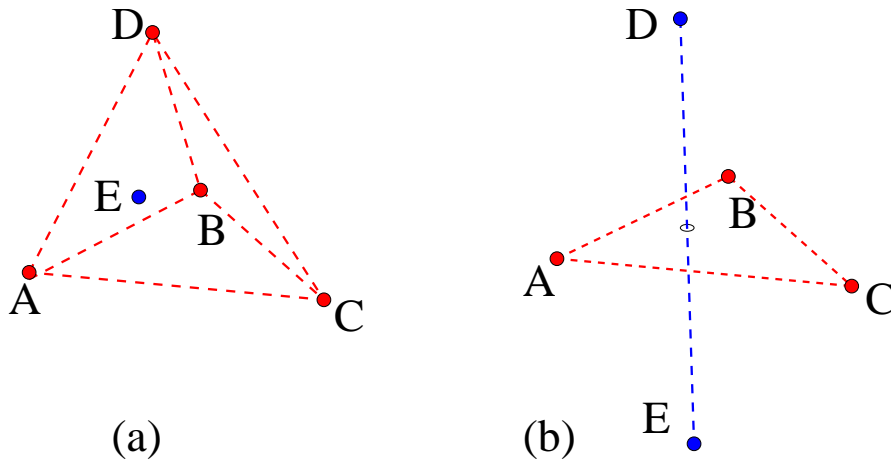
Figure 2.3: Illustration of the Radon partition in three dimensions. There exist two possible partitions into two sets (marked blue and red) of the 5 points A, B, C, D, E in three dimensions such that their convex hulls (marked with dashed lines) intersect. **Left:** In (a) the point E (blue) lies within the simplex formed by (A, B, C, D). **Right:** In (b) none of the vertices lies within the simplex formed by the other ones.

(a)   (b)
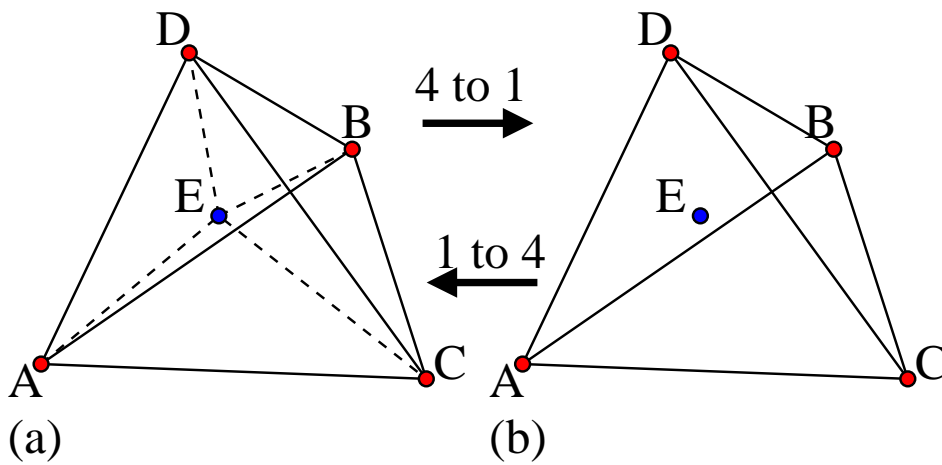
Figure 2.4:   Possible triangulation of five points in three dimensions (insertion case). The vertex E has been marked blue and edges that are invisible from all directions have been drawn with dashed lines.   In the case (a) one has exactly four simplices: $(A, B, C, E), (A, B, D, E), (A, C, D, E), (B, C, D, E)$, whereas in picture (b) the unconnected vertex E lies within the simplex (A, B, C, D). Switching between the two configuration corresponds to adding $(1 \rightarrow 4)$ the vertex E to an existing triangulation or deleting it $(4 \rightarrow 1)$, respectively. Note that for these operations to be possible, the point E must lie within the simplex (A, B, C, D).

case in figure 2.4 left panel) is rarely ever present in a triangulation. In addition, in three dimensions there exist polyhedra (for example Schönhardts polyhedron [34]) that do not admit a decomposition into simplices having only the polyhedral boundary points as endpoints. Additional points (called Steiner points) need to be introduced to obtain a tetrahedralization of these polyhedra [35]. These problems complicate the deletion of vertices from three-dimensional triangulations [36].

The second partition in figure 2.3 right panel requires a more careful evaluation (see figure 2.5). The
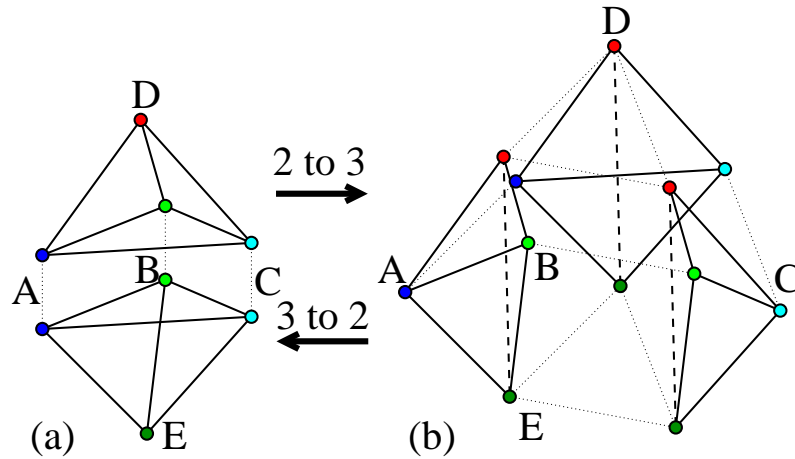
Figure 2.5: Possible triangulation of five points in three dimensions (connection case). In (a) there are two simplices: $(A, B, C, D), (A, B, C, E)$, sharing the common triangle (A, B, C), whereas picture (b) consists of three simplices $(A, B, D, E), (B, C, D, E), (C, A, D, E)$. The simplices have been taken apart for clarity and the dotted lines have been drawn to connect the identical points (drawn in like colours). Edges invisible from all directions have been drawn with dashed lines. Note that the flips can only be performed, if the polyhedron (A, B, C, D, E) is convex, since otherwise the flips will result in overlaps with additional neighbouring simplices (not shown here).

flip $2 \rightarrow 3$ replaces two simplices by three simplices and thereby automatically creates a connection between previously unconnected vertices. In adjacency detection, this corresponds to establishing a neighbourship relation. The flip $3 \rightarrow 2$ reverses the operation. Note that these flips can only be performed if the polyhedron formed by the five points in $\mathbb{R}^3$ is convex, otherwise the operation would yield overlapping simplices in the triangulation. The convexity of (A, B, C, D, E) in figure 2.5 can be tested by checking if for every edge A, B and B, C and C, A there exists a hyperplane which has the remaining three points $(D, E, A/B/C)$ on the same side [29, 30, 37], which becomes evident in figure 2.3 right panel. In the following, the different flip operations will be shortly denoted by the transformation operators $\mathcal{F}_{14}, \mathcal{F}_{41}, \mathcal{F}_{23}$, and $\mathcal{F}_{32}$.

2.3.3 The Delaunay Criterion

Every tetrahedron $(\boldsymbol{v}_1, \boldsymbol{v}_2, \boldsymbol{v}_3, \boldsymbol{v}_4)$ in $\mathbb{R}^3$ has a uniquely defined circumsphere, if the four vertices $\boldsymbol{v}_i$ are in general position. Then, the position and radius of the circumsphere can be derived from the four sphere equations

$$(\boldsymbol{m} - \boldsymbol{v}_i)^2 = R_m^2 \qquad i = 1, \dots, 4, \tag{2.5}$$

where $\boldsymbol{m}$ defines the position and R_m defines the radius of the sphere (see figure 2.7 left panel). This gives rise to the central definition of this section:

> The **Delaunay triangulation** is a triangulation where all the simplices satisfy the **Empty-Circumsphere-Criterion**, that no vertex of the triangulation may lie inside the circumspheres of the triangulation simplices.

Thus, the Delaunay triangulation is uniquely defined if the vertices fulfil the extended general position assumption [33] (see figure 2.6).

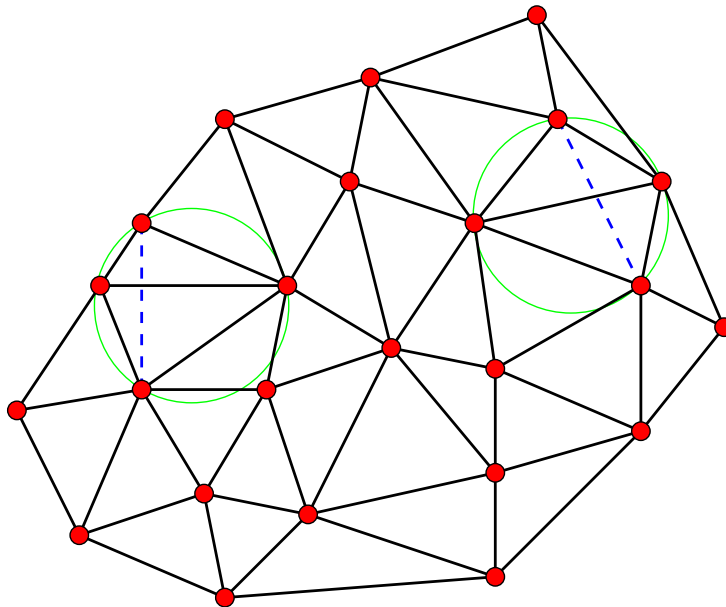**Figure 2.6:** Example of a two-dimensional Delaunay triangulation. Vertices (red) are connected to simplices that fulfil the Delaunay criterion. In this example, there are two locations where a different triangulation (dashed lines) would also fulfil the Delaunay criterion, as the extended general position assumption is not fulfilled: In these locations, four points reside on the same circle (green).

The Delaunay criterion can be extended towards a more general concept: By extending the Euclidean distance measure to vertices with weights, one defines the orthogonal distance between $\hat{x} = (x, \omega_x)$ and $\hat{y} = (y, \omega_y)$ as

$$\pi(\hat{x}, \hat{y}) = (x - y)^2 - \omega_x - \omega_y, \tag{2.6}$$

which sacrifices positive definiteness. For positive weights $\omega_x > 0$ these vertices can be associated with balls situated at x having the radius $R_x = \sqrt{\omega_x}$. Two weighted vertices $\hat{x}$ and $\hat{y}$ are then called **orthogonal** if $\pi(\hat{x}, \hat{y}) = 0$ in equation (2.6). Consequently, the **orthosphere** of a set of n weighted vertices is defined as the set of all weighted points being orthogonal to all n vertices. For example, in three dimensions the orthosphere $(m_\perp, R^2_{m\perp})$ of the four weighted vertices $\hat{v}_1 = (v_1, R^2_1), \hat{v}_2 = (v_2, R^2_2), \hat{v}_3 = (v_3, R^2_3), \hat{v}_4 = (v_4, R^2_4)$ is defined by the four equations

$$(m_\perp - v_i)^2 = R^2_{m\perp} + R^2_i. \tag{2.7}$$

Naturally, for equal weights $R_i = R_{\text{sphere}}$, this definition reduces to the normal circumsphere criterion (2.5) with $R^2_m = R^2_{m\perp} + R^2_{\text{sphere}}$. The naming "orthogonal" results from the fact that the orthosphere intersects the spheres associated with the vertices perpendicularly (see figure 2.7 right panel). Consequently, the extended criterion reads:

> The **regular Delaunay triangulation** is a triangulation where all the simplices satisfy the **Empty-Orthosphere-Criterion**, implying that no weighted vertex of the triangulation may lie inside the orthospheres of the triangulation simplices.

The simplest method to determine whether a weighted vertex V lies outside or inside the circumsphere/orthosphere of a simplex (A, B, C, D) is to solve the associated four sphere equations (2.5) or (2.7) in the weighted case. However, this problem can be solved more efficiently by adding one more dimension [27, 30, 32, 38]. In this ansatz, the coordinates in $\mathbb{R}^n$ are projected onto a paraboloid in $\mathbb{R}^{n+1}$ via

$$\hat{A} = (A; \omega_A) = (A_1, \ldots, A_n; \omega_A) \rightarrow A^+ = \left(A_1, \ldots, A_n, \sum_i A^2_i - \omega_A\right). \tag{2.8}$$

In the three-dimensional case, the four points A^+, B^+, C^+, D^+ thus define a hyperplane in $\mathbb{R}^4$. If E is within the circumsphere of (A, B, C, D), then E^+ will be below this hyperplane in $\mathbb{R}^4$ and above otherwise. Consequently, the in-circumsphere-criterion in $\mathbb{R}^3$ reduces to a simple orientation computation in $\mathbb{R}^4$, as is illustrated for a one-dimensional example in figure 2.8.
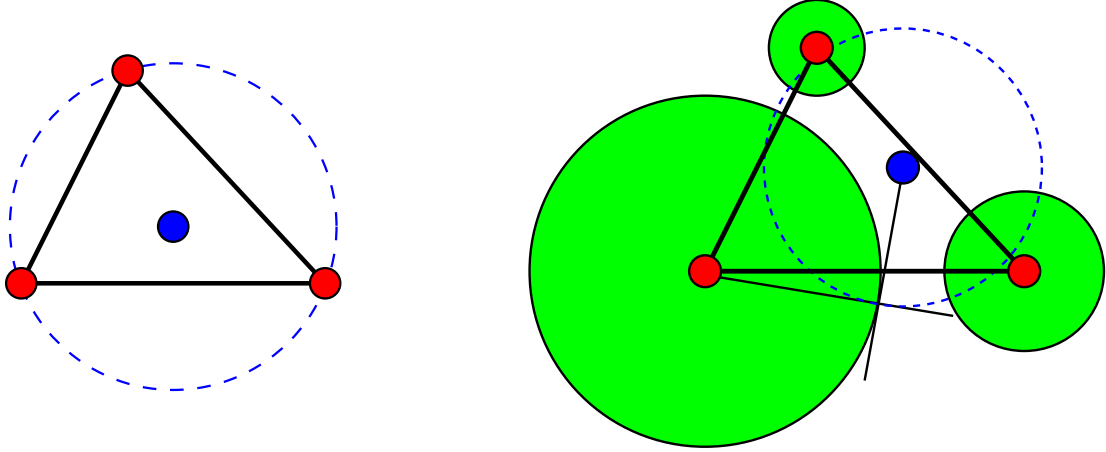
Figure 2.7: Two-dimensional illustration of circumspheres and orthospheres. **Left:** Circumsphere (dashed blue) of a 2-simplex in $\mathbb{R}^2$. **Right:** Orthosphere (dashed blue) resulting from the same vertices, supplemented with different positive weights $\omega_i = R_i^2$ (green circles). The orthosphere intersects perpendicularly with the vertex spheres.

By virtue of this lifting transformation one finds [27]

$$
\begin{aligned}
\text{in\_ortho\_sphere}[(\hat{A}, \hat{B}, \hat{C}, \hat{D}), \hat{E}] &= \text{oriented}(A^+, B^+, C^+, D^+, E^+) \\
&= \text{sign}
\begin{vmatrix}
A_x & A_y & A_z & A_x^2 + A_y^2 + A_z^2 - \omega_A & 1 \\
B_x & B_y & B_z & B_x^2 + B_y^2 + B_z^2 - \omega_B & 1 \\
C_x & C_y & C_z & C_x^2 + C_y^2 + C_z^2 - \omega_C & 1 \\
D_x & D_y & D_z & D_x^2 + D_y^2 + D_z^2 - \omega_D & 1 \\
E_x & E_y & E_z & E_x^2 + E_y^2 + E_z^2 - \omega_E & 1
\end{vmatrix} \\
&= \text{sign}
\begin{vmatrix}
A_x - E_x & A_y - E_y & A_z - E_z & (A_x^2 + A_y^2 + A_z^2 - \omega_A) - (E_x^2 + E_y^2 + E_z^2 - \omega_E) \\
B_x - E_x & B_y - E_y & B_z - E_z & (B_x^2 + B_y^2 + B_z^2 - \omega_B) - (E_x^2 + E_y^2 + E_z^2 - \omega_E) \\
C_x - E_x & C_y - E_y & C_z - E_z & (C_x^2 + C_y^2 + C_z^2 - \omega_C) - (E_x^2 + E_y^2 + E_z^2 - \omega_E) \\
D_x - E_x & D_y - E_y & D_z - E_z & (D_x^2 + D_y^2 + D_z^2 - \omega_D) - (E_x^2 + E_y^2 + E_z^2 - \omega_E)
\end{vmatrix},
\end{aligned}
\tag{2.9}
$$

where a positive sign is to be taken as an affirmative answer, if the simplex (A, B, C, D) is positively oriented in three dimensions.

Obviously, for numerical implementations, the error induced by numerical inaccuracy will become important if the determinants in (2.9) are close to zero. Therefore, the exact arithmetics as proposed by [39] had been extended to a form supporting weights [40], which has been used within this thesis (see appendix A).

The lifting transformation therefore gives rise to a different viewpoint of Delaunay triangulations: An n-dimensional Delaunay triangulation is determined by the boundary of the convex hull of the lifted
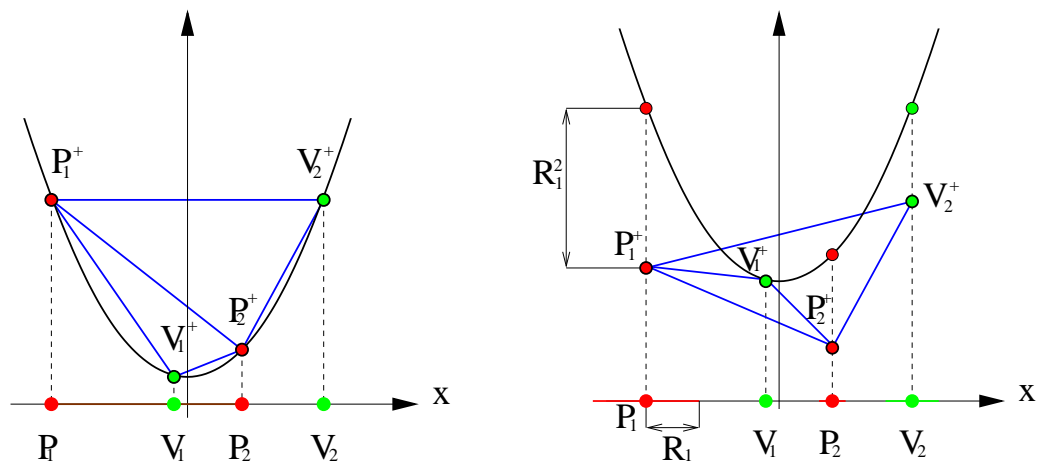
Figure 2.8: Illustration of the lifting transformation in one dimension. **Left:** Reduction of the insphere criterion in one spatial dimension to an orientation computation in two dimensions. All points are projected onto a paraboloid in two dimensions. Then, the question whether V_i (green border-less points) is within the circumsphere (brown line) of the (P_1, P_2) (red border-less points) is equivalent to asking whether (P_1^+, P_2^+, V_i^+) is positively oriented (blue triangles). **Right:** For power-weighted triangulations, the weights (indicated by the coloured bars on the x-axis) shift the vertices off the paraboloid by the squared radius (exemplified for the vertex P_1 only). This example demonstrates that a weighted vertex may lie within the normal circumsphere of a simplex, but not within its orthosphere. For this example, neither V_1 nor V_2 lie within the weighted circumsphere of (P_1, P_2).

vertices in $n + 1$ dimensions.

Within this thesis, the following definition of adjacency will be used: Two vertices are called **adjacent** if they are endpoints of the same simplex (i. e., if they are connected in the Delaunay triangulation) and two simplices are adjacent if they share a common face. Natural adjacency for a set of spheres is defined by the weighted Delaunay triangulation and the involved vertices/simplices will be called (mutual) **neighbours**.

2.3.4 Implementation and Data Structure

Unlike in two dimensions, where a constant number of vertices implies a constant number of simplices [28] – regardless of their relative position, in three-dimensional kinetic triangulations the number of simplices will change even for constant numbers of moving vertices. Therefore, kinetic triangulations in three dimensions will require efficient support for insertion and deletion of simplices. Furthermore, since in addition the number of vertices is allowed to change for dynamic triangulations, the same holds true for the vertices. A list provides efficient access for both operations.

The main elements of a vertex are a position and a weight

$$\hat{V} = (\textbf{double } x, \textbf{double } y, \textbf{double } z, \textbf{double } \omega) \,. \tag{2.10}$$

Within the numerical implementation, for efficiency reasons a vertex as well contains vectors of adjacent neighbour vertices and adjacent simplices, that are dynamically updated. Since the information of the triangulation is completely stored within the vertices, it would normally suffice to store the simplices as pointers on four vertices. However, the walking strategy employed for point location (compare subsection 2.3.7) requires for efficient access that simplex-simplex-adjacency is stored within the simplices as well [41]. Therefore, in this implementation a simplex in addition contains information on its neighbours

$$\mathcal{S} = \left(\hat{V}_1^{\text{ptr}}, \hat{V}_2^{\text{ptr}}, \hat{V}_3^{\text{ptr}}, \hat{V}_4^{\text{ptr}}, \mathcal{S}_{1,\text{opp}}^{\text{ptr}}, \mathcal{S}_{2,\text{opp}}^{\text{ptr}}, \mathcal{S}_{3,\text{opp}}^{\text{ptr}}, \mathcal{S}_{4,\text{opp}}^{\text{ptr}} \right) \,, \tag{2.11}$$

where $\mathcal{S}_{i,\text{opp}}^{\text{ptr}}$ denotes a pointer to the adjacent simplex opposite to vertex $\hat{V}_i$. Furthermore, for efficiency the simplices contain a placeholder for a point denoting its weighted centre and a set of flags denoting the Delaunay status of its faces to avoid superfluous calculations of the Delaunay property. Note, that in order to avoid many orientation calculations, the used implementation automatically constructs its simplices in a positively-oriented way.

The triangulation has been implemented in the object-oriented programming language C++ [42] as an independent class that is capable of triangulating balls. These balls can be connected with in principle arbitrary objects, which opens a wide range of applications: The triangulation may be used

for adjacency/collision detection of cells, grains, atoms or other objects that can be approximated by a spherical shape. In the context of this thesis, these objects are biological cells of an off-lattice agent-based simulation.

In addition, the class provides test functions, calculations of (weighted) Voronoi volumes and contact surfaces, etc.

2.3.5   Delaunay Maintenance for kinetic vertices

Within the context of adjacency detection between a number of moving agents, any triangulation will have to cope with the fact that adjacencies may change. Reconstruction of the triangulation using the incremental construction (see subsection 2.3.6) would be a method with a poor algorithmic scaling. If only a small subset of vertices is moving, a simple method handling them would be to delete them at their old position and to perform an insertion at the new position [25, 43], which necessarily requires insertion (subsection 2.3.6) and deletion (subsection 2.3.8) to be implemented first. Since these operations would involve too many simplices, a more efficient approach has been chosen here:

Evidently, in the case of moving vertices the Delaunay criterion may be violated, i. e., after the vertices have moved one may end up with a triangulation where some vertices reside within the (weighted) circumspheres of the simplices. Even worse, if the vertices move too far, e. g. if one vertex moves inside another simplex, the triangulation will become invalid (contain overlapping simplices), compare subsection 2.3.1 and figure 2.9 right panel. In the present implementation, this must be avoided by either computing a safe maximum stepsize [26] (see subsection 2.3.8) or by simply keeping the displacements safely small. Within this thesis, the first approach has been chosen.

Therefore, the problem to be solved is that after vertex movement one is left with a valid triangulation which possibly violates the Delaunay criterion.

Reconstructing the whole triangulation is usually not an option for large data sets. The elementary topological transformations in subsection 2.3.2 however can be exploited to restore the Delaunay criterion. Since neither vertices will be added nor deleted in this subsection it is evident that the flips $\mathcal{F}_{14}$ and $\mathcal{F}_{41}$ are not necessary. This however will be different for for weighted triangulations, as vertex movement might lead to trivial (unconnected) vertices that are not endpoints to any simplices. In this thesis, such cases are not considered, since they correspond to physically unrealisable situations anyway: If the sphere associated with a vertex is not completely covered by the spheres of other vertices (realistic case), the vertex will be connected in the triangulation [27]. If only two spheres are involved, this would correspond to a small sphere that is completely covered by a larger one. Consequently, the transformations $2 \rightarrow 3$ and $3 \rightarrow 2$ will suffice to transform the given triangulation

into a Delaunay triangulation [27, 29, 30]. Note that the application has to ensure that the vertex trajectories satisfy the above conditions (for a possible solution see subsection 2.5.2). With a glance at figure 2.5 one can see that indeed $\mathcal{F}_{23}$ effectively creates a neighbourship connection, whereas the flip $\mathcal{F}_{32}$ destroys it. Therefore, routines have been implemented to check either the complete list of simplices or only a small subset for violations of the Delaunay criterion. The simple data structure enables a convenient calculation of the flip criteria in three dimensions. The main advantage of the flip algorithm is that it is – in average – linear in the number of simplices, which is linear with the number of vertices in most practical applications. The list of simplices is iterated through to check every simplex (called **active simplex** in this context) for flipping-possibilities with its neighbours (**the passive simplices**). Thus, for every simplex S in the list the following tests (in the given order) are performed

1. The operation $\mathcal{F}_{23}$ is performed on S and its passive neighbour simplex N_i ($i = 1, 2, 3, 4$) if

   - the neighbour pair (S, N_i) violates the Delaunay criterion, i. e., the opposing vertex of the neighbour N_i lies within the circumsphere of S (and *vice versa*[3]) and

   - the five points in the union of the two simplices lie on the boundary of the convex hull of the associated polyhedron.

   The first condition implies the invalidation of the Delaunay criterion, and the second condition is necessary to ensure for convexity of the simplex pair. Technically, it suffices in the last criterion to check whether for all edges of the common triangle [without loss of generality (S_A, S_B, S_C)] there exists a hyperplane containing the edge that has the simplices (S_A, S_B, S_C, S_D) and $(S_A, S_B, S_C, N_{opp}^i)$ on the same side [29, 30] (see figure 2.9 left panel).

2. If no flip $\mathcal{F}_{23}$ has been performed, the algorithm checks the neighbouring simplex triples for $\mathcal{F}_{32}$. The operation $\mathcal{F}_{32}$ is performed on S and its neighbours $N_i \neq N_j$ if

   - the simplices N_i and N_j are mutual neighbours and

   - the neighbour pairs (S, N_i), (S, N_j) and (N_i, N_j) mutually[4] violate the Delaunay criterion.

   Note that in three dimension the first condition already ensures for convexity of the set of five points.

---

[3]Note that Delaunay invalidity of (S, N_i) automatically implies Delaunay invalidity of (N_i, S), since an algebraically equivalent determinant has to be computed.

[4]Due to algebraic equivalence it suffices to calculate the violation of the Delaunay criterion just once.

3. If a flip operation has been performed, the new simplices must be inserted at the end of the list of simplices to be checked again. In contrast, if neither the operations $\mathcal{F}_{23}$ nor $\mathcal{F}_{32}$ have been performed, it could either be the case that the simplex S is Delaunay-valid (which is the normal case) or that a $\mathcal{F}_{23}$ operation has been impossible due to a non-convex point configuration. At this stage, such non-convex configurations are detected and following a practitioners approach the corresponding active simplex is spliced to the end of the list.

The algorithm terminates as the end of the list of simplices is reached. Afterwards either all simplices fulfil the Delaunay property or in rare cases it is possible that the algorithm ends up with a non-flippable configuration. In this case, the Delaunay property is recovered by complete reconstruction.
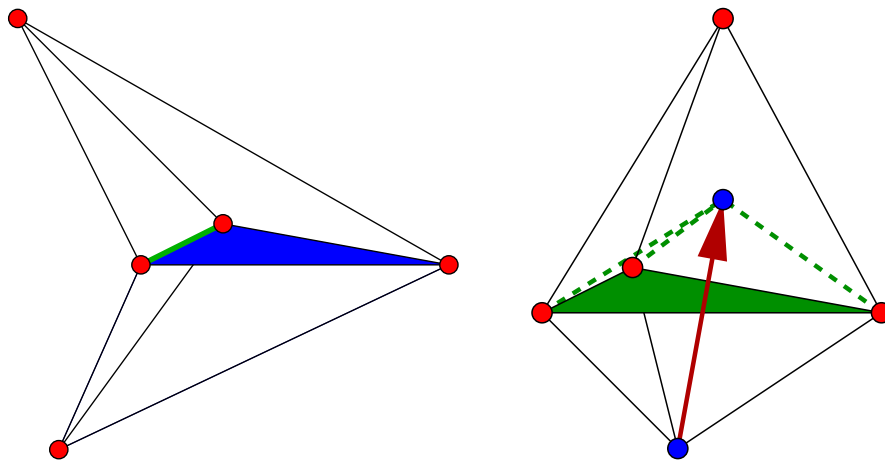
Figure 2.9: Three-dimensional non-flippable and invalid triangulations of five points. Edges that are invisible from all directions have been drawn with dashed lines. **Left:** For one edge (green) of the common triangle (blue) there exists no hyperplane having both simplices on the same side. Therefore, the configuration cannot be transformed by flips without changing the occupied volume: If an $\mathcal{F}_{23}$ operation would be performed, overlaps with neighbouring simplices (not shown here) would result. **Right:** If for kinetic vertices the step-size is not limited, a vertex (blue) may move into another simplex. As in the data structure simplices are realised as references on vertices, this results in an invalid triangulation (dashed lines).

Recall however, that for these flips to be possible, all simplices must be disjoint (the intersection of two simplices may at most be a triangle), i. e., the triangulation must be valid (compare figure 2.9). The flips as introduced here however only relate to valid triangulations and do not change the volume occupied by the simplices. Therefore, they cannot be used to recover from such a situation [27]. By computing a maximum stepsize for the vertex kinetics, such situations can be avoided (compare subsection 2.3.8). It is the task of the application using the module to ensure for that. Note that – though internally all vertex movements are performed in an asynchronous manner – the implementation supports a synchronous update of vertex movements for external applications.

2.3.6 *Incremental Delaunay Construction*

In Delaunay triangulations the insertion of one new vertex can change the whole triangulation, but this only holds true for some extreme vertex configurations [28]. In practice, the effect of adding a new vertex to a Delaunay triangulation will nearly always be local.

A valid Delaunay triangulation with n vertices can be supplemented with a new vertex lying within its convex hull by the following algorithm (see figure 2.10):

1: Identify all invalid simplices in the triangulation.
   {These contain the new vertex within their circumsphere.}
2: Collect the external faces of the invalid simplices.
   {Those are the triangles facing valid simplices.}
3: Replace the invalid simplices by new ones formed via combining the external faces with the new vertex.

Evidently, the validity of the simplices not contained in the list defined by step 1 of the algorithm will not be harmed, as only one vertex is added. In addition, the circumspheres (orthospheres) of the created simplices (third step) cannot contain vertices of the external faces, since these lie exactly on the orthospheres. Note however, that for weighted triangulations vertices might be disconnected by this procedure, if they are not part of the external faces but belong to the list of invalid simplices. Here, such cases can be detected and the vertex can be rejected, before any changes are performed. In addition, for weighted triangulations the simplex containing the new vertex within its convex hull is not necessarily invalid, since its orthosphere does not generally contain the complete simplex, compare figure 2.7. If no orthosphere contains the new vertex, then this case corresponds to the case of a vertex unconnected to the triangulation – the vertex is trivial and would therefore be unconnected in the triangulation.

In the case of vertex acceptance the result of this procedure is a Delaunay triangulation with $n + 1$ vertices. Note that for the above-mentioned extreme cases the list of invalid simplices would contain all simplices of the triangulation.

This incremental algorithm is called **Bowyer-Watson Algorithm** [44, 45]. Once all the invalid simplices have been found, its computational cost is very low (linear with the total number of invalid simplices). At first, it actually suffices to find the one simplex which contains the new vertex within its convex hull – the remaining simplices can be found by iteratively checking all neighbours for violating the Delaunay criterion with the new vertex (compare figure 2.10).

The algorithm shown in figure 2.10 is slightly different from the **Green-Sibson Algorithm** [44], which needs the simplex containing the new vertex as an input. Then the elementary topological
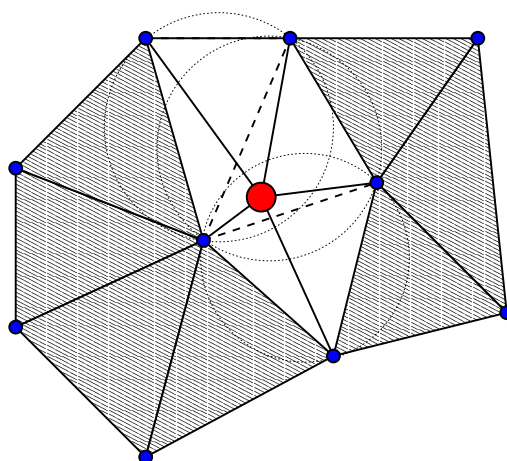
Figure 2.10: Two-dimensional illustration of the Bowyer-Watson algorithm. In this example, a new vertex (large red point) is inserted into an existing triangulation (not all simplices are shown). Most of the simplices remain valid (shaded region), but 3 simplices (dashed lines) contain the new vertex within their circumspheres (dotted lines). These are replaced by 5 new simplices (solid lines) formed by the new vertex and the external faces (lines in two dimensions). The resulting triangulation automatically fulfils the Delaunay criterion.

transformation $\mathcal{F}_{14}$ (see figure 2.4) is performed with this simplex and the resulting triangulation (that possibly violates the Delaunay criterion) is transformed to a Delaunay triangulation by performing $\mathcal{F}_{23}$ and $\mathcal{F}_{32}$ flips (figure 2.5), until all simplices fulfil the Delaunay property (see subsection 2.3.5).

These construction algorithms differ from the face expansion approach [40], where the triangulation is constructed starting from a single vertex by expanding the faces of the previous triangulation with unconnected vertices. The face expansion ansatz has a non-favourable scaling, but displays a fast performance for small vertex numbers.

The initial triangulation can be represented by an artificial large simplex which contains all the data to be triangulated within its convex hull. Therefore, the convex hull of the points to be triangulated is contained within the artificial simplex, i. e., the boundary of the convex hull of the total triangulation is static. In the framework of kinetic proximity structures this has the advantage that one does not have the problem of maintaining the convex hull of moving points. The initial simplex must therefore be large enough to contain the data within its insphere throughout the full time evolution of the simulation[5].

---

[5]One choice for such an initial simplex is a CH_4 configuration, where the carbon atom resides at the origin and the four hydrogen atoms are the endpoints of the artificial simplex.

2.3.7   Localisation of Simplices

The incremental insertion algorithm requires an initial simplex that contains the new vertex within its (weighted) circumsphere. Such a simplex can be found by locating the simplex that contains the new vertex within its convex hull. Many implementations of Delaunay triangulations perform a walk in the triangulation, for an overview of different walking strategies see e. g. [46]. Note that points can be located by using the triangulation construction history (e. g. using the so-called history dag [47] or Delaunay tree [44]) as well. However, within this thesis kinetic triangulations will be used, where the length of a history stack could not be controlled.

Therefore, a stochastic visibility walk [46] to locate a simplex containing a point will be discussed. Starting with an arbitrary initial simplex A and a new vertex $\hat{v}$ to be inserted in the triangulation, in the normal visibility walk one of the four neighbour simplices of A is chosen using the following criterion:

1: for all four vertices $\hat{a}_{i=1,2,3,4}$ of the simplex A check with the new vertex $\hat{v}$:
    Are the vertices $\hat{a}_i$ and $\hat{v}$ on different sides of the plane defined by the other three vertices $\hat{a}_{j \neq i}$?
    {An equivalent question is: Are the vertices mutually invisible if the plane is non-transparent?}

2: **if** yes **then**

3:      Jump to the simplex opposite to a_i.

4: **end if**

5: If no neighbour simplex is found, the vertex v is contained within the simplex A {and the destination is thus reached} or the walk has left the triangulation.

For a valid triangulation, the walk can only leave the triangulation if the new vertex lies outside the convex hull, which has been excluded by assumption.

Obviously, the algorithm can take different pathways (see figure 2.11) since there may be more than one neighbour fulfilling the criterion. Which path is actually chosen, depends on the order of testing the four vertices of the simplices. Due to numerical roundoff errors the normal visibility walk – that does not contain any stochastic elements – may loop when triangulating regular lattices (such as cubic, . . .) that violate the general position assumption. Such situations can be avoided by using the stochastic visibility walk, where the order of the vertices to be checked is randomised. The stochastic visibility walk terminates with unit probability [46].

The complexity of the walk is directly proportional to the length of the path – measured in units of traversed simplices. For n uniformly distributed vertices for example, the average total number of simplices will grow linearly (n) with the number of vertices, whereas one can expect the average distance between two arbitrarily selected simplices to grow like $n^{1/3}$. Once the invalid simplex has

been found, the average remaining complexity for the incremental insertion will be in average constant (in n). Therefore, one can expect the overall theoretical complexity to behave like $\alpha n^{4/3} + \beta n$ for uniformly distributed points (compare appendix A.1) and in higher dimensions d as $\alpha n^{1+1/d} + \beta n$ [26, 48]. The algorithms with the best known scaling have an expected complexity of $O(n \log n)$ [29, 33],
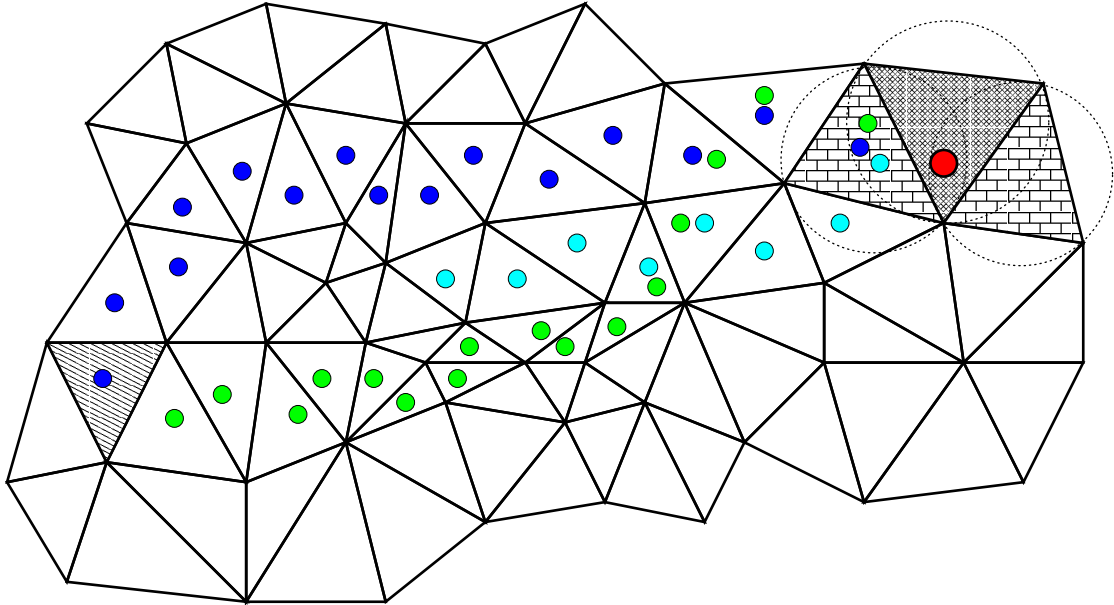
Figure 2.11: Two-dimensional illustration of the stochastic visibility walk. Not all simplices are shown. Starting from the hatched initial simplex, the algorithm finds a way towards the invalid cross-hatched simplex that contains the new vertex (large point). As indicated by the smaller coloured points, the algorithm may take different pathways towards its destination, if the stochastic version is chosen. The time necessary for the walk algorithm is proportional to the number of traversed simplices.

but for the purposes of kinetic triangulations the incremental construction algorithm is needed just once and therefore its actual performance is not dominantly important.

Obviously, the efficiency of the algorithm strongly depends on a good choice of the starting simplex. The method can therefore be improved by checking whether the new vertex lies within a certain subregion which means preprocessing, or it can be sped up by initially using larger stepsizes, e. g. by using several triangulations of subsets of vertices [49]. Alternatively, one can choose the closest vertex out of a random subset of the triangulation to find a good starting simplex [50]. The last method does not require the maintenance of an additional triangulation in the case of kinetic vertices. In many practical simulations, some neighbourship relations may already be known when building the initial triangulation. The implementation in this thesis expects the vertices to be included in order, such that

successive vertices are very close to each other in the final triangulation and therefore chooses the starting simplex in the walk algorithm as being the last simplex created if no other guess is given. Especially for processes as cell proliferation, the choice of a starting simplex is evident: New cells can be created by cell division, which corresponds to the insertion of a new vertex close to an existing one. Consequently, one always has a nearly perfect guess for the starting simplex in these cases.

2.3.8 Incremental Vertex deletion

In many problems (e. g. mesh generation) the deletion of vertices from a Delaunay triangulation is not of great importance, since there is no great advantage other than a negligible gain in efficiency. However, if the triangulation is used for example for proximity structures or data interpolation, vertex deletion may become important. Within the context of this thesis, vertex deletion corresponds to the removal of agents from the system – usually as a consequence of cell death.

Several algorithms have been developed to manage the deletion of vertices in two dimensions [51, 52, 53]. There exist some fundamental differences between the two-dimensional and the higher-dimensional case. Simply removing a vertex together with its incident simplices leaves a star-shaped hole in the triangulation, which is not necessarily convex. Unlike in the two-dimensional case, where a star-shaped polygon always admits a triangulation which can be transformed by flips into the Delaunay triangulation [51, 52] in three dimensions a general star-shaped polyhedron may not admit a tetrahedralization without insertion of artificial points. The simplest example for such a polyhedron is Schönhardt's polyhedron [34], reported among others in [36, 54]. However, it has been proven in [55] that the holes emerging in unconstrained Delaunay triangulations via removal of vertices with their incident simplices will always possess a tetrahedralization[6].

Another approach for deletion is given in [56], where the triangulation construction history is used to reconstruct the triangulation without the corresponding vertex. For the same reasoning as before, this approach is not favourable for kinetic triangulations.

Deletion via Vertex-Merging

The basic idea of this approach is to move the corresponding vertex towards its nearest neighbour in several steps, each followed by a sequence of flips $\mathcal{F}_{23}$ and $\mathcal{F}_{32}$ restoring the Delaunay property, until the simplices between the two vertices are very flat and can be removed from the triangulation

---

[6]This does not generally hold true for constrained Delaunay triangulations [36], i. e., triangulations where the boundary of the convex hull is fixed to a given (not necessarily convex) shape.

without harming its validity [26]. Thus, the problem of vertex deletion is mapped to the problem of Delaunay maintenance for kinetic vertices. Figure 2.12 illustrates the idea of the algorithm.

(a)   (b)
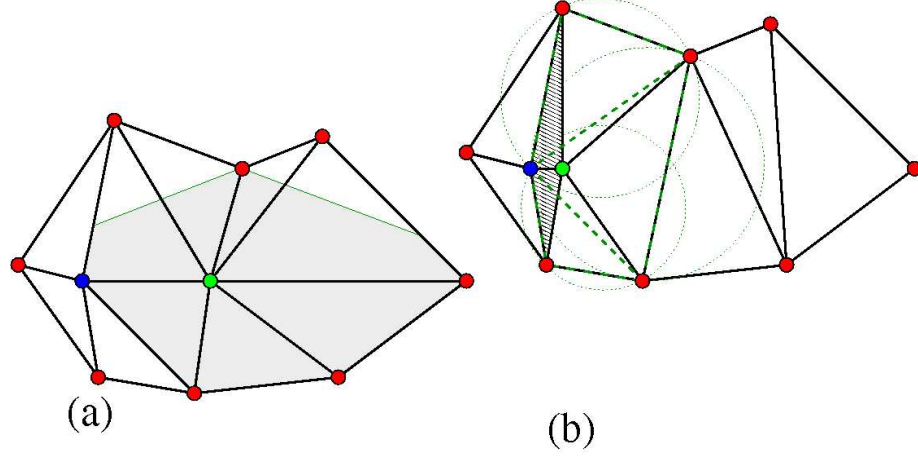
Figure 2.12: Two-dimensional illustration of vertex deletion from a Delaunay triangulation (not all simplices are shown). **Left:** The vertex to be deleted (green point) is moved in several steps followed by flips restoring the Delaunay property towards its closest neighbour (blue point), until the inner simplices (shaded region) can be safely deleted. The area within which the green vertex can move without invalidating the triangulation is marked in light grey. **Right:** Afterwards, the two vertices are simply merged and the remaining opposing simplices are connected as neighbours (green dashed lines). This corresponds to the last step and therefore the Delaunay criterion is finally restored by using flips.

The main questions to be answered all reduce to the problem of the stepsize. How far can a vertex v_i be moved into a certain direction Δ without invalidating the triangulation, i. e., without creating overlapping simplices? Such overlapping simplices can be created if the vertex v_i penetrates one of the planes defined by the opposite faces of its incident simplices (compare figure 2.12 left panel). If overlapping simplices occur, the orientation of at least one of the simplices incident to v_i will change. Consequently, one can derive a stepsize criterion by demanding that the orientation of the simplices incident to v_i does not change sign. One can define the pseudo-orientation of a simplex $S_i = (A^{(i)}, B^{(i)}, C^{(i)}, D^{(i)})$ as follows:

$$
\mathcal{V}_0^{(i)} = \begin{vmatrix} A_x^{(i)} & A_y^{(i)} & A_z^{(i)} & 1 \\ B_x^{(i)} & B_y^{(i)} & B_z^{(i)} & 1 \\ C_x^{(i)} & C_y^{(i)} & C_z^{(i)} & 1 \\ D_x^{(i)} & D_y^{(i)} & D_z^{(i)} & 1 \end{vmatrix} = \begin{vmatrix} A_x^{(i)} - B_x^{(i)} & B_x^{(i)} - C_x^{(i)} & B_x^{(i)} - D_x^{(i)} \\ A_y^{(i)} - B_y^{(i)} & B_y^{(i)} - C_y^{(i)} & B_y^{(i)} - D_y^{(i)} \\ A_z^{(i)} - B_z^{(i)} & B_z^{(i)} - C_z^{(i)} & B_z^{(i)} - D_z^{(i)} \end{vmatrix}, \tag{2.12}
$$

where after the second equality the terms have been reordered, such that the vertex to be moved –
without loss of generality A – is in the first column. In fact, this is – up to a factor of $1/6$ – the
signed volume of the simplex S_i. Now suppose that A is moved along the direction of Δ, i. e.,
$A \rightarrow A' = A + \lambda \Delta$ with $\lambda > 0$ and $\Delta = (\Delta_x, \Delta_y, \Delta_z)$. For the algorithm the vector Δ will point to the
next neighbour of A. Then the new pseudo-orientation is obtained via

$$\mathcal{V}_1^{(i)} = \mathcal{V}_0^{(i)} + \lambda \begin{vmatrix} \Delta_x & B_x^{(i)} - C_x^{(i)} & B_x^{(i)} - D_x^{(i)} \\ \Delta_y & B_y^{(i)} - C_y^{(i)} & B_y^{(i)} - D_y^{(i)} \\ \Delta_z & B_z^{(i)} - C_z^{(i)} & B_z^{(i)} - D_z^{(i)} \end{vmatrix} . \tag{2.13}$$

If the orientation of the simplex $S_i = (A_i, B_i, C_i, D_i)$ is not allowed to change, this produces a constraint
on λ

$$\lambda \leq \lambda_i^{\max} = \frac{\left| \left(\mathcal{V}_0^{(i)} \right) \right|}{\text{abs} \begin{vmatrix} \Delta_x & B_x^{(i)} - C_x^{(i)} & B_x^{(i)} - D_x^{(i)} \\ \Delta_y & B_y^{(i)} - C_y^{(i)} & B_y^{(i)} - D_y^{(i)} \\ \Delta_z & B_z^{(i)} - C_z^{(i)} & B_z^{(i)} - D_z^{(i)} \end{vmatrix}} . \tag{2.14}$$

In order to secure the validity of the triangulation, this check has to be performed for all simplices
incident to the moving vertex A, i. e., with

$$\lambda \leq \lambda^{\max} = \min_{S_k : A \in S_k} \lambda_k^{\max} \tag{2.15}$$

one has an overall measure of the maximum step size of A in the direction of Δ. If $\lambda^{\max} > 1$,
then the vertex can simply be moved along the complete path $(\Delta_x, \Delta_y, \Delta_z)$ without invalidating the
triangulation, whereas if $\lambda^{\max} < 1$ the vertex A can only be moved by a fraction $\alpha \Delta \; : \; \alpha < \lambda^{\max}$. Note
that technically, the determinants in equation (2.14) can be rewritten as the orientation of a virtual
simplex, such that adaptive precision arithmetics [39] can be applied in the control of the step-sizes.
If one defines A' to be the nearest neighbour of A, these vertices will in three dimensions have at least
three simplices in common, if they do not reside directly on the boundary of the convex hull of the
triangulation. A subset of the simplices incident to A can be defined as the set of all simplices that
are incident to A, but not to A'. For these, one can define the quantity λ_{REST} in analogy to λ via

$$\lambda_{\text{REST}}^{\max} = \min_{S_k : A \in S_k \wedge A' \notin S_k} \lambda_k . \tag{2.16}$$

The simplices incident to both A and A' will change their orientation in the last step, since their
volume vanishes when A and A' merge. However, since these simplices are deleted anyway, their
orientation does not need to be maintained within this last step. The orientation of the simplices

incident to A but not A' (described by $\lambda_{\text{REST}}^{\text{max}}$) however, needs to be maintained, since these simplices will not be deleted afterwards. Therefore, the quantity $\lambda_{\text{REST}}^{\text{max}}$ should be the criterion for the last vertex step, whereas λ^{max} accounts for the maximum length of the previous steps.

The algorithm for deleting a vertex A can be summarized as follows:

1: Find the nearest neighbour vertex of A.

2: **repeat**

3:     set $\Delta = A' - A$,

4:     determine $\lambda^{\text{max}} = \min\limits_{S_k\,:\,A \in S_k} \lambda_k$,

5:     determine $\lambda_{\text{REST}}^{\text{max}} = \min\limits_{S_k\,:\,A \in S_k \,\wedge\, A' \notin S_k} \lambda_k$,

6:     **if** $\lambda_{\text{REST}}^{\text{max}} \leq 1.0$ **then**

7:         move $A \to A + \alpha\lambda^{\text{max}}\Delta$ with $\alpha < 1$,

8:         update the simplices surrounding A with flips to restore Delaunay property

9:     **end if**

10: **until** $\lambda_{\text{REST}}^{\text{max}} > 1.0$,

11: delete the simplices incident to both A and A',

12: replace A by A' in all simplices surrounding A,

13: set the correct neighbourship relations in these simplices,

14: update the simplices incident to A' with flips.

A problem can be posed by rounding errors in equation (2.14): If the numerator becomes very small – i. e., if one has simplices with an extremely small volume or very skinny simplices, then λ may tend to assume very small values. Rounding errors are then likely to happen. This problem can be weakened by using exact arithmetics [57] when computing (2.14).

Deletion via partial Re-Triangulation

The previous algorithm relies on the method of moving vertices and needs many operations (flips) until the simplices can finally be deleted from the triangulation. More important, the numerical rounding errors may pose a problem for realistic applications. Therefore, for the applications within this thesis a different approach – as presented in [58] – has been chosen. This approach can be summarized as follows:

1: delete the corresponding vertex,

2: collect the external faces of its incident simplices,

3: delete the incident simplices,

4: recompute the local Delaunay triangulation – constrained by the external faces.

Note that in the case discussed here, the constrained Delaunay triangulation can always be computed without adding artificial vertices, since the constraining faces fulfil the Delaunay property [55].

The CPU time necessary for the successive deletion of 5000 vertices with the partial re-triangulation method is with 1.0 s slightly smaller than the 1.2 s [26] necessary for deletion of the same number via vertex-merging.

2.3.9 The Geometric Dual

The most general Voronoi tessellation (sometimes called Dirichlet tessellation, too) of a set of generators $\{c_i\}$ in $\mathbb{R}^d$ is defined as a partition of space into regions V_i:

$$V_i \;=\; \{x \in \mathbb{R}^n \;:\; \mathcal{P}(x, c_i) \le \mathcal{P}(x, c_j) \qquad \forall j \ne i\}, \tag{2.17}$$

where $\mathcal{P}(x, c_i)$ is a distance measure between x and c_i.

In the simplest case of unweighted Voronoi tessellations this weight function reduces to the normal euclidian distance $\mathcal{P}(x, c_i) = |x - c_i|$. In other words, the normal Voronoi cell around the generator c_i contains all points in $\mathbb{R}^d$ that are closer to c_i than to any other generator c_j. Voronoi tessellations can be constructed like the well-known Wigner-Seitz cell in solid state physics [59], but fortunately there are much more efficient ways to construct the Voronoi tessellation. Note that this partition is – unlike the Delaunay triangulation – always uniquely defined even for point sets that do not fulfil the extended general position assumption. Voronoi tessellations have many interesting applications in practice [28], since they can be used to describe influence regions.

For weighted points $\{\hat{c}_i\} = \{(c_i, \omega_i)\}$, the orthogonal distance measure as defined in equation (2.6) will be used with unweighted points x to define the weighted Voronoi cell – sometimes called Laguerre cell [27] or radical plane construction [60]:

$$V_i \;=\; \{x \in \mathbb{R}^n \;:\; (x - c_i)^2 - \omega_i \le \left(x - c_j\right)^2 - \omega_j \qquad \forall j \ne i\}. \tag{2.18}$$

In two dimensions, (weighted) Voronoi cells are convex polygons (see figure 2.13). In addition, the boundaries of these polygons are perpendicular to the connection lines between the generators. This finding generalises to arbitrary dimensions: The boundaries between two d-dimensional Voronoi regions V_i and V_j as defined in (2.18) reduce to the equation for a $(d-1)$-hyperplane, since the quadratic contributions cancel. In addition, the corresponding hyperplane will be perpendicular to the line connecting two neighbouring Voronoi generators. Therefore, per definition the Voronoi cells around those generators Z_i that are situated on the boundary of the convex hull of the point set $\{Z_1, Z_2, \ldots, Z_n\}$ will extend to infinity and thus will have an infinite volume.

In three dimensions, the intersection of two boundary-planes defines a boundary line and the intersection of three boundary-planes defines a corner of the three-dimensional Voronoi/Laguerre cell. If one supplements the three equations defining a Voronoi corner

$$
\begin{aligned}
(\boldsymbol{x} - \boldsymbol{c}_1)^2 - \omega_1 &= (\boldsymbol{x} - \boldsymbol{c}_2)^2 - \omega_2 \,, \\
(\boldsymbol{x} - \boldsymbol{c}_2)^2 - \omega_2 &= (\boldsymbol{x} - \boldsymbol{c}_3)^2 - \omega_3 \,, \\
(\boldsymbol{x} - \boldsymbol{c}_3)^2 - \omega_3 &= (\boldsymbol{x} - \boldsymbol{c}_4)^2 - \omega_4
\end{aligned}
\tag{2.19}
$$

by the definition of a weight belonging to the corner point $\omega = (\boldsymbol{x} - \boldsymbol{c}_1)^2 - \omega_1$, one can (with using that $\omega_i = R_i^2$) show that the system of the resulting four equations is equivalent to the system (2.7). By identifying $\boldsymbol{x} = \boldsymbol{m}$ and $\omega = R_{m\perp}^2$, the fundamental duality between Voronoi tessellations and weighted Delaunay triangulations is revealed:

> If the Voronoi generators are equal to the Delaunay vertices, the corners of the (weighted) Voronoi regions are the centres of the Delaunay-simplex circumspheres (orthospheres).

This finding holds true in any dimension, for a two-dimensional illustration see figure 2.13. Consequently, two Voronoi generators sharing a common boundary of the Voronoi regions will be connected in the dual Delaunay triangulation. Disconnected vertices in the triangulation correspond to empty Voronoi regions. Thus, it becomes visible that a vertex that is not completely covered by the spheres of other vertices will always be connected in the weighted Delaunay triangulation: The associated sphere contains at least one point that is not contained in the spheres of other vertices. This point will belong to the associated Laguerre region [27], which is therefore non-empty.

In this work, the geometric duality with the Delaunay triangulation will be exploited by generating the Delaunay triangulation and computing the dual only if necessary.

The introduction of influence regions extends the definition of proximity between vertices: Two vertices are **direct neighbours** (in the sense that their influence regions touch) if they share a common face in their Voronoi diagram or – equivalently – if they are direct neighbours in the dual Delaunay triangulation (see figures 2.13 and 2.14 right panel).

Further possible choices for weight functions can be found in [28, 61], but these do not have the advantage of planar contact surfaces. This thesis is restricted to the weights as introduced. In addition, this particular choice has the advantage that the Laguerre tessellation or its geometric dual – the weighted Delaunay triangulation – is suitable for contact detection between differently sized spheres [27].

Within the framework of growth models [31], off-lattice tissue simulations [6, 23, 24, 62] and the solution of partial differential equations on irregular grids [63, 64], not only the neighbourship relations
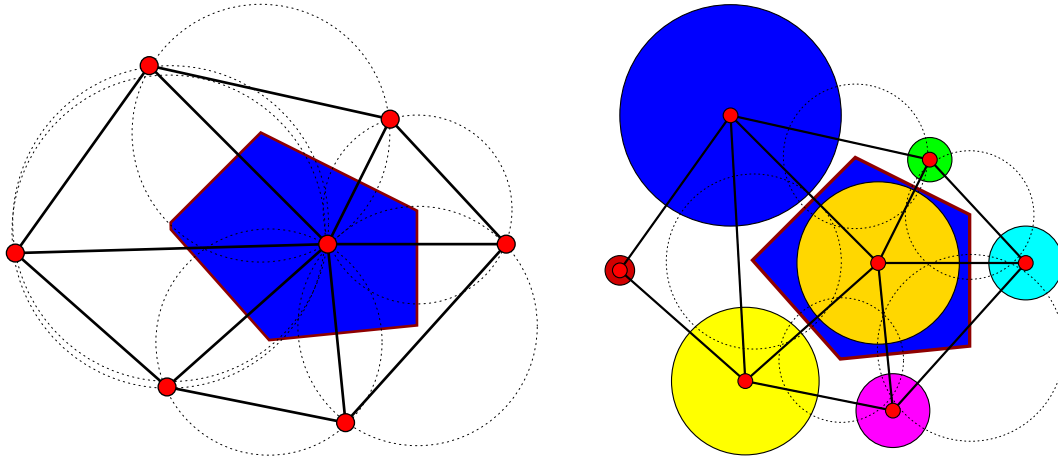
Figure 2.13: Duality between Delaunay triangulations and Voronoi tessellations. **Left:** The blue region denotes the normal Voronoi cell belonging to the central generator (red points). The centres of the circumcircles (dotted lines) mark the corners of the Voronoi cells. Note that the Voronoi contact surface between two generators does not necessarily intersect the connection lines between the generators (leftmost point). **Right:** Same point configuration as left, but here a weight ($w_i = R_i^2$, radii of the large coloured disks) is introduced. Still, the duality between weighted Delaunay triangulations and weighted Voronoi tessellations holds: The centers of the orthospheres (dotted lines) mark the corners of the weighted Voronoi cell (blue polygon). The orthospheres intersect perpendicularly with the weight circles.

in the Delaunay triangulation but in addition the corresponding Voronoi cell volumes as well as the contact surface between two Voronoi cells will become important.

In the used implementation, the Voronoi contact surfaces A_{ij}^{VOR} are calculated as follows:

1: Pre-compute the centers of the orthospheres of all simplices in the triangulation.

{This increases efficiency by avoiding superfluous calculations if the Voronoi contact areas of adjacent cells are to be calculated.}

2: For the contact polygon constituted of N weighted centres c_i of the simplices incident to both neighbouring vertices, define the central point via

$$z = \frac{1}{N} \sum_{i=1}^{N} c_i.$$ (2.20)

{Recall that the connection line between two neighbouring vertices may not always intersect with the Voronoi contact surface, compare figure 2.13.}

3: Subdivide the polygonal Voronoi contact region into triangles incident to z and sum their areas.
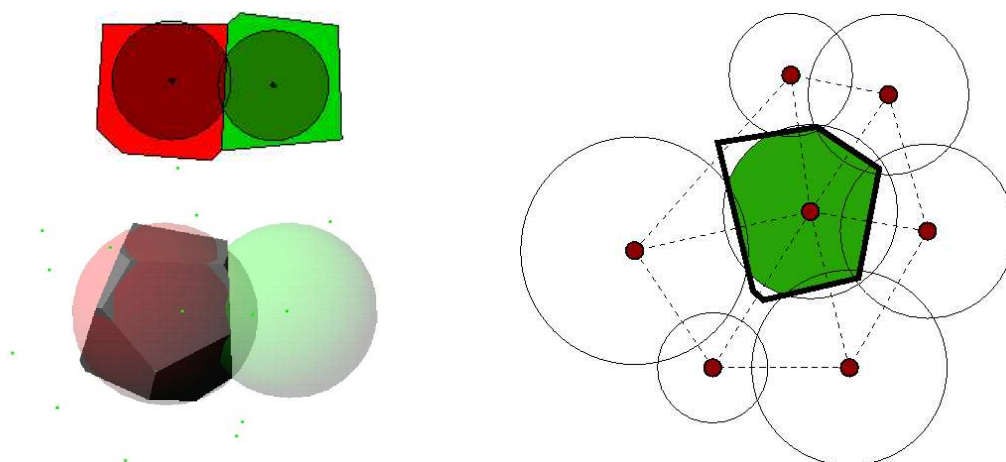
Figure 2.14: Relation of spherical and Voronoi contact surfaces in two and three dimensions. **Top left:** In a two-dimensional representation, the position of the Voronoi contact surface (lines) is identical with the position of the spherical contact surface (further spheres shaping the Voronoi cells are not shown here). The set intersection of sphere and Voronoi volumes is indicated in darker colours. **Bottom left:** In a three-dimensional configuration the position of the Voronoi contact surface (grey) coincides with the position of the sphere overlap surface. The position of further spheres shaping the three-dimensional Voronoi cells is indicated by the green points. **Right:** This can be exploited to yield an improved contact surface estimate in dense systems consisting of differently-sized spheres (two-dimensional illustration), where multiple sphere overlaps can occur. The set intersection of sphere and Voronoi volume is indicated green.

The total volume of the Voronoi cell is then calculated similarly from the contact surfaces A_{ij}^{VOR}

$$V_i^{\mathrm{VOR}} = \sum_{j \in \mathcal{NN}(i)} \frac{1}{3} A_{ij}^{\mathrm{VOR}} h_j \,, \tag{2.21}$$

where h_j represents the distance of the contact surface with neighbour j from the centre point of the Laguerre cell, which is calculated by the arithmetic average of the corner points as well.

The above calculation will fail at the boundary of the triangulation. However, as the boundary is given by an artificial simplex, it will never be referenced in practice.

The numerical complexity of the volume computation is linear with the number of simplices surrounding the vertex, whereas the complexity of contact surface calculation between two generators grows linear with the number of simplices incident to both generators. Such algorithms have been tested using a Monte-Carlo simulation.

2.4 The Finite-Differencing Scheme

2.4.1 Spatial discretisation

Though the analytical solutions of partial differential equations (PDEs) are differentiable, their numerical representation will be discrete in both time and space. Within the finite-difference-approach, the spatial discretisation can be performed as follows: The computational domain under consideration is divided into disjoint volume elements V_i. Within these volume elements, one locally defines spatially averaged quantities via

$$u_i(t) = \frac{1}{V_i} \int_{V_i} u(\boldsymbol{x}, t) \, dx \,, \tag{2.22}$$

where $u(\boldsymbol{x}, t)$ denotes the quantity which is described by the PDE. The spatial derivatives occurring in the PDE can then be transformed into finite differences, i. e.,

$$\left. \frac{\partial u(\boldsymbol{x}, t)}{\partial \boldsymbol{x}} \right|_{\partial V_i \cap \partial V_{i'}} \rightarrow \frac{u_{i'}(t) - u_i(t)}{|\boldsymbol{x}_{i'} - \boldsymbol{x}_i|} \frac{\boldsymbol{x}_{i'} - \boldsymbol{x}_i}{|\boldsymbol{x}_{i'} - \boldsymbol{x}_i|} \,, \tag{2.23}$$

where $\boldsymbol{x}_i$ denotes centers of the volume element V_i. Higher-order derivatives can be discretised in this way as well. For rectangular lattices, symmetry properties can be used to improve spatial accuracy. For other discretisations, Gauss's theorem can be employed on the volume elements to reduce the order of the derivatives. The general effect of this spatial averaging is that the original PDE is transformed into a system of coupled ordinary differential equations (ODEs). This system is – after discretising u_i in time, if necessary – transformed into an algebraic linear system, which can be solved

by iterative methods (compare e. g. appendix B). For the examples of reaction-diffusion equations (RDEs) and continuum mechanics, the discretisation procedure will be performed explicitly in the following sections.

2.4.2 Reaction-Diffusion Equations

Reaction-diffusion equations (RDEs) are PDEs of the general form

$$\frac{\partial u}{\partial t} = \nabla [D(\boldsymbol{x}, t)\nabla u(\boldsymbol{x}, t)] + Q(\boldsymbol{x}, t), \tag{2.24}$$

where $u(\boldsymbol{x}, t)$ describes the local concentration of a soluble substance (or the local temperature), $D(\boldsymbol{x}, t)$ the local diffusion measure (or thermal conductivity), and $Q(\boldsymbol{x}, t)$ stands for a reaction term (or a heat source/sink). Note that the diffusion measure $D(\boldsymbol{x}, t)$ is not necessarily a scalar [65], though within this thesis only scalar diffusion will be considered. For example, within the context of tissue modelling, $u(\boldsymbol{x}, t)$ may represent the local concentration of nutrient, whereas the sink term $Q(\boldsymbol{x}, t)$ is associated with the nutrient consumption by the cells.

If the reaction volumes V_I do not change in time, one can average equation (2.24) as described in equation (2.22) to obtain (using Gauss's theorem)

$$\frac{\partial u_I}{\partial t} = \frac{1}{V_I} \oiint_{\partial V_I} D(\boldsymbol{x}, t)\nabla u(\boldsymbol{x}, t) \cdot d\boldsymbol{f} + Q_I(t), \tag{2.25}$$

where for rectangular lattices in three dimensions the index $I = \{i, j, k\}$ is a triple of indices, each denoting the spatial position in one dimension. The algebraic structure of the numerical discretisation depends on the specific geometry under consideration. For some specific examples the modes of discretisation are given below:

- If one uses the Voronoi (Laguerre) tessellation [63] (compare equation (2.18) in sub-subsection 2.3.9) as the definition of volume elements V_I, equation (2.25) reduces to

$$\frac{\partial u_I}{\partial t} = \frac{1}{V_I} \sum_{J \in \mathcal{NN}(I)} \frac{A_{IJ}}{|\boldsymbol{x}_I - \boldsymbol{x}_J|}(u_J - u_I)D_{IJ} + Q_I, \tag{2.26}$$

  where V_I is the volume of the Voronoi (Laguerre) cell I, and $J \in \mathcal{NN}(I)$ denote the next neighbours of cell I with generator $\boldsymbol{x}_I$ arising from the (weighted) Delaunay triangulation. Consequently, the terms A_{IJ} denote the contact area of the adjacent Voronoi (Laguerre) regions I and J. Linear interpolation on the connection lines between the generators of I and J yields for the diffusion coefficient

$$D_{IJ} = D_{J,I} = \frac{1}{2}D_I\left[1 + \frac{\omega_J - \omega_I}{(\boldsymbol{x}_J - \boldsymbol{x}_I)^2}\right] + \frac{1}{2}D_J\left[1 - \frac{\omega_J - \omega_I}{(\boldsymbol{x}_J - \boldsymbol{x}_I)^2}\right] \tag{2.27}$$

at the position of the Voronoi boundary defined by equation (2.18). This reduces to the simple arithmetic average in case of equal weights $\omega_I = \omega_J$.

- For problems with spherical symmetry, the system (2.25) reduces to an effectively one-dimensional system, which can for constant lattice spacings Δr be discretised on concentric shells [66] as

$$
\begin{aligned}
\frac{\partial u_i}{\partial t} &= \frac{1}{V_i} \left[\frac{A_{i,i+1}}{\Delta r} (u_{i+1} - u_i) \frac{1}{2} (D_i + D_{i+1}) - \frac{A_{i,i-1}}{\Delta r} (u_i - u_{i-1}) \frac{1}{2} (D_i + D_{i-1}) \right] \\
&\quad + Q_i(t), \tag{2.28} \\
A_{i,i\pm1} &= 4\pi \left[R_0 + (i \pm 1/2) \Delta r \right]^2, \\
V_i &= \frac{4\pi}{3} \left[(R_0 + i\Delta r + \Delta r/2)^3 - (R_0 + i\Delta r - \Delta r/2)^3 \right] \\
&= \frac{4\pi}{3} \left[3 (R_0 + i\Delta r)^2 \Delta r + \Delta r^3/4 \right], \tag{2.29}
\end{aligned}
$$

where $A_{i,i\pm1}$ denote the contact surface between shells i and $i \pm 1$ and V_i the volume of the ith shell, respectively. The term R_0 denotes the smallest radius of the volume under consideration, i. e., it is set to zero for most applications.

- For the simplest and most common case of rectangular grids in three dimensions with lattice constants Δx, Δy, Δz one can improve the accuracy by directly discretising (2.24)

$$
\begin{aligned}
\frac{\partial u_{i,j,k}}{\partial t} &= + \frac{\left(D_{i+1,j,k} - D_{i-1,j,k}\right)\left(u_{i+1,j,k} - u_{i-1,j,k}\right)}{4\Delta x^2} + D_{i,j,k} \frac{u_{i+1,j,k} - 2u_{i,j,k} + u_{i-1,j,k}}{\Delta x^2} \\
&\quad + \frac{\left(D_{i,j+1,k} - D_{i,j-1,k}\right)\left(u_{i,j+1,k} - u_{i,j-1,k}\right)}{4\Delta y^2} + D_{i,j,k} \frac{u_{i,j+1,k} - 2u_{i,j,k} + u_{i,j-1,k}}{\Delta y^2} \\
&\quad + \frac{\left(D_{i,j,k+1} - D_{i,j,k-1}\right)\left(u_{i,j,k+1} - u_{i,j,k-1}\right)}{4\Delta z^2} + D_{i,j,k} \frac{u_{i,j,k+1} - 2u_{i,j,k} + u_{i,j,k-1}}{\Delta z^2} \\
&\quad + Q_{i,j,k}, \tag{2.30}
\end{aligned}
$$

which is second-order accurate[7] in space [67]. The above equation is only valid for the volume elements not residing on the boundary of the reaction volume. There, the boundary conditions (for example Dirichlet or von-Neumann) have to be discretised independently.

---

[7]The discretisation of the second derivatives can be derived by using a virtual grid with halved lattice constants.

The general handling of equations (2.26), (2.28) and (2.30) differs in the way how their right-hand-side is discretised. All these equations can be written as

$$\frac{\partial u_I}{\partial t} = \mathcal{L}u_I + Q_I(t) \,, \tag{2.31}$$

where $\mathcal{L}$ is a linear operator describing the geometry and diffusional properties of the system. Discretisation in time is introduced by

$$\frac{\partial u_I}{\partial t} \rightarrow \frac{u_I^{n+1} - u_I^n}{\Delta t} \,, \tag{2.32}$$

with $u_I^{n+1} = u_I(t + \Delta t)$ and $u_I^n = u_I(t)$. This definition is symmetric around $t + \Delta t/2$. Depending on at which time the right hand side is evaluated, one distinguishes between three numerical schemes:

1. The simplest possibility is an explicit scheme (Forward-Time-Centred-Space, FTCS), which is realised by evaluating the right hand side at time t, i. e.,

$$u_I^{n+1} = \{\mathbb{1} + \Delta t \mathcal{L}^n\} u_I^n + \Delta t Q_I^n \,, \tag{2.33}$$

which has the advantage that the solution $u(t + \Delta t)$ can be readily obtained from $u(t)$ without necessitating matrix inversion. However, already for constant diffusion coefficients a von-Neumann stability analysis [68] on rectangular grids shows that this solution scheme becomes numerically unstable if

$$\frac{D\Delta t}{\Delta x^2} + \frac{D\Delta t}{\Delta y^2} + \frac{D\Delta t}{\Delta z^2} \geq \frac{1}{2} \,, \tag{2.34}$$

a constraint which is known as **Courant-condition**. Numerical instability implies that the numerical errors will increase exponentially in time, which is a serious limitations for practical applications. As the Courant condition involves both spatial (Δx) and temporal (Δt) resolutions, one can either decrease the timestep or decrease the spatial resolution to obtain correct numerical solutions with the FTCS method. In addition, it is evident from (2.33) that the solution is only first order accurate in time.

2. Numerical stability can be recovered if one applies a fully implicit scheme (Backward-Time-Centred-Space, BTCS), i. e., by evaluating the right hand side of (2.31) at time $t + \Delta t$ one yields

$$\left\{ \mathbb{1} - \Delta t \mathcal{L}^{n+1} \right\} u_I^{n+1} = u_J^n + \Delta t Q_J^{n+1} \,, \tag{2.35}$$

which is still only first order accurate in time. However, one can show by von-Neumann stability analysis, that this scheme is unconditionally stable, i. e., timesteps larger than allowed by the Courant condition do not lead to an exponential increase of the numerical errors. Note that the existence of $\mathcal{L}$ on the left hand side necessitates the inversion of a sparsely populated matrix.

3. The best choice is to combine the advantages of explicit and implicit methods by a simple average, i. e.,

$$\left\{ \mathbb{1} - \frac{\Delta t}{2} \mathcal{L}^{n+1} \right\} u_I^{n+1} = \left\{ \mathbb{1} + \frac{\Delta t}{2} \mathcal{L}^{n} \right\} u_I^{n} + \frac{\Delta t}{2} \left(Q_I^{n} + Q_I^{n+1} \right) , \qquad (2.36)$$

which is a sparsely populated linear system that can be solved for u_I^{n+1} by knowledge of u_I^{n}, Q_I^{n}, and Q_I^{n+1}. This method is known as the **Crank-Nicholson scheme** [68] and by von-Neumann stability analysis [68] one can show for the free diffusion case that it is unconditionally stable. In addition, it is second order accurate in time, since here both the left and right-hand sides are centred at time $t_n + \Delta t/2$. The resulting system is tri-diagonal in one dimension, which enables a fast and simple algorithmic matrix inversion. This however does not hold true in higher dimensions. In this case, approaches such as operator splitting [68] can help to reduce sparse matrices to several tri-diagonal ones. For the example of two dimensions, the way how to employ the **alternating-direction implicit method** (ADI) is demonstrated explicitly in [68]. The basic idea is to divide each timestep into several sub-steps. Within each sub-step, a single dimension is treated implicitly, whereas the other dimensions are treated explicitly. In two dimensions, this procedure preserves unconditional stability, whereas in three dimensions the updating scheme from [68] can be generalised with $\mathcal{L} = \mathcal{L}_x + \mathcal{L}_y + \mathcal{L}_z$ to (with reaction terms omitted)

$$
\begin{aligned}
\left\{ \mathbb{1} - \frac{\Delta t}{3} \mathcal{L}_x^{n+1/3} \right\} u_{i,j,k}^{n+1/3} &= \left\{ \mathbb{1} + \frac{\Delta t}{3} \mathcal{L}_y^{n} + \frac{\Delta t}{3} \mathcal{L}_z^{n} \right\} u_{i,j,k}^{n} , \\
\left\{ \mathbb{1} - \frac{\Delta t}{3} \mathcal{L}_y^{n+2/3} \right\} u_{i,j,k}^{n+2/3} &= \left\{ \mathbb{1} + \frac{\Delta t}{3} \mathcal{L}_x^{n+1/3} + \frac{\Delta t}{3} \mathcal{L}_z^{n+1/3} \right\} u_{i,j,k}^{n+1/3} , \\
\left\{ \mathbb{1} - \frac{\Delta t}{3} \mathcal{L}_y^{n+1} \right\} u_{i,j,k}^{n+1} &= \left\{ \mathbb{1} + \frac{\Delta t}{3} \mathcal{L}_x^{n+2/3} + \frac{\Delta t}{3} \mathcal{L}_y^{n+2/3} \right\} u_{i,j,k}^{n+2/3} ,
\end{aligned}
\qquad (2.37)
$$

which replaces a sparse system by three tri-diagonal ones. Unfortunately, the above splitting scheme sacrifices numerical stability at $D\Delta t/\Delta x^2 \geq 1/2$ (see appendix C.1.1). Therefore, the full sparse system (2.36) has been solved directly. Numerically, this has been achieved by the iterative biconjugate gradient method (compare appendix B.2).

The FTCS scheme and the ADI as well as the full CNS scheme have been implemented and tested (see appendix C.1.1).

If one is only interested in steady-state values of the numerical solution of equation (2.24), i. e., in the case

$$\frac{\partial u}{\partial t} = \nabla \left[D(\boldsymbol{x}, t) \nabla u(\boldsymbol{x}, t) \right] + Q(\boldsymbol{x}, t) \approx 0 \,, \tag{2.38}$$

the problem effectively reduces to a Poissonian one

$$\nabla \left[D(\boldsymbol{x}) \nabla u(\boldsymbol{x}) \right] = -Q(\boldsymbol{x}) \qquad \text{or} \qquad \mathcal{L} u_I = -Q_I \,. \tag{2.39}$$

Three numerical methods for obtaining the solution of the above equation have been implemented and tested (see appendix C.1.1):

1. The by far most efficient method – both in computational time and numerical accuracy – is a rapid method based on the Fast Fourier Transform (FFT) that has been extended from a 2-dimensional example in [68] to three dimensions. However, it can only be applied if

   - the diffusion coefficient is constant and
   - the computational domain is rectangular.

   It is based on the idea of Fourier-expanding both the solution and the reaction rates (compare appendix C.1.1). Thereby, equation (2.39) is reduced into a diagonal algebraic system for the Fourier coefficients, which can be solved immediately. By using the inverse Fourier transform, the solution is obtained. This procedure is sped up extremely for large numbers of grid nodes N by using FFT, which has an improved complexity of $N \log N$ versus N^2 for the normal Fourier transform [68]. As a small drawback, the use of the FFT restricts the number of grid points in every dimension to $N_i^{\mathrm{grid}} = 2^n + 1$ with $n \in \{1, 2, 3, \ldots\}$.

2. A further efficient method that can handle variable diffusion coefficients is the Multigrid method that has been extended from an example in [69] to non-constant diffusion coefficients. It still requires that

   - the computational domain is rectangular.

   The scheme as implemented uses Gauss-Seidel relaxation [68] and increases convergence by averaging the solution from finer grids to coarser grids, solving the system exactly on the coarsest grid, and finally interpolating from the coarse grids down to the fine grid again. For the simple averaging and interpolation chosen here, this approach restricts the number of grid points

in every dimension as before to $N_i^{\text{grid}} = 2^n + 1$. For simplicity, this procedure of averaging and interpolating has only been performed once from the finest grid down to the coarsest grid and up again. Since this procedure resembles the shape of the latter V, this scheme is called V-cycle-multigrid [68]. The V-cycle method has good performance only when the initial guess for the solution is close to the analytic solution.

3. The above methods are still restricted to rectangular geometries. Other simple geometries can in principle be realised by the Multigrid method and even using a rapid method if a system of eigenfunctions is known, but in order to have one tool generally handling different geometries, the linear system arising from (2.39) has been solved iteratively by a biconjugate gradient method as provided in [68] with the routine **linbcg** (compare appendix B.2). This approach allows for

- varying diffusion coefficients,
- varying geometries,
- arbitrary grid resolutions in every dimension,
- arbitrary boundary conditions.

2.4.3   Continuum Mechanics in solids

The discrete element method can as well be applied to more complicated equations, which will be demonstrated in this subsection. The elastic parameters of this theory can be used for an approximate description of cellular compressibility later on.

Linear elastic solids that are constrained by boundary forces obey – in equilibrium – the following equations [70]

$$
\begin{aligned}
\partial^\beta \sigma^{\alpha\beta} &= f^\alpha &:& \quad \boldsymbol{x} \in V, \\
n^\beta \sigma^{\alpha\beta} &= p^\alpha &:& \quad \boldsymbol{x} \in \partial V,
\end{aligned}
\tag{2.40}
$$

where the f^α denote force volume densities that act in the interior of the solid (such as e. g. gravity or forces induced by thermal elongation) and p^α denote the force surface densities acting at the boundary of the solid – parametrised by the components of the normal vectors n^β. For small deformations, the symmetric stress tensor $\sigma^{\alpha\beta}$ is assumed to be linearly related with the strain tensor [70]

$$
\sigma^{\alpha\beta} = \frac{E}{1+\nu}\left(U^{\alpha\beta} + \frac{\nu}{1-2\nu}U^{\sigma\sigma}\delta^{\alpha\beta}\right),
\tag{2.41}
$$

$$
U^{\alpha\beta} = \frac{1}{2}\left(\frac{\partial U^\alpha}{\partial x^\beta} + \frac{\partial U^\beta}{\partial x^\alpha}\right).
\tag{2.42}
$$

The quantity U^α describes the α-component of the local deformation vector from the equilibrium value (where one has neither boundary nor any internal forces), whereas the elastic properties of the solid are characterized by the quantities E and ν. The Young modulus E is generally defined as the ratio of stress versus strain and describes by how much a piece of material deforms in the direction of a force $F_\perp$ acting perpendicularly to the boundary of the material

$$E\frac{\Delta L}{L} = \frac{F_\perp}{A}, \tag{2.43}$$

compare also appendix C.1.3. As the strain $\Delta L/L$ is dimensionless, E has the dimension of pressure. Typical values range from kPa (cells) over GPa (wood, bone) to 200 GPa (steel). However, solids subject to external forces do usually not only express longitudinal deformations, but also transversal ones. The ratio of the deformation in transversal versus the deformation in longitudinal direction is described by the Poisson modulus ν. For no transversal deformation one has $\nu = 0$, but most realistic solid materials have Poisson moduli between 0 and 0.5: bone has $\nu = 0.32$ [71], steel has $\nu = 0.33$. The case of $\nu = 0.5$ corresponds to an incompressible medium (compare appendix C.1.3). By inserting the above definitions into (2.40) one obtains a PDE for every component of U

$$\frac{1}{2}\left(\frac{\partial U^\alpha}{\partial x^\beta} + \frac{\partial U^\beta}{\partial x^\alpha}\right)\frac{\partial}{\partial x^\beta}\left(\frac{E}{1+\nu}\right) + \frac{\partial U^\sigma}{\partial x^\sigma}\frac{\partial}{\partial x^\alpha}\left(\frac{\nu E}{(1+\nu)(1-2\nu)}\right)$$

$$+\frac{E}{2(1+\nu)}\frac{\partial^2 U^\alpha}{\partial x^\beta \partial x^\beta} + \frac{E}{2(1+\nu)(1-2\nu)}\frac{\partial^2 U^\sigma}{\partial x^\sigma \partial x^\alpha} = f^\alpha \qquad x \in V,$$

$$\frac{E}{2(1+\nu)}\left(\frac{\partial U^\alpha}{\partial x^\beta} + \frac{\partial U^\beta}{\partial x^\alpha}\right)n^\beta + \frac{E\nu}{(1+\nu)(1-2\nu)}\frac{\partial U^\sigma}{\partial x^\sigma}n^\alpha = p^\alpha \qquad x \in \partial V, \tag{2.44}$$

where the fractions of the elastic coefficients in the first line are often called Lamé coefficients [72]. Using the short-hand notation

$$f_1(E,\nu) = \frac{E(1-\nu)}{(1+\nu)(1-2\nu)},$$

$$f_2(E,\nu) = \frac{E\nu}{(1+\nu)(1-2\nu)},$$

$$g(E,\nu) = \frac{E}{2(1+\nu)}, \tag{2.45}$$

and by sorting the terms in (2.44) by the order of the derivatives, one obtains (with sums worked out

explicitly)

$$\left\{ f_1 \left(\partial^\alpha\right)^2 + g \sum_{\beta\neq\alpha} \left(\partial^\beta\right)^2 + \left(\partial^\alpha f_1\right)\partial^\alpha + \sum_{\beta\neq\alpha} \left(\partial^\beta g\right)\partial^\beta \right\} U^\alpha$$

$$+ \sum_{\beta\neq\alpha} \left\{ \frac{1}{2}\left(f_1 + f_2\right)\partial^\alpha\partial^\beta + \left(\partial^\beta g\right)\partial^\alpha + \left(\partial^\alpha f_2\right)\partial^\beta \right\} U^\beta = f^\alpha \qquad \boldsymbol{x} \in V,$$

$$\left\{ f_1 n^\alpha \partial^\alpha + g \sum_{\beta\neq\alpha} n^\beta \partial^\beta \right\} U^\alpha + \sum_{\beta\neq\alpha} \left\{ g n^\beta \partial^\alpha + f_2 n^\alpha \partial^\beta \right\} U^\beta = p^\alpha \qquad \boldsymbol{x} \in \partial V. \qquad (2.46)$$

In three dimensions, where on a rectangular lattice with lattice constants Δx, Δy, and Δz, the local deformation U^α is discretised on volume elements V_{ijk} as U^α_{ijk}, the partial derivatives can be represented inside the volume as

$$\frac{\partial U^\alpha}{\partial x} \rightarrow \frac{U^\alpha_{i+1,j,k} - U^\alpha_{i-1,j,k}}{2\Delta x}, \qquad \frac{\partial^2 U^\alpha}{\partial x^2} \rightarrow \frac{U^\alpha_{i+1,j,k} - 2U^\alpha_{i,j,k} + U^\alpha_{i-1,j,k}}{\Delta x^2}, \qquad (2.47)$$

$$\frac{\partial^2 U^\alpha}{\partial x \partial y} \rightarrow \frac{U^\alpha_{i+1,j+1,k} + U^\alpha_{i-1,j-1,k} - U^\alpha_{i+1,j-1,k} - U^\alpha_{i-1,j+1,k}}{4\Delta x \Delta y}, \qquad (2.48)$$

and likewise for the other directions. The existence of mixed derivatives implies that the diagonal neighbours in a rectangular lattice contribute as well. In addition, at the boundary of the volume, the derivatives cannot be expressed in a centred way. Instead, the derivative can only be computed using the allowed interval (within the reaction volume), see figure 2.15 left panel. Thus, the PDEs (2.44) are transformed for N lattice sites into an algebraic system

$$A\boldsymbol{U} = \boldsymbol{f} \qquad\qquad\qquad\qquad\qquad\qquad\qquad\qquad\qquad\qquad\qquad\qquad (2.49)$$

of dimension $3N \times 3N$, where terms with U^α_{ijk} in (2.47) contribute to the diagonal entries of A (compare appendix B.3). If the boundary conditions are properly set (thus allowing a solution), this linear system can be solved with the iterative biconjugate gradient method as provided with the routine **linbcg** in [68] (compare appendix B). In three dimensions, the derivatives lead to a maximum of 22 off-diagonal entries, compare figure 2.15 right panel. At the boundaries, one would formally obtain 14 off-diagonal entries from equation (2.46) and no entries on the diagonal. However, in aid of the diagonal entries, the number of off-diagonal matrix elements on the boundary is reduced, since depending on the position of the volume element on the boundary at least one direction is constrained such that the derivatives cannot be expressed in a centred way.
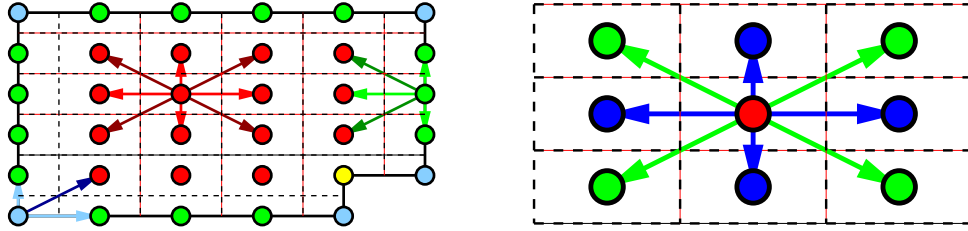
Figure 2.15: Discretisation of derivatives for a rectangular lattice. **Left:** Derivatives for points in red can be centred in any direction, whereas for points in green one direction is constrained in this two-dimensional illustration. For points in blue, both directions are constrained. Dashed lines indicate the volume elements, within which averaging is performed, whereas the solid lines denote the boundary of the computational domain. Mixed second derivatives lead to connections with the diagonal neighbours (arrows with dark colours, requires Moore neighbourhood), whereas first and second derivatives with respect to a single variable only require the adjacent cells to interact (arrows with light colours, von-Neumann neighbourhood). With increasing grid resolution, arbitrary shapes can be approximated (yellow point). **Right:** In three dimensions, one obtains from equation (2.46) up to 22 references to the next neighbours. Here, only a cross-section perpendicular to the direction α is shown. For the second derivatives of U^{α} one has to access the 6 direct neighbours once (not shown). Then, the mixed second derivatives of $U^{\beta \neq \alpha}$ require 8 references to the diagonal neighbours (green points). Finally, the first derivatives of $U^{\beta \neq \alpha}$ require 8 references to the direct neighbours (blue points).

2.5 Cellular Interactions

2.5.1 Mechanical Cellular Properties

Many cellular constituents (see figure 2.16) contribute to the mechanical properties of the cell. Adhesive properties are mediated by the receptor and ligand molecules distributed on the cell surface [73], whereas the repulsive features arise from the combined action of nucleus, cytoplasm, and cell membrane [74]. Obviously, the cell is a complicated multi-component system. According to [75], the mechanics of the cytoplasm can be approximately described by viscoplastic gel properties on larger scales. Via the cytoskeleton the cell nucleus is connected to the cell membrane as well. These constituents yield the rigid cell structure at equilibrium. The cell membrane can presumably be described as elastic for small deformations.

2.5.2 Contact Models

In view of the sophisticated cell composition, models with a small number of parameters have only been able so far to approximate the cellular behaviour in a simple way [8, 76, 77]. The dynamics of solids in contact is a difficult problem, as already the local geometry at the contact region will strongly influence the involved forces. Most models applied in practice are not motivated by underly-
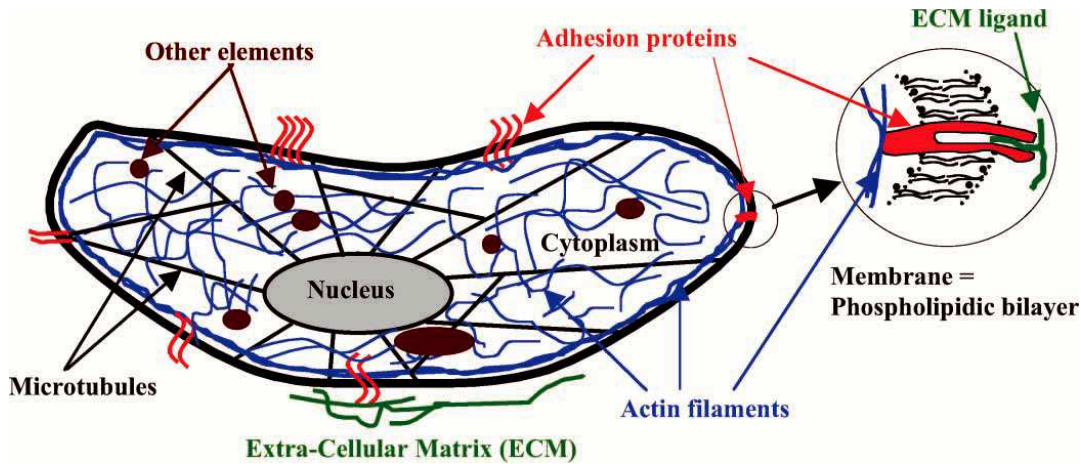
Figure 2.16: Sketch of a typical eucaryotic cell [75]. Adhesion is mediated by receptor and ligand molecules distributed on the cell surface. Actin filaments effectively increase the viscosity of the cytoplasm, whereas microtubules connect the cell membrane with the viscoelastic nucleus.

ing assumptions on the material properties but rather mimic the realistic behaviour. In principle, these contact models all fulfil two basic conditions:

1. They exhibit strong repulsive forces for large overlaps and

2. they have a bound state for small overlaps.

For example, the Lennard-Jones potential

$$V(x) = Ax^{-\alpha} + Bx^{-\beta}, \tag{2.50}$$

where x denotes the distance, has been successfully applied in physics to model the interactions of atoms [78]. As A, B, α, and β are parameters, the Lennard-Jones model has enough intrinsic freedom to approximate even the interaction of macroscopic systems such as e. g. grains [27].

Viscous and plasticity effects can be incorporated by constructing a model from mechanical analogues: In this approach, simple mechanical elements such as the dashpot and the spring (see figure 2.17), are connected to a mechanical network. These diagrams define a set of linear ODEs, which can be solved to obtain the solution as a function of time. Thus, it is possible to incorporate viscous (Kelvin element) and viscoplastic (Maxwell element) effects in cellular contact interactions, see e. g. [79, 80]. These models however require a large set of parameters and facing the large uncertainty about inner-cellular elastic or dampening constants they must be used as fit models since currently these parameters cannot be measured independently.
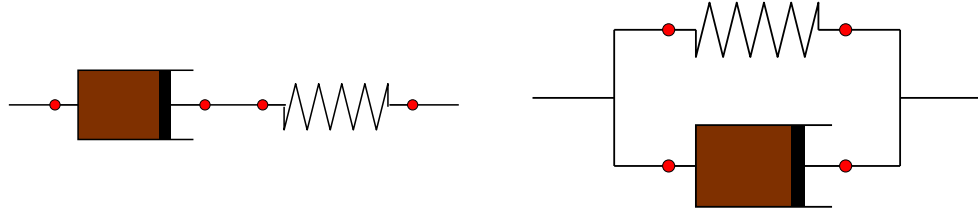
Figure 2.17: Basic elements of mechanical networks. **Left:** A Maxwell element consists of a dashpot and a spring in series, which leads to viscoplastic behaviour: After external forces have acted, the system does not necessarily relax to its initial position. **Right:** In contrast, for a Kelvin element these are connected in parallel, which only leads to viscous behaviour: The system will always relax to the same equilibrium position. By using more complicated circuits, a good agreement with rheologic measurements can be achieved.

Another approach would be to derive the elastic and viscous constants of a mechanical network from a microscopic model of the cell. If one only considers the contribution of the cytoskeleton, a popular ansatz is the explanation of cellular properties by tensegrity structures [81, 82] – an acronym derived from "tensional integrity". Such structures can be envisioned as a combination of rigid elements (usually bars) that are connected by elastic cables, where pressure and tension cooperate to stabilise them. A complete model involving all these elements for every cell would exceed the capabilities of multicellular simulations.

Here, another approach to treat the adhesive and elastic interactions will be followed: Based on the assumption that cells can be approximated by a uniform and isotropic material, the theory of continuum mechanics – compare subsection 2.4.3 – can be applied. Note, that here the additional constraint of only small relative deformation enters. In this case, the elastic equilibrium forces between two solids i and j in contact (compare also figure 2.19) can be derived from equation (2.40) using the method of Greens functions: Assuming that the contact surface between the spheres is situated in the $z = 0$ plane, one has [70]

$$U_\alpha(x, y) = \iint G_{\alpha\beta}(x - x', y - y')p_\beta(x', y') \, dx' \, dy' \,, \tag{2.51}$$

where $p_\beta(x', y')$ denotes the pressure field acting on the contact surface and $G_{\alpha\beta}$ is the Greens function. Due to the given symmetry, only the *zz*-component of the Greens function

$$G_{zz}(x, y) = \frac{1 - v^2}{\pi E} \frac{1}{\sqrt{x^2 + y^2}} \tag{2.52}$$

is of interest. The above Greens function is derived from the solution of the equilibrium equations (2.44) in the simplified case of a homogeneously elastic medium (characterized by E and v) filling the halfspace $z < 0$ subject to the point-like force $F_z(x, y) = F_0\delta(x)\delta(y)$ [70]. In the present case one has

to consider two objects with different elastic properties and thus, one obtains the relative deformations

$$U_z^{i/j}(x,y) = \frac{1 - v_{i/j}^2}{\pi E_{i/j}} \iint \frac{p_z(x',y')}{\sqrt{(x-x')^2 + (y-y')^2}} \, dx' \, dy' \,, \tag{2.53}$$

where $E_{i/j}$ and $v_{i/j}$ denote the Young modulus and the Poisson modulus of the solids, respectively. If only forces normal to the contact regions act, the surface of contact will be flat. If in addition the origin of the coordinate system is placed in the centre of the contact region and if the local deformations are not too large, the deformation field at the contact surface can be approximated by an ellipsoidal parametrisation. Consequently, the relation

$$B_1 x^2 + B_2 y^2 + U_z^i(x,y) + U_z^j(x,y) = h_{ij} \,, \tag{2.54}$$

where h_{ij} denotes the overall indentation due to the load, must hold throughout the contact region (compare figure 2.19 left panel). The constants $B_{1/2}$ are related to the radii of curvature of the surfaces in contact [70, 83]. Comparing the resulting integral equation for the unknown pressure distribution

$$\frac{1}{\pi} \left(\frac{1 - v_i^2}{E_i} + \frac{1 - v_j^2}{E_j} \right) \iint \frac{p_z(x',y')}{\sqrt{(x-x')^2 + (y-y')^2}} \, dx' \, dy' = h_{ij} - B_1 x^2 - B_2 y^2 \tag{2.55}$$

with the mathematical identity

$$\iint\limits_{(x'/a)^2 + (y'/b)^2 \leq 1} \sqrt{\frac{1 - \left(\frac{x'}{a}\right)^2 - \left(\frac{y'}{b}\right)^2}{(x-x')^2 + (y-y')^2}} \, dx' \, dy' = \frac{\pi ab}{2} \int\limits_0^\infty \frac{\left[1 - \frac{x^2}{a^2+t} - \frac{y^2}{b^2+t}\right]}{\sqrt{(a^2+t)(b^2+t)t}} \, dt \,, \tag{2.56}$$

one finds that both right hand sides are quadratic forms in x and y. Consequently, a solution for the integral equation is given by the pressure distribution

$$p_z(x,y) = \frac{3}{2} \frac{F^{\text{el}}}{\pi ab} \sqrt{1 - \left(\frac{x}{a}\right)^2 - \left(\frac{y}{b}\right)^2} \,, \tag{2.57}$$

where the normalisation constant results from integration over the ellipsoidal contact surface. From the mathematical identity, this choice of the pressure distribution is certainly not unique, but it leads to the unique analytical solution of the system (2.40). In the special case of two spheres in contact with (unperturbed) radii R_i and R_j the contact ellipse becomes circular and one obtains

$$B_1 = B_2 = \frac{1}{2} \left(\frac{1}{R_i} + \frac{1}{R_j} \right) = \frac{1}{2R_{ij}} \,, \tag{2.58}$$

where R_{ij} is the effective curvature. Thus, one finally derives from comparing the coefficients for the total repulsive elastic Hertz force

$$F^{\text{Hertz}} = R_{ij}^{1/2} K_{ij} h_{ij}^{3/2} \,. \tag{2.59}$$

The elastic properties are combined in the coefficient K_{ij}, which has the dimension of pressure

$$\frac{1}{K_{ij}} = \frac{3}{4}\left(\frac{1-v_i^2}{E_i} + \frac{1-v_j^2}{E_j}\right). \tag{2.60}$$

This contact problem had initially been solved by Heinrich Hertz in 1882 [84] and does not include effects of adhesion. Note that it can be applied to a sphere in contact with a plane as well by setting one radius to infinity.

In [85] Johnson, Kendall and Roberts (JKR) showed that the contact radius a_{ij} is enlarged (in comparison to the Hertz contact problem) in presence of adhesive forces. They introduced an apparent Hertz load F^{app}, and a corresponding apparent Hertz indentation h^{app}, which would yield the same contact radius a_{ij} in the purely elastic Hertz model. For adhesive spheres however, the contact radius a_{ij} will already occur at indentations h_{ij} smaller than h_{ij}^{app}. In [85] it is assumed that this correction arises from an additional pressure distribution

$$p_{\mathrm{ad}}(x,y) = \frac{F_{\mathrm{ad}}}{2\pi a_{ij}^2}\left(1 - \frac{x^2+y^2}{a_{ij}^2}\right)^{-1/2}, \tag{2.61}$$

which results in a constant displacement over the contact area for the Boussinesq problem [83], but corresponds to a negative adhesive total force $F_{\mathrm{ad}} < 0$. The normalisation constant is calculated analogously to equation (2.57). Thus, the combined pressure is positive (repulsive) at the centre of the contact region but becomes negative (tensile) at the boundary. This implies the enlargement of contact radius in JKR theory in comparison with purely elastic Hertz contact and has been observed using optical interferometry [85]. Then, the total stored elastic energy as well as the mechanical potential energy of the load applied can be calculated. If one additionally assumes that the surface energy is uniformly distributed on the contact surface, one obtains

$$U_{\mathrm{adh}} = -\pi\epsilon_{ij}a_{ij}^2 \tag{2.62}$$

with the energy density ϵ_{ij} denoting the combined free surface energy density of both spheres. From minimizing the total energy one then finds in equilibrium an equation connecting the realistic contact surface radius a_{ij} with the net JKR-force between the two spheres i and j [83, 85, 86]

$$a_{ij}^3 = \frac{R_{ij}}{K_{ij}}\left(F_{ij}^{\mathrm{JKR}} + 3\pi\epsilon_{ij}R_{ij} + \sqrt{6\pi\epsilon_{ij}R_{ij}F_{ij}^{\mathrm{JKR}} + (3\pi\epsilon_{ij}R_{ij})^2}\right) \tag{2.63}$$

and for the corresponding indentation

$$h_{ij} = \frac{a_{ij}^2}{R_{ij}} - \frac{2}{3}\sqrt{\frac{6\pi\epsilon_{ij}a_{ij}}{K_{ij}}}. \tag{2.64}$$

The JKR theory has been verified experimentally for materials such as rubber and is used within the context of cell-cell interaction [75] as well. It is known to fit the behaviour of strongly adhesive materials very well [83]. One obtains for the JKR force in dependence of the contact radius

$$F_{ij}^{\text{JKR}} = \frac{K_{ij}a_{ij}^3}{R_{ij}} - \sqrt{6\pi\epsilon_{ij}K_{ij}a_{ij}^3}\,. \tag{2.65}$$

For numerical purposes a direct load-displacement relationship would be more favourable, since the indentation h_{ij} is much simpler to calculate than the actual contact radius a_{ij}. In addition, there are parameter regimes, where equation (2.64) admits two solutions a_{ij} for a given indentation. This becomes obvious if one defines the functions $g_1(a) = -h_{ij} + a_{ij}^2/R_{ij}$ and $g_2(a) = (2/3)\sqrt{6\pi\epsilon_{ij}a_{ij}/K_{ij}}$, and examines their intersections in dependence on h_{ij} (see figure 2.18 left panel). Numerically, the two roots of equation (2.64) in the delicate ambiguity case can be found using a defined algorithm: For negative virtual overlaps h_{ij}, two values $a_{ij}^{\text{min/max}}$ can be found for which the function $f(a) = g_2(a) - g_1(a)$ is negative by setting $f(a_{ij}^{\text{min/max}}) = h_{ij}$. In addition, one can show that the function $f(a)$ has a positive maximum in this regime at a_{ij}^{mean}. With the knowledge of two existent roots, the bisection method [67] can be used on the intervals $\left[a_{ij}^{\text{min}}, a_{ij}^{\text{mean}}\right]$ and $\left[a_{ij}^{\text{mean}}, a_{ij}^{\text{max}}\right]$. A major problem however is that these solutions correspond to formation and disruption of contact. Therefore, the time-evolution of cell-cell distance determines which branch is of interest and would thus have to be tracked for every individual cell pair.

Note that the JKR model does not include viscous effects, these will be added independently in subsection 2.5.4.

For relatively small adhesion however, i. e., $\epsilon_{ij}/(K_{ij}R_{ij}) \ll 1$, one can simplify equation (2.64) by neglecting the second term on the right hand side. This yields

$$a_{ij} \approx \sqrt{h_{ij}R_{ij}}\,, \tag{2.66}$$

or

$$A_{ij}^{\text{JKR}} \approx \pi h_{ij}R_{ij} \tag{2.67}$$

for the JKR contact surface, respectively. Equation (2.66) can be inserted into equation (2.63) to obtain an approximate load-displacement relation for the JKR force

$$F_{ij}^{\text{JKR}} \approx \left[K_{ij}R_{ij}^2\left(\frac{h_{ij}}{R_{ij}}\right)^{3/2} - \sqrt{6\pi\epsilon_{ij}K_{ij}R_{ij}^3}\left(\frac{h_{ij}}{R_{ij}}\right)^{3/4}\right], \tag{2.68}$$

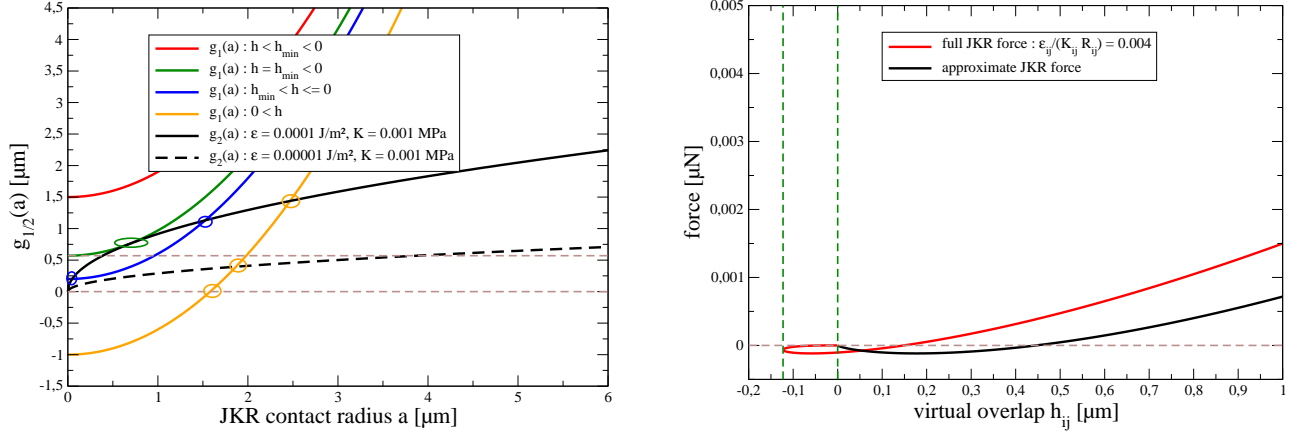compare figure 2.18 right panel. This expression will be used as the JKR-force further-on.

Figure 2.18: Ambiguity of the full JKR model. The figures refer to $R_{ij} = 2.5$ μm. **Left:** The functions $g_1(a)$ (coloured) and $g_2(a)$ (black) have been plotted versus a. For clarity, all other indices have been dropped. Values of a at the intersections (marked by the ellipses) of both functions are roots of equation (2.64). If the indentation h (negative intersection of $g_1(a)$ with the ordinate axis) is smaller than the minimum value $h_{\min} = -3R_{ij}^{1/3} \left[\pi\epsilon_{ij}/(6K_{ij})\right]^{2/3}$, no solution can be found (red). If $h_{ij} = h_{\min}$, one has one solution with $a^* = \left[\pi\epsilon_{ij}R_{ij}^2/(6K)\right]^{1/3}$ (green), and if $h_{\min} < h_{ij} \leq 0$, two solutions can be found (blue). For positive h_{ij}, one always has only one solution (orange). The region of two solutions for $\epsilon_{ij} = 0.0001$ μN μm^{-1} is marked by the brown dashed lines at 0 and $-h_{\min}$. Note that for small adhesion (dashed black curve), the solution of (2.64) and the solution of the approximate equation (2.66) (orange intersection with the lower horizontal line) are close together. **Right:** Full and approximate JKR forces versus the virtual overlap h_{ij}. The ambiguity of the JKR model (red line, region marked by vertical dashed lines) in the case of negative overlaps corresponds to the formation or loss of contact.

The JKR-force is negative (adhesive) for small virtual overlaps and becomes positive (repulsive) for larger overlaps. In figure 2.18 right panel it is visible that in the full model, there is even interaction for negative overlaps. This property is neglected in the approximate version. Note that the minimum JKR force (maximum adhesive force) is – independently on the approximation used – given by

$$F_{ij}^{\text{adh}} = -\frac{3}{2}\pi\epsilon_{ij}R_{ij}, \tag{2.69}$$

which is independent of the elastic properties and thus allows an estimate of ϵ_{ij} from cell-binding-rupture experiments such as e. g. [87, 88]. For the the approximate model, an interaction potential can be defined with $d_{ij} = |\boldsymbol{x}_i - \boldsymbol{x}_j|$ via

$$F_{ij}^{\text{JKR}} = -\frac{\partial V^{\text{JKR}}}{\partial d_{ij}} = +\frac{\partial V^{\text{JKR}}}{\partial h_{ij}} = \frac{1}{R_{ij}}\frac{\partial V^{\text{JKR}}}{\partial h_{ij}/R_{ij}}, \tag{2.70}$$

where the corresponding potential is given by

$$V_{ij}^{\text{JKR}}\left(h_{ij}/R_{ij}\right) = \frac{2}{5}K_{ij}R_{ij}^3\left(\frac{h_{ij}}{R_{ij}}\right)^{5/2} - \frac{4}{7}\sqrt{6\pi\epsilon_{ij}K_{ij}R_{ij}^5}\left(\frac{h_{ij}}{R_{ij}}\right)^{7/4}, \tag{2.71}$$

as is illustrated in figure 2.19. The quantity h_{ij}/R_{ij} describes the relative position of both spheres. It is related with the orthogonal sphere distance for the spheres $\hat{\boldsymbol{r}}_i = (\boldsymbol{r}_i, R_i^2)$ and $\hat{\boldsymbol{r}}_j = (\boldsymbol{r}_j, R_j^2)$ in equation (2.6) via

$$\pi(\hat{\boldsymbol{r}}_i, \hat{\boldsymbol{r}}_j) = \left(\frac{h_{ij}}{R_{ij}}\right)^2 R_{ij}^2 - 2\left(\frac{h_{ij}}{R_{ij}} - 1\right)R_iR_j, \tag{2.72}$$

compare figure 2.20 left panel. In contrast to the Lennard-Jones potential (2.50), the JKR model has been derived from underlying physical assumptions, i. e., its parameters E and ν can in principle be determined from independent experiments.

The normal JKR-theory as introduced above has several shortcomings.

1. It neglects the polarized structure of the cytoskeleton [76], since it is based on the assumptions of a homogeneous elastic solid. To incorporate these effects into a more realistic theoretical model, one would have to consider a multi-component system, which is currently out of reach for multicellular simulations.

2. As its underlying theory [70] is only valid for small deformations $h_{ij}/R_{ij} \ll 1$, equation (2.63) will be subject to the same constraints. Since a complete sphere overlap has never been observed in reality, in the simulations where strong forces occur (e. g. due to additional constraints [89]), a modified interaction potential $V(x) = f(x)V^{\text{JKR}}(x)$ has been used with

$$f(x) = \begin{cases} \frac{(x_d - x_m)^2}{(x_d - 2x_m)(x_d - x)} - \frac{x}{x_d - 2x_m} & : \quad x_m \leq x \leq x_d \\ 1 & : \quad \text{else} \end{cases}, \tag{2.73}$$
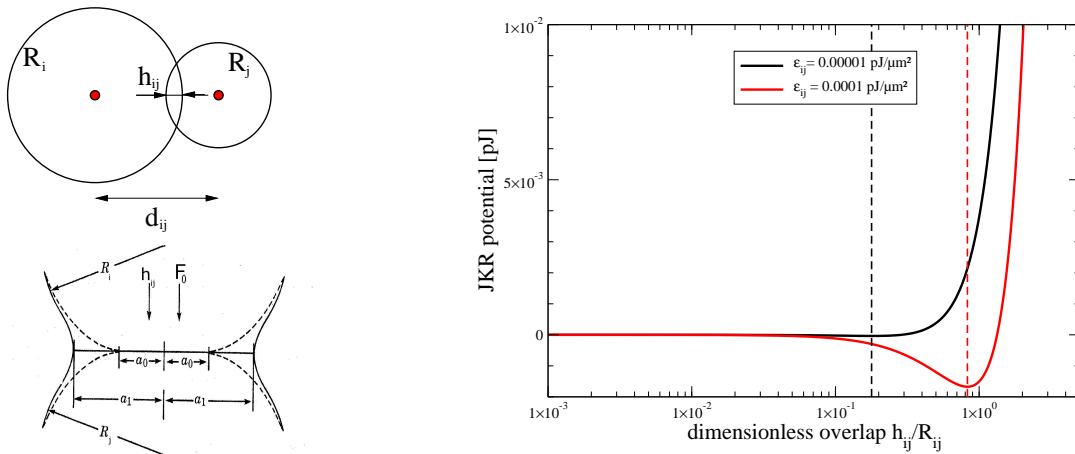
Figure 2.19: Illustration of the JKR interaction model. **Top left:** Two spheres in contact can approximately be described with the JKR-potential (right). The virtual sphere overlap h_{ij} is equivalent to the displacement of the spheres under load and can be calculated via $h_{ij} = R_i + R_j - |\boldsymbol{x}_i - \boldsymbol{x}_j|$. **Bottom left:** Illustration adapted from [85]. In real-world scenarios, the spheres will evidently deform. Due to short-ranged adhesive forces, the pressure distribution at the contact surface is only positive in the centre, whereas it becomes negative at the boundaries. This leads to an enlargement of JKR contact surfaces (contact radius a_1) in comparison to pure Hertz theory (contact radius a_0). **Right:** The existence of adhesive forces gives rise to bound states (minimum at dashed lines). Their position and depth strongly depends on the parameters ϵ_{ij} and K_{ij}. Note that the potential does not diverge at $h_{ij}/R_{ij} = 2 + 2\min\{R_i, R_j\}/\max\{R_i, R_j\}$ (complete overlap). The curves on the right have been computed using the following (physiological) values $K_{ij} = 1000$ Pa, $R_{ij} = 2.5\ \mu$m.
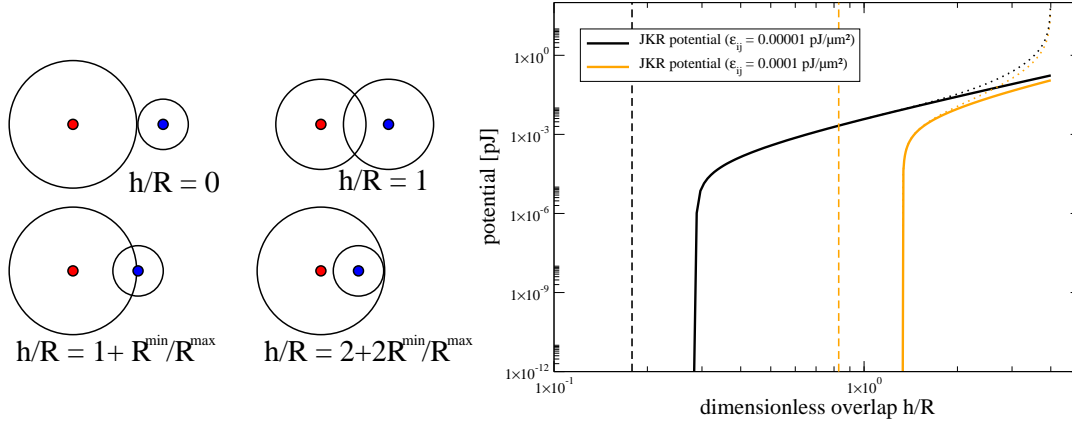
Figure 2.20: Sphere overlaps and modification of the JKR-potential. **Left:** Meaning of the dimensionless sphere distance h_{ij}/R_{ij}. For clarity, the indices have been dropped, i. e., all quantities refer to two specific spheres i and j. For vanishing overlap, one obtains $h_{ij}/R_{ij} = 0$, whereas for the case when the smaller sphere is placed exactly on the boundary of the larger one one has $h_{ij}/R_{ij} = 1 + R_{\min}/R_{\max}$ with $R_{\min} = \min\{R_i, R_j\}$ and $R_{\max} = \max\{R_i, R_j\}$. In this regime, JKR theory is not valid anymore. Matching has been performed at $h_{ij}/R_{ij} = 1$, where one has $\pi(\hat{r}_i, \hat{r}_j) = R_{ij}^2$. **Right:** For this reason, the JKR interaction (solid curves) has been supplemented with a pole at complete sphere overlap (dotted curves). In the physiological regime, the JKR potential is unchanged. Parameters have been chosen as in figure 2.19.

which is differentiable continuous at $x = x_{\mathrm{m}}$ and diverges at $x = x_{\mathrm{d}}$. As matching point $x_{\mathrm{m}} = 1$ and as point for divergence $x_{\mathrm{d}} = 2 + 2R_{\min}/R_{\max}$ (minimum and maximum radius) have been chosen (compare figure 2.20).

3. The original result (2.63) has been derived as a pure two-body interaction [85], which is as well the case for its purely elastic precursor [70, 84]. However, for many adhering spheres already for small individual deformations additional forces will come into play, since

   - the spheres are pre-stressed and

   - the circular contact regions may overlap.

This will critically depend on the current adjacency topology which makes an analytical approach infeasible. A simple manifestation of this fact is that also for incompressible cells ($\nu = 1/2$) the cell volume is not conserved for multiple overlaps. For numerical ease and due to missing estimates in this thesis the following (practitioners) approach has been chosen: Below the target cell volume $V_{i/j}^{\mathrm{target}}$ the cell experiences additional – isotropic – forces due to

compression of the cytoplasm. Then, the resulting additional repulsive force can be written as

$$F_{ij}^{\text{comp}} = A_{ij} \left[\frac{E_i}{3(1 - 2\nu_i)} \left(1 - \frac{V_i}{V_i^{\text{target}}} \right) + \frac{E_j}{3(1 - 2\nu_j)} \left(1 - \frac{V_j}{V_j^{\text{target}}} \right) \right], \qquad (2.74)$$

where $V_{i/j}$ denote the current cellular volumes (compare subsection 2.5.3).

4. Whereas the used forces do only depend on the relative cellular positions, a more realistic scenario would have to include hysteresis effects, as adhesive intercellular bonds form after contact. Within some of the simulations, this has been modelled by making ϵ_{ij} time-dependent, i. e.,

$$\epsilon_{ij}(t) = \frac{\epsilon^0}{2} \left[C_i^{\text{rec}}(t) C_j^{\text{lig}}(t) + C_i^{\text{lig}}(t) C_j^{\text{rec}}(t) \right], \qquad (2.75)$$

where the $0 \leq C_{i/j}^{\text{rec/lig}}(t) \leq 1$ represent the normalised receptor or ligand densities on the cell membranes, respectively, and ϵ^0 is the maximum adhesion energy.

5. The JKR-model neglects dampening forces that will evidently occur in realistic systems [90, 91]. As in the case of the Kelvin element, these will simply be added separately (compare subsection 2.5.4). In the derivation of the JKR model it has been assumed that only forces perpendicular to the contact surface act. However, cell-cell friction will lead to shear deformation, which is neglected here.

Clearly, the JKR-model does not correctly represent the mechanics of the cytoskeleton. For normal cellular deformations, one might expect other than purely elastic responses for larger time-scales, since the cytoskeleton in general reorganises [75]. These effects may be incorporated by using mechanical networks such as in [92]. However, for such a model, the underlying parameters should be derived either from experiments or motivated from microscopic properties of the cytoskeleton. Thus, the modified JKR ansatz presented here should be interpreted as a simple approximation for elastic and adhesive forces in a multi-component system only exhibiting key properties such as divergence at complete cellular overlaps, an adhesive bound state for small overlaps, modified interactions for multi-particle overlaps, and possibly time-dependent elastic and adhesive parameters.

2.5.3 Cell volume

In order to be consistent with the spherical cell shape, the volume of a free cell of radius R_i is directly deduced from the cell radius. For bound cells, the cell volume is corrected by subtracting the volumes

of the spherical segments [67] occupied by the neighbouring cells via

$$V_i = \frac{4\pi}{3} R_i^3 - \frac{\pi}{3} \sum_{j \in \mathcal{NN}(i)} h_j^2 \left(3R_i - h_j \right) , \tag{2.76}$$

where h_j denotes the height of the spherical segment occupied by neighbour cell j such that one has $h_{ij} = h_i + h_j$. One should be aware that this volume correction represents an approximation:

If there are multiple overlaps of the virtual (undeformed) cell boundaries, the occupied subtraction volume will be over-estimated. By the example in figure 2.14 right panel this is illustrated in two dimensions, where volume is represented by area and multiple virtual overlaps exist. Multiple virtual overlaps may exist in three dimensions as well. In fact, the volume as defined above can become negative for extreme (non-physiological) configurations. Even the non-overlapping Voronoi tessellation does not yield a correct estimate of the cell volume, since the Voronoi volume is not bounded for cells residing on the convex hull of the cell population, compare equation (2.18). There, and also in regions where the cellular packing is not dense, the Voronoi tessellation volumes obviously overestimates the actual cell volume.

A way to combine both the limits of densely and sparsely populated cell tissues consistently within a single concept would be to define the cell volume as the set intersection of the (weighted) Voronoi cell volume and the sphere volume via

$$V_i^{\text{cell}} = \left\{ \boldsymbol{x} \in \mathbb{R}^3 \; : \; (\boldsymbol{x} - \boldsymbol{r}_i)^2 - R_i^2 \leq \left(\boldsymbol{x} - \boldsymbol{r}_j \right)^2 - R_j^2 \quad \forall j \in \mathcal{NN}(i) \quad \wedge \quad (\boldsymbol{x} - \boldsymbol{r}_i)^2 \leq R_i^2 \right\} , \tag{2.77}$$

compare figure 2.14. This concept has not yet been realised in the numerical implementation. However, even the above definition has a significant shortcoming, if combined with the JKR model: The cell boundary defined by equation (2.77) is not consistent with the boundary following from the JKR model: Though the position of the contact area is the same in the JKR model and in equation (2.77), the size of the contact areas is different. This is due to the cell deformation in the JKR model. In consequence, this would lead to a wrong estimate of the cell volume. For numerical calculations, a second obstacle is given by the relatively tedious calculation of the volume in (2.77): The actual subtraction volume that is occupied by neighbouring cells has to be calculated from the occupied steradian. This value in turn can be obtained from the geometry of spherical triangles using the L'Huilier equations [67], which involve many trigonometric functions implying a computationally expensive evaluation (compare e. g. [60] for a related problem).

Therefore, for the simulations in this thesis where the cell volume is of importance, it has been determined from equation (2.76).

2.5.4 Equations of Motion

For N cells with positions $\boldsymbol{x}_i(t)$ and radii R_i subject to cell-cell as well as cell-medium and cell-substrate interactions, the equations of motion arising from the intercellular forces can in the reference frame of motionless medium and boundaries be summarized as [79]

$$m_i \ddot{x}_i^\alpha \;=\; F_i^\alpha + \sum_{j\in\mathcal{NN}(i)} F_{ij}^\alpha - \sum_\beta \left(\gamma_i^{\alpha\beta} + \sum_{J\in\mathcal{NB}(i)} \Gamma_{iJ}^{\alpha\beta} \right) \dot{x}_i^\beta - \sum_{j\in\mathcal{NN}(i)} \sum_\beta \gamma_{ij}^{\alpha\beta} \left(\dot{x}_i^\beta - \dot{x}_j^\beta \right), \tag{2.78}$$

where $\alpha, \beta \in \{0, 1, 2\}$ denote the Cartesian coordinates and $i, j \in \{0, 1, \ldots, N-1\}$ the cellular indices. The terming $\mathcal{NN}(i)$ denotes all cells having contact with cell i – a set containing these cells with direct contact can be provided by the Delaunay triangulation module introduced in section 2.3. In contrast, $\mathcal{NB}(i)$ denotes the boundaries in contact with cell i. Since for most problems few and static boundary conditions will be given, these are hard-wired in the computer code for every specific problem individually.

One should note that above equation will in general have to be accompanied by an equation describing the torque [27, 93], which is only taken into account effectively here by the energy dissipation via drag forces. With the strong cellular bindings existent in tissue, torque could only lead to macroscopically spinning tissues. However, since most tissues are attached firmly to static boundaries, torque is neglected here.

The first term F_i^α on the right-hand side of (2.78) includes deterministic and stochastic forces on a single cell (for example crawling forces on a substrate and stochastic forces due to random collisions with molecules), whereas the second term $\sum_{j\in\mathcal{NN}(i)} F_{ij}^\alpha$ includes the intercellular two-body forces (e. g. JKR-force or random intercellular forces). The third term $\left(\sum_\beta \gamma_i^{\alpha\beta} + \sum_\beta \sum_{J\in\mathcal{NB}(i)} \Gamma_{iJ}^{\alpha\beta} \right) \dot{x}_i^\beta$ incorporates cell-medium as well as cell-boundary friction. Finally, the fourth term $\sum_{j\in\mathcal{NN}(i)} \sum_\beta \gamma_{ij}^{\alpha\beta} \left(\dot{x}_i^\beta - \dot{x}_j^\beta \right)$ includes cell-cell friction.

A usual choice for cell-medium friction is the well-known Stokes-relation

$$\gamma_i^{\alpha\beta} = 6\pi\eta R_i \delta^{\alpha\beta}, \tag{2.79}$$

which is to a good approximation valid for drag forces on a sphere in a fluid with viscosity η [94].

The friction coefficients and two-body forces fulfil the following conditions:

$$
\begin{aligned}
\gamma_{ij}^{\alpha\beta} &= \gamma_{ji}^{\alpha\beta}, \\
F_{ij}^{\alpha} &= -F_{ji}^{\alpha} \qquad : \qquad \text{(Newton's third axiom)}, \\
\gamma_{ij}^{\alpha\beta} &= \gamma_{ij}^{\beta\alpha}, \\
\gamma_{i}^{\alpha\beta} &= \gamma_{i}^{\beta\alpha} \qquad : \qquad \text{(isotropy)}, \\
\gamma_{ii}^{\alpha\beta} &= 0 \qquad\quad : \qquad \text{(no self-friction)}.
\end{aligned}
\tag{2.80}
$$

The drag forces expressed by the friction coefficients may be divided in perpendicular drag forces (acting in the direction of the connection line) and tangential (shear) drag forces. The perpendicular drag forces are predominantly determined by the dampening properties of the cytoskeleton, whereas the tangential drag forces result from the breaking of cell-cell bindings due to movements tangential to the contact surface [76]. If for the cell-cell interaction a purely elastic model (without dampening) is assumed, the perpendicular drag forces should vanish. Assuming that the intercellular drag forces are proportional to the effective contact area between two cells i and j

$$
A_{ij}^{\text{eff}} = A_{ij} \frac{1}{2} \left[C_i^{\text{rec}}(t) C_j^{\text{lig}}(t) + C_i^{\text{lig}}(t) C_j^{\text{rec}}(t) \right]
\tag{2.81}
$$

and to the tangential projection of the velocity differences, the friction coefficients take the form

$$
\begin{aligned}
\gamma_{ij}^{\alpha\beta} &= A_{ij}^{\text{eff}} \left(\gamma_{\parallel} \mathcal{P}_{ij,\parallel}^{\alpha\beta} + \gamma_{\perp} \mathcal{P}_{ij,\perp}^{\alpha\beta} \right) \left(1 - \delta_{ij} \right), \\
\Gamma_{iJ}^{\alpha\beta} &= A_{iJ} \left(\gamma_{\parallel} \mathcal{P}_{iJ,\parallel}^{\alpha\beta} + \gamma_{\perp} \mathcal{P}_{iJ,\perp}^{\alpha\beta} \right),
\end{aligned}
\tag{2.82}
$$

with the intercellular tangential and perpendicular projectors

$$
\mathcal{P}_{ij,\parallel}^{\alpha\beta} = \delta^{\alpha\beta} - n_{ij}^{\alpha} n_{ij}^{\beta}, \qquad \mathcal{P}_{ij,\perp}^{\alpha\beta} = n_{ij}^{\alpha} n_{ij}^{\beta},
\tag{2.83}
$$

and the cell-boundary projectors

$$
\mathcal{P}_{iJ,\parallel}^{\alpha\beta} = \delta^{\alpha\beta} - n_{iJ}^{\alpha} n_{iJ}^{\beta}, \qquad \mathcal{P}_{iJ,\perp}^{\alpha\beta} = n_{iJ}^{\alpha} n_{iJ}^{\beta}.
\tag{2.84}
$$

In the above projection operators, $\boldsymbol{n}_{ij}$ represents the normal vector pointing from cell i towards cell j (compare figure 2.21), whereas $\boldsymbol{n}_{iJ}$ denotes the normal vector of the boundary J at the contact point with cell i. Therefore, their action on any vector $\boldsymbol{a}$ projects the vector into its tangential or perpendicular part

$$
\boldsymbol{n}_{ij}^{\text{T}} \cdot \left(\mathcal{P}_{ij,\parallel} \boldsymbol{a} \right) = 0, \qquad \boldsymbol{n}_{ij}^{\text{T}} \cdot \left(\mathcal{P}_{ij,\perp} \boldsymbol{a} \right) = \boldsymbol{n}_{ij} \cdot \boldsymbol{a}.
\tag{2.85}
$$

The projection operators (2.83) automatically obey the symmetries demanded in equation (2.80) on the friction coefficients.
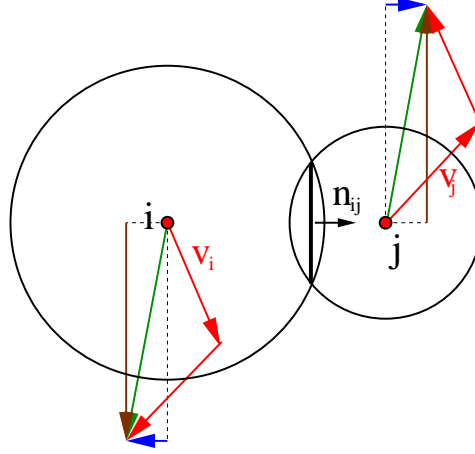
Figure 2.21: Two-dimensional illustration of intercellular drag forces. The differential velocities between two cells *i* and *j* (green) in contact may give rise to different drag forces, one proportional to the tangential part of the velocity difference (brown) and one proportional to the perpendicular part (blue).

Cells nearly always move in highly dissipative environments. This has the (in view of the numerical solution fortunate) consequence that the cellular movement is highly overdamped [92, 95, 96]. In the overdamped approximation ($m\ddot{x} \approx 0$), equation (2.78) can be cast into the following form,

$$\sum_{k,\beta} \left\{ \left[\gamma_k^{\alpha\beta} + \sum_j \gamma_{kj}^{\alpha\beta} + \sum_J \Gamma_{kJ}^{\alpha\beta} \right] \delta_{ik} - \gamma_{ik}^{\alpha\beta} \right\} \dot{x}_k^\beta = F_i^\alpha + \sum_j F_{ij}^\alpha. \tag{2.86}$$

From the properties of the friction coefficients it is evident, that the above linear system is symmetric and in addition diagonally dominant as long as $\gamma_i^{\alpha\alpha} + \sum_J \Gamma_{iJ}^{\alpha\alpha} > 0 \qquad \forall i, \alpha$, which holds true if the viscosity η in equation (2.79) does not vanish, as all diagonal entries in the projection operators (2.83) and (2.84) are positive. In addition, it should be noted that the system will under normal circumstances be sparsely populated, since the friction coefficients vanish for all cells not being in direct contact. An iterative method such as the method of conjugate gradients – compare appendix B.2 – can be used to find the solution of equation (2.86). Technically, one will be interested in the positions at time $t + \Delta t$ starting from knowledge of the positions at time t. The new positions can be obtained by discretising the time derivative via $\dot{x} = [x(t + \Delta t) - x(t)]/\Delta t$ and using the method of conjugate gradients to solve for $x(t + \Delta t)$. Note however, that the stochastic forces may depend on the timestep size Δt (see appendix C.2.3).

So far the cellular radii have been assumed to be constant. If one simply uses time-dependent radii [77] – as is done within this thesis – one assumes that the cellular ability to grow is not directly

affected by other processes, i. e., the direct back-reaction of the force distribution on cell growth is neglected.

An example including cell-cell and cell-boundary friction is illustrated in figure 2.22. Indeed, for this special example all non-isotropic friction coefficients vanish except $\gamma_{03}^{\alpha\beta}, \gamma_{04}^{\alpha\beta}, \gamma_{23}^{\alpha\beta}, \gamma_{34}^{\alpha\beta}, \Gamma_0^{\alpha\beta}, \Gamma_4^{\alpha\beta}$. Consequently, for this example the system (2.86) would assume the form
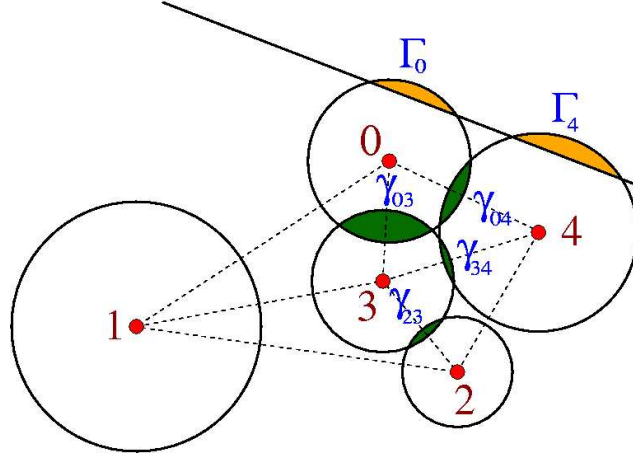

Figure 2.22: Two-dimensional example for the calculation of drag forces. The dotted lines denote the weighted Delaunay triangulation of the set of spheres. Only spheres with cell-cell contact (overlap, marked green) will contribute to intercellular friction (constants marked in blue). Contacts with external boundaries (overlap, marked orange) will contribute to cell-boundary friction. Spheres that are not connected in the Delaunay triangulation will not overlap, whereas the inverse conclusion is not valid.

$$
\begin{pmatrix}
\Gamma_0 + \gamma_0 + \gamma_{03} + \gamma_{04} & \mathbb{O} & \mathbb{O} & -\gamma_{03} & -\gamma_{04} \\
\mathbb{O} & \gamma_1 & \mathbb{O} & \mathbb{O} & \mathbb{O} \\
\mathbb{O} & \mathbb{O} & \gamma_2 + \gamma_{23} & -\gamma_{23} & \mathbb{O} \\
-\gamma_{03} & \mathbb{O} & -\gamma_{23} & \gamma_3 + \gamma_{03} + \gamma_{34} & -\gamma_{34} \\
-\gamma_{04} & \mathbb{O} & \mathbb{O} & -\gamma_{34} & \Gamma_4 + \gamma_4 + \gamma_{04} + \gamma_{34}
\end{pmatrix}
\begin{pmatrix}
\dot{x}_0 \\
\dot{x}_1 \\
\dot{x}_2 \\
\dot{x}_3 \\
\dot{x}_4
\end{pmatrix}
=
\begin{pmatrix}
F_0 \\
F_1 \\
F_2 \\
F_3 \\
F_4
\end{pmatrix},
$$
(2.87)

where in three dimensions the symbols F_i and x_i denote vectors in $\mathbb{R}^3$ and γ_{ij}, γ_i, and Γ_i denote 3×3 matrices. The symbol $\mathbb{O}$ denotes identically vanishing matrices. This system is sparsely populated[8], which is a great advantage for iterative methods, since the number of necessary multiplications scales with the number of non-zero matrix entries – provided a sparse storage scheme (compare

---

[8]Note that the degree of sparseness will increase further for larger systems, as the average number of off-diagonal neighbours will become independent on the system size.

appendix B.1) is used. For the applicability of iterative schemes such as the method of conjugate gradients it is more important that the system is symmetric and irreducibly diagonally dominated as long as $\gamma_i^{\alpha\alpha} + \Gamma_i^{\alpha\beta} > 0 \qquad \forall \qquad i, \alpha$. This suffices to guarantee the positive definiteness required by the conjugate gradient algorithm, since any matrix $A = (A)_{ij}$, which is symmetric (i. e., $A_{ij} = A_{ji}$), irreducibly diagonally dominant (i. e., $|A_{ii}| \geq \sum_{j \neq i} |A_{ij}|$ and for one k one has $|A_{kk}| > \sum_{j \neq k} |A_{kj}|$), and has only positive diagonal entries ($A_{ii} > 0$) is always positive definite:

A symmetric matrix can be diagonalised using an orthogonal transformation, which implies real eigenvalues. Using diagonal dominance and the positiveness of all diagonal entries, one has

$$A_{ii} \geq \sum_{j \neq i} |A_{ij}| \qquad \forall i, \tag{2.88}$$

where one can use the Gerschgorin circle theorem to deduce that all eigenvalues of the matrix A are non-negative. In addition, the determinant will not vanish. This implies that the eigenvalues are all positive, which is equivalent to positive definiteness.

2.5.5 The cell cycle

Without representations of internal cellular states, the model would merely calculate the mechanical interaction between a number of adhesive and elastic spheres. Comparisons with experimental data should be as simple as possible. Therefore, the position in the cell cycle has been characterized by a discrete variable, which determines the actions of the cellular agents. Within the models discussed in this thesis, the following internal states are distinguished: G_1-phase, S/G_2-phase, M-phase, G_0-phase, necrotic, cornified. The states of the cell cycle are illustrated in figure 2.23. It is assumed that during G_1-phase, the cell volume grows at a constant rate r_V, i. e., the radius increases according to $\dot{R} = \left(4\pi R^2\right)^{-1} r_V$, until the cell reaches its final mitotic radius $R^{(m)}$. The volume growth rate r_V is deduced by assuming that the cellular volume doubles during G_1-phase

$$r_V = \frac{2\pi \left(R^{(m)}\right)^3}{3\tau_{G_1}}, \tag{2.89}$$

where τ_{G_1} can be deduced from the minimum observed cycle time τ^{min} and the durations of the S/G_2-phase and the M-phase. Afterwards, no further cell growth is performed. At the end of the G_1-phase, a checkpointing mechanism is performed where the cell can switch into G_0-phase. The nature of this checkpointing mechanism has been chosen depending on the current application within this thesis. Possible choices include:

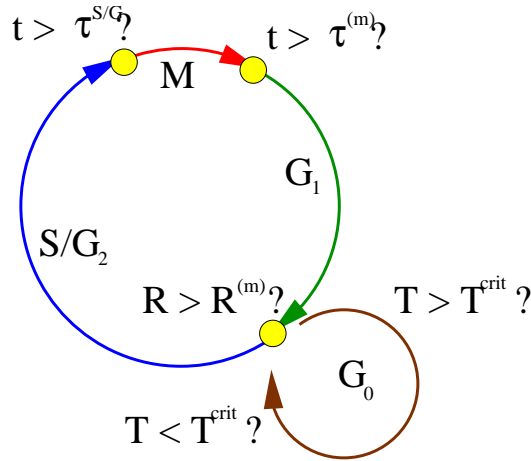- the actual cellular compression [76],

Figure 2.23: Agent-based model realisation of the cell cycle. During cell division, cells reside in the M-phase for $\tau^{(m)}$. Afterwards, the cell volume increases at a constant rate in the G_1-phase, until the pre-mitotic radius $R^{(m)}$ has been reached. At the end of the G_1-phase, the cell can either continue the cell cycle or enter the G_0-phase, if the necessary conditions are fulfilled – here exemplified by the critical value T^{crit}. The S/G_2-phase lasts for a time τ^{S/G_2}, after which mitosis is initiated deterministically. The necrotic state (not shown) can be entered at all times in the cell cycle.

- the cellular tension [77],

- the local nutrient supply,

- the local concentration of toxic substances etc.

After this checkpoint, the cell can either enter the G_0-phase or the S/G_2-phase. During the S-phase, the DNA for the new cell division is synthesised, whereas during G_2-phase the quality of the produced DNA is controlled. As this thesis deals with the distribution of cellular tissues on a more macroscopic level, within the current implementation the S-phase and G_2-phase are not distinguished. At the beginning of the phase the individual phase duration is determined using a normally-distributed random number generator [97] with a given mean and width. After this individual time has passed, the cells deterministically enter mitosis.

At the beginning of the mitotic phase – which lasts for about half an hour for most cell types – a mother cell divides and is replaced by two daughter cells. As a modelling assumption, the initial direction of mitosis can either be chosen randomly [77] (see subsection 2.5.6) or also oriented [76]. For isotropic tissues such as multicellular tumour spheroids (MTS), the first assumption led to acceptable tissue morphology, whereas for oriented tissues, an initial orientation of mitosis due to polarized cells might be expected. Afterwards, the daughter cells are left to their initially dominating repulsive forces

(2.68). As in the S/G$_2$-phase the individual duration of the M-phase is determined using a normally-distributed random number generator. The daughter cells enter the G$_1$-phase thus closing the cell cycle. Note that this model does not differentiate between the internal phases of mitosis such as interphase, prophase, pro-metaphase, metaphase, anaphase, and telophase.

During G$_0$-phase, the chosen critical parameter (e. g. cellular volume, tension, etc.) is monitored. Cells then re-enter the cell cycle where they left it if the conditions that led to entrance into the G$_0$-phase are relaxed. Similar to the S/G$_2$-phase no growth is performed. Therefore, within this agent-based model, the difference between the S/G$_2$-phase and the G$_0$-phase is that the duration of the first is determined by the normally distributed individual time that can be derived from experiments, whereas for the duration of the latter the temporal evolution of the critical mechanism chosen for G$_0$-induction is the determining factor. Consequently, if the critical mechanism is limited space, the cells in G$_0$-phase can serve as a reservoir of cells ready to start proliferating as soon as there becomes enough space available, which is common to many wound-healing models [76]. In chapters 3 and 4 two different critical mechanisms will be specified.

Intuitively, cells enter necrosis at any time as soon as for example the nutrient concentration at the cellular position falls below a critical threshold. Within this thesis, different mechanisms for the induction of necrosis will be discussed (see subsection 3.4.1). Naturally, necrotic cells do not consume any nutrients. In addition, they do decay and expel their content into the surroundings [98]. In the model this fact is simply represented by removing these cells from the simulation (compare subsection 3.2).

Note that the stochastic elements involved in the dynamics of the discrete cellular states are the direction of mitosis and the durations of the M-phase and S/G$_2$-phase. If applied, the first is required by the local assumption of isotropy, whereas the latter is required by the fact that proliferating cells having a common progenitor desynchronise rather quickly (usually after about 5 generations [99]): For these small systems of $O\left(2^5\right)$ cells mechanisms such as nutrient depletion or contact inhibition cannot explain the desynchronisation. It is an empirical fact that times observed in macroscopic biological systems underly significant stochastic deviations. Therefore, these stochastic elements have been inserted in the durations of the cell cycle stations.

2.5.6 Proliferation

Within the model, a cell will divide deterministically when the end of the S/G$_2$ phase has been reached. As discussed before, the initial direction of mitosis can be chosen randomly from a uniform distribution on the unit sphere [97]. Note however, that since within dense tissue the cellular

movement during the M-phase is not only determined by the mitotic partners but by the surrounding cells as well, the effective direction of mitosis may generally change during M-phase. The radii of the daughter cells are decreased $R^{(d)} = R^{(m)}2^{-1/3}$ to ensure conservation of the target volume during M-phase and the daughter cells are placed at the distance $d_{ij}^0 = 2R^{(m)}(1 - 2^{-1/3})$ to ensure that in this first discontinuous step the daughter cells do not leave the region occupied by the mother cell (see figure 2.24). From a numerical point of view, this has the advantage that the surrounding cells are not immediately disturbed by the mitotic cells. It should be kept in mind that in reality mitosis is a more continuous process. Furthermore, depending whether one has a symmetric (e. g. in MTS, see chapter 3) or an asymmetric cell division (e. g. in the basal layer of the epidermis, see chapter 4), the daughter cells either have the same or a different cell type as the mother cell, respectively. One should
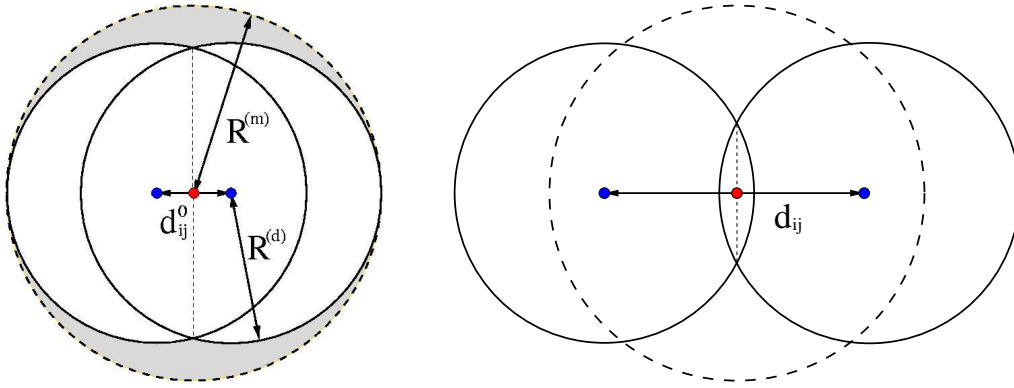

Figure 2.24: Cell configuration during mitosis. **Left:** At cell division, the radii of the daughter cells $R^{(d)}$ (solid circles) are smaller than the radius of the mother cell $R^{(m)}$ (dashed circle) to ensure conservation of the target volume during M-phase. For symmetric cell division, both daughter cells have the same cell type, whereas for asymmetric cell division cell types differ. The region of possible contact loss with further neighbours (not shown) is marked in light grey. **Right:** The resulting repulsive forces drive the cells apart quickly. An adaptive timestep control ensures that the daughter cells do not lose contact with each other during M-phase. Note that the initial direction of mitosis will in general change due to interactions with additional neighbouring cells (not shown here). Further intercellular contact may be lost with cells residing perpendicular to the direction of mitosis.

be aware that at this stage the forces derived from a physically-motivated elastic/adhesive model such as e. g. the JKR-model (2.68) cannot represent the actual mitotic separation forces, since for the considerable initial overlap $h = R^{(m)}(2^{5/3} - 2) = R^{(d)}(4 - 2^{4/3})$, these elastic theories have been applied far beyond their region of validity (compare section 2.5.2). The chosen procedure represents a trade-off between a good agreement with reality and model simplicity. To increase agreement with realistic mitosis, it would be possible to set up a more accurate model of cell division that includes conservation of the actual cell volume during bell-shape mitosis. This however would imply the introduction of a new dynamic theory which is not backed by quantitative experimental evidence.

It is visible in figure 2.24 left panel that in the initial step of mitosis, the contact to neighbour cells (residing off the mitotic axis) may at least temporarily be lost. In dense tissue, such contacts will be re-established, as the local topology will change to relax mechanical tensions. There is experimental evidence that for EMT6/Ro tumour spheroids, cell-cell contacts may be lost during mitosis [100]. Consequently, the potential loss of neighbours during mitosis might be regarded a physiological property of the model.

With the simple model chosen, it must be kept in mind that with a fixed timestep width, the strong initial separation forces could lead to instantaneous separation of the daughter cells in the numerical solution. This technical problem is avoided by an adaptive timestep, which must be applied in the numerical solution of equation (2.86). This timestep is chosen small enough, such that a defined maximum spatial stepsize is not exceeded. Even with an adaptive timestep, the initial separation of mitosis will still happen on a timescale shorter than in reality. One should keep in mind that the relative shortness of the M-phase in comparison with the complete cell cycle leads to a small fraction of cells being in the M-phase at a given time. Therefore, one can expect the consequences of this simplifying assumption to be relatively small.

2.5.7 Model application

For biological applications, the model as introduced in the previous subsections is not specific enough. Though it is intrinsically consistent, it does not grasp the variety for example of different cell types. Therefore, the model properties proposed in this section should be interpreted as a basic framework, upon which further approximations (to enable a computational treatment) and specifications (to approach a biological model system) can be applied. The more specific models applied in the following chapters refer to this section as the basic model. Consequently, the basic limitations of the presented model apply to the discussion in the following chapters as well.

It is evident that agent-based models relying on an intrinsic spherical cell shape do not reflect the variety of cellular shapes in reality. This does not have to restrict the model to applications, where the unperturbed cell shape is approximately spherical. In addition, one can consider biological problems where one can suspect that cell shape and functional mechanisms under consideration are not causally connected.

Chapter 3

Multicellular Tumour Spheroids

Having the currently widely-accepted hypothesis of monoclonal origin of cancer in mind [101], agent-based models evidently bear an advantage in comparison to continuum approaches, since they allow to track the fate of individual cells. In addition to the cellular automaton approach applied usually [7, 102], an off-lattice approach allows for continuous cell positions [103, 89]. In these models, the extent to which cellular interactions have to be replaced by effective rules is smaller than in corresponding cellular automata. Consequently, the model parameters for physical interactions can – in principle – be directly measured in independent experiments. The drawback of agent-based – and in particular off-lattice agent-based – models is their enormous computational complexity. Therefore, they should not be preferred generally but only after a detailed examination of their use in the chosen application. In this chapter, two modelling concepts (off-lattice agent-based and continuum) will be applied to experimental data on multicellular tumour spheroids (MTS). Unlike sometimes done for continuum models that link the instantaneous cell distribution to the corresponding nutrient levels [104, 105], the cellular population density will be treated as a dynamic parameter. In addition, both the distributions of the oxygen and glucose concentrations will be analysed simultaneously.

3.1   Limitations on cell growth

Healthy cells in eucaryots do not follow the exponential growth law, which is expressed in other organisms such as bacteria in presence of favourable growth conditions. Instead, fully-differentiated cells usually do not proliferate at all. The large cell numbers encountered in our organism are produced by populations of asymmetrically-dividing stemcells. There exist many control mechanisms that ensure that differentiated cells do not proliferate. For example, the endings of the chromosomes

are protected by telomeres. These telomeres lead to an upper bound on the number of cell divisions, since in differentiating cells they are shortened with every division. In absence of the telomere protection, complete failure of the DNA transcription is implied and thus the proliferation cycle is halted. The resulting theoretical boundary for cell proliferation has been estimated to be about 50 cell divisions [101]. However, for cells with a diameter of 10 μm and the specific density of water, this would still correspond to 590 kg of cell mass! Clinically manifest and stationary tumours are much smaller which implies that further control mechanisms – leading to loss of cancerous cells – must be at work: It is known that after the initial malignant mutation, many tumour cells are not able to complete the cell cycle [101]. However, some immortal tumour cell lines seem to divide indefinitely – at least they exceed the theoretical boundary of 50 cell divisions by far. Consequently, not only the primary control mechanisms but in addition the shortening of the telomere endings must be severely disturbed in these cell lines. A corresponding enzyme – telomerase – has been discovered in stemcells and some immortal tumour cell lines. The immortality of tumour cells would normally lead to an exponential growth law. Within culture of solid tumours however, this exponential growth law is observed only initially:

1. In two-dimensional (monolayer) culture, proliferation of cells in the interior becomes inhibited – though these are adequately supported with nutrients. Cells situated at a free boundary of the population will always have enough space and nutrients to follow the normal course of the cell cycle. If there is not enough space available, cells cease to proliferate – a phenomenon termed contact inhibition [76, 106]. In unconstrained populations then only a subpopulation continues to proliferate, which leads to polynomial growth only [77].

2. In three-dimensional spheroid culture, the cells in the interior of the spheroid cannot be supported adequately with nutrients. Here, the process of contact inhibition is cooperating with the lack of nutrients emerging in the interior of the cell population [107]. Usually, this lack of nutrients causes cells to undergo apoptosis or necrosis – processes that differ in many aspects [98] but in terms of population dynamics result in the same outcome: cell death. Hence, cell growth is limited further and even complete saturation of spheroid growth has been observed [108].

The final stages of spheroid growth exhibit a typical pattern in the cross-sections: A core consisting of mainly necrotic cells is surrounded by a viable layer of quiescent (non-proliferating) cells, which in turn is surrounded by a layer of proliferating cells [14] (see figure 3.1). This general appearance is found for many avascular *in vivo* tumours as well. For many medical applications, MTS constitute a popular experimental model system, since they are closely mimicking avascular tumours within living

tissues [109, 110]. This opens the possibility to test the effect of e. g. chemotherapeutic agents under conditions close to the *in vivo* system.
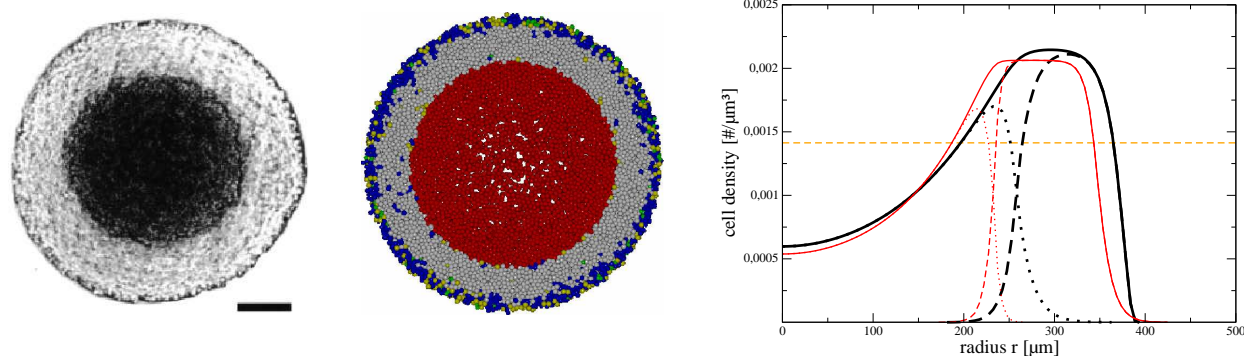

Figure 3.1: Typical morphology of *in vitro* [14] and *in silico* [66, 77] MTS. **Left:** Cross-Section through a three-dimensional MTS, taken from [14]. The inner necrotic core is surrounded by a layer of quiescent cells, which in turn is surrounded by a layer of viable cells – the bar represents 250 μm. **Middle:** This qualitative picture can be reproduced in an agent-based model [77], calculated for 0.28 mM oxygen and 16.5 mM glucose concentrations, and cell diameters of 10 μm. **Right:** In a continuum model [66] cellular dynamics is represented by partial differential equations. For different modelling assumptions (black and red), the radial distribution of cell densities yields the same qualitative picture (dashed curves mark viable cell densities, whereas dotted curves denote necrotic cells).

Even such a simple experimental model represents a highly-coupled system of many involved factors: As there are evident differences in object sizes – $\mathcal{O}(\mu\text{m})$ for cells, $\mathcal{O}(\text{nm})$ for nutrient molecules – and nutrient molecules do not move actively, the dynamics of the nutrients can be well-described by RDEs using effective diffusion coefficients and reaction rates [66, 103, 105, 111]. The dynamics of the cellular movement however is not fully understood at present. Agent-based models provide many possibilities to test hypotheses on cellular kinetics and the cell numbers observed in EMT6/Ro spheroids (in the order of $10^5 \ldots 10^6$ cells [107]) are at the feasibility limit of current agent-based models.

3.2 An agent-based approach : Model details

3.2.1 Dynamics of cells

Within agent-based approaches to cell tissue, every cell is interpreted as a separate entity interacting with its neighbours. For the calculation of the dynamics of these entities, the model has been built on

the basic description given in subsections 2.5.4, 2.5.5, and 2.5.6. In addition, owing to the large cell numbers encountered in MTS, the following simplifications/specifications have been performed [77]:

1. Intercellular friction has been assumed to be small in comparison to cell-matrix friction, i. e., with the assumption $\gamma_{ij}^{\alpha\beta} \approx 0$ the equations of motion (2.86) become diagonal in the absence of boundaries. Note that for systems of $O\left(10^6\right)$ cells the solution of the complete system would become virtually impossible in reasonable time by using the method of conjugate gradients (compare figure B.2 in the appendix for at most 40000 cells). However, in order to preserve the fact that cells having many bounds to their next neighbours will experience stronger drag forces than free-floating cells, the diagonal entries in the dampening matrix have been modified according to

$$\gamma_i^{\alpha\beta} = \delta^{\alpha\beta}\left[6\pi\eta R_i + \gamma^{\mathrm{max}} \sum_{j\in\mathcal{NN}(i)} \frac{1}{2}\left(1 - \frac{\boldsymbol{F}_i \cdot \boldsymbol{n}_{ij}}{|\boldsymbol{F}_i|}\right)\frac{A_{ij}(t)}{2}\left(c_i^{\mathrm{rec}}c_j^{\mathrm{lig}} + c_i^{\mathrm{lig}}c_j^{\mathrm{rec}}\right)\right], \tag{3.1}$$

   where the first term represents the usual Stokes friction terms (with R_i denoting the radius of cell i), and $A_{ij}(t)$ denotes the contact surface between cells i and j. The model parameter γ^{max} determines the degree of intercellular friction. With this choice, movements leading to cell separation are suppressed strongest, whereas for movements of cells towards each other one has no additional friction. Note that despite the occurrence of $\delta^{\alpha\beta}$ this is not an isotropic choice, since the net force on a single cell $\boldsymbol{F}_i = \sum_{j\in\mathcal{NN}(i)} \boldsymbol{F}_{ij}$ directly contributes to the calculation of the friction coefficient. This is in direct contradiction with with equations (2.86), as there the net differential velocity determines the magnitude of the drag forces.

2. As a contact model a simple linear combination of the purely repulsive Hertz model [70, 84] and an adhesive contribution scaling linearly with the effective contact surface has been chosen

$$F_{ij} = +\frac{h_{ij}^{3/2}(t)}{\frac{3}{4}\left(\frac{1-\nu_i^2}{E_i} + \frac{1-\nu_j^2}{E_j}\right)\sqrt{\frac{1}{R_i(t)} + \frac{1}{R_j(t)}}} - f^{\mathrm{ad}}\frac{A_{ij}(t)}{2}\left(c_i^{\mathrm{rec}}c_j^{\mathrm{lig}} + c_i^{\mathrm{lig}}c_j^{\mathrm{rec}}\right), \tag{3.2}$$

   where the first term is as well yielded from the JKR-model (2.63) in the special case of vanishing contact surface energy $\epsilon_{ij} = 0$, and the second term is the simplest possible choice motivated by the assumption that the adhesive forces are proportional to the effective contact surface. The force is positive (repulsive) for large virtual overlaps, and negative (attractive) for small virtual overlaps h_{ij}.

3. For the calculation of the intercellular contact surfaces the pure sphere contact area may yield a wrong estimate of actual contact surfaces (compare subsection 2.3.9). Therefore, as an improved measure for intercellular contact, the minimum of the sphere and the Voronoi contact surfaces has been chosen to calculate the intercellular contact surfaces in equations (3.2) and (3.1)

$$A_{ij} = \min\left\{A_{ij}^{\text{Sphere}}, A_{ij}^{\text{Voronoi}}\right\}.$$ (3.3)

   This yields reasonable estimates for intercellular contact surfaces both in the low-density and the high-density limit (compare subsection 2.5.3).

4. The possible cellular states are given by M-phase, G_1-phase, S/G_2-phase, G_0-phase, and necrotic. No distinction between necrosis and apoptosis has been made.

5. In the agent-based model [77], the criterion for entering G_0-phase has been chosen to be the sum of the normal tensions T^{crit}, whereas in some other applications [89] the free cell volume as defined in subsection 2.5.3 has been chosen. Both choices result in the common effect that in overcrowded regions cell growth will be halted. Whether cell sense the acting normal tensions or whether they sense their admitted volume should be discriminated in microscopic experiments.

With using these approximations, the system (2.86) becomes diagonal, i. e., if no additional boundary conditions are imposed, one has

$$\dot{r}_i^\alpha = \frac{F_i^\alpha}{\gamma_i^{\alpha\alpha}} = \frac{\sum\limits_{j\in\mathcal{NN}(i)} F_{ij}^\alpha}{6\pi\eta R_i + \gamma^{\max} \sum\limits_{j\in\mathcal{NN}(i)} \frac{1}{2}\left(1 - \frac{F_i \cdot n_{ij}}{|F_i|}\right) \frac{A_{ij}(t)}{2}\left(c_i^{\text{rec}} c_j^{\text{lig}} + c_i^{\text{lig}} c_j^{\text{rec}}\right)}.$$ (3.4)

In general, the force terms may contain additional random forces. Thereby, both passive cell movements (resulting from Brownian motion) and random active cell movements will contribute. For the chosen example of EMT6/Ro tumour cells, only passive random motion (compare appendix C.2.3) has been assumed. Via the Stokes-Einstein relation

$$D = \frac{k_B T}{6\pi\eta R}$$ (3.5)

the diffusion constant for passive random motion can be estimated. The corresponding diffusion constants lead to rather small cellular displacements. Nevertheless, at the boundary of growing tumour spheroids this might lead to separation of cells on the proliferating front. However, it has turned

out during the simulations that after some time the proliferation-driven tumour front will generally overtake cells that have separated due to random movements. In addition, it turned out that the stochastic nature contained in the mitotic direction and the duration of the cell cycle obviously suffices to yield isotropic tumour spheroids. Therefore, the agent-based simulations on tumour spheroids have been performed without explicit stochastic forces, unless otherwise noted.

3.2.2 Nutrient consumption and Cell Death

The nutrient uptake rates can in principle depend on the cell type, the local concentration of both nutrients, the existence of internal cellular nutrient reservoirs and many other factors. However, few information about the dependence on determining factors is known: Many rates in the literature [104, 112] are average values given in units of mol per seconds and volume of tissue, since these data are obtained from whole cell populations without regard to the individual cell size, position in the cell cycle and other factors. There is evidence for a dependence of the nutrient uptake rates on the local nutrient concentration [113]. For example, when dealing with a single nutrient, quite often a Michaelis-Menten-like concentration-dependent nutrient uptake rate

$$r_{\text{nut}} = \frac{r_{\max} u_{\text{nut}}}{u_{1/2} + u_{\text{nut}}} \tag{3.6}$$

is assumed [99, 111, 114, 115]. This however means the introduction of a further parameter that may be difficult to fix depending on the data available. The values obtained for $u_{1/2}$ in the literature for oxygen-dependent proliferation ([116], $u_{1/2} = 0.0083$ mM) point into the direction that the oxygen consumption rates are within the range of saturation for the data in [107], since in the agent-based simulations [77] the local oxygen concentration has always been considerably larger (≥ 0.04 mM throughout the spheroid volume). For simplicity, constant cellular oxygen and glucose uptake rates have been assumed for non-necrotic cells in the present model.

Depending on the cell type and on the local nutrient concentrations cells undergo apoptosis and/or necrosis when subject to nutrient depletion [107]. For simplification, in this application necrosis has been chosen as the dominant pathway to cell death and the effects of apoptosis have been neglected, though there is experimental evidence that these processes are linked with each other [98]. Necrotic cells tend to decay, thereby expelling their content. *In vivo* this leads to processes such as inflammation, whereas in *in vitro* experiments their content is passed into the fluid phase: The pressure of this fluid phase is assumed to be equilibrated at all times throughout this thesis, therefore its existence does have no further consequences than the removal of necrotic cells. These are removed randomly from the simulation with a rate r^{necr}. The effect of apoptosis in the simulation would be similar, though apoptotic cells do not break apart like necrotic cells but shrink and afterwards dissolve into small

apoptotic bodies [117]. Thus, for the overall outcome of the total growth curve in *in vitro* systems – where macrophages lysing these apoptotic bodies are not included – insignificant changes can be expected by including apoptosis into the model.

With the computer simulation model, different hypotheses on which critical parameters may influence the onset of necrosis can be tested: First, the possibility that there exist critical concentrations for the two nutrients separately has been tested. However, in this case either the glucose or oxygen concentration dominantly limit the cell population dynamics. This does not reproduce the experimental data, since low oxygen and large glucose concentrations can result in similar population dynamics as large oxygen and low glucose concentrations [107] and when both nutrients are kept at the minimum values, the overall growth dynamics is even more suppressed. Therefore, both nutrients have to be considered to be limiting in the special cases. This is further underlined by the fact that the growth curves for one of the nutrient concentrations being kept constant depend strongly on the concentration of the other nutrient. In addition, there could be other processes such as necrotic waste material inducing apoptosis and/or necrosis [7, 105], which will not be considered here. The simplest ansatz fulfilling this condition is the product of both nutrient concentrations as a critical parameter.

Here, only the case of *in vitro* (avascular) tumour growth is considered and therefore it is assumed that the transport of nutrients is performed passively by diffusion. The diffusion through tumour tissue and through the culture medium is described by RDEs

$$\frac{\partial u^{\text{ox/gluc}}}{\partial t} = \nabla \left[D^{\text{ox/gluc}}(\boldsymbol{x};t) \nabla u^{\text{ox/gluc}}(\boldsymbol{x},t) \right] - r^{\text{ox/gluc}}(\boldsymbol{x};t), \tag{3.7}$$

where $u^{\text{ox/gluc}}(\boldsymbol{x},t)$ describes the local oxygen or glucose concentration, $D^{\text{ox/gluc}}(\boldsymbol{x};t)$ the local effective oxygen or glucose diffusion coefficient (which depends implicitly on time via the cellular positions) and $r^{\text{ox/gluc}}(\boldsymbol{x};t)$ the local oxygen or glucose consumption rate. Though formally equation (3.7) admits negative nutrient concentrations (even at low concentrations negative sink terms may in principle exist), this can never happen in reality (provided the timestep is not too large): Cells will enter necrosis (thereby stopping nutrient consumption) if the local nutrient concentrations become too small. As the reaction rates depend on the cellular viability, they become implicitly dependent on the nutrient concentrations (see subsection 2.5.5).

Since the diffusion coefficients of oxygen and glucose are 6 orders of magnitude larger than typical motilities obtained for random cellular movement, the pseudo-steady-state approximation has been applied for the RDEs of the nutrients [104, 111, 115, 118]. This included the recalculation of the nutrient concentrations from the time-dependent cellular positions at fixed timesteps of $\Delta_t = 500$ s in the steady-state approximation. The pseudo-steady-state approximation is justified for timesteps $\Delta t_{\text{nut}} \overset{\geq}{\sim} 500$ s, because the associated diffusion length $L_{\text{D}} = \sqrt{6D\Delta t_{\text{nut}}}$ for $\Delta t_{\text{nut}} = 500$ s

and the smallest occurring diffusion coefficient (glucose in tissue) is with 560 μm larger than the largest spheroid radius (380 μm) observed during the agent-based simulations. This implies that after Δt_{nut}, the steady-state will be nearly reached (if not already present from the beginning, compare appendix C.2.3). However, this argument does not consider that during the time Δt_{nut}, the cell position and number changes. The error contribution arising from the cellular mobility can be neglected, since cellular movement is much slower than diffusion of nutrients in this example. An upper bound on the error contribution arising from cell proliferation can be estimated as follows: Since for large tumour spheroids cell division is desynchronised, the number of created cells will behave as $\Delta N/N \approx (\Delta t_{\mathrm{nut}}/\tau_{\mathrm{min}})$, if growth retardation effects like contact inhibition are absent (worst case estimate). With constant cellular nutrient uptake rates, this ratio directly translates to the change of the sink terms $r^{\mathrm{ox/gluc}}(\boldsymbol{x}; t)$ in equation (3.7). Consequently, the time Δt_{nut} should be chosen considerably smaller than the characteristic length of the cell cycle as well (compare table 3.1 on page 89).

As the numerical discretisation of (3.7) will be discrete on a rectangular lattice (see subsection 2.4.2) and the cellular positions are continuous, tri-linear interpolation has been used to determine the local nutrient concentration at the position of a cell

$$
\begin{aligned}
u\left[\boldsymbol{r}(t), t\right] \;=\; & u_{000}(1 - \lambda_x)(1 - \lambda_y)(1 - \lambda_z) \\
& + u_{100}\lambda_x(1 - \lambda_y)(1 - \lambda_z) + u_{010}(1 - \lambda_x)\lambda_y(1 - \lambda_z) + u_{001}(1 - \lambda_x)(1 - \lambda_y)\lambda_z \\
& + u_{110}\lambda_x\lambda_y(1 - \lambda_z) + u_{101}\lambda_x(1 - \lambda_y)\lambda_z + u_{011}(1 - \lambda_x)\lambda_y\lambda_z + u_{111}\lambda_x\lambda_y\lambda_z \,, \qquad (3.8)
\end{aligned}
$$

where the time-dependent $u_{ijk}(t)$ denote the concentration on the lattice nodes of the cuboid containing $\boldsymbol{r}$ and the implicitly time-dependent $\lambda_{x/y/z}\left[\boldsymbol{r}(t)\right]$ denote the normalised coordinates relative to the cuboid front left bottom corner. Likewise, the cellular reaction rates – given in mol cell^{-1} s^{-1} – are distributed amongst the eight corners of the cuboid after being renormalised by the cuboid volume. Note that tri-linear interpolation yields a continuous, but not a continuously differentiable function. In order to describe processes such as some forms of chemotaxis [7, 119, 120], where cells sense concentration gradients without temporal integration of the local signal [121, 122], a higher-order spline must be used that is continuously differentiable.

3.3 A continuum modelling approach : Model details

3.3.1 Dynamics of Cells and Nutrients

A continuum model that is closely related to the agent-based model discussed previously can be given by the following partial differential equations of the RDE type [66]

$$
\begin{aligned}
\frac{\partial C_{\text{ox}}}{\partial t} &= \nabla \left[D_{\text{ox}}(\boldsymbol{r};t) \nabla C_{\text{ox}}(\boldsymbol{r},t) \right] - \lambda_{\text{ox}} C_{\text{vb}}(\boldsymbol{r},t) , \\
\frac{\partial C_{\text{gl}}}{\partial t} &= \nabla \left[D_{\text{gl}}(\boldsymbol{r};t) \nabla C_{\text{gl}}(\boldsymbol{r},t) \right] - \lambda_{\text{gl}} C_{\text{vb}}(\boldsymbol{r},t) , \\
\frac{\partial C_{\text{vb}}}{\partial t} &= \nabla \left[D_{\text{cell}}(\boldsymbol{r};t) \nabla C_{\text{vb}}(\boldsymbol{r},t) \right] + \alpha \left[C_{\text{nc}}, C_{\text{vb}} \right] C_{\text{vb}}(\boldsymbol{r},t) - \beta \left[C_{\text{ox}}, C_{\text{gl}} \right] C_{\text{vb}}(\boldsymbol{r},t) , \\
\frac{\partial C_{\text{nc}}}{\partial t} &= \nabla \left[D_{\text{cell}}(\boldsymbol{r};t) \nabla C_{\text{nc}}(\boldsymbol{r},t) \right] + \beta \left[C_{\text{ox}}, C_{\text{gl}} \right] C_{\text{vb}}(\boldsymbol{r},t) - \gamma C_{\text{nc}}(\boldsymbol{r},t) ,
\end{aligned}
\tag{3.9}
$$

where $C_{\text{ox}}(\boldsymbol{r},t), C_{\text{gl}}(\boldsymbol{r},t), C_{\text{vb}}(\boldsymbol{r},t), C_{\text{nc}}(\boldsymbol{r},t)$ represent the concentrations of oxygen and glucose, and the densities of viable and necrotic cells, respectively. The coefficients $D_{\text{ox/gl}}(\boldsymbol{r};t)$ represent the effective diffusivities of oxygen and glucose. As in real tissue the presence of cells and extracellular matrix significantly changes the effective diffusion coefficients for the nutrients [65] (compare table 3.1 on page 89) – this has been incorporated into the model by assuming the simple linearised relationship

$$
D_{\text{ox/gl}} \left[C_{\text{nc}} + C_{\text{vb}} \right] =
\begin{cases}
D_{\text{ox/gl}}^{\text{H}_2\text{O}} - \dfrac{C_{\text{nc}} + C_{\text{vb}}}{C^{\text{thresh}}} \left(D_{\text{ox/gl}}^{\text{H}_2\text{O}} - D_{\text{ox/gl}}^{\text{tissue}} \right) & : \quad C_{\text{nc}} + C_{\text{vb}} < C^{\text{thresh}} \\
D_{\text{ox/gl}}^{\text{tissue}} & : \qquad\quad \text{else}
\end{cases}
\tag{3.10}
$$

where $D_{\text{ox/gl}}^{\text{H}_2\text{O}}$ and $D_{\text{ox/gl}}^{\text{tissue}}$ are the measured diffusivities in water and tissue, respectively, and the cellular threshold concentration is just the inverse cell volume $C^{\text{thresh}} = 0.74/V_{\text{cell}}$, where the correction factor 0.74 arises from the maximum cell packing density that could be achieved with the agent-based model of section 3.2 if hard spheres are considered. The choice of a linear dependence on the cellular density is the simplest dependence that approximates theoretical investigations [123, 124] for heterogeneous media. Therefore, the diffusivities for oxygen and glucose become implicitly space and time-dependent, as the populations of necrotic and viable cells evolve. Many authors in the literature use non-variable diffusion constants for the dynamics of nutrients. For small molecules such as oxygen, this approach is well justified but for glucose, the diffusion coefficients within water and tissue may vary by nearly one order of magnitude (compare table 3.1 on page 89). Note that in the agent-based approach, intermediate values for the diffusion coefficient are not included. However, in the numerical discretisation, also in the agent-based approach the solution is obtained by linearly interpolating the diffusion coefficients between neighbouring volume elements (see subsection 2.4.2).

The cellular diffusion coefficient D_{cell} is a rough measure for describing cellular mobility: For example, when starting from mass balance equations of the form $\frac{\partial C}{\partial t} + \nabla(vC) = R(r,t)$, where C is a concentration, v denotes the flux velocity and $R(r,t)$ the local net production rate [125], one recovers the law of diffusion by assuming that the velocity is directly proportional to the gradient of concentration $v = -D\nabla C$. In a simple ansatz the diffusion coefficient may be influenced by the total cellular density $C_{\text{vb}} + C_{\text{nc}}$. In analogy to a model for animal dispersion [9], the relationship

$$D_{\text{cell}}[C_{\text{vb}} + C_{\text{nc}}] = D_{\text{cell}}^0 \left(\frac{C_{\text{vb}} + C_{\text{nc}}}{C^{\text{thresh}}} \right)^m \tag{3.11}$$

has been chosen here, where $m \geq 0$ is assumed. In case $m > 0$ the above choice ensures that the net diffusion coefficient will increase if the cellular concentration exceeds the dense packing (thus effectively modelling intercellular repulsion) and that it will decrease if the total cellular concentration is very small (approaching intercellular adhesion). Naturally, for $m = 0$ the normal diffusion constant is recovered. Note however that the above choice fails to correctly reproduce adhesion: It is – in contrast to other theoretical approaches [115, 126, 127] – positive definite which implies that the flux is always directed towards regions of lower concentrations.

With equations (3.9) it is tacitly assumed that the nutrient uptake rates of viable cells are independent of the cellular status and the local nutrient concentrations and hence, the constants $\lambda_{\text{ox/gl}}$ should be interpreted as cellular nutrient uptake rates that have been averaged over the whole ensemble of cells present in a MTS. The coefficient $\alpha\,[C_{\text{nc}}, C_{\text{vb}}]$ denotes the cellular proliferation rate. To compare with the agent-based model, it should reflect at least the phenomenon of contact inhibition. One of the simplest functional dependencies fulfilling this requirement is given by the continuous function

$$\alpha\,[C_{\text{nc}}, C_{\text{vb}}] = \alpha\,[C_{\text{nc}} + C_{\text{vb}}] = \begin{cases} \alpha_{\max} & : & C_{\text{nc}} + C_{\text{vb}} \leq C^{\text{thresh}} \\ \alpha_{\max} \frac{C^{\text{crit}} - (C_{\text{nc}} + C_{\text{vb}})}{C^{\text{crit}} - C^{\text{thresh}}} & : & C^{\text{thresh}} < C_{\text{nc}} + C_{\text{vb}} \leq C^{\text{crit}} \\ 0 & : & \text{else} \end{cases} , \tag{3.12}$$

where $\alpha_{\max}$ is the largest cellular proliferation rate for the chosen cell type (compare table 3.1 on page 89). Note that this is different than in the agent-based approach, where the sum of the normal tension T^{crit} was considered as the quiescence-inducing factor. The constant C^{crit} can be related to agent-based models [76]: The criterion that cells can proliferate only if they are not compressed by more than a factor $K^{\text{crit}} < 1$ is equivalent to defining

$$C^{\text{crit}} = \frac{C^{\text{thresh}}}{K^{\text{crit}}} , \tag{3.13}$$

where $0 < K^{\text{crit}} < 1$ is a free parameter which denotes the compression factor below which cells are contact-inhibited. Note that in contrast to other approaches, where the compression only decreases the

global growth rate indirectly by effectively transporting cells from overcrowded regions into regions with a net negative growth rate [125, 126, 128], here the compression directly acts on the proliferation rate.

In order to account for the emergence of a necrotic core, the transition from the viable cell state to the necrotic cell state should be determined by the local concentrations of nutrients. In order to be consistent with the agent-based attempt and following the arguments in subsection 3.2.2, the local product of both concentrations has been chosen as the critical parameter inducing necrosis:

$$\beta\left[C_{\mathrm{ox}}, C_{\mathrm{gl}}\right] = \beta\left[C_{\mathrm{ox}} \cdot C_{\mathrm{gl}}\right] = \begin{cases} \beta_{\mathrm{max}} & : \quad C_{\mathrm{ox}} \cdot C_{\mathrm{gl}} \le P_{\mathrm{crit}} \\ 0 & : \qquad \mathrm{else} \end{cases} , \tag{3.14}$$

where β_{max} is a maximum transition rate and P^{crit} denotes the minimum nutrient concentration product to sustain cellular life functions without triggering necrosis or apoptosis. Note that it is assumed that necrosis is a faster process than cell proliferation, which implies that $\beta_{\mathrm{max}} > \alpha_{\mathrm{max}}$ should hold. More important, for necrosis to be able to effectively reduce the cell number, the inequality must hold strictly, since for cell concentrations below the threshold level C^{thresh} the effective death rate in necrosis-inducing regions is determined by $\beta_{\mathrm{max}} - \alpha_{\mathrm{max}}$. Assuming a necrosis duration of roughly 3 hours [129] and a minimum cell doubling time of 15 hours [107] one would obtain $\beta_{\mathrm{max}} \approx 6.5 \cdot 10^{-5}$ s^{-1} versus $\alpha_{\mathrm{max}} \approx 1.3 \cdot 10^{-5}$ s^{-1}. As in the agent-based model (compare subsection 3.2.2), the pressure of the fluid phase is assumed to be equilibrated and therefore the removal of necrotic cells results into the sink term γC_{nc} for the necrotic cell population, with γ being the necrosis removal rate. In order to enable comparisons with the agent-based approach, the value of γ has been chosen identically (compare table 3.1 on page 89 and the discussion in subsection 3.4.4).

3.3.2   *Solution of the model equations*

Since the coefficients α and β in (3.9) depend on the concentrations themselves, it is obvious that even for $m = 0$ the model equations constitute a nonlinear system which may give rise to nontrivial dynamics. Some model parameters – compare table 3.1 on page 89 – can be used as fit parameters for experimental MTS data. This is especially interesting for the nutrient uptake rates λ_{gl} and λ_{ox} and the critical compression K^{crit}, since these parameters can hardly be accessed directly in experiments. In addition, different hypotheses on the functional dependence of α and β as well as m can in principle be tested to be in accordance with experimental data.

Since most *in vitro* tumour spheroids are approximately spherical [14, 110, 130], spherical symmetry has been assumed in all equations, which simplifies the numerical solution of equations (3.9) considerably. It is possible however, to extract simple characteristics of the model analytically from direct

examination of equations (3.9): The only back-reaction of the nutrients to the population of viable cells is mediated via the death rate β. Since in (3.14) a non-continuous dependence has been assumed, the dynamics of the viable cells C_{vb} will decouple from the nutrient concentrations in spatiotemporal domains where $\beta = 0$. In accordance with the (ideal) experiment, one will usually start with initial conditions, where there is an identically vanishing population of necrotic cells, a very localised distribution of viable cells, and nutrients in abundance. In this regime, the death rate β will vanish. In case of $m = 0$ and approximating the Laplace operator for large radii, the equation for the viable cells can then be rewritten as

$$\frac{\partial C_{vb}}{\partial t^*} = \frac{\partial^2 C_{vb}}{\partial r^2} + f[C_{vb}], \tag{3.15}$$

with $t^* = D_{cell}^0 t$ and $f[C_{vb}] = \left(\alpha[C_{vb}]/D_{cell}^0\right) C_{vb}$. Since $f[C_{vb} = 0] = 0$ and $f[C_{vb} = C^{crit}] = 0$, above equation will asymptotically exhibit travelling wave solutions (see [9] and references therein) for large radii with velocity $v = 2D_{cell}^0 \sqrt{f'(0)} = 2\sqrt{\alpha_{max} D_{cell}^0}$, which is reproduced in the numerical solution (see figure 3.2). Note that this wave velocity is obtained as well if cell death is admitted: The death rate β will not contribute to the velocity of the advancing wave front because there the nutrient levels are comparably large. Instead, it will lead to a temporally-exponential decrease of the viable cell density within regions through which the wave has passed.

In case of $m > 0$ the situation is more difficult: Considering the dynamics of viable cells in the same regime ($\alpha = \alpha_{max}$ and $\beta = 0$) one obtains (under radial symmetry and for large radii) in travelling-wave coordinates [9, 111, 131] an ordinary nonlinear differential equation

$$\frac{D_{cell}^0 \alpha_{max}}{v^2} \left(\frac{C_{vb}}{C^{thresh}}\right)^{m-1} [C_{vb}'' C_{vb} + m C_{vb}' C_{vb}'] + C^{thresh} (C_{vb}' + C_{vb}) = 0, \tag{3.16}$$

where C' denotes differentiation with respect to the travelling wave coordinate $z = \frac{\alpha_{max}}{v}(r - vt)$. Equation (3.16) has no obvious analytical solution. The general structure however suggests that in the vicinity of $m = 0$ no singularities occur and therefore one can expect that the solutions will exhibit a continuous transition. This is well reflected in the numerical solution (figure 3.2): For $m > 0$ a travelling wave is found as well, but the wave front is steeper and the apparent wave velocity is decreased considerably.

The existence of a travelling wave solution with constant amplitude and width already implies that the system (3.9) will not exhibit a steady-state in terms of the number of viable cells

$$N_{vb}(t) = 4\pi \int_r r^2 C_{vb}(r, t)\, dr, \tag{3.17}$$

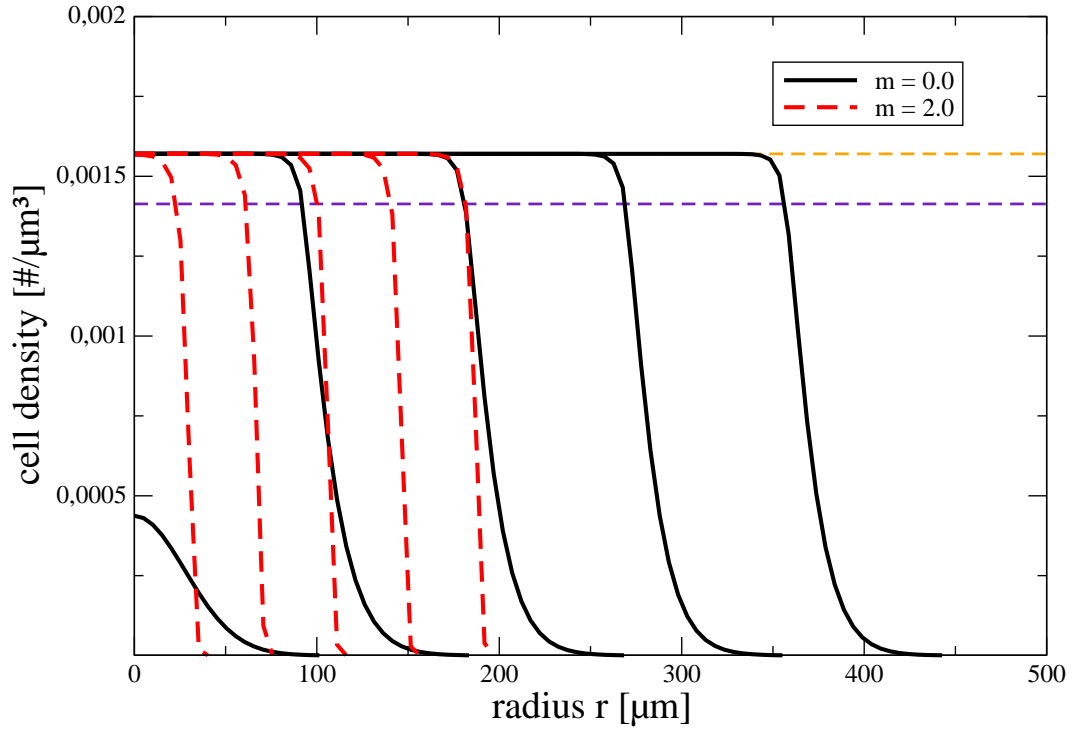since the radial volume element would still lead to polynomial growth.

Figure 3.2: Travelling waves in the continuum approach [66]. The concentration of viable cells resembles travelling waves – here calculated for situations where the cellular dynamics decouples from the existence of nutrients ($\beta_{max} = 0$) with $\alpha_{max} = 1.28 \cdot 10^{-5}$ s^{-1}, $D^0_{cell} = 0.001$ μm^2 s^{-1}, and $K^{crit} = 0.9$. Curves advancing from left to right represent densities of viable cells after 4.63 days, 9.26 days, 13.89 days, 18.52 days, and 23.15 days. For $m = 0$ (bold black lines), the asymptotic analytical wave velocity is 19.6 μm day^{-1} [9], which is found in the numerical solution as well. It can be shown by a stability analysis of (3.16) that the concentration must reach the critical cell density C^{crit}, that has been marked together with the threshold cell density $C_{thresh} < C^{crit}$ by dashed horizontal lines. For $m = 2$ (dashed red lines), the apparent wave velocity of the numerical solution decreases considerably to $v \approx 9$ μm day^{-1}. In addition, the cells tend to aggregate leading to more localised distributions, which is reflected by the steeper decaying cell front.

For the numerical solution, a sphere with radius of 500 μm – divided into 100 concentric shells of constant thickness Δr – and Dirichlet boundary conditions for all populations has been considered (for the details of the numerical discretisation see subsection 2.4.2 or [66]). The choice of Dirichlet boundary conditions for the nutrient concentrations is motivated by the experiment [107], where the measured nutrient concentrations outside the spheroids remained approximately constant between the periodic refills of nutrient. Dirichlet boundary conditions for the cell populations emerge naturally in a multiphase approach [115] as well. However, with the stationary boundaries employed here, it should be verified that the assumption of vanishing Dirichlet boundary conditions for the cell populations does not make a difference to no-flux von-Neumann boundary conditions in the observed time-range of 25 days, i. e., essentially that the cell population does not interact with the boundary. This approximation is only valid for the small cellular diffusion coefficient, since larger diffusion coefficients lead to an increased velocity of the advancing tumour front. As already argued in subsection 3.2.2, the pseudo-steady-state approximation (compare appendix C.1.2) has been applied for the RDEs of the nutrients. The volume integral (3.17) of all densities yields the total cell numbers for viable and necrotic cell populations or the total number of glucose and oxygen molecules in the reaction volume, respectively. This opens the possibility of comparison with an experimental signature.

3.4   Results

Some parameters have been fixed from values from independent experiments (see subsection 3.4.4) and based on observations on MTS with EMT6/Ro cells [107], several computer simulations with the agent-based and the continuum model have been performed. The difference to experimental growth curves has been minimized by applying a deterministic multi-dimensional fitting procedure [68] to the models (see appendix C.3), but owing to the long runtime of the agent-based model, this procedure was only successful for the continuum approach. Following the assumption that whole spheroid populations were grown from single tumour cells (monoclonality of spheroids), all simulations have been started with a single cell in a localised (stepwise) distribution, such that the density was non-vanishing in the innermost volume compartment only. Note that within the continuum approach, this over-extrapolation of continuum theory to few initial cells did not lead to significant errors for the chosen discretisation, as these initial deviations from the agent-based approach were small, compare figure 3.3. From the culturing conditions described in [107] it is not clear whether the spheroids started from single cells. In fact, it is highly probable that tumour cells already aggregated before spheroid formation. Nevertheless, this would mainly correspond to a shift in time – as can be verified in the models – since the initial conditions can still be safely assumed to exclude processes such as

contact inhibition or nutrient depletion. Using the models from sections 3.2 and 3.3, growth curves have been calculated for different nutrient concentrations and different hypotheses on nutrient uptake, necrosis induction, and cellular mobility. The simulations have been compared with four series of experimental data, where four different combinations of oxygen and glucose concentrations have been investigated. Naturally, within one set of simulations all parameters but the nutrient concentrations have been kept fixed. The fitting procedure has been started from different parameter sets and the best minimum has been kept.

3.4.1 Population Dynamics

The overall cell number is a parameter which can be quantified experimentally by either indirectly calculating cell numbers from observed tissue volumes or directly by extensive automated cell-counting. In [107] the cell number has been determined directly for moderate cell numbers and different concentrations of oxygen and glucose. Qualitatively, one can see that for all the simulations the initial exponential growth phase soon enters a crossover to a polynomial growth. Within the model this crossover is due to two distinct mechanisms – contact inhibition and nutrient depletion – which lead to the similar outcome that after a certain time dominantly the spheroid surface will contribute to the proliferation, i. e.,

$$\frac{dN}{dt} = \alpha N^{2/3} \, , \tag{3.18}$$

which has the polynomial solution $N(t) = N_0 \left[1 + \beta t + \beta^2 t^2/3 + \beta^3 t^3/27 \right]$ with $\beta = \alpha/N_0^{1/3}$. Apart from the fact that necrosis is evidently more likely when nutrients are rare, the mechanisms cannot be clearly distinguished with a glance at the total growth curves in figure 3.3.

The total cell numbers in figure 3.3 demonstrate that the assumption of the nutrient concentration product being a critical candidate for necrosis suffices to explain experimental data within the level of their own uncertainty. This is independent of the model chosen and thus can be considered a robust feature. Unfortunately, no error bars are given in [107] and the experimental data scatter considerably even on a logarithmic scale. The visual difference between agent-based and continuum models reflects beyond inherent model differences also the fact that due to the long runtime the automated minimization procedure (compare appendix C.3) can be applied to agent-based models with limited success only. In addition, it is found that for the continuum model the possibility of leaving m as a fit parameter does not significantly improve the quality of the fit. The corresponding differences become visible in other experimental signature such as the spheroid morphology (compare figure 3.6). Note that none of the model approaches displays a saturation of growth. However, such a saturation is not clearly indicated by the quantified experimental data as well.
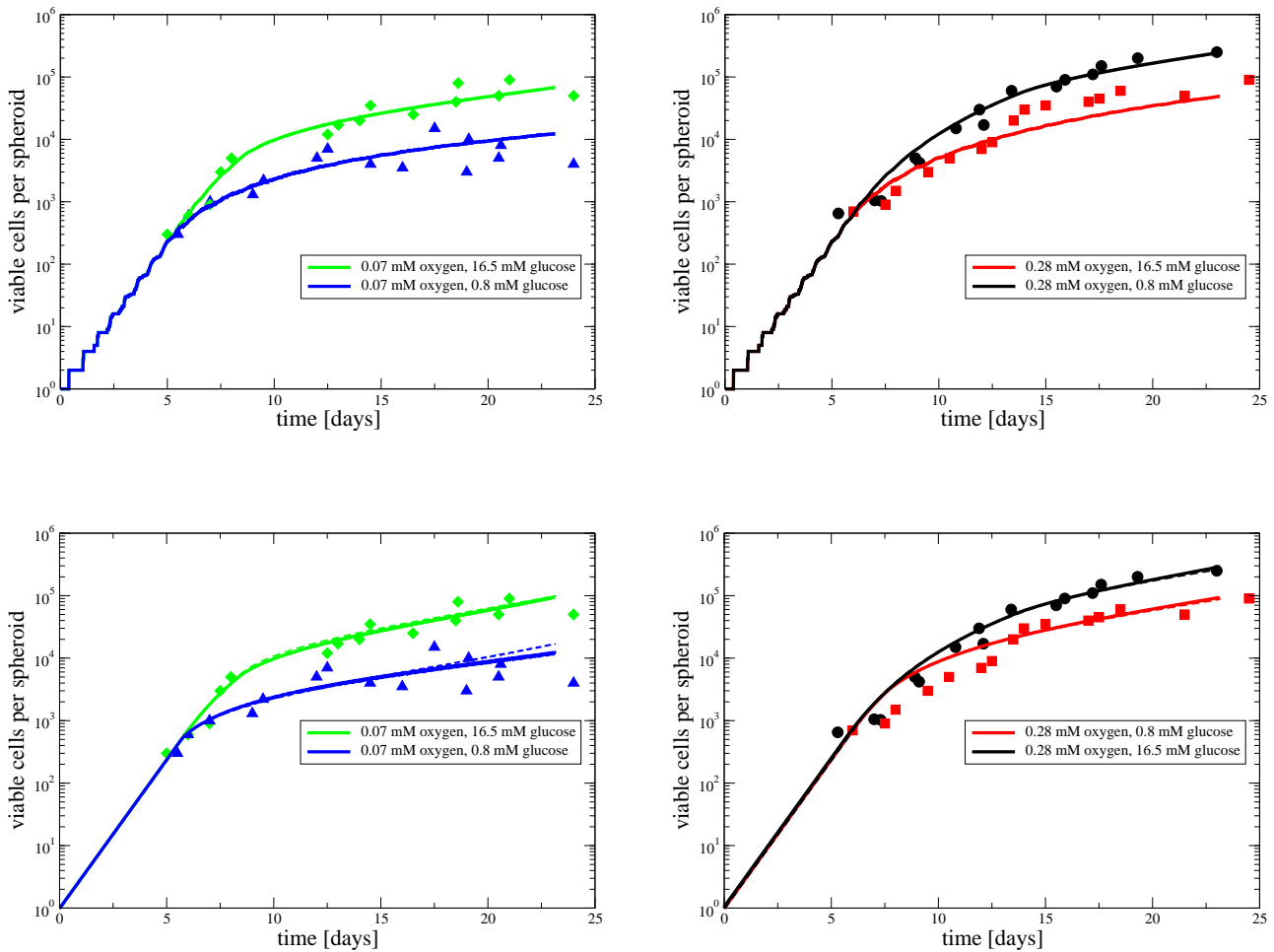
Figure 3.3: Number of viable cells per spheroid [66, 77] for different nutrient concentrations. Comparison of the agent-based model (**top row**) and different versions of the continuum model (**bottom row**) to experimental data (symbols, read off from [107]). Nutrient concentrations correspond to the conditions in the experiment. The simulations (solid lines) have been started with a single cell (or the closest realisable cell distribution in the continuum case). For small cell numbers, the discreteness of the agent-based model is visible by the initial discontinuities in the cell numbers. For the continuum model, dashed lines (visible for low nutrients) indicate the special variant with $m = 0$, whereas for the solid lines m has been varied as a fit parameter.

Since the mechanism of contact inhibition leads to cells resting in G_0 rather than cells entering necrosis the differences can be analysed in the cell cycle distribution in figure 3.4 (compare also figure 3.6 for the PDE model). In figure 3.4 it is evident that for 0.07 mM oxygen and 0.8 mM glucose concentrations (upper left panel) the nutrient starvation is the dominant limiting factor to cell cycle inhibition, since there are nearly no cells in G_0-phase and the majority of cells is necrotic. In the case of nutrient abundance (0.28 mM oxygen and 16.5 mM glucose, figure 3.4 lower right panel) however, the majority of cells resides in G_0-phase during days 6-23, which is an indication for contact inhibition being the dominant reason for the crossover, as is also assumed in other models [76]. This is as well confirmed by the cross-sections of the computer simulated tumour spheroids (figure 3.5). Though in the case of nutrient abundance necrosis sets in much later, the number of necrotic cells rises at a much stronger slope and it is to be expected that necrosis will displace the contact inhibition as the major cause for surface-dominated growth after 25 days (with overall roughly $5 \cdot 10^5$ cells involved, the simulations become very extensive and memory-consuming). Such a displacement of dominating mechanisms is already visible for some intermediate nutrient concentrations. For example, in the case of 0.07 mM oxygen and 16.5 mM glucose concentrations (figure 3.4 top right panel) the number of cells in G_0-phase first rises to reach its maximum after 10 days and afterwards decays in combination with a strong rise in necrotic cells. Such a behaviour is not observed in the regime of large oxygen and low glucose concentrations, where necrosis and contact inhibition set in simultaneously and nutrient starvation is the main limiting factor (figure 3.4 bottom left panel). This is due to the considerably decreased glucose diffusion coefficient in tumour tissue, whereas the diffusion coefficient of oxygen is nearly the same in tissue and water. Consequently, the already low glucose concentration of 0.8 mM at the boundary drops rapidly when the number of tumour cells increases, since new glucose supply diffuses very slow from the outside.

The reduced PDE model does not resolve the internal states of the cell cycle. However, in figure 3.6 it is visible that for low nutrient concentrations contact inhibition is not existent, whereas for large nutrient concentrations contact inhibition dominates necrosis as the cause for growth retardation. This is in qualitative agreement with the agent-based approach. However, in contrast to the agent-based model, the PDE model hardly differentiates between cases where only one nutrient is limited.

3.4.2 *Tumour Spheroid Morphology*

To estimate the quality of a mathematical model one has to find experimentally accessible parameters. This is especially difficult when thinking about tissue morphology, since very often the patterns are hard to quantify in terms of numbers. It is evident that the spherically-symmetric continuum model
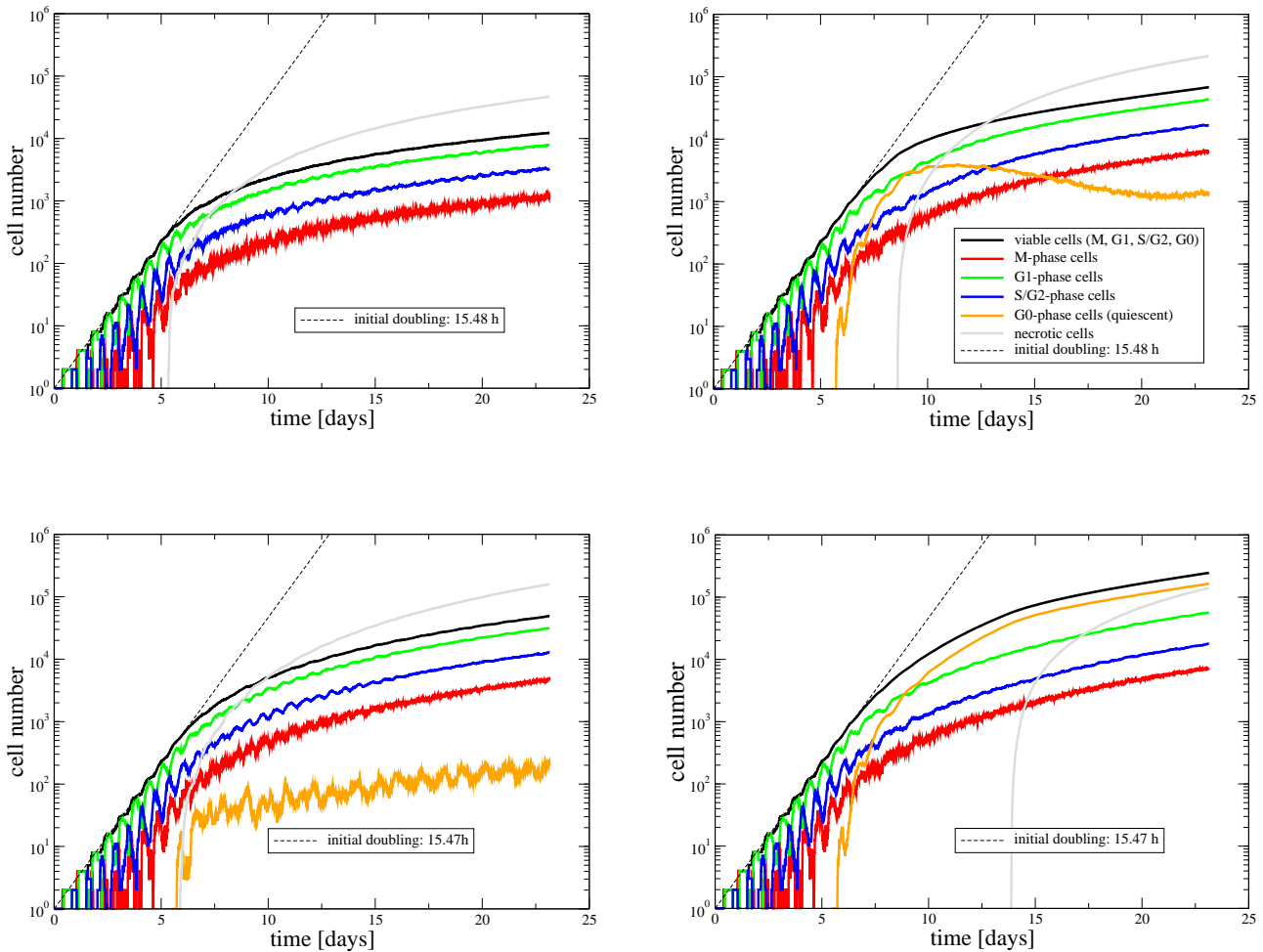
Figure 3.4: Cell cycle distributions for agent-based *in silico* MTS [77]. Depending on the external nutrient concentrations, significant differences mark the dominance of different mechanisms to limit the cell cycle. The nutrient concentrations have been chosen as follows: **Top left**: 0.07 mM oxygen, 0.8 mM glucose, **Top right**: 0.07 mM oxygen, 16.5 mM glucose, **Bottom left**: 0.28 mM oxygen, 0.8 mM glucose, **Bottom right**: 0.28 mM oxygen, 16.5 mM glucose. Fits to the regions of exponential growth (dashed lines) – marked by the complete absence of necrotic and quiescent cells – reproduce the shortest observed cycle time within statistical fluctuations depending on the random number generator seed. The initial oscillations in the sub-populations in the cell cycle stem from the fact that the cells divide synchronously at the beginning. Their frequency is the inverse cell cycle time. After each cell division, the daughter cells draw new duration times for the S/G_2-phase and the M-phase from a normal distribution (compare table 3.1 on page 89), which leads to a dampening of the oscillations and finally to complete desynchronisation of cell division. The occurrence of contact inhibition or necrosis increases the dampening effect, since the advance through the cell cycle is disturbed. In the case of few nutrients (top left), contact inhibition does not play a role as there are no quiescent cells.

will produce nothing but spherically-symmetric morphologies. However, further parameters such as spheroid size, thickness of the viable rim etc. can still vary. Qualitatively, the typical spheroid morphology (proliferating rim, quiescent layer, necrotic core) is well reproduced in the case of nutrient abundance by both models (figures 3.5 and 3.6). In addition, both models predict that in the case of nutrient starvation there is virtually no layer of quiescent cells, as contact inhibition is not of importance in this scenario. Note however, that this would be different if quiescence is induced by nutrient limitations: In this case, the necrotic core would always be surrounded by a layer of quiescent cells. For both models it is evident that the size of the layers depends on the boundary concentrations. In addition, it depends on the nutrient consumption rates and diffusivities of oxygen and glucose within the tumour tissue.

Due to the removal of necrotic cells with rate γ^{necr}, the cellular density within the necrotic core is considerably decreased in comparison to the viable layers in both the agent-based model (figure 3.5) and in the continuum model (figure 3.6). In the agent-based model, this is reflected in the decline of the cell tensions in the necrotic core (bottom row of figure 3.5). For different situations, namely in *in vivo* tumours, sometimes large pressures of the fluid phase in the necrotic core have been observed (private communication with Prof. Dr. Peter Walden, Charité Berlin). This is neglected in the current model, since the pressure of the fluid phase is assumed to be equilibrated.

Note that in the spheroid cross-sections (figure 3.5) it is evident that – if oxygen and/or glucose are limited – a relatively small number of cells with constant nutrient uptake rates suffices to drop the nutrient levels under the critical threshold thus leading to the onset of necrosis and the absence of a layer of quiescent cells in the end of the simulations (compare figure 3.4). This would be different for a model with concentration or cell-cycle dependent nutrient uptake rates. In the first case the absolute value of the nutrient concentration gradients would be decreased thus giving rise to a broader viable layer which – in turn – could allow for the existence of a quiescent layer. In the second case the intermediate emergence of cellular quiescence would as well decrease the absolute value of the nutrient concentration gradient towards the necrotic core, which would prolong and possibly stabilise the existence of a quiescent layer also for nutrient-depleted configurations. Therefore, in order to distinguish between nutrient uptake models, the tumour spheroid morphology is an important criterion, whereas the simple total growth curve is not sufficient to make quantitative predictions about the mechanisms at work.

Interestingly, the spheroids in figure 3.5 are fairly round, especially for the case where nutrients are provided in abundance. This is due to the stochastic nature of the mitotic direction which forces initial differences to average out after some time. The general growth characteristics is hardly sensitive to the specific order of the stochastic events (different instantiations can be created by restarting the code

with equal parameters but different seed values for the random number generator) – the growth curves initially display slight differences but recombine soon (data not shown). This is in agreement with many spheroids observed in the experiment [107] and in other computer simulations [103]. However, the spheroids are less spherical for extreme nutrient depletion, since firstly the small cell number yields less stochastic events that contribute to the averaging and secondly the emergence of localised holes in the necrotic core is not counterbalanced by a strong mainly isotropic proliferative pressure from the proliferating rim – as is the case for large nutrient concentrations. The deviations from the spherical form as sometimes observed in experiments [98, 110] can have the additional reason that in the experiments the spheroids might be heteroclonal while all cells in the simulation are assumed to be monoclonal: A spheroid developing from genetically differing subpopulations might display anisotropic growth.
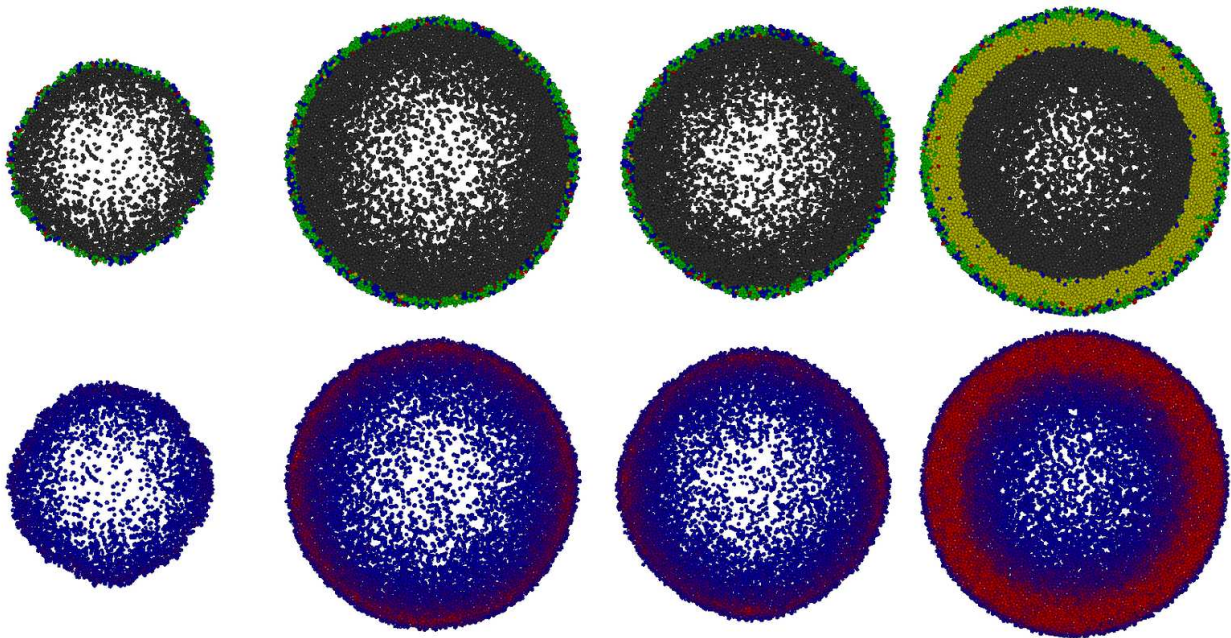

Figure 3.5: Cross-sections of *in silico* MTS in the agent-based model [77]. The cross-sections correspond to the configurations after 23 days. Nutrient concentrations from left to right are given by 0.07 mM oxygen with 0.8 mM glucose, 0.07 mM oxygen with 16.5 mM glucose, 0.28 mM oxygen with 0.8 mM glucose, and 0.28 mM oxygen with 16.5 mM glucose. The spheroid sizes are indicated in figure 3.6 as well. **Top row:** Shown is the cellular status (necrotic cells painted grey, quiescent cells yellow, mitotic cells in red, cells in G_1-phase green, and cells in S/G_2-phase blue, respectively). **Bottom row:** Displayed is the cellular tension T^{crit} (free cells in blue, strongly compressed cells in red). The removal of necrotic cells in the necrotic core leads to a relaxation of the cell tensions in the model.

For the agent-based model, there are considerable size differences between spheroids with nutrients

in abundance and spheroids with low nutrient levels. This is in good qualitative agreement with experimental data. To this degree, this behaviour is not found by all variants of the continuum approach. For example, for $m = 0$ the velocity of the travelling wave solely depends on the cellular diffusion coefficient and the maximum proliferation rate (compare figure 3.2) and therefore it is equal between test runs with different nutrient concentrations. Consequently, for $m = 0$ the calculated spheroids have the same macroscopic size for all nutrient concentrations, as is confirmed in figure 3.6: Half of the maximum spheroid cell density is reached at a radius of 350 μm – regardless of the nutrient concentration. In this model ansatz, the differences in the overall cell number result from the local density amplitude only. The assumption $m = 0$ is therefore in direct contradiction with (unquantified morphologic) experimental data and the corresponding agent-based approach. One might expect from figure 3.2 that if one allows for a variable diffusion exponent $m > 0$ in the continuum model, the effective velocity of the travelling waves should decrease considerably. However, in figure 3.6 this is not the case except in the case of poor nutrient support: In this case the spheroid grows to a radius of 300 μm, whereas in case of nutrient abundance the spheroid front can be found at 380 μm. In cases where only one nutrient is limited, the spheroids are negligibly smaller with roughly 370 μm. In this respect one should keep in mind that neither m nor the cellular diffusion constant D^0_{cell} have been fixed in this scenario. Therefore, in order to fit the overall cell numbers to experimental data, the cellular diffusion constant must necessarily increase: The local cellular density is bound by C^{crit} and the only way to harbour enough cells within the tumour spheroid is to increase the velocity of the propagating wave. Consequently, it does not come as a surprise, that the macroscopic spheroid sizes in the scenarios where the threshold concentration C^{thresh} is reached do not differ very much. The difference becomes manifest only in the case of nutrient starvation, where contact inhibition does not play a role at all. Here the resulting size differences of the spheroids reproduce the results of the agent-based model (figure 3.5) much better. Still, it must be said that the spheroid size differences in the agent-based model have not been fitted directly to experimental data, for which a quantification of these morphologic parameters would be necessary. A possible improvement resulting from the choice of $m > 0$ is the more sharply-pronounced transition at the spheroid boundary, since this agrees much better with experimental observations and the agent-based model (compare figure 3.1 left panel). However, it should be kept in mind that the procedure of obtaining the cross-sections of spheroids is rather invasive, as for example their fixation results in a shrinkage of 10-20 % [107]. One may speculate that cells only bound loosely to the spheroid may be removed by fixation.

In case of nutrient starvation, the cellular concentrations of both models never reach densities that might induce contact inhibition and the only mechanism inhibiting cellular growth is necrosis (compare figures 3.4, 3.5 and 3.6). In all other test configurations, the cellular density of the continuum

model (figure 3.6) locally exceeds the threshold concentration C^{thresh}. Cells residing within regions, where the cellular concentration lies above C^{thresh}, have a decreased proliferation rate and are therefore interpreted as quiescent within this continuum model. Consequently, both contact inhibition and necrosis play an important role in all other scenarios. The first initially dominates if nutrients are provided in abundance, whereas the latter dominates if nutrients are rare. Note that the difference in comparison with the previous definition of quiescence in the agent-based model (subsection 3.2) consists of two facts: Firstly, here a different – volume-related as in [76] – criterion for quiescence has been chosen. Secondly, in contrast to the agent-based model definition this criterion is continuous, i. e., proliferation is only diminished between C^{thresh} and C_{crit}. Consequently, one may question whether this model feature correctly represents contact inhibition: If in the continuum approach the dependence is made discontinuous by setting $C^{\text{thresh}} = C_{\text{crit}}$ then – provided initially the cell density is always below C^{thresh} – one will not observe cellular densities above C^{thresh}, since even a slight overpopulation results in a vanishing growth term and is worn away by diffusion or death terms. Consequently, one would not encounter contact-inhibited cells in the continuum model at all in this case.

Within the time frame of the experiment and the given nutrient concentrations, the model will always predict the emergence of a necrotic core as soon as a sufficient number of cells has developed. As quiescent cells consume nutrients as well within this model, it can be expected that the number of quiescent cells will always be outgrown by necrotic cells after some time. Note that the present continuum model poorly differentiates between the scenarios where only one of the nutrients is restricted: For both scenarios, a thin contact-inhibited layer followed by a large necrotic core is predicted. In contrast, in the agent-based model, contact inhibition is more pronounced when glucose is provided in abundance and oxygen is restricted in comparison to the case where more oxygen than glucose is provided. So far however, the quantitative experimental signature is too poor to differentiate between the models in this aspect.

3.4.3   Distribution of nutrients

The stoichiometry of the clean combustion of glucose: $C_6H_{12}O_6 + 6O_2 \rightarrow 6H_2O + 6CO_2$ would require the molar nutrient uptake rate of oxygen to be 6 times the molar glucose uptake rate. However, for tumour tissue this cannot be the case as it is well-known that in the direct vicinity of tumours the concentration of lactic acid increases considerably which is a direct evidence for the incomplete combustion of glucose.

Since the evolution of the nutrients is coupled to the cellular distribution, the concentration of nutrients
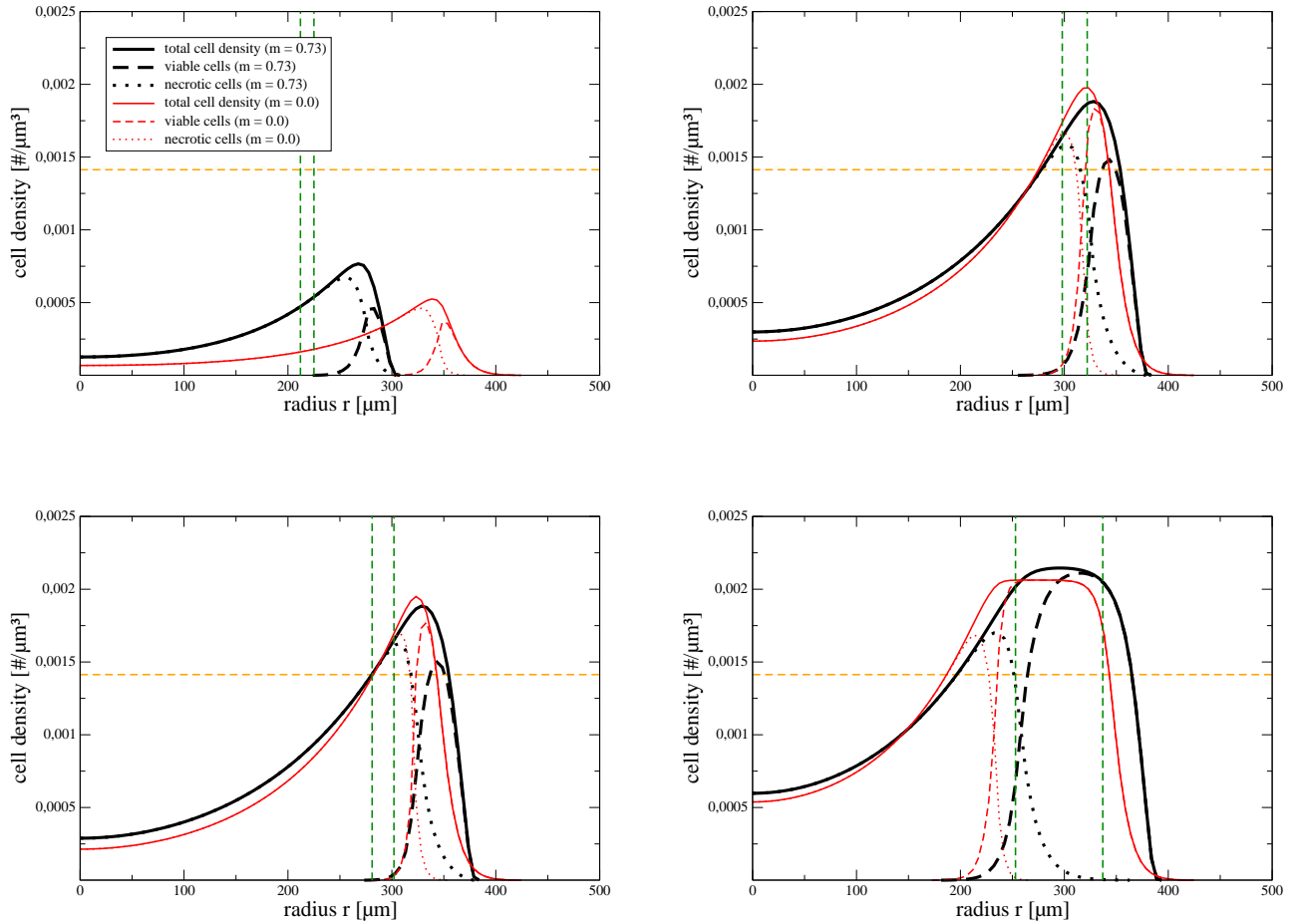
Figure 3.6: Cell densities for different nutrient concentrations in the PDE model [66]. Results refer to the distributions after 23 days. The black bold lines denote simulations where the exponent *m* has simultaneously been determined as a fit parameter, whereas the red thin lines represent simulations with $m = 0$. The cellular threshold concentration C^{thresh} has been marked by the horizontal dashed orange line. Within each panel, the two vertical dashed green lines denote the approximate size of the necrotic core (left line) and the complete spheroid (right line) in the agent-based model (compare figure 3.5), which has been estimated using the largest distance of a necrotic or viable cell from the spheroid centre, respectively. **Top Left:** Cellular concentrations for 0.07 mM oxygen and 0.8 mM glucose concentrations. As the concentrations never reach C^{thresh}, contact inhibition does not play a role within this scenario. **Top Right:** Cellular concentrations for 0.07 mM oxygen and 16.5 mM glucose concentrations. A thin layer of partially contact-inhibited cells emerges. **Bottom Left:** This is similar for 0.28 mM oxygen and 0.8 mM glucose concentrations. **Bottom Right:** Cellular concentrations for 0.28 mM oxygen and 16.5 mM glucose concentrations. The spheroid exhibits a thick layer of contact-inhibited cells.

will fall wherever viable cells consume nutrients (figure 3.7). The distribution of nutrients has been calculated with the pseudo-steady-state approximation (compare appendix C.1.2), which enforces the immediate reaction of the nutrient concentration to the cellular positions. The region of steepest concentration descent coincides with the localisation of viable cells, i. e., with the sink terms. This relation is found in both models and for both nutrients. Due to the larger diffusion coefficients of oxygen, the gradients of the oxygen concentration tend to be smaller (not shown). For $m = 0$ the qualitative appearance in the PDE model hardly changes: Due to the slightly increased glucose uptake rates (see table 3.1 on page 89) the baselines are a bit lower than in figure 3.7.
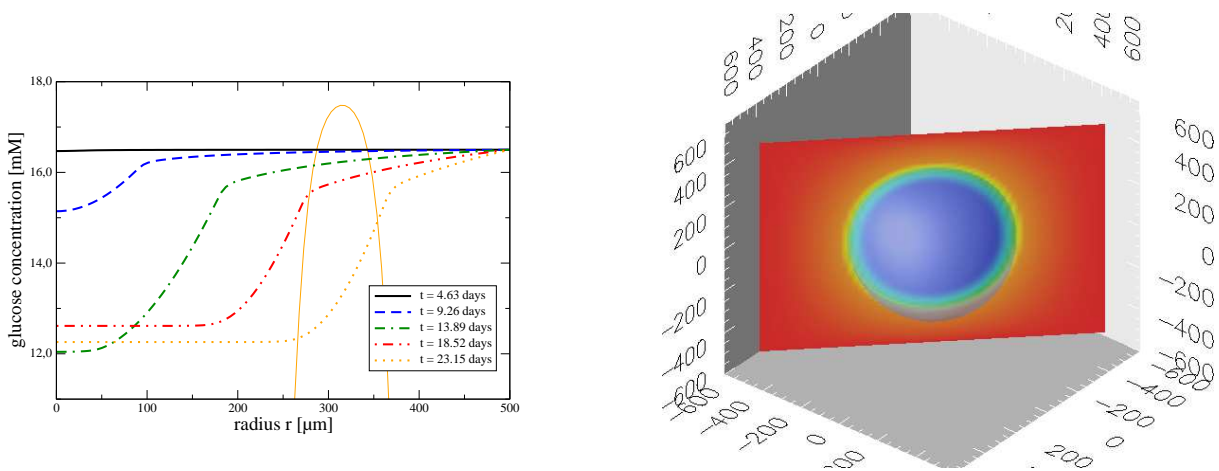

Figure 3.7: Plot of the glucose and oxygen distributions. **Left:** In the continuum model with radial symmetry, the glucose concentration has been calculated for 0.28 mM oxygen and 16.5 mM glucose boundary concentrations and m being determined as fit parameter. During tumour growth, the concentration of glucose drops as soon as the density of viable cells reaches significant concentrations. The region of steepest descent coincides with the travelling localisation of viable cells (rescaled population density shown after 23 days, thin full line). **Right:** This is similar in the agent-based model (after 23 days, same boundary conditions, numbers denote μm), where the oxygen concentration displays spherical symmetry (transparent isosurface at 0.1 mM) for large spheroids as well.

3.4.4 Parameter Sensitivity

The growth curves shown in figure 3.3 have been calculated using the parameters in table 3.1 on page 89. Generally, one can say that in order to correctly fit the global cellular growth curves, a necrotic core always emerges. The emergence of a necrotic core is not an intrinsic ingredient of the models – there are local minima in the parameter space that did not exhibit a necrotic core in the observed time range, but these parameters did not fit the data with acceptable quality. Therefore, it is a robust

parameter	value [66]	value [77]	remark
mitotic phase $\tau^{(m)}$	-	(1.0 ± 0.25) h	[132]
S/G$_2$-phase τ^{S/G_2}	-	(5.0 ± 2.0) h	[132]
cell elastic modulus E	-	1000 Pa	[133]
cell Poisson number ν	-	0.5	[134]
adhesive coefficient f^{ad}	-	$1.0 \cdot 10^{-4}\ \mu N\ \mu m^{-2}$	[88]
ECM viscosity η	-	$5 \cdot 10^{-3}\ kg\ \mu m^{-1} s^{-1}$	[76]
adhesive friction γ^{max}	-	$0.1\ kg\ \mu m^{-2} s^{-1}$	[76]
oxygen diffusivity $D_{ox}^{H_2 0}$	$2440.0\ \mu m^2 s^{-1}$	$2440.0\ \mu m^2 s^{-1}$	[135]
oxygen diffusivity D_{ox}^{tiss}	$1750.0\ \mu m^2 s^{-1}$	$1750.0\ \mu m^2 s^{-1}$	[136, 137]
glucose diffusivity $D_{gl}^{H_2 O}$	$691.0\ \mu m^2 s^{-1}$	$691.0\ \mu m^2 s^{-1}$	
glucose diffusivity D_{gl}^{tiss}	$105.0\ \mu m^2 s^{-1}$	$105.0\ \mu m^2 s^{-1}$	[138]
cell proliferation	$\alpha_{max} = 1.28 \cdot 10^{-5}\ s^{-1}$	$\tau^{min} = (15.0 \pm 2.0)$ h	[100, 107, 113]
threshold density C^{thresh}	$1.41 \cdot 10^{-3}\ \mu m^{-3}$	$R_{cell} = 5\ \mu m$	
necrosis removal rate γ	$2.0 \cdot 10^{-6} s^{-1}$	$2.0 \cdot 10^{-6} s^{-1}$	
contact inhibition criterion	$K^{crit} = (0.64 \pm 0.28)\ (0.69)$	$T^{crit} = 600$ Pa	[76, 106], fit
oxygen uptake rate λ_{ox}	$(21.9 \pm 5.1)\ (20.0)$ amol cell^{-1}s^{-1}	20.0 amol cell^{-1}s^{-1}	[113, 139], fit
glucose uptake rate λ_{gl}	$(34.0 \pm 9.3)\ (40.0)$ amol cell^{-1}s^{-1}	95.0 amol cell^{-1}s^{-1}	[112, 113, 139], fit
nutrient product P^{crit}	$(0.040 \pm 0.003)\ (0.045)$ mM^2	0.025 mM^2	fit
exponent m	$(0.73 \pm 0.37)\ (0.0)$	$-$	fit (fixed)
cell diffusion constant D_{cell}^0	$(2.7 \pm 1.4)\ (0.9) \cdot 10^{-3}\ \mu m^2\ s^{-1}$	$(1.0 \cdot 10^{-4}\ \mu m^2 s^{-1})$	[76, 77, 120], fit
necrosis rate β_{max}	$(11.3 \pm 7.7)\ (7.9) \cdot 10^{-5}\ s^{-1}$	$-$	fit

Table 3.1: Best fit parameters for agent-based and continuum models of MTS. Model parameters that have reproduced the best fit to experimental growth curves in figure 3.3. The first section contains parameters exclusively used in the agent-based model, the second section parameters used in both models, and the last section parameters used in the continuum model. The uncertainties in the first column have been estimated by calculating the projection of the hyperellipsoids of constant $\Delta\chi^2$ (subjectively defined by an increase of χ^2 by 5% for acceptable fit quality) to the parameter axes. For the values in the first column in parenthesis, the exponent m has been fixed to $m = 0$. If widths are given, the values correspond to one standard deviation. Note that the cellular radius of 5 μm as assumed in the agent-based model directly corresponds to the value used for C^{thresh} if maximum cellular packing density of 74% is assumed. Similarly, the minimum cycle time and the maximum proliferation rate are inter-related. Citations in the right column contain evidence supporting the particular choice of parameters. For detailed explanations see the text.

feature – independent of the choice of the model and can be considered a qualitative prediction. The model is not equally sensitive to changes of the parameters:

Since parameters of the agent-based model such as the length of the M-phase $\tau^{(m)}$ and the S/G_2-phase $\tau^{(S/G_2)}$ do not directly affect the overall cycle time τ^{min}, but the length of the G_1-phase in this model and thereby the growth velocity of single cells, their overall effect on the total population dynamics is rather small. Instead, these parameters control the relative distribution of cells in the cell cycle. In addition, their widths combine to a normal distribution of the effective cycle time and thereby control the dampening of the oscillations in figure 3.4 in absence of contact inhibition or nutrient depletion. For a reliable estimate of these parameters an analysis of the cell cycle distribution would be necessary.

The elastic and adhesive parameters of EMT6/Ro tumour cells might differ from those relevant in the agent-based simulation, where incompressibility has been assumed with choosing $\nu = 0.5$. For example, assuming reduced Poisson ratios $\nu \approx 0.3$ and cell elasticities of $E \approx 750$ Pa [76, 116], one may obtain deviations in the elastic forces in (3.2) in the range of up to 50 percent. The adhesive constant f^{ad} is a rather unknown parameter as well. It can can be estimated from the elastic constants by comparing the visual appearance of cell doublets (see e. g. [88]) with the equilibrium distance resulting from equation (3.2). As with all biological systems, considerable variance even within single cell types can be expected [116, 133, 134, 140]. However, with moderate changes in these parameters, the growth characteristics for the overall cell number does not vary strongly: With the given friction parameters, the cellular tensions relax on a shorter timescale than the cell cycle time (compare equation (3.2) and figure C.7 in the appendix).

The combined viscosity of the extracellular matrix η chosen here corresponds to that of viscous honey, whereas the typical surface-related friction coefficient γ^{max} has been estimated in [76] from independent experiments [141]. As with the adhesive and elastic parameters, these friction parameters determine the relaxation time for cellular interaction. As long as these relaxation times are much smaller than the cell cycle time, little influence can be expected.

The diffusion coefficients of the nutrients $D^{tiss/H_2O}_{ox/gluc}$ evidently influence the nutrient distribution. Within physiological windows [136, 138] however, the model is robust against changes of these parameters. Note that the diffusion coefficient for oxygen is nearly the same in tissue and water. For the continuum approach it turned out that the assumption of a spatially uniform oxygen diffusivity hardly made a difference in comparison to varying oxygen diffusivity [66]. Therefore, the approximation of assuming a constant oxygen diffusivity [111, 115] is well justified. This does not hold true for glucose, as can be expected from the large differences of the diffusion constants in water and tissue.

The proliferation rate of the continuum model is related to the shortest cycle time of the agent-based

approach via $\ln 2 = \alpha_{\max}\tau_{\min}$. In [107] an initial cycle time of 17 h has been obtained using a Gompertz fit [compare equation (2.2)] to the spheroid volume. This fit had been applied to already existing small spheroids that may exhibit growth retardation effects. Therefore, it does not come as a surprise that the cell doubling times obtained from [113] range between 13 and 17 hours. Naturally, the initial evolution of the cell numbers (figure 3.3) critically depends on the cycle time. Note that the deviation given for $\tau_{\min}$ results from the quadratically added standard deviations of $\tau^{(m)}$ and τ^{S/G_2}. In the model, it is necessary for the desynchronisation of proliferation.

Similarly, the threshold density C^{thresh} and the free cell radius R are inter-related (see subsection 3.3). In the continuum model however, a dense packing has been assumed by including the correction factor 0.74 into the definition of C^{thresh}, which does not have to be realised neither in reality nor in the agent-based model. The consequences of such a misestimate are inter-related with the contact inhibition parameters (see below).

The removal rate of necrotic cells γ has been fixed to the same value for both models here. If – in the agent-based model – adhesion (f^{ad}) is not much stronger than the value given, this rate mainly determines the density of the necrotic core. Since the fit is done to the number of viable cells and since these are only weakly coupled to the density of necrotic cells, its quality is hardly sensitive to γ over several orders of magnitude. This is illustrated by the bottom row in figure 3.5, where the tension in the necrotic core is relaxed due to removal of necrotic cells. For very strong intercellular adhesion however, where growth saturation may actually be obtained within the agent-based model (compare subsection 3.4.5), this parameter determines the total size of the necrotic core and thus the size of the whole spheroid as well. In addition, if the parameter is set to vanish, no necrotic cells will be removed and one can expect intercellular tensions to persist within the necrotic core.

In both models, the contact inhibition (represented by the critical compression K^{crit} in the continuum case or the critical normal tension T^{crit} in the agent-based approach) strongly influences the growth curve when nutrients are supplied in abundance. The value that is obtained as fit parameter in the agent-based model is considerably larger than that which one would obtain from the corresponding normal tension of an isotropically compressed sphere via $\sigma_{\text{n}} = E/[3(1-2\nu)](\Delta V/V)$ (with $E = 750$ Pa, $\nu = 0.33$, and $\Delta V/V = 0.1$ in [76]). Since a different cell type is considered here, these model parameters cannot be compared directly. In part, the discrepancy between the agent-based models in this thesis and the one presented in [76] may be due to the Voronoi surface correction in equation (3.3) – surfaces tend to be smaller than the sphere surfaces used in [76] – which leads to generally larger normal tensions. However, the continuum model points to stronger cell growth ($\Delta V/V \approx 0.35 > 0.1$) than in [76] as well. As argued before, the dense packing might neither be realised in realistic MTS [107] nor in the agent-based model. Still, when combining the compression of the continuum model

with the elastic parameters of [76], one obtains an inhibition tension of $O(250$ Pa), which is much closer to the value of K^{crit} in the agent-based model than to the corresponding isotropic compression as defined above. Finally, in the original experimental investigation [106], a much larger cell tolerance than in [76] regarding compression is obtained for a different cell type. One should keep in mind that both the continuum model and the agent-based model in the overdamped approximation do not correctly describe the distribution of pressure. For strongly compressed tissue, it will rather obey a wave equation involving secondary time derivatives.

The fit to the growth curves is very sensitive to λ_{gl}, λ_{ox}, and P_{crit}. Though these parameters have the same order of magnitude for both models, the glucose uptake rate λ_{gl} is by a factor of 2 to 3 smaller in the continuum model. It is not surprising, that a smaller glucose uptake rate than in the agent-based model must come with an increased nutrient threshold P^{crit} to fit the experimental data. However, the continuum model – started with the parameters of the agent-based model – does not produce a fit of similar quality (data not shown). The difference may be a consequence of the different cell density distribution in both models, which is due to the replacement of cellular adhesion and repulsion by an effective diffusion coefficient. A clean combustion of glucose would require the ratio of oxygen and glucose uptake rates to be around 6 : 1 – in the agent-based model this is actually contradicted with ratios of about 1 : 5. In the continuum model, this surprising effect is still existent, but less pronounced with a ratio of 1 : 2. However, it is well known that tumour cells do not cleanly combust glucose thereby leading to acidification of the tumour environment. Experimental estimates concerning a different cell line point to a ratio of 1 : 1 [112], whereas [139] reports a ratio of 1 : 4 for EMT6/Ro cells. Generally, uptake rates of both oxygen and glucose will depend on the local nutrient concentration and thereby indirectly on the EMT6/Ro spheroid size under consideration. The absolute value of the cellular glucose consumption rate λ_{gl} compares with experimental data on EMT6/Ro spheroids [139] – where $\lambda_{\text{gl}} = 156 \pm 53$ amol/(cell s) (n=6) have been measured – and with other tumour cell lines [130]. Wehrle *et al.* [139] report the original experimental uptake rates in [142] to be in the range of $\lambda_{\text{gl}} = 90$ amol/(cell s). These values support the glucose uptake rate found in the agent-based model. A value for the consumption of oxygen is given in [139], where $\lambda_{\text{ox}} = 40$ amol/(cell s) is reported. Generally, the late stages of spheroid growth depend critically on the nutrient-related parameters. In summary, the resulting parameters for nutrient uptake rates are well within the range observed in the literature [114, 118], but some considerable variances within the literature exist. Apart from the fact that often different cell lines are analysed, the additional problem exists that the values in the literature are usually volume-related uptake rates that have been fitted to experimental data. Equally important however, is the strong dependence of nutrient uptake rates on further conditions such as nutrient concentration, position in the cell cycle, metabolite concentration

etc.

In the continuum model, the quality of the fit to the overall cell number can be increased slightly by varying the exponent *m* as a fit parameter. However, the model is very sensitive to the cellular diffusion constant via the cell density distribution: D_{cell}^0 is automatically tuned to obtain a similar apparent wave velocity (regardless of the value of *m*), which manifests itself in a threefold D_{cell}^0 for *m* = 0.73 in comparison to *m* = 0. This underlines the sensitivity of the fitting procedure (compare appendix C.3). By determining these mobility parameters with an independent experiment, and by fixing the rather approximate parameters for mechanical cell interaction in the agent-based model one would have a possibility of model falsification. This however should rely on a well-defined experimental model. The fact that the resulting diffusion constants are more than one order of magnitude larger than the typical diffusion constants from stochastic forces in the agent-based model should come as no surprise, as cellular movement in the agent-based model is dominated by elastic and adhesive interaction forces, whereas in the continuum model random cellular movements account for all cell mobility.

The necrosis transition rate β_{max} mainly determines the spatial width of the region where viable and necrotic cells coexist and has little impact on the produced cell number over several orders of magnitude. Therefore, the fact that the derived necrosis transition rate β_{max} – implying transition durations of roughly 2 hours – is well within the expected range must be interpreted as a direct consequence of choosing this value as a starting position for the fitting procedure rather than a prediction of the model.

Since the movement-related parameters *m* and D_{cell}^0 are used in (3.11) to mimic elastic and adhesive cellular properties, one can state that the agent-based model has an advantage in this respect, since it inherently incorporates parameters with a physical meaning. However, the existence of a continuum model with similar results proves, that on this macroscopic scale (by comparing the total cell numbers) a discrimination is possible neither between the PDE models of constant and varying diffusivity nor between continuum and agent-based models. In the present example of MTS, in addition the morphology must be compared. This is only possible if it is given in quantitative form, i. e., reliable measurements including error estimates of relative sizes of the quiescent layer, the necrotic core and the proliferating rim under well-defined initial conditions.

3.4.5 Saturation of growth

A complete saturation of the cell number or spheroid size – as observed in [107] and others [108] – cannot be reproduced in the computer simulations with the parameters in table 3.1 on page 89. The large scatter of the data in the case of nutrient depletion (figure 3.3 left panel) does not exhibit

a clear saturation within 25 days, which is not reached in the other configurations anyway. For the explanation of a growth saturation the nature of the additional mechanism remains controversial. For example, in [108] an effective movement of cells towards the necrotic core has been observed leading to the assumption of a chemotactic signal secreted by necrotic cells. The corresponding computer simulations in [7] did lead to saturation. Here, a simpler hypothesis may be tested:

In the spheroid cross section (figure 3.5), macroscopic holes are visible within the necrotic core – created by the removal of necrotic cells from the simulation. Once such a hole is established, it even tends to grow, since the intercellular adhesion is of short range only. An increase of the adhesive normal forces could inevitably couple the proliferating ring to the necrotic core which finally leads to growth saturation: In such a system, the volume loss generated by removing necrotic cells with rate γ must be balanced by a movement of proliferating or quiescent cells from the outer layers into the necrotic core. Consequently, the cell density will then not exhibit fluctuations, which results in a spatially uniform distribution of cell tensions in the necrotic core. In addition, the outward component of the proliferative pressure on the outer layer is counterbalanced by the increased cellular adhesion as well. Then a growth saturation is inevitable: As in the late stages of spheroid growth the cellular birth rate can be assumed to be proportional to the spheroid surface $R_{\text{birth}} \approx \alpha N^{2/3}$ and the rate of cell removal is proportional to the number of necrotic cells residing in the centre, the total cell number can be described by

$$\frac{dN}{dt} = \alpha N^{2/3}(t) - \beta \left[N(t) - \gamma N^{2/3}(t) \right] \tag{3.19}$$

with α, β, γ being positive constants. Via combining the terms with $N^{2/3}$ one can see that above equation resembles the growth law of Bertalanffy [12]. The solution of this equation reaches the steady state $N_\infty = \left(\frac{\alpha}{\beta} + \gamma \right)^3$, which is stable for $\beta > 0$. Therefore, in this regime the nutrient depletion is the dominant factor limiting tumour spheroid growth.

It turned out that an increase of adhesive normal forces by a factor of 3 to $f^{\text{ad}} = 0.0003 \ \mu N/\mu m^2$ suffices to close the visible holes completely and led to growth saturation in the observed time range. This may be due to displaced equilibrium distances resulting from equation (3.2), which induce multiple virtual overlaps at intercellular contact regions. Thereby, the removal of a single necrotic cell may significantly influence the surrounding cells. A lower bound for the equilibrium distance can be obtained by using the virtual spherical contact surface A_{ij}^{sphere} occurring in equation (3.2). Then, for the two spheres with radii $R_{i/j}$ the equilibrium distance d_{ij}^{eq} can be derived by using $h_{ij} = R_i + R_j - d_{ij}$ and

$$A_{ij}^{\text{sphere}} = \frac{\pi}{2} \left\{ R_i^2 + R_j^2 - \frac{1}{2} d_{ij}^2 \left[1 - \frac{\left(R_j^2 - R_i^2 \right)^2}{d_{ij}^4} \right] \right\} \tag{3.20}$$

in equation (3.2). The equilibrium distance has to obey

$$\frac{K_{ij}}{f_{ij}^{\text{ad}}} = \frac{\pi}{2} \frac{\sqrt{R_i + R_j} \left[R_i^2 + R_j^2 + \frac{\left(R_i^2 - R_j^2\right)^2}{2\left(d_{ij}^{\text{eq}}\right)^2} - \frac{1}{2}\left(d_{ij}^{\text{eq}}\right)^2 \right]}{\sqrt{R_i R_j}\left(R_i + R_j - d_{ij}^{\text{eq}}\right)^{3/2}},$$ (3.21)

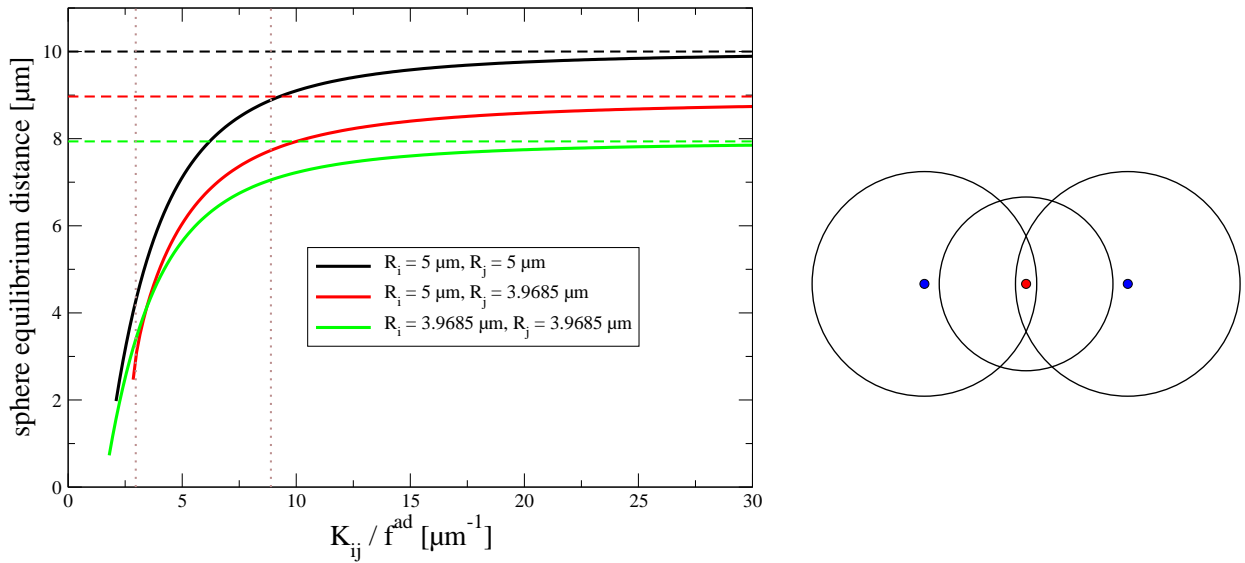which can be solved numerically for d_{ij}^{eq} (see figure 3.8 left panel). Note that the actual equilibrium

Figure 3.8: Lower bounds on the equilibrium distance for selected parameters. **Left:** For all $f^{\text{ad}} > 0$, there exists a lower bound on the equilibrium distance. Horizontal dashed lines correspond to contact distances $(R_i + R_j)$, whereas vertical dotted lines correspond to the values of $f^{\text{ad}} = 0.0003\ \mu\text{N}/\mu\text{m}^2$ (left line) and $f^{\text{ad}} = 0.0001\ \mu\text{N}/\mu\text{m}^2$ (right line) that were used in the simulations. All other parameters have been chosen as in table 3.1 on page 89. Note that for the left dotted line, the lower bound on the equilibrium sphere distance is smaller than the sphere radii. However, since the contact surface in equation (3.2) is improved using a Voronoi estimate, the actual distances will be larger. **Right:** For extreme cases, removal of a vertex may establish sphere-sphere contact of two vertices that had not been in contact before.

sphere distance will mostly be larger than the lower bound given in figure 3.8 left panel, since the smaller Voronoi contact surface for dense packings could also be simulated by a smaller value of f^{ad}. Nevertheless, large overlaps will exist that enable a quick formation of cell-cell contact as in the right panel of the same figure. Since the model is based on the intrinsic spherical shape, such large virtual overlaps may seem unphysiological. At least, they extrapolate the intercellular contact model into regions for which it has not been intended. However, in reality the breakup of a necrotic cell is a continuous process. The membrane of a necrotic cell will rupture and expel the cell content into

the surrounding fluid phase. Thereby, the intrinsic cell shape will not be spherical anymore. If the membrane is removed after some time as well, re-establishment of the contact may be possible.

A pseudo-Brownian cellular motion can either be incorporated by simulating a symmetric and δ-correlated stochastic force (see appendix C.2.3) or by adding to every coordinate a normally-distributed cellular displacement of mean 0 and width $\sigma_i = \sqrt{2D^{\text{cell}}\delta t}$ [143], with $D^{\text{cell}} \approx 0.0001 \ \mu\text{m}^2\text{s}^{-1}$ being an effective cellular diffusion constant. Generally, Brownian motion may lead to the escape of cells at the boundary of the spheroid, which would make a complete growth saturation impossible. Note that another candidate for a cell loss mechanism is shedding of cells at the spheroid surface [144, 145]. For example, for EMT6/Ro mammary tumour cultures, shedding rates of $O(200)$ cells mm^{-2} h^{-1} have been observed [100], which represents a significant source of cell loss. In *in vitro* culture, the separated cells are removed from the culture during replenishments of the growth medium. Within the model, such effects are not included. However, for the time frame usually observed in experiments, a pseudo-saturation of both cell number and spheroid radius could be reproduced in off-lattice agent-based computer simulations [77]. Interestingly, during the period of saturation, deviations from the spherical shape can emerge: The position of unstable intermediate holes within the necrotic core is randomly distributed and gives rise to macroscopic deviations from spherical shape on the spheroid surface. Therefore, an irregular spheroid shape can be explained by individual durations of the necrotic process as well. All these mechanisms might be combined with an involvement of metabolic waste products in the induction of necrosis.

Since in line with other continuum approaches [115, 131] saturation of growth can be explained mechanically, the assumption of a diffusing signal triggering a chemotactic response [7] is not necessary. In the multi-phase continuum approaches, the mass balance equations are not reduced to simple RDEs by preserving the attractive part of the cellular interaction. A reaction-diffusion model with a positive-definite diffusion coefficient as in equation (3.10) is incapable of predicting a steady-state of the cell numbers with realistic assumptions: If one assumes a spatially-heterogeneous steady-state to exist, such that the cell concentration is localised, one can consider a region outside the spheroid that extends to infinity. Within this region, the net cell production rate is non-negative. Then one obtains via Gauss's theorem for this region V

$$\frac{dN_V}{dt} = \oiint_{\partial V} D(\boldsymbol{r})\nabla C(\boldsymbol{r}) \cdot d\boldsymbol{f} + \int_V Q(\boldsymbol{r})\,dV\,, \qquad (3.22)$$

where N_V is the number of cells within V. The assumption of a steady-state demands that $\dot{N}_V = 0$, which cannot be fulfilled, since $Q(\boldsymbol{r}) \geq 0$, $D(\boldsymbol{r}) > 0$ and $\nabla C(\boldsymbol{r}) \cdot d\boldsymbol{f} > 0$ in the inner boundary of ∂V by assumption. At the outer boundary, no contribution can be expected, since it resides at infinity, where the concentrations (and derivatives) vanish.

3.5 Discussion

It has been demonstrated that the Voronoi/Delaunay hybrid model can very well be used to aid agent-based tissue simulations. The introduced agent-based model is rich in features and therefore allows for many comparisons with experiments. It can easily be combined with established models on cellular adhesion and elasticity that rely on direct experimental observables.

Unlike previous models that only considered the influence of a single nutrient on the dynamics of three-dimensional MTS [7, 103, 104, 111, 115], it has been possible to reproduce experimental growth curves with a single parameter set by considering the spatiotemporal dynamics of both the oxygen and glucose concentrations simultaneously. In addition, the typical morphology could be reproduced qualitatively.

With introducing a second similar model based on continuum equations, a comparison between the two modelling approaches could be performed. It should be noted that the two models are not completely analogous as for example the representation of contact inhibition differs. Nevertheless one can discuss key properties of both models.

When considering macroscopic data such as growth curves, the simpler continuum model of the RDE type did reproduce the experimental data with similar quality as the agent-based approach. In the continuum model, the net effect of cellular interactions (adhesion, elasticity, and viscous friction) could be combined in a density-dependent cellular diffusion coefficient, which leads to a qualitative improvement in the reproduction of the macroscopic spheroid sizes in comparison to non-varying cellular mobility. However, it turned out that the necessity to fit experimental data considerably changed the effective cellular diffusion coefficient. The description of cellular movement by mere diffusion coefficients presents a limitation of the continuum model. In many properties the continuum model reproduces the analogous agent-based model qualitatively: For example, the emergence of a necrotic core was necessary to fit the data correctly for all nutrient configurations. However, the dependence of spheroid size on the total cell number and thereby indirectly on the nutrient conditions was not very pronounced whenever the cellular density reached threshold values. For real tumours however, one can – as also predicted by the agent-based model – expect the cellular density to reach the threshold value, since cells tend to adhere. The present PDE model has not been able to reproduce this qualitative effect. In the agent-based model, a saturation of growth could be obtained by increasing intercellular adhesive forces threefold, whereas the continuum model is not able to predict such a steady state.

Since continuum models have the advantage of being computationally simple to solve, the first step towards more refined tissue models should be to analyse the phase space with a simple continuum

approach. The agent-based models are advantageous because cellular properties that have been determined from independent experiments (such as e. g. adhesion and repulsion) can be inherently included to yield improved predictions. Conversely, with a sufficiently accurate experimental signature, the model parameters can be adapted to achieve agreement with experimental observations. Since the parameters of off-lattice agent-based models correspond to experimental observables, their estimation can be regarded a quantitative model prediction.

One of the major difficulties of experimental systems on the level of cell tissues is their poor definition. In the chosen example of MTS this is due to several reasons:

1. In order to obtain the cell numbers, spheroids had been destroyed during the measurements. Therefore, a whole ensemble of spheroids had to be measured.

2. Since the monoclonality of these spheroids is not ensured, it is not *a priori* clear whether a single spheroid might contain several species or whether different spheroids might belong to different species with individual growth characteristics.

3. In addition, it cannot be controlled whether mutations changing the growth characteristics of tumour spheroids take place during their culture. However, when considering culturing times in the order of weeks, such mutations should be rare in cell lines that did not change fundamental properties over years.

The used experimental data exhibit too much scatter to determine parameters with accuracy. Therefore, more effort must be spent in establishing a defined experimental system including a well-defined cell line. With such a system, extensive measurements of the time evolution of growth curves and morphologic parameters could be performed. A combined experimental and theoretical investigation of MTS of a single well-defined cell line is of urgent interest to discriminate between different theoretical models.

3.6   *Towards a realistic tumour model*

It can be questioned whether the presented model grasps essential features of *in vitro* multicellular tumour spheroids. It can be said with certainty that it does not resemble many properties of *in vivo* tumours. In view of the effects of surgery or chemotherapeutic agents, especially the case of a realistic tumour model is of particular interest. Some extensions that need to be included to approach more realistic systems (compare [15] and [146] for reviews) are summarized below:

- Since only a single cell type has been considered, the model will have to be extended by tumour host interaction, which includes

  - competition with the surrounding healthy tissue (compare chapter 4) for space, nutrients, and other factors,

  - interaction with cells of the immune system [120] and processes as inflammation,

  - secretion of angiogenetic factors and the process of tumour vascularisation [147],

  - invasion by tumour cell and metastasis [148, 149, 150, 151] etc.

- Many self-interactions of tumour cells have been neglected in the present model. In addition, one would have to include

  - the effect of metabolic waste products and acidification of the tumour environment [152],

  - plasticity of tumour cell properties [101] (for example, the process of de-differentiation),

  - apoptosis and necrosis induced by further control mechanisms within the cell cycle [101],

  - retardation effects in necrosis due to intracellular nutrient reservoirs,

  - possible intercellular communication with diffusing signals etc.

  in an extended model.

A simultaneous treatment of all these effects within a single and with moderate effort manageable model is currently out of reach. In order to identify physiological subregions, more information on the included mechanisms is necessary. In addition, some mechanisms can lead to similar experimental signatures, such that they cannot be distinguished clearly within the model [153].

A model however should be more than a mere tool of visualisation: With the inclusion of further unknown parameters the volume of the parameter space will grow exponentially. In order to gain predictive power, the allowed volume of the parameter space must be decreased. This could for example be achieved by studying the mechanism separately in controlled *in vitro* experiments that include for example the co-culture of tumour and host cells.

Chapter 4

The Epidermis

The epidermis is a stratified squamous epithelial tissue. Epithelia are membranous tissues that are composed of at least a single cell layer. In multicellular animals they cover the external and internal surfaces of the organism. This chapter will deal with an *in silico* representation of the epidermis, which serves as a protective buffer between the organism and the environment.

4.1 Introduction

The epidermis does not contain separate blood vessels and is therefore dependent on diffusion of nutrients from the dermis below. It can be divided into several layers [154] (compare figure 4.1 left panel):

The innermost *stratum germinativum* or *stratum basale* (basal layer) is a monolayer, in which most cell divisions occur. It is separated from the dermis below by a basal membrane, which has a ruffled structure at fingers, palms and soles of feet. A fraction of the cells created by cell division travels upwards into the *stratum spinosum*, where most cells are interconnected by desmosomes, which leads to a spiny appearance. Within this layer, the process of cornification begins: The cytoplasm looses water and is filled with keratin filaments. Within the *stratum granulosum*, cells die off and their shape flattens. This special case of cell death is called **anoikis**. The *stratum lucidum* is a thin layer that is dominantly expressed at hand and feet and functions as a barrier against all possible intruders. Completely cornified cells mark the *stratum corneum*, which is clearly distinguishable from the layers below. This layer does not contain viable cells and constitutes an efficient barrier for water and its solutes. Note that the thickness of this layer varies strongly for different regions of the skin [154]. The upper part of this layer, where the cellular material detaches due to dissolving intercellular contacts,

is called *stratum disjunctum*.

Within the *in silico* model, only three layers will be distinguished: The term *stratum medium* will be used as a combination of all layers not belonging to the *stratum germinativum* or the *stratum corneum*. The cell types encountered in the epidermis are keratinocytes, melanocytes, Langerhans cells, and Merkel cells. Of these, the dominant fraction is constituted by the keratinocytes with roughly 75000 cells per square mm [155, 156].

Keratinocytes are produced in the *stratum germinativum* by cell division. In order to maintain epidermal homeostasis, in average one of the two keratinocyte daughter cells must leave the basal layer and travel upwards. The keratinocyte remaining in the basal layer will be termed stemcell further-on. The cell travelling upwards transforms – undergoing several transit cell divisions [157] – into a fully-differentiated keratinocyte and reaches the surface after about 12 to 14 days. During this passage, the keratinocytes follow the process of cornification.

Melanocytes migrate to the dermis during embryonic development. These dendritic cells are distributed within the basal layer, and their density is relatively constant between individuals and races with approximately 2000 cells per square mm [154, 155, 158]. They adhere to the basal membrane via hemi-desmosomes. The known purpose of melanocytes is to produce melanin and to provide it to keratinocytes and hair with their dendrites – the connected cells are termed epidermal melanocyte unit [154]. This pigment protects the skin from the ionising effects of electromagnetic radiation, and it is accumulated above the keratinocyte nuclei. Differences in skin colour mainly result from different levels of melanin. Tumours arising from melanocytes are called melanoma. Since most cancerous melanocytes still produce melanin, such tumours mostly have a characteristic black colour (see figure 4.1 right panel). If they are diagnosed and excised via surgery at an early stage, the general chances of total recovery are comparably large. This prognosis degrades rapidly for melanoma at later stages. Therefore, the early and secure diagnosis of this disease is a challenging problem.

Langerhans cells are dendritic cells of the immune system. There is evidence that they collect antigens via phagocytosis and present them on their surface after transforming to dendritic cells in the lymph nodes.

Merkel cells are found close to some hair follicles in mammalian epidermis. Though there is no definite function in skin known, it is believed that these cells play a role in sensation.

Since neither effects of the immune system nor the mechanisms of sensation will be studied here, the latter two cell types will not be contained in the *in silico* representation and will not be discussed further.

The diffusional properties of the skin have important implications on medical treatment applied to this tissue [159]. With an observed increase of the manifestation of melanoma [158], studies of melanoma
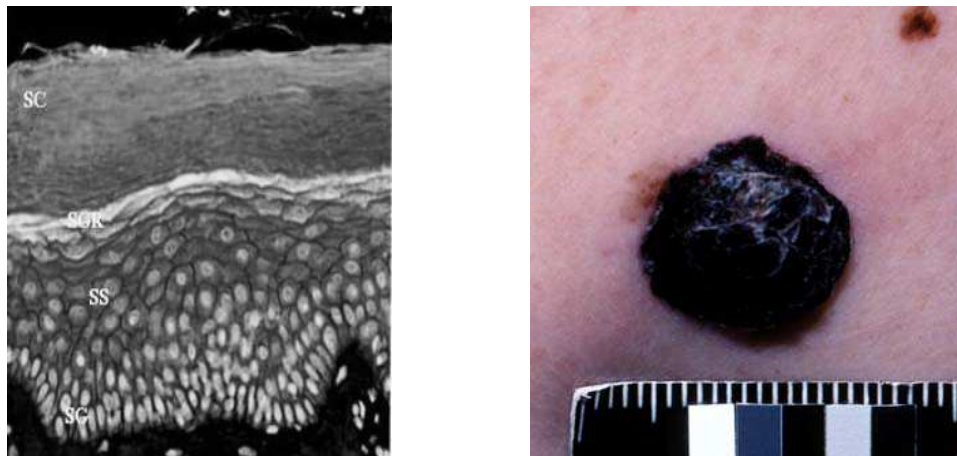
Figure 4.1: Section of human epidermis and top view on a nodular melanoma. Both pictures have been adapted from [158]. **Left**: Section of human epidermis in 500-fold magnification. Indicated from top to bottom are the *stratum corneum* (SC), the *stratum granulosum* (SGR), the *stratum spinosum* (SS), and the *stratum germinativum* (SG). **Right**: Top view on a nodular melanoma.

development are of huge importance. Within this chapter, some simple questions will be addressed using an off-lattice agent-based approach.

4.2 Modelling assumptions

As in the case of section 3.3, the used agent-based model has been built on the basic description given in subsections 2.5.4, 2.5.5, and 2.5.6. However, in contrast to the previous case of MTS, the full equation for the cellular dynamics (2.86) has been solved.

In addition, the model displays specifications [160] that are introduced in the following subsections.

4.2.1 Proliferation and cell death

In contrast to MTS, different cell types are present in the epidermis. The model distinguishes between three cell types: keratinocyte stemcells, keratinocytes, and melanocytes. It is assumed here that these cells follow the cell cycle as depicted in figure 2.16 in subsection 2.5.5, but differ in several properties discussed below.

The mitotic direction in cell divisions has always been chosen randomly on the unit sphere. In the special case of stemcells dividing at the basal layer, the asymmetry in terms of the cell types is included as follows: The daughter cell with the greater distance from the basal membrane is transformed to a keratinocyte, whereas the other daughter cell stays a stemcell.

The fact that in reality a stable flow equilibrium of the epidermis exists should translate to an *in silico* representation. It can be speculated that the decreasing concentration of nutrients provided in the dermis constitutes a signal that may cause keratinocytes to cornify. However, the blood supply provided in the dermis by far exceeds the metabolic demands of normal skin, it is necessary for the temperature regulation instead. Therefore, other mechanisms on homeostasis should be analysed as well. In tape-stripping experiments [161, 162] it has been observed that the removal of the *stratum corneum* results in prolonged hyperproliferation of keratinocytes of the skin. It has been proposed that simply the local concentration of water may be a marker that causes the proliferative response of the keratinocytes.

In contrast to the MTS in chapter 3, two pathways to cell death are considered here: Stemcells and melanocytes enter necrosis as soon as the local nutrient concentration falls below a critical threshold. In contrast, keratinocytes enter anoikis after completion of the cell cycle (i. e., after completion of S/G$_2$-phase) in the fourth generation. This assumption is motivated by the cellular pedigree concept [157, 161], which assumes that differentiating cells undergo an approximately constant number of transient cell divisions before entering a differentiated (nonproliferative) state. Furthermore, healthy melanocytes in the model are regarded as fully-differentiated cells that do not proliferate. A malignant transformation however may cause melanocytes to proliferate.

There is strong experimental evidence that the removal of the protective *stratum corneum* influences the proliferation turnover rate of the epidermis [161, 162]. In [161] it is hypothesised that an intraepithelial diffusible signal might control proliferation. In this chapter, as a simple candidate for such a signal the extracellular water content will be considered. Therefore, in the model the proliferation rate of the keratinocytes and stemcells is influenced by the local water concentration. Since in the model representation of the cell cycle (subsection 2.5.5) the overall cycle time can be controlled by the length of the G_0-phase, here the local water concentration has been as the critical mechanism. Keratinocytes (and their stemcells) are assumed to enter G_0-phase after completion of G_1-phase only if the local water concentration is above a critical threshold. The duration of the G_0-phase is determined by a normally distributed random number if the local water concentration does not fall below the critical threshold before. Thus, a large water concentration may prolong the cycle time of keratinocytes and their stemcells in the model. Note that further influences on the cell cycle (e. g. contact inhibition as in chapter 3) are thus neglected here.

Naturally, necrotic or cornified cells do not consume any nutrients. In view of the unknown details of the cell loss process, an exponential decay of receptor and ligand molecules on the cell membrane with a given rate α^{loss} has been assumed, i. e.,

$$\dot{C}_i^{\text{rec/lig}} = -\alpha^{\text{loss}} C_i^{\text{rec/lig}} . \tag{4.1}$$

This choice resembles the dissolution of intercellular connections in the *stratum corneum*. In order to minimize the perturbation of the equilibrium distance following from equation (2.68), this implies a decreasing elastic modulus as well. The simple demand, that the equilibrium distance between two identical cells should not change, can be satisfied with

$$\dot{E}_i = -2\alpha^{\text{loss}} E_i, \tag{4.2}$$

which follows from equations (2.60) and (2.75). A measure for the cellular binding strength can then be defined from the sum of all binding energies with the next neighbours

$$\epsilon_i = \sum_{j \in \mathcal{NN}(i)} \epsilon_{ij}(t) A_{ij}(t). \tag{4.3}$$

Assuming that cells with low binding are shed of from the skin surface, both necrotic and cornified cells are removed from the simulation as soon as their binding strength falls below a critical value $\epsilon_i \leq \epsilon^{\text{min}}$. Note that this choice has the consequence that all non-viable cells without contact to other cells ($A_{ij} = 0$) are removed instantaneously from the simulation. This is not a contradiction, since cells without anchorage are assumed to be shed off in the realistic epidermis anyway. Though the loss of receptors and ligands as well as decreasing cell elasticity may be reasonable assumptions for cornified and necrotic cells, the overall time course may certainly differ considerably from the above equations. Other forms of necrotic cell removal might also be plausible: For example, one could think of removing non-viable cells randomly at a constant rate as was done in chapter 3. This choice however did significantly disturb the layered structure of the *stratum corneum*. In this case, holes in this protective layer emerged and did lead to sudden loss of water in the epidermal layer and thereby to irregular proliferative behaviour and considerable oscillations in epidermal thickness. The same problem occurred when assuming a (normally-distributed) cell-specific eigentime after which non-viable cells were removed from the simulation.

4.2.2 Cell mobility

All cells are assumed to be subject to delta-correlated random forces (see appendix C.2.3). Note that these forces act on every cell separately, such that active cellular movement is not considered.
As the computational domain, a rectangular volume has been considered. The obvious anisotropy of epidermal tissue translates to the boundary conditions on the cellular agents. The simplest possibility to resemble the basal layer is a static plane boundary with constant normal vector (without loss of generality e_z is chosen here). Within the JKR model (2.63), such a boundary can be well implemented by assuming contact with a cell of infinitely large radius. The *z*-boundary of the basal layer has been

assumed to be of infinite elasticity. Since the elastic parameters enter additively in equation (2.60), this choice slightly shifts the position of the basal layer but does not sensitively change the global model behaviour. The corresponding adhesive anchorage in the basal layer has been made dependent on the cell type. In order to minimize the boundary effects in x and y direction, periodic boundary conditions on the cells could in principle be used. This however would necessitate a rather tedious mirroring of cells close to the boundary and would in addition conflict with the boundary conditions on the reaction-diffusion grids. Therefore, here a different approach has been chosen: Every cell in contact with a x or y boundary, is assumed to be in contact with a cell of similar type, size, receptor and ligand equipment, etc. Thus, it interacts with a virtual mirror copy of itself, where the contact area is situated within the boundary plane. In comparison to a planar boundary as is used at the bottom this technical implementation has the additional advantage that special drag forces with a static boundary need not be considered. In upper z-direction there are no boundary conditions on the cells, but necrotic or cornified cells that have lost intercellular contact are removed instantaneously from the simulation (compare subsection 4.2.1).

Note that for an in x and y homogeneous cell distribution, the problem would effectively reduce to a one-dimensional one. However, the existence of fluctuations and of heterogeneously distributed melanocytes destroys that symmetry.

4.2.3 Water and Nutrients

Though the theoretical foundation of the diffusion equation relies on vanishing self-interactions of the described molecules (which can for example be assumed for small concentrations), it has been found empirically that the distribution of water in the tissue can be described approximately by diffusion as well [163]. However, it is known that the apparent diffusive properties of the epidermis vary extremely within the different layers. For example, the *stratum corneum* has apparent diffusion coefficients of water that are three orders of magnitude lower than the diffusive properties of the layers below (see table 4.1 on page 120). Technically, this is reflected in the model by averaging the diffusion coefficients for the different cell types residing in a volume element of the reaction-diffusion grid.

Within the model, it is assumed that the net consumption/production rate of water by the cells vanishes. Consequently, it is assumed that the distribution of extracellular water can be described with a normal diffusion equation with spatially heterogeneous diffusion coefficients. In such an equation, the units may be rescaled such that the water concentration can be expressed in fractions of the maximum concentration at the basal layer.

The dynamics of nutrients such as glucose differs in the aspect that sink terms have to be considered as

well and thus, a full reaction-diffusion problem has to be solved for the nutrients. In order to calculate the dynamics of water and nutrients, the problem has to be treated with time-dependent boundary conditions. Above the cell layers (dynamic thickness) the concentrations of water and nutrients have been fixed to vanish. Technically, this has been implemented by setting the concentrations to vanish at all grid volume elements not containing any cells[1]. At the *x* and *y* boundaries, no-flux von Neumann boundary conditions have been used, i. e., at these boundaries one has $\partial_x u = 0$ and $\partial_y u = 0$.

4.3 Results

The model parameters that have not been changed during the simulations can be found in table 4.1 on page 120. As the computational domain, a rectangular volume of dimensions 200 μm $\times$ 200 μm $\times$ 400 μm has been considered. The initial conditions in the *in silico* experiment have been determined as follows: A monolayer of keratinocyte stemcells has been distributed on the basal layer – following the pattern of a perturbed square lattice. In addition, at the centre of the *stratum germinativum*, a single (initially non-proliferating) melanocyte was added. Afterwards, the position of the cells in the cell cycle was randomised uniformly to avoid initial artifacts. This configuration could for example mimic a severely perturbed epidermis, where suddenly not only the *stratum corneum* but in addition the *stratum medium* was removed. Consequently, a strong proliferative response should be expected. After a steady-state flow equilibrium had been established (see subsection 4.3.1), different perturbations have been performed. These include removal of all cornified cells (tape-stripping experiments) and changes in the melanocyte properties (subsection 4.3.2).

4.3.1 Homeostasis control

The first question to be answered is whether the control mechanism of the water-concentration-induced prolongation of the keratinocyte cycle time (compare subsection 4.2.1) can actually reproduce the macroscopically observed flow equilibrium of skin in an *in silico* model. In particular, the resulting flow equilibrium should be stable against perturbations such as complete removal of the *stratum corneum* that is performed for example in tape-stripping experiments [162].

It turns out that such a steady-state flow equilibrium exists and that it is stable for some regions in parameter space (see figure 4.2).

---

[1]Note that this requires that the grid resolution is low enough in order not to generate unphysiological sink terms in intercellular cavities.
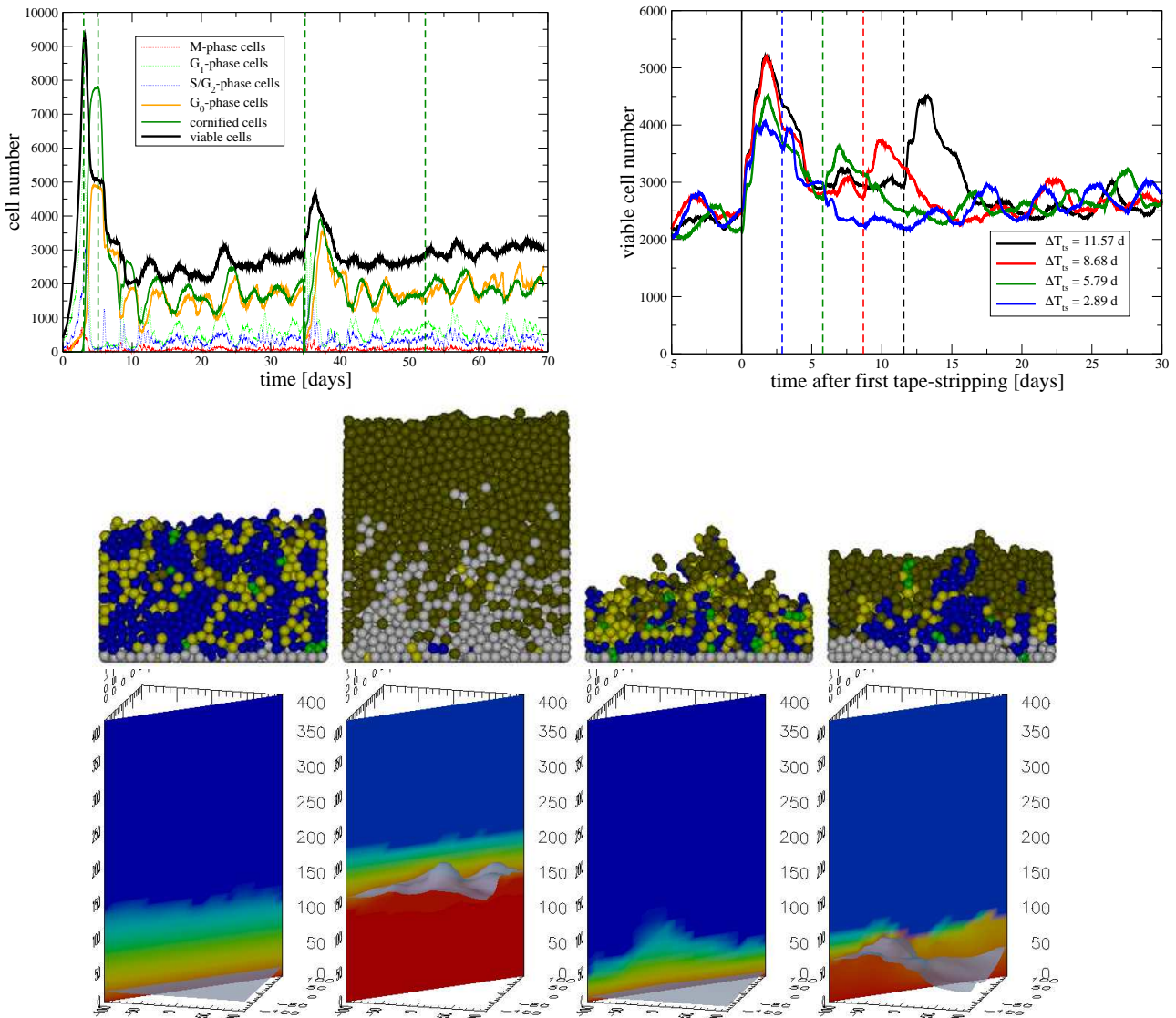
Figure 4.2: Maintenance of an epidermal steady-state flow equilibrium [160]. **Top Left**: Distribution of cells in the cell cycle versus time. The vertical dashed lines indicate times where frames of the cross-sections of the cell distribution (first row below) and the water concentration (bottom row below) provide spatially-resolved information. **Top Right**: Number of viable cells versus time for two successive tape-stripping events. Simulations have been started with different seed values of the random number generator. The vertical dashed lines denote the respective times of the second tape-stripping experiment, whereas the first tape-stripping has been performed at time 0 (vertical solid line). **Second row from below**: Spatial distribution of cells in the cell cycle (frames from top left to bottom right). Cells in G_0-phase are encoded grey, whereas cornified cells are shown brown. The remaining colours denote the other phases in the cell cycle. The horizontal diameter of a single frame corresponds to 200 μm. **Bottom row**: For every frame, the colours in the diagonal cross-section encode the water concentration (blue for 0 % and red for 100 %). The transparent isosurface encodes the critical water concentration.

Starting from a monolayer of cells, the water concentration throughout the tissue (bottom row, left-most frame) is very low such that no keratinocyte enters cell cycle prolongation. The net effect is an initial exponential growth phase (top left panel), where stemcells in the basal layer and also transit amplifying keratinocytes – that have not yet reached their fourth generation – proliferate. After three days the stemcells in the basal layer enter prolongation of the cell cycle (second row from the bottom, leftmost frame). After four generations, cornification of the first keratinocytes begins, followed by the rapid formation of a strong *stratum corneum* after five days with a considerably decreased diffusion coefficient for water. This in turn leads to an increased water concentration in the *stratum medium* (bottom row, second frame) and thereby a large fraction of non-cornified keratinocytes residing in G_0-phase (second row from below, second frame): The initial exponential growth is halted. Afterwards, the cell number decreases, since cornified keratinocytes are shed off at the outer surface of the *stratum corneum*. The dynamics equilibrates slowly. After 35 days, the *in silico* analogue to a tape-stripping experiment has been performed: All cornified cells are suddenly removed from the simulation. This leads again to a proliferative response. However, since this time the cornified layer quickly re-establishes due to the abundant keratinocytes in the G_0-reservoir, the proliferative response is considerably smaller than initially. Interestingly, the oscillations around the equilibrium value are remarkably strong. In figure 4.2 second row from below it visible in the rightmost (latest) frame that the cornified layer exhibits a small hole (blue cells) in the *stratum corneum*. Through such holes, a considerable amount of water can be lost, which causes even distant keratinocytes in the model to leave their cell cycle arrest (white cells changing to blue cells). This sensitivity of the model to small water concentration changes leads to the strong perturbations of the equilibrium and to the slight upward tendency. The equilibrium thickness of the epidermis in the model corresponds to approximately $120\,\mu$m above the basal membrane and with the ground surface of $200 \times 200\ \mu$m^2 the resulting equilibrium cell numbers do well correspond to values in the literature of 75000 cells per square mm epidermis [156].

If the tape-stripping is performed twice (figure 4.2 top right panel), the relative magnitudes of the proliferative responses display an interesting behaviour. Already in the first tape-stripping event (vertical solid line) there is a considerable variance in the heights of the proliferative responses. This is a mere result of different seed values in the random number generator. More important, the relative magnitude of the secondary proliferative responses is generally smaller than in the first tape-stripping events. In the subpopulations (not shown) it becomes visible that in the second tape-stripping, the *stratum corneum* is re-established much faster. This is due to the larger number of viable cells in between the experiments in comparison to the number of viable cells before the first tape-stripping experiment. These cells constitute a larger reservoir for cornification. After the *stratum corneum*

has been re-established, the water concentration increases quickly and the proliferative response is halted. Especially for the case when the second tape-stripping experiment is performed at the peak of the cellular response (blue curve), the time needed for restoration of the *stratum corneum* is shortest, which is reflected in the relative magnitude of the secondary response as well.

In addition, it is visible that with a decreasing ΔT_{ts} between the tape-stripping events, the relative magnitude of the secondary proliferative responses decreases: For large distances (11.6 days, black curve) the epidermis approximately reacts as strong as in the first experiment but with smaller distances between the experiments (red and green curves), the magnitude of the response decreases. This has a different reason than the decrease between primary and secondary response: In the cell cycle distribution (second row from below) right after a tape-stripping event (third frame) it is visible that the basal layer dominantly remains in G_0-phase. Since these are the cells that produce the keratinocytes of the first generation, the overall cell reservoir of keratinocytes will – for the time of an unprotected epidermis – decrease. The net effect is that the reservoir can regenerate during ΔT_{ts} and the secondary proliferative response will be stronger with larger regeneration times.

4.3.2   Effects of melanocyte anchorage

In a second assay, the single melanocyte in the basal layer was turned cancerous after the flow equilibrium was approached. Previously, the non-proliferating melanocyte was as firmly attached to the basal membrane as keratinocyte stemcells, such that it did not separate during equilibrium formation. Note that in the model, the property "cancerous" is only reflected by suddenly allowing for melanocyte proliferation. As in the model the cell cycle of melanocytes is not influenced by the local water concentration, these cells have a competitive advantage in comparison to the keratinocytes. In a first attempt, the degree of melanocyte anchorage to the basal membrane has been varied concomitantly with the malignant transformation. It is known that most human melanoma cell lines display decreased or no expression of cadherins and therefore exhibit a decreased ability to adhere [164].

One might think that a decreased basal adhesion of cancerous melanocytes would lead to a decreased fraction of melanocytes bound to the basal membrane and thereby to a larger fraction of melanocytes that is shed to regions where the nutrient supply falls below necrosis-inducing levels. Thus, the total number of tumour cells should intuitively be sensitive to the basal anchorage. Starting from experience with MTS (compare table 3.1 on page 89), the cycle time of the cancerous cells has been assumed to be in the order of 15 hours. It turned out that with such short cycle times for melanocytes and the turnover time chosen for the stemcells in the basal layer, the overall growth dynamics was hardly dependent on the anchorage to the basal layer (see figure 4.3 left panel). Even with completely

absent adhesion to the basal membrane, comparable numbers of tumour cells were found. The reason is that with the given proliferation rate, exponential growth simply outperformed the epidermal flow induced by the turnover at the basal layer. Consequently, the proliferation rate of the cancerous cells has been reduced and new simulations were performed in combination with complete loss of melanocyte basal membrane anchorage (see figure 4.3 right panel). There it is visible that there is
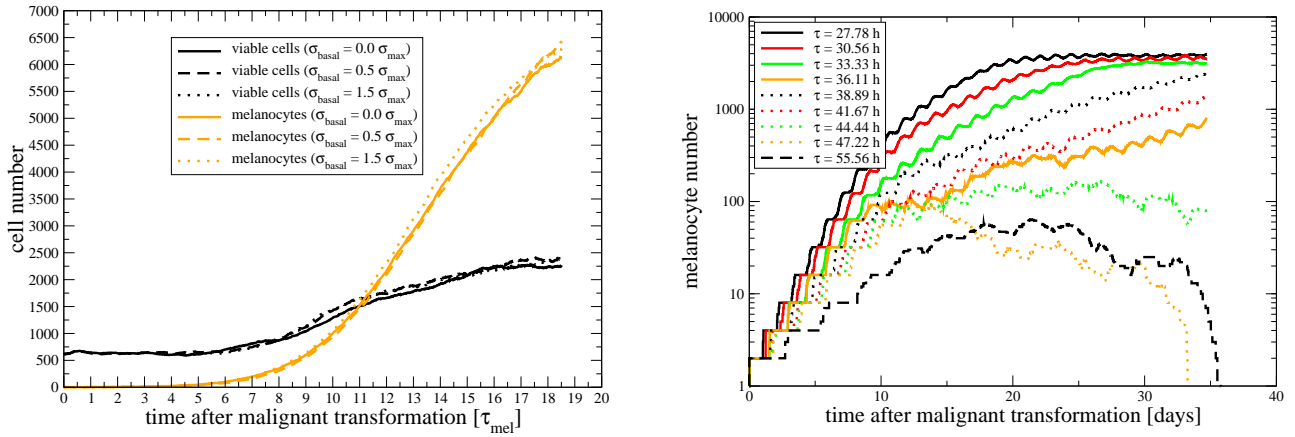

Figure 4.3: Melanocyte growth after the malignant transformation [160]. **Left**: Total number of melanocytes (orange, including necrotic and viable melanocytes) and viable cells (black, including stemcells, keratinocytes, and melanocytes) for different degrees of basal adhesion versus time – expressed in units of the cancerous melanocyte cycle time. With the melanocyte cycle time set to $\tau_{mel} = (15.0 \pm 2.0)$ h and other parameters chosen as in table 4.1 on page 120, the basal anchorage has no significant effect on the overall dynamics. Initially, the growth of melanocytes follows an exponential growth, which is soon slowed down since the melanocytes reach distant regions from the basal layer, where nutrients are provided scarcely. Since the number of viable cells already indicates saturation, the total number of melanocytes will saturate eventually. A further increase in the cell numbers can in reality be achieved by angiogenesis or by surface-dominated growth by leaving the computational domain. **Right**: With considerably slower melanocyte proliferation, a parameter regime can be found where melanoma do not persist within the steady-state flow equilibrium. Interestingly, in this case the period of coexistence of healthy skin and transformed cells may be remarkably long, which – if transferred to reality – would give time for further malignant transformations. In this parameter regime, the system is very sensitive to stochastic effects, as is indicated in the disturbed order (some curves intersect). The damped oscillations stem from the standard deviations of cell cycle durations (2.01 h in every run).

a region of melanocyte proliferation rates with considerable fraction of the melanocytes being shed into regions distant from the basal layer, where the glucose concentration falls below life-sustaining levels. In these regions, necrosis is induced. Interestingly, the number of melanocytes at 35 days after the malignant transformation is not a monotonously decreasing function of the cycle time (compare

for example solid yellow and red dotted curves in figure 4.3 right panel). This is due to stochastic effects:

The region between melanoma persistence and complete tumour shed-off has been examined further by adjusting the melanocyte cycle time to $\tau_{\mathrm{mel}} = (44.44 \pm 5.56)$ h. Generally, one can see in figure 4.4 bottom panels, that the usual spherical form one observes for *in vitro* MTS (compare chapter 3) is considerably deformed for this system to cylinder-shaped or cone-shaped. This is due to the pre-existent flow-equilibrium of the surrounding tissue and the effectively one-dimensional diffusion problem. The shapes of these structures appear to be dynamically fluctuating in the model in these initial phases. Note that the boundaries of the melanoma are rather diffuse. From the cross-sections in figure 4.4 it may be hypothesised that the micrometastases sometimes observed around primary melanoma in skin may correspond to branches of melanoma clones that have separated from the main clone during the upward flow. For the whole epidermis it can be seen that its thickness increases in those situations where considerable numbers of melanocytes develop. In the model, this is due to the displacement of the surrounding keratinocytes, which are constrained in the perpendicular directions, and also to the increased loss of water through tumour tissue.

Initially, a thin column of cancerous melanocytes is formed. Then, in some simulation runs (see figure 4.4 bottom rows), the melanocytes can persist within the life-sustaining zone until their growth velocity outperforms the upward-directed flow velocity and direct contact with the basal membrane is re-established. Afterwards, in the middle of the column of cancerous cells the upward drag forces are decreased, since for the interior cells there is no direct contact with keratinocytes moving upwards. Using different seed values for the random number generator, several simulations with otherwise equal parameters have been performed (coloured curves in figure 4.4 top panel). It turns out that completely different outcomes may occur. Thereby, one should keep in mind that the stochastic effects do not only result from stochastic forces, but from the randomly chosen mitotic directions and the cell cycle durations as well. The initial phases are most important, as for the small cell number in the initial melanoma growth phase stochastic effects do not average out completely. In this first experiment, the different seed value did already lead to different configurations before the malignant transformation, i. e., stochastic effects had already entered the initial conditions for the cancerous melanocytes. To elucidate this context further, another series of simulations has been performed, this time with equal initial seed values. On the contrary, in this second series the seed value of the random number generators was reset to different values right at the time of the malignant transformation. Thus, the initial environment of the cancerous melanocyte was the same in these simulations. It turned out that the variance of the outcomes narrowed considerably (thin grey curves in figure 4.4 top panel). Thus, it can be concluded that the variance in the initial environment of

cancerous melanocytes contributes significantly to the final outcome in the *in silico* model. Note that these secondary stochastic effects do not only include the spatial cellular position, but also the local proliferative state and thereby the local upward flow velocity: The upward drag forces will be larger if the cancerous cell is surrounded by many proliferating keratinocytes with a net upward flow velocity.

4.3.3 Model parameters

Reasonable dynamics has been achieved with the parameters in table 4.1.

The viscosity of the extracellular matrix η determines the friction on loosely bound cells and – since friction arising from the cytoskeleton was assumed to be small ($\gamma_\perp \approx 0$) – dominates friction in directions normal to the cell contact surfaces. This contributes for example in proliferation and thus, in addition the speed of cell division in M-phase is dependent on η. As long as the mechanical relaxation occurs on a shorter timescale than the cell doubling time, this does not have macroscopic effects on the evolution of the tissue. When $\gamma_\perp$ has the same order of magnitude as $\gamma_\parallel$, it will dominate the contribution inflicted by the viscosity η. If the magnitude of the total drag force coefficient $\gamma^2 = \gamma_\perp^2 + \gamma_\parallel^2$ does not change, it turned out by comparing the three extreme cases (that is, $\gamma_\perp = 0, \gamma_\parallel = \gamma$ and $\gamma_\perp = \gamma, \gamma_\parallel = 0$ and $\gamma_\perp = \gamma_\parallel = \gamma/\sqrt{2}$), that the differences in the overall population dynamics are rather small (not shown). It may be speculated that this is due to the fact that in the present calculations, the relaxation speed has no direct back-reaction on the number of cells, as for example contact inhibition is not included. As here absence of perpendicular friction has been assumed, the tangential friction coefficient $\gamma_\parallel$ dominantly determines the speed of relaxation within the tissue. The chosen value led to reasonable dynamics and has been estimated from [76].

The adhesion energy density $\epsilon^{\max}$ determines the cell-cell equilibrium distance and the binding strength, which was a marker for the removal of necrotic or cornified cells. Generally, this value will in reality be time-dependent. For example, for cell-cell contact durations shorter than 30 seconds, average rupture forces of 20 nN have been measured [88]. Assuming $K_{ij} = 1000$ Pa and $R_{ij} = 2.5$ μm one would thereby find from equation (2.69) an adhesion energy density of $\epsilon^{\max} \approx 0.0017$ μN μm^{-1}. However, then the equilibrium distances resulting from equations (2.63) or (2.68), respectively, are inconsistent with the equilibrium distances in [88]. This indicates that neither the full JKR model (2.63) nor its approximate version (2.68) is directly applicable to cells. For larger times, the discrepancy becomes even worse. Therefore, the binding energy density has been derived from the observed equilibrium distance [88] solving (2.68) instead. With this procedure, the equilibrium distances are in a physiological regime. Note that larger adhesion will lead to smaller equilibrium distances (leading to moderately increased contact surfaces and drag forces) but in addition to longer persistence
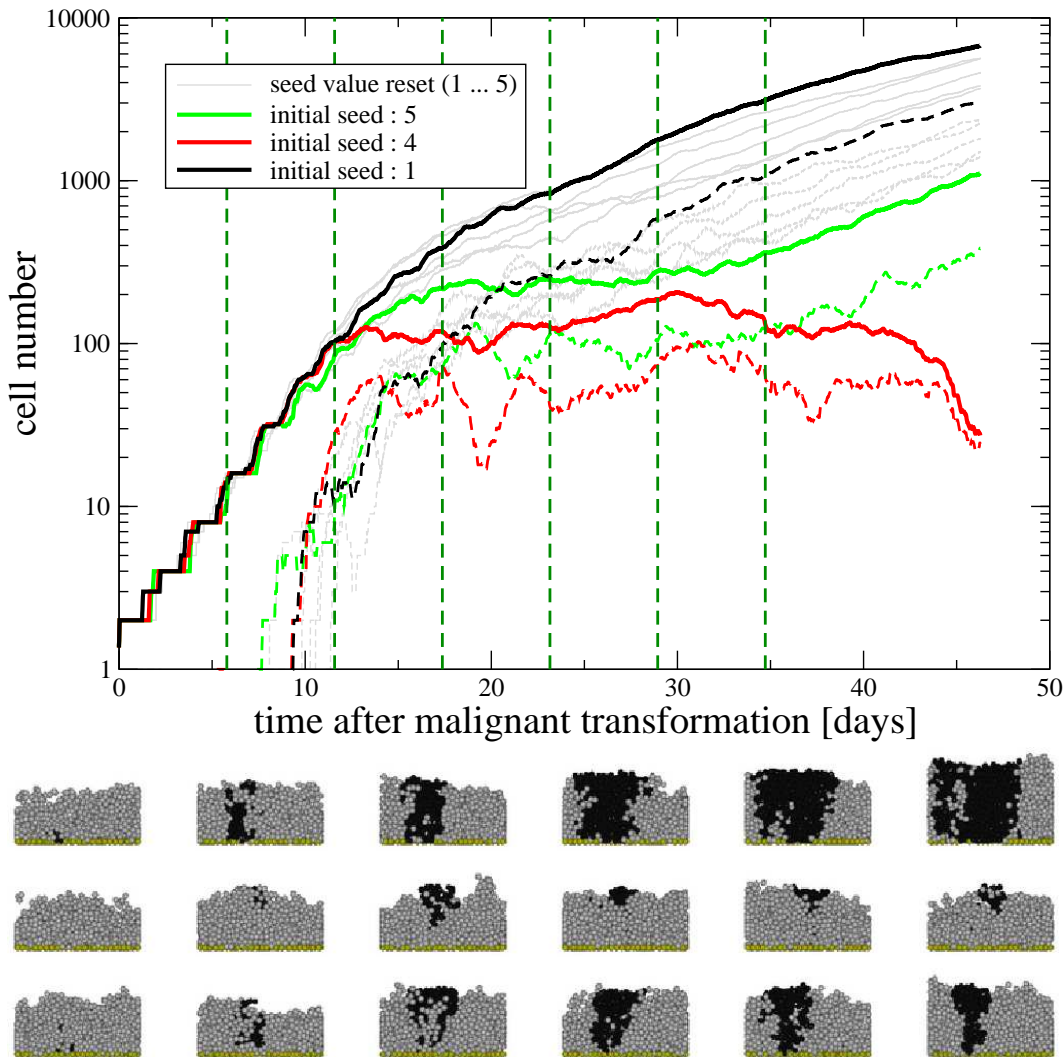
Figure 4.4: Primary and secondary stochastic effects on the initial stages of melanoma [160]. **Top**: Total number of melanocytes (solid lines) and the necrotic cell subpopulation (dashed lines) after the malignant transformation with melanocyte cycle times $\tau_{\mathrm{mel}} = (44.44.0 \pm 5.56)$ h and other parameters as in table 4.1. Different colours correspond to different initial seed values of the random number generator with otherwise equal parameters. Completely different outcomes may occur. Vertical dashed lines mark times where the frames of the cross-sections (below) have been obtained. For seed value 4 (red), the melanocyte population is nearly extinct after 45 days, as nearly all melanocytes are necrotic (curves combine). The curves in grey correspond to simulations that have been started with initially equal seed values, which have been reset to differing values at the time of the malignant transformation. **Bottom cross-sections**: Time frames of the *in silico* evolution of cancerous melanocytes (black) within an epidermal population containing keratinocytes (light grey) and stemcells (yellow). The diameter of a single frame corresponds to 200 μm. The colours do neither differentiate between viable and necrotic melanocytes nor viable and cornified keratinocytes, respectively. The first row corresponds to the seed value 1 (black curves in the top panel), the second row to seed value 4 (red in top panel), and the last row to seed value 5 (green in top panel). The existence of the flow equilibrium of skin leads to cylinder- or cone-shaped tumours.

times of dead cells, which results in an increased thickness of the *stratum corneum*. However, due to equation (4.1) this latter effect only enters logarithmically. Even if the adhesion energy $\epsilon^{\max}$ and the minimum anchorage $\epsilon^{\min}$ are decreased simultaneously, differences in the numerical solution may occur: This is due to the fact that for these reduced values, the equilibrium distance and the contact distance are much closer together, such that the maximum spatial stepsize allowed in the numerical solution must be decreased.

The elastic parameters E_i and ν_i correspond to approximate physiological values for cells [76, 134, 140]. However, it is known that – depending on the cell type – significant deviations may occur. With the given drag forces, mechanical relaxation occurs on a shorter scale than the cell cycle times, such that changes in physiological windows have only small macroscopic consequences. It should be noted however that already for moderately changed Young moduli (and/or reduced Poisson moduli) the equilibrium distance between cells will be shifted, which might decrease the maximum allowed spatial stepsize in the numerical solution to avoid unphysiological losses of contact.

As has already been discussed in subsection 4.3.2, stochastic perturbations may have significant influence on melanoma development in the model, both as primary (i. e., occurring after the malignant transformation) and secondary (i. e., as variations of the initial conditions) effects. Generally, these can be divided in stochastic forces, randomly distributed mitotic directions, and randomly distributed cellular cycle times.

Stochastic forces contribute to the detachment of cornified and necrotic cells, which do neither divide nor advance through the cell cycle. Small variations in their strength ξ change the fluctuations in the epidermal thickness around the equilibrium value. For completely absent stochastic forces, the existence of a planar basal layer sometimes led to planar cell configurations, which is unfavourable for the Delaunay triangulation (compare the general position assumption in subsection 2.3.2). Considerably larger stochastic forces have a strong influence on the thickness of the *stratum corneum*, since loosely bound cells are removed much faster and the protective layer is lost. Then, the probability of water loss is increased and as a compensatory reaction the thickness of the epidermis increases. The thickness of the cornified layer will thus be strongly dependent on the receptor loss rate α^{loss}, as follows from equation (4.1).

The values of the durations of M-phase $\tau^{(\mathrm{m})}$, the S/G_2-phase τ^{S/G_2} and the prolongation of the cell cycle $\tau^{(G_0)}$ influence the relative distribution of cells within the cell cycle (compare figure 4.2 left panel), whereas the sum of their squared widths primarily determines the speed of desynchronisation of cell division. This becomes important after the removal of all keratinocytes. Due to missing specific data, these values have been adopted from chapter 3. The shortest observed cycle time determines the proliferation time for keratinocytes if the water concentration is below the critical threshold. The

system is most sensitive to the G_0-phase prolongation time τ^{G_0}, which has been estimated from [162], where the cell cycle time was found to range between 14 and 200 hours. Note that the large width of this prolongation time was necessary to obtain desynchronisation of cell proliferation in reasonable time. With a smaller width, the time for the establishment of a steady-state flow equilibrium and the perturbations were much larger.

The simplest assumption of randomly distributed mitotic directions did not conflict with the layered structure of the epidermis. This however does not refer to the model constraint that after asymmetric cell divisions of keratinocyte stemcells, the daughter cell with the larger *z*-component of the position differentiates to a keratinocyte. Without this assumption, the basal layer would loose stemcells that would eventually be shed off at the outer surface.

The average cell volume of keratinocytes varies from 425 μm^3 for cornified cells to 800 μm^3 for *stratum medium* keratinocytes [165]. Therefore, with the intrinsic assumption of spherical shape, the maximum cell radius has been fixed to $R^{(m)} = 5.0$ μm, which influences the time-dependent target volume. Note however, that within the *stratum corneum* the cornified cells flatten considerably and the intrinsic cell shape cannot be regarded as spherical anymore.

The glucose uptake rate for cancerous melanocytes $\lambda_{\text{gluc}}^{(\text{mel})}$ has been chosen considerably larger than the glucose uptake rate of keratinocytes $\lambda_{\text{gluc}}^{(\text{ker})}$. This is motivated by the assumption that cancerous melanocytes have a considerably increased metabolism. The actual values are in the range observed for tumour cells [139]. The minimum nutrient concentration $U_{\text{gluc}}^{\text{crit}}$, below which for melanocytes necrosis is induced, has been chosen to be in the order of 1 mM, since necrosis of tumour cells becomes visible at these nutrient concentrations *in vitro* [107, 172]. The combination of melanocyte nutrient uptake rate and minimum glucose concentration define a region, within which melanocytes can survive.

The critical relative water concentration $U_{\text{H}_2\text{0}}^{\text{crit}}$ has been adjusted to obtain a reasonable thickness of the *stratum medium* with $O\,(5)$ cell layers, as is reported for example in [162].

The apparent water diffusivity $D_{\text{H}_2\text{0}}^{\text{strat.germ.}}$ in *stratum medium* as well as in *stratum corneum* $D_{\text{H}_2\text{0}}^{\text{strat.corn.}}$ has been estimated experimentally by various researchers. Though strong variances exist, all of them predict a strong decline of the apparent diffusion coefficient [163, 168, 169]. The local water diffusion coefficients influence the gradient of water concentration: Large diffusion coefficients correspond to a small gradient. For an intact *stratum corneum* the water concentration is approximately constant throughout the *stratum medium* and then falls rapidly (compare figure 4.2 bottom row).

The same general features hold true for the glucose diffusion coefficient $D_{\text{gluc}}^{\text{tiss}}$, which has specifically been determined for the human skin [170]. The glucose concentration at the basal layer $U_{\text{gluc}}^{\text{bound}}$ has been fixed to values that are normal for blood [171] for non-diabetic patients. However, it should be

noted that in reality the blood glucose concentration varies significantly – for example after ingestion. In the model, the low glucose concentration in upper layers of the epidermis strongly influences the chances of melanoma survival.

In order not to loose stemcells at the basal layer migrating upwards to the *stratum corneum*, the basal adhesion energy for keratinocyte stemcells and non-proliferating melanocytes has been chosen to be twice the maximum adhesion energy density ϵ^{max}. This did suffice to disable detachment of these cells. For cancerous melanocytes, the basal adhesion has been varied as discussed and for differentiating keratinocytes, no basal adhesion has been assumed.

4.4 Discussion

With a more complete treatment of the equations of motion than in chapter 3, it has been demonstrated that agent-based models can still be used for tissue simulations in the order of $10^4 \ldots 10^5$ cells.

From a biological point of view, a diffusible substance can serve as a moderator on cellular proliferation in the epithelium. The model does not contradict that the extracellular water concentration may be a candidate for such a moderator. However, since any other diffusible signal that is not consumed or secreted by the cells themselves in the epidermis but is released at the basal layer and that has a considerably decreased effective diffusivity in the *stratum corneum* would lead to formally equivalent model equations, other signals fulfilling these conditions would yield the same model behaviour. Consequently, the moderating substance cannot be extracted from the model without quantitative comparisons. Simple assumptions on the moderating substance can explain the homeostasis of the epidermis, which is in the model stable against perturbations. The consequences of varying adhesive properties of cancerous melanocytes to the basal membrane have been studied. It turned out that these are strongly interlinked with the balance of melanocyte and keratinocyte proliferation rates. In particular, it has been shown that in some regions of parameter space, stochastic effects play an important role in the *in silico* representation of melanoma growth. In particular, the variance of the initial local environment of cancerous melanocytes was found to have strong consequences.

It is the truth content of the used assumptions and the quality of the applied approximations that determine the applicability of these results in reality. The model introduced in this chapter has a number of shortcomings:

A significant macroscopic failure of the model is its inability to explain the reduced thickness of the *stratum corneum*. This is due to the fact that the inherent cell shape is spherical, whereas cornified cells flatten and form polarized adhesive bindings. In reality, this will lead to a greater stability of the *stratum corneum* in comparison to the model, which would for example imply a smoother evolution

around the steady-state flow equilibrium than exhibited in figure 4.2 left panel. Possibly, choosing ellipsoids in contrast to spheres as the intrinsic cell shape [92] may provide an alternative. Another possibility would be to use boundary-based models such as e. g. the extended Potts model [173], which however should be carefully adapted to cellular processes and has the disadvantage of using enormous computational resources due to the many degrees of freedom.

From the theoretical point of view, the model could be significantly improved by deriving a model valid for the two-body contact of objects that admits non-normal forces acting and does not underlie the constraints of only small deformations. In addition, for *in vitro* cell populations that are not fixed to a substrate, the effects of torque may become important. Furthermore, the effects of cell shape plasticity should be included to a greater extent. These refined theories however require much better experimental resolution than currently provided. It appears questionable whether centre-based models are able to cope with the increasing degree of complexity resulting from these improvements.

The basal layer has been approximated with a plane boundary condition in this article. As already mentioned in subsection 4.1, the basal layer is known to have a corrugated structure (see figure 4.1 left panel). This would significantly enlarge the region where water and nutrients are provided in abundance and thereby lead to a far greater cell reservoir that is able to start a proliferative response in case of injury. It may be speculated that this is one of the reasons that led to the emergence of ruffled basal layers the skin.

Technically, the stochastic elements within the simulations include the length of the individual sub-states of the cell cycle, the stochastic forces acting on single cells and the randomly chosen direction of mitosis. Note however, that though within the basal layer the direction of mitosis was chosen randomly, only the upper cell differentiated to a keratinocyte within the model. A more realistic model assumption would use a loss of contact with the basal membrane as a signal of keratinocyte differentiation. Such a model would first densely populate the basal layer with stemcells before building the epidermis. In general, these stochastic elements did not contradict the characteristic morphology of the epidermis. From the numerical point of view, they are necessary ingredients to avoid planar configurations that are unfavourable for the adjacency detection (compare subsection 2.3.2). From the biological point of view, it is interesting that the stochastic variation of the initial conditions of *in silico* melanocytes can lead to qualitatively different outcomes.

The dynamics of the nutrients and of water has been described with a reaction-diffusion approach here. However, due to the cellular movement, there will be an additional contribution by active transport that is completely neglected. To a first approximation, this effect (and others) may be absorbed into the apparent diffusion coefficient as is done in the experimental measurements. Note that the polarized structure of the cornified cells in the *stratum corneum* may give rise to non-isotropic diffusion, where

the diffusion coefficient is not a scalar value anymore.

The cell cycle has been approximated here by a small number of internal cellular states only. It may be questioned whether a subdivision into discrete substates makes sense. One may expect a much smoother reaction of the epidermis to the removal of all keratinocytes if transition into and out of G_0-phase would not depend on a threshold water concentration, but would be determined by transition probabilities that may continuously depend on the water concentration. This may be judged with quantified experimental data.

4.5   Realistic model extensions

Though in comparison to chapter 3, a more complicated system including some effects of tumour host competition has been studied, in addition to the shortcomings discussed before, further properties of the realistic system have been neglected. Many of these, for example tumour immune interactions, plasticity of tumour cell properties, tumour cell sensitivity to other diffusing factors than just nutrients etc., have been mentioned already in section 3.6. Several further processes occur in a realistic epidermis, some of these are summarized below:

- Healthy cells often require further environmental signals (such as e. g. contact with other cells or with a membrane) that must be continuously supplied. If the supply of these signals fails, these cells undergo apoptosis. This dependence on external signals is also investigated for proliferation in a theoretical model [174].

- In processes such as wound healing in epithelial sheets, active cellular movement has been observed [175].

- In reality, the epidermis can react as well to mechanical irritations that leave the *stratum corneum* intact with a proliferative response. This is not accomplished by the current model.

- The protective function of melanin [154] is not included in the model. Consequently, the effects of electromagnetic radiation cannot be studied.

Living organisms presumably host a plethora of interactions that are currently not even known. This number would be considerably constrained by an *in vitro* co-culture of the cell types encountered in the epidermis. If such an experimental system could be established, it could be used to study isolated mechanisms under better-defined conditions.

parameter	value	comment
ECM viscosity η	0.001 kg μm^{-1}s^{-1}	[76, 77]
adhesion energy density ϵ^{max}	0.0001 Nm m^{-2}	[88]
minimum anchorage ϵ^{min}	0.00001 pJ	
receptor loss rate α^{loss}	0.00001 s^{-1}	
tangential friction coefficient $\gamma_{\parallel}$	$0.1 \cdot 10^{12}$ N s m^{-3}	[76]
stochastic force coefficient ξ	$0.001 \cdot 10^{-6}$ kg m s$^{-3/2}$	$D = 0.0001$ μm^2 s^{-1}
keratinocyte M-phase duration $\tau^{(\text{m})}$	(1.0 ± 0.25) h	[77]
keratinocyte S/G$_2$-phase duration $\tau^{(\text{S/G}_2)}$	(5.0 ± 2.0) h	[77]
keratinocyte G$_0$-phase prolongation $\tau^{(\text{G}_0)}$	(138.9 ± 138.9) h	[162]
shortest observed keratinocyte cycletime τ^{min}	(15.0 ± 2.0) h	[77, 162]
pre-mitotic cell radius $R^{(\text{m})}$	5.0 μm	[165]
cell elastic modulus E_i	0.000750 MPa	[140]
cell Poisson ratio ν_i	1/3	[134]
melanocyte glucose uptake rate $\lambda_{\text{gluc}}^{\text{mel}}$	150.0 amol cell^{-1} s^{-1}	[139]
keratinocyte glucose uptake rate $\lambda_{\text{gluc}}^{\text{ker}}$	10.0 amol cell^{-1} s^{-1}	
critical water concentration $U_{\text{H20}}^{\text{crit}}$	90.0 %	[163]
critical glucose concentration $U_{\text{gluc}}^{\text{crit}}$	1.0 mM	[107]
water diffusivity $D_{\text{H}_2\text{0}}^{\text{strat.germ.}}$	1000.0 μm^2 s^{-1}	[166, 167]
water diffusivity $D_{\text{H}_2\text{0}}^{\text{strat.corn.}}$	0.2 μm^2 s^{-1}	[168, 169]
water boundary concentration $U_{\text{H20}}^{\text{bound}}$	100.0 %	by definition
glucose diffusivity $D_{\text{gluc}}^{\text{tiss}}$	256.0 μm^2 s^{-1}	[170]
glucose boundary concentration $U_{\text{gluc}}^{\text{bound}}$	5.0 mM	[171]
stemcell basal adhesion energy density ϵ^{basal}	$2\epsilon^{\text{max}}$	

Table 4.1: Parameters for the agent-based model of the epidermis. As far as possible, model parameters have been derived from independent experiments or they have been varied as fit parameters. Parameters not included in the table have been varied and are discussed separately in the text.

Chapter 5

Critical Reflections

5.1   Numerical algorithms

Several numerical algorithms have been used in this thesis. Being a compromise of algorithmic simplicity and execution efficiency, all of these algorithms can profit from further improvements. Evidently, to model realistic systems of a larger size, parallelisation of the algorithms [40] is of urgent interest.

The numerical tool of the Delaunay triangulation may be improved significantly both in terms of efficiency and numerical stability:

- The efficiency of the triangulation could be improved by using a different data structure based on faces and not on tetrahedra [27].

- In the evaluation of the orthosphere criterion (2.7) with adaptive precision arithmetics (compare appendix A.2) it is assumed that the vertices are in general position, i. e., planar configurations should not occur. If they do occur, the triangulation is reconstructed following slight perturbations of the vertex positions. For most realistic applications, one can expect stochastic effects to rule out these planar configurations. However, for these rare cases, the error-handling of the algorithm could be significantly improved. Thus, unnecessary reconstructions could be avoided.

- The flip algorithm presented in subsection 2.3.5 will fail if within a single timestep the trajectories of two balls intersect such that – in an intermediate flipping configuration – a ball is covered by another one. In such a case, the intermediate spatial steps arising from equation (2.15) become infinitely small and the error-handling performs a complete reconstruction of the triangulation with all positions updated. Though it turned out, that with an adaptive timestep

such situations are reduced to rare exceptions, a more efficient approach would simply delete the corresponding balls at their old position and insert them at their new ones. This would contribute to avoid unnecessary reconstructions. In addition, the modification of the cell-cell interactions in equation (2.73) does not completely rule out overlapping balls but makes them highly improbable. Note that a smaller value for the divergence point (e. g. $x_d = 1 + R_{\min}/R_{\max}$) in this correction would conflict with the present implementation of mitosis.

- For some applications, it may be necessary to calculate the set intersection of Voronoi volume and sphere volume as defined in equation (2.77). Though currently a Monte-Carlo approach for the calculation of such volumes is provided, an efficient numerical routine is still missing.

The discretisation of PDEs with the discrete element method (DEM) is numerically stable under well-defined conditions. However, based on DEM, the algorithms may still be improved significantly:

- The size of sparse linear systems such as equation (B.1) strongly influences the computation time necessary for their iterative solution. Currently, the boundary conditions on the PDE are implemented as separate equations. With an efficient algorithm that could use time-dependent boundary conditions to reduce the dimension of the system one could considerably decrease the computational time for obtaining a solution, compare figure B.1 left panel.

- In the full solution of equation (2.36) with the method of biconjugate gradients, currently no preconditioning beyond the inverse of the diagonal is used. The general matrix structure of these equations suggests, that the use of the side diagonals for preconditioning might improve convergence.

- In order to calculate a continuous gradient of concentration in RDE problems, a spline function of higher order than the linear interpolation in equation (3.8) must be used (compare subsection 3.2.2), since the chosen tri-linear interpolation is not continuously differentiable.

The numerical solution of the cellular equations of motion (2.86) has been performed using a first-order scheme that used an adaptive timestep (compare appendices C.2.1 and C.2.3). This approach may be improved significantly as well:

- The order of the numerical scheme could be increased by using Runge-Kutta methods [68], but these require intermediate recalculations of the forces (and thus, an intermediate update of the Delaunay triangulation). This drawback is not displayed by predictor-corrector methods [176] that require the maintenance of a history of the dynamics instead. However, these methods may fail if the involved forces are not continuous (as for example in the present implementation of mitotic separation forces).

- At present, the timestep used in the adaptive scheme is reduced simultaneously for all particles (cells) in the simulation as soon as too large spatial stepsizes are encountered. This is also the case if the maximum spatial stepsize has been exceeded in a small region only. Therefore, the efficiency of the numerical solution can be increased by using timesteps that are individualised to every single cell. However, such a scheme must not exhibit artifacts.

5.2 Underlying models

Different models for cell-cell and cell-medium interaction have been introduced for the agent-based approach within this thesis. Inevitably, these models cannot grasp the full spectrum of the interaction properties:

- As discussed in subsection 2.5.2, the chosen JKR interaction model has many shortcomings. It would be interesting to derive a fundamental theoretical contact model that incorporates viscous and plastic effects under the influence of normal and shear forces. Thus, the effects of friction could already be included as well. Such a model should be derived from a microscopic model (e. g. tensegrity) and should be verified experimentally. For the numerical solution, such a model could then be replaced by a simpler mechanical network as well, where the parameters have been adjusted such that the dynamics of this network resembles the full theoretical model.

- To model active and possibly random forces exerted by eucaryotic cells using *filopodia*, *lamellipodia*, or *pseudopodia* [96], the dynamics of these cellular projections should be understood. For passive random movement, the stochastic forces should in reality differ considerably in solution and in dense tissue. Consequently, at the interface of solution and dense tissue, the isotropy of the stochastic forces should be abandoned in a realistic model.

- For strongly compressed tissue, the involved forces will be large and the overdamped approximation in equation (2.86) may not apply anymore. If acceleration is included in the equations, the dimension of the system (2.86) will double, but the same general techniques could be applied. For example, in the case of MTS, the assumption of pressure relaxation within the fluid phase may not be valid *in vivo*, as it is known from surgery that excised tumours may be under strong pressure. The influence of the extracellular pressure distribution on the cell kinetics [111, 115] should be included in these cases.

In addition to the last item, further model limitations apply to the PDE model presented:

- As has already been discussed, the description of the cell dynamics by positive-definite diffusion does neglect the attractive part of cellular adhesion. The approximate analytic form of a realistic effective diffusion coefficients could well be derived from comparisons with an agent-based modelling approach including repulsion and adhesion, if experimental data are not available.

- If corresponding experimental data become available, it would be interesting to analyse the cell cycle distribution in an extended continuum approach as well.

The simple model of calculating the distribution of nutrients with RDEs is quite limited:

- If pressure differences exist, this would imply fluid flow and the assumption that the nutrients are transported using pure diffusion would have to be discarded.

- Depending on the culturing conditions of the tumour spheroids, the boundaries of the spheroids should be treated as time-dependent Dirichlet boundary conditions in well-stirred growth media.

- In all modelling approaches, the simple assumptions of constant cellular uptake rates should be improved by comparing with experimental observations on a single well-defined model cell line. This could for example be achieved by employing the Michaelis-Menten kinetics (3.6) for the nutrient uptake rates. As a further advantage, this would directly preserve positive definiteness of the RDE for the nutrient concentrations.

5.3   Data Improvements

The quantitative experimental signature used in this thesis is too weak to falsify the proposed models or to determine model parameters with acceptable certainty. However, the present work can well be interpreted as a feasibility study on large-scale simulations.

Specifically for the continuum approach applied to multicellular tumour spheroids it turned out that due to the moderate computational demands of the PDE model under spherical symmetry, the multi-dimensional fitting procedure is well applicable. The conclusions drawn from the best-fit parameters would benefit greatly if the experimental data contained error estimates. Then, an estimate on the error of the parameters can be extracted from the fitting procedure as well. With such data, the current continuum model could well have been falsified.

Consequently, to reduce the number of mathematical models currently available, new experiments should be carried out. Multicellular tumour spheroids constitute a popular experimental model system

already and seem under reasonable experimental control. It seems therefore promising to analyse the growth dynamics of multicellular spheroids on a single (well-defined) cell line. In such an experiment, the culturing conditions could be varied as in [107] and in addition, the cellular response to growth inhibition could be studied in line with [106]. The data (including relative distribution of cells in the cell cycle, total cell number, quantitative morphologic data with error bars) could be studied with spherically symmetric continuum approaches that also account for the cellular dynamics [66, 111, 115] to extract information on nutrient uptake rates and necrosis- or growth-inhibition inducing mechanisms.

Having established parameters (with estimates on their uncertainties), these may be used in agent-based models to analyse the additional effects that arise from the discreteness. Since stochastic effects seem to be of great importance in the discrete simulations in the epidermis, one should aim at deriving probabilistic statements of the discrete effects. In comparison with experiments it remains then to be seen whether tissues display Emergence or not. The other way round, continuum models can profit from agent-based approaches by incorporating effects arising from discreteness.

The models in this thesis produce a large variety of experimental signatures, not all of which could be thoroughly discussed here. In table 5.1, different proposals for the experimental falsification of these model predictions are summarized.

5.4 Limits of Current Theoretical Biology

Theoretical Biology is an interdisciplinary science. Its strongest contributions arise from biology and mathematics. This remains valid for its strongest limitations as well.

Biology has contributed detailed observations on natural phenomena and is now evolving from a qualitative empirical science to a quantitative science within which hypotheses can be accepted or rejected with confidence levels. This process has not been completed up to now. Even in modern experiments, where error estimates on a defined confidence level are included, the measured quantities underlie large variations. Historically, this has made it difficult for the quantitative scientific method to be established in biology. These large variations have several reasons:

Firstly, it is very difficult to keep biological material under good experimental control. Empirically, specimens collected in nature are not identical and their antecedent is not known. But for *in vitro* experiments this is not different: Apart from intrinsic genetical differences, one has so far not been able to establish defined initial and boundary conditions in the experiments. For example, the metabolic needs of cells in culture are not completely understood such that the growth medium used in many *in vitro* experiments has to be prepared or extracted from existing biological systems [98, 107, 139],

proposal	reference
In the initial growth phases of monoclonal MTS, the model predicts oscillations within the occupation numbers of the cell cycle substates. This relative distribution of cells in the cell cycle could be measured by staining methods to falsify the model.	chapter 3 figure 3.4
Both the agent-based model and the continuum approach make quantitative predictions about the sizes of the spheroids and the nutrient distribution.	figure 3.5 figure 3.6 figure 3.7
In the model for the epidermis, tape stripping events lead to a synchronisation of the cellular proliferation, which could be observed by staining methods afterwards.	figure 4.4 top left panel
By measuring the proliferative response to successive tape-stripping experiments, information about the time spent in the G_0-phase can be gained.	figure 4.4 top right panel

Table 5.1: List of proposals for the falsification of predictions made by agent-based models. The proposals are ordered by the occurrence of the corresponding discussion in this thesis.

which are under limited control only. Hopefully, improved control on culture conditions will be gained in future.

Secondly, most biological systems above the protein level underlie large intrinsic variations, as for example two cells are never identical. Since many current measurement techniques are invasive, measured quantities have to be averaged over a whole ensemble of not completely identical constituents. The origin of these variations is not entirely genetic, as even organisms with identical genotype may express different phenotype. In fact, if one includes the DNA of our suspected endosymbiotes – the mitochondrions that occur in eucaryots – into the definition of the genotype, the variance in the genotype becomes even larger. In addition, the time-dependent internal cellular state of expression and transcription will determine the cellular behaviour. Knowledge of this internal state would require information about spatial distributions of proteins within the cell. Still, using less invasive measurements in combination with an improved control of experimental conditions would enable a time-average performed on single individuals, which would reduce the intrinsic uncertainties. However, the results obtained from such measurements could not directly be transferred to other individuals. In addition, having medical applications in mind, one should rather be interested in real-world scenarios. In conclusion, it should be accepted that this second source of error will not be definitely eliminated.

Mathematics alone is a science that examines self-made abstract structures for their properties and patterns. It is the field of applied mathematics, which analyses correspondents of these abstract structures in reality. Impressive success of applied mathematics in many natural sciences – especially in physics – has even put up the philosophical question whether mathematics provides a model of the world or whether the world is just a realisation of an abstract mathematical model. Independent of the philosophical outcome, there is the strict requirement that mathematical models must yield conclusions that are consistent with experimental observations and predictions that can be falsified in future experiments.

The questions that can be answered with current scientific means are a lot simpler: It is established that biology can profit from the use of mathematical methods for the analyses of experiments, but possibly one can use mathematics for more. As discussed before, modern experiments are expensive and often under poor control. An abstract mathematical model has the potential to perform *in silico* experiments at a fraction of the costs and under complete control. The method of mathematics to study abstract structures has brought great advantages, since mathematicians do not have to struggle with the pains of everyday life. However, this tendency to abstraction can turn fatal in the sense that scientific benefit is lost when predictions of mathematical models cannot be falsified in reality. In such a case, the effort invested in mathematical modelling is a glass bead game [177].

Within the plethora of mathematical models that already constitute a universe, one has to identify

the subset that is intrinsically consistent and within this subset, the models that are consistent with current experimental data and make differing predictions are of special interest. Models that do not make falsifiable predictions cannot contribute to scientific progress.

Chapter 6

Summary

It has been possible to create previously not existent software that meets the computational requirements of off-lattice agent-based model approaches. This included the creation of a triangulation for adjacency detection and the numerical implementation of algorithms for the solution of reaction-diffusion equations. For specific examples it has been demonstrated that the tool of weighted kinetic and dynamic Delaunay triangulations can be used in off-lattice agent-based cell tissue simulations for adjacency detection. The presented implementation is able to calculate the specifics of a weighted Voronoi tessellation such as contact surfaces and volumes. The method allows for interesting extensions such as a consistent concept of volume calculation in cellular tissues. The tool has been applied to off-lattice agent-based simulations in the case of multicellular tumour spheroids and epidermal tissue.

With simplifying assumptions on cellular interactions and cellular nutrient uptake rates, the model could reproduce experimental growth curves on multicellular tumour spheroids. An even simpler continuum approach has been able to reproduce these experimental growth curves as well. Owing to missing quantitative data on tissue morphology and limited quality of experimental data sets, one could not distinguish between the two models on this level. Beyond the simple growth curves, the agent-based model exhibits more physiological properties than the analogous continuum approach. For example, initial oscillations within the relative occupation of the cell cycle states should be observable in small and monoclonal spheroids.

For epidermal tissue, the model has qualitatively reproduced simple key features of a realistic evolution. For the smaller cell numbers considered in this system, the equations of motion could be treated with less approximations. In particular, a suspected control mechanism for epidermal homeostasis, where the extracellular water concentration influences the proliferation rate, has been tested using an agent-based model. The resulting homeostasis was stable against perturbations such as removal of

the *stratum corneum*. The consequences of a varying basal adhesion of cancerous melanocytes were found to be strongly interlinked with the balance between melanocyte and keratinocyte proliferation rates. In addition, it turned out that for the initial (avascular) growth phases of melanoma stochastic effects are very important within the model, in particular the stochastic variation of the initial environment. The model predicts a cone-like (and dynamically changing) diffuse shape of melanoma in pre-clinical stages.

Though the kinetic and dynamic Delaunay approach constitutes a great benefit for off-lattice agent-based approaches, the disadvantage of strong computational demands persists. In addition, it turns out that the vast amount of information produced by agent-based models currently misses sufficiently quantified experimental signatures for falsification. Consequently, the current experimental signature does not suffice to fix the parameters of the theory with sufficient accuracy. Nevertheless, different mechanisms could be tested for consistency with realistic tissue dynamics within the *in silico* models.

Appendix A

Delaunay triangulation

A.1 Expected algorithmic scaling

A theoretical analysis on the expected algorithmic complexity of the construction algorithm of sub-section 2.3.6 is provided in [29]. In order to determine the overall performance of the triangulation code, the CPU time necessary for the construction of the triangulation has been recorded for different numbers of randomly-distributed vertices. To exclude time delays arising from disconnected vertices in the triangulation, all weights have been set to zero. For randomly distributed vertices, the expected average total algorithmic complexity can then be deduced as follows: A first contribution results from the stochastic visibility walk [46], where the length of the hopping path – measured in units of passed simplices (which in average scales as the number of vertices) – can in three dimensions be expected to scale as $N^{1/3}$. For randomly distributed points, this is well fulfilled (compare figure A.1 right panel). A second contribution arises from updating the triangulation using either the Green-Sibson or the Bowyer-Watson algorithms. If the vertices are not in an extreme configuration (which can be expected for randomly distributed data), this contribution to complexity will in average be constant. To obtain the total complexity of Delaunay construction, one has to integrate over the two contributions, which yields the scaling $\alpha N^{4/3} + \beta N$, where N is the final number of vertices (compare figure A.1 left panel).

Since for realistic applications in adjacency detection a complete reconstruction of the triangulation will require too much time, especially the times necessary for restoration of the Delaunay criterion after slight vertex movements will be of interest (see figure A.2). It turns out that this time scales linearly with the number of vertices and provides an advantage in comparison to complete reconstruction of the triangulation.
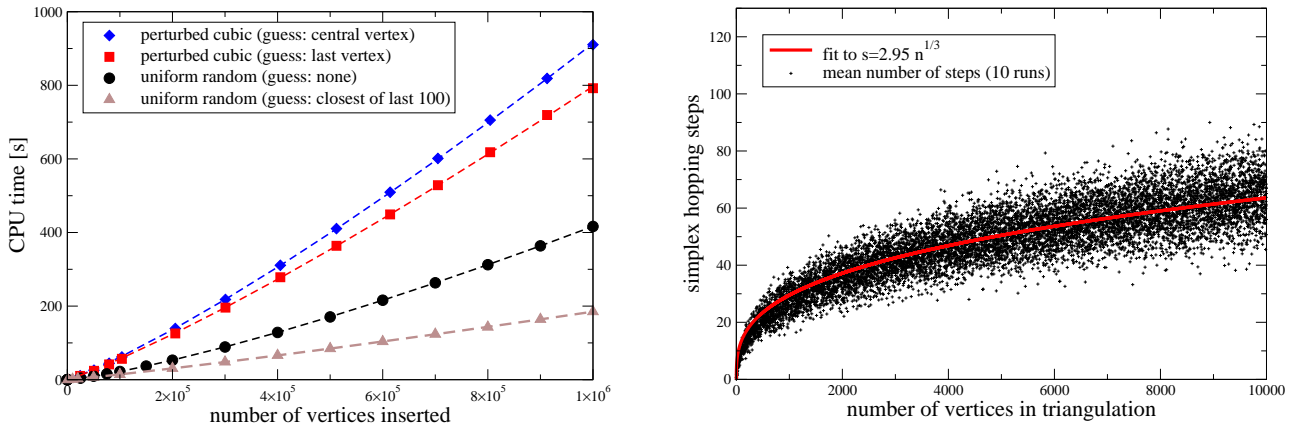
Figure A.1: Algorithmic scaling for the total Delaunay construction and the visibility walk [26]. **Left:** CPU times necessary for the tetrahedralization of different point numbers (unweighted case) for different distributions. Dashed lines are fits to the expected overall algorithmic complexities $\alpha_i N^{4/3} + \beta_i N$. Cubic lattices are known to produce many flat simplices (slivers). In the case of the points distributed on perturbed lattices, the cost of the simplex location can be reduced by giving a good first guess. In the case of randomly distributed points, the walk in the triangulation can be considerably shortened by choosing a better guess for a starting simplex. **Right:** The number of necessary steps starting from an arbitrary simplex in the triangulation towards another arbitrary simplex scales for uniformly distributed points in three dimensions as $n^{1/3}$. Note that number of steps necessary for a specific location may vary considerably, as each data point resembles the mean out of ten runs.
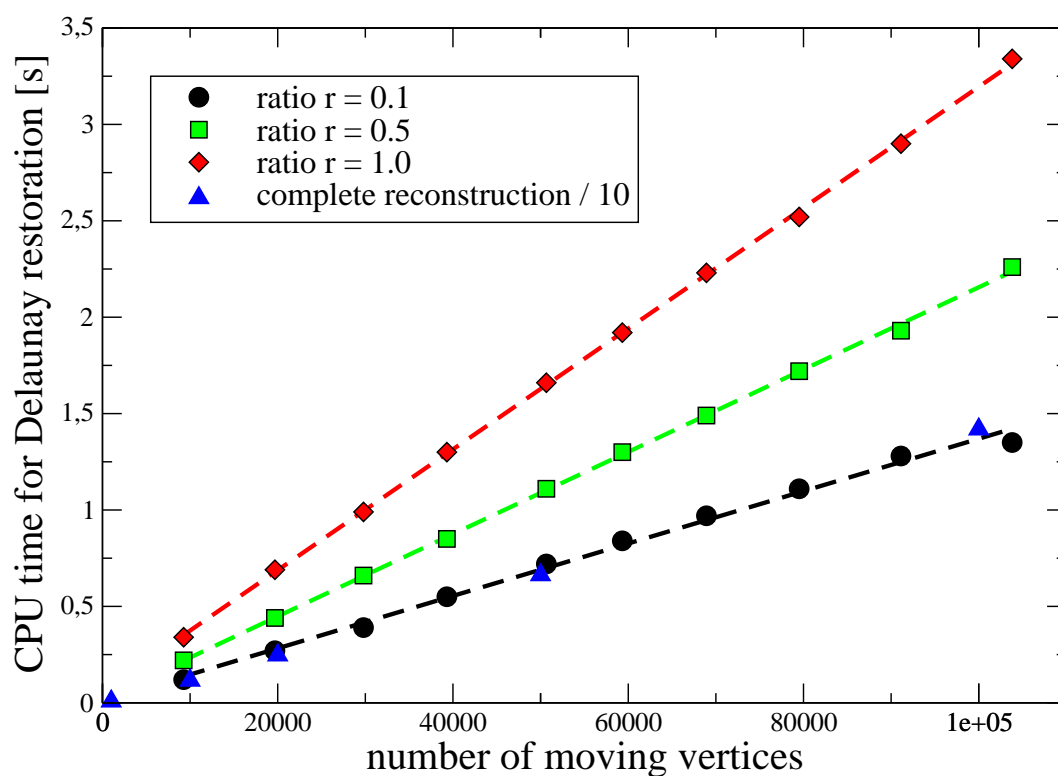
Figure A.2: CPU times necessary for the restoration of the Delaunay criterion [26]. The times have been obtained after vertex movement for different relative step-sizes defined by the ratios $r = m/d_{min}$ (step size over the minimum distance). The expected linear relation (dashed lines correspond to linear regressions) is found with slopes increasing with the step size. In the ideal case, this update method is about 20 times as fast as computing a new triangulation. Here, for a ratio of $r = 0.1$ the flip restoration method is by a factor of 10 faster in comparison to complete reconstruction. Blue symbols correspond to the black curve in figure A.1.

points	deletions (total)	insertions (total)	flips (total)	CPU time per timestep [s]
20000	59	41	426	0.26
40000	51	49	1098	0.54
60000	52	48	2067	0.84
80000	46	54	2749	1.15
100000	42	58	3521	1.47
120000	47	53	5154	1.81
140000	62	38	6297	2.14
160000	56	44	7207	2.49
180000	50	50	7918	2.84
200000	49	51	9766	3.21

Table A.1: Mixed performance of the triangulation for different numbers of vertices. In every run, 100 timesteps have been performed. In each timestep, with probability $p = 1/2$ either an old vertex was deleted or a new vertex was inserted into the triangulation (second and third columns). Then all the vertices were moved by a small amount (corresponding to a fraction of $r = 0.1$ in figure A.1) and the flips necessary to restore the Delaunay criterion have been counted – the fourth column does not include the flips necessary for the deletion process.

Within the context of cellular tissue, a simulation must be able to cope with a varying number of kinetic vertices. For this case, the performance of the combined algorithms on vertex insertion, vertex deletion and vertex movement is of interest. In table A.1, for different numbers of uniformly distributed vertices 100 time steps have been performed. In each time step, with probability $p = 0.5$ an arbitrary vertex was deleted from the triangulation and with probability $p = 0.5$ a random vertex was inserted. Afterwards, all the vertices were slightly displaced followed by the restoration of the Delaunay criterion. The resulting computation time increases in average linearly (see table A.1).

For the actual runtime of an application, evidently the additional computing time required by the application will be important. This will heavily depend on the analysed interactions, but sometimes an estimate of the mean number of expected interactions may be of use. For the example of MTS, compare chapter 3, the distribution of the number of next Delaunay-neighbours is given in figure A.3, where from the Delaunay triangulation in average 14 neighbours can be expected. In the logarithmic plot in figure A.3 it becomes visible that the number of highly connected vertices exceeds the normal distribution. This behaviour is not due to the existence of cavities within the tumour spheroid, as it is found for spheroids right at the onset of necrosis (not shown) as well. Note that only a subset of this number contributes to actual interaction forces, as adjacency in the Delaunay triangulation does not necessarily imply a spherical overlap.
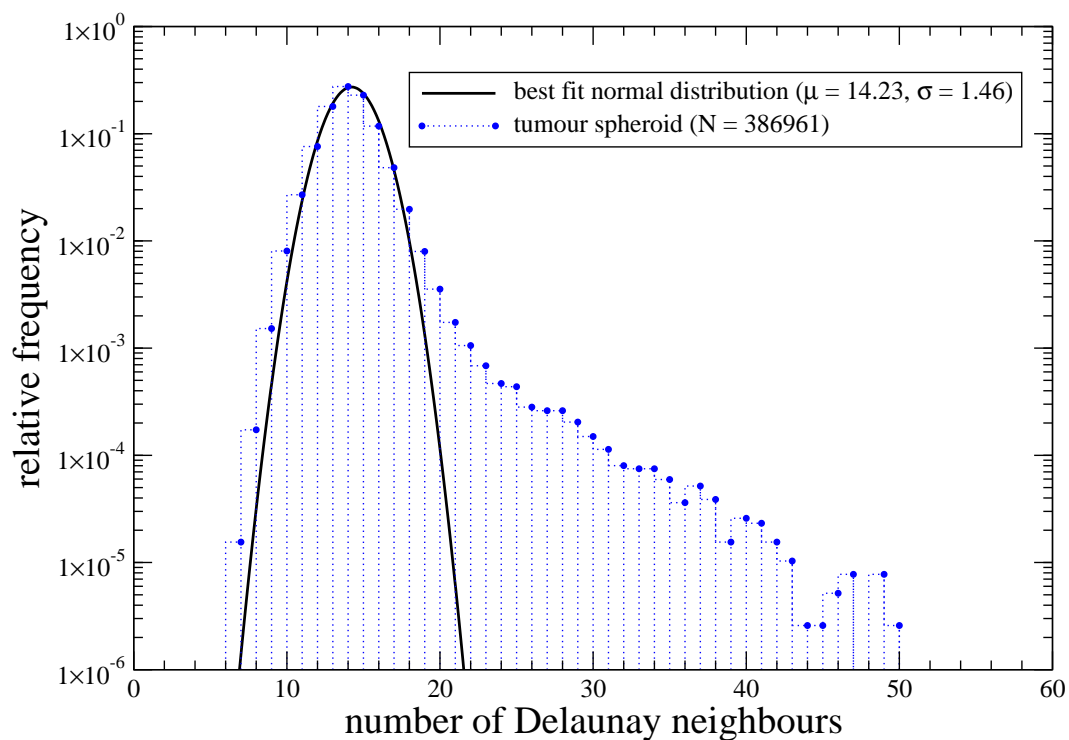
Figure A.3: Relative frequency of the next neighbours in *in silico* MTS. For a large tumour spheroid (grown at 0.28 mM oxygen and 16.5 mM glucose concentrations, compare figure 3.5), the relative frequency of occurrence is displayed versus the number of next Delaunay neighbours in a logarithmic plot. The cell sizes were allowed to range from $5 \cdot 2^{-1/3}$ μm to 5 μm. The histogram (blue circles) is well fit by a normal distribution with mean 14.23 and width 1.46 in the region of less than 20 Delaunay neighbours. This deteriorates rapidly for larger connectivities.

A.2   *Adaptive Precision Arithmetics*

In modern computers, floating point variables are usually stored by a sign bit, p significant bits, and some bits describing the exponent of the number. For example, in the common IEEE-standard [67] the 64 bits required to store a **double** variable x, consist of a single bit to store the sign of the mantissa, $p = 52$ bits to store the most significant bits of the mantissa, a single bit to store the sign of the exponent, and the remaining 10 bits are used to store the exponent

$$x = \pm \times \underbrace{bb\ldots bbb}_{p=52} \times 2^{\pm \overbrace{bb\ldots bb}^{10}}. \tag{A.1}$$

Numerical roundoff error may occur, when the p significant bits do not suffice to store all information. For example, for adding the numbers 118 and 3 in binary representation with $p = 6$ one obtains

$$1110110 + 11 = 1111001 \approx 1111000. \tag{A.2}$$

This however would require 7 significant bits, and thereby the last bit is lost. Numerical roundoff may occur for all basic operations. A simple way to circumvent this would be to use a much larger (or variable) number of significant bits. This however would considerably decrease the efficiency of all operations – and be superfluous most of the time. The adaptive approach is based on the idea of representing a number by several other numbers via an expansion [39]

$$x = x_n + x_{n-1} + \cdots + x_2 + x_1, \tag{A.3}$$

where

- the x_i are ordered such that x_n is largest and

- the expansion is non-overlapping in the sense that the least significant bit of x_{i+1} is more significant than the most significant bit of x_i.

The above expansion is not unique (consider, for example, $1110110 = 1110000 + 100 + 10 = 110000 + 110$), but due to the second condition, all expansions fulfil that x and x_n have the same sign. This is especially interesting for geometric predicates such as the computation of an orthosphere criterion in equation (2.9). The determinants can be expanded as described in [39] (compare [27, 40]) such that an order by order evaluation is possible.

Appendix B

Large Sparse systems

B.1   Sparse Matrix Storage

A problem often encountered in the numerical solution of fundamental equations is the inversion of large matrices, i. e., a problem of the form

$$A_{ij}x_j = b_i \qquad \text{or} \qquad A\boldsymbol{x} = \boldsymbol{b}\,, \tag{B.1}$$

where the b_i on the right hand side as well as the matrix elements A_{ij} are known and the values x_j ought to be found. The usual procedure of computing the inverse of A is not always practical for numerical purposes, which is especially true for larger dimensions of A. For most systems encountered in this thesis the full matrices would not even fit into computer main memory. Fortunately however, most matrix elements vanish identically for these problems and thus need not be stored (compare figure B.1). For the numerical calculations, the row-indexed sparse storage mode as provided in [68] has been used, which is summarized below.

To store an $N \times N$ matrix of type **double**, a vector of type **double** SA and another vector of type **unsigned int** IJA are created. Then the matrix entries of A are saved in SA and IJA as follows:

1: store the N diagonal entries of A in the first N locations of SA,
2: store the off-diagonal values of A at locations $\geq N + 1$ in SA, ordered by rows and – within each row – by column,
3: set location 0 of IJA to $N + 1$,
4: store the index of SA that stores the first off-diagonal element of the corresponding row in the first N locations of IJA
5: store the column number of the corresponding element in SA in IJA at location $N \geq N + 1$.
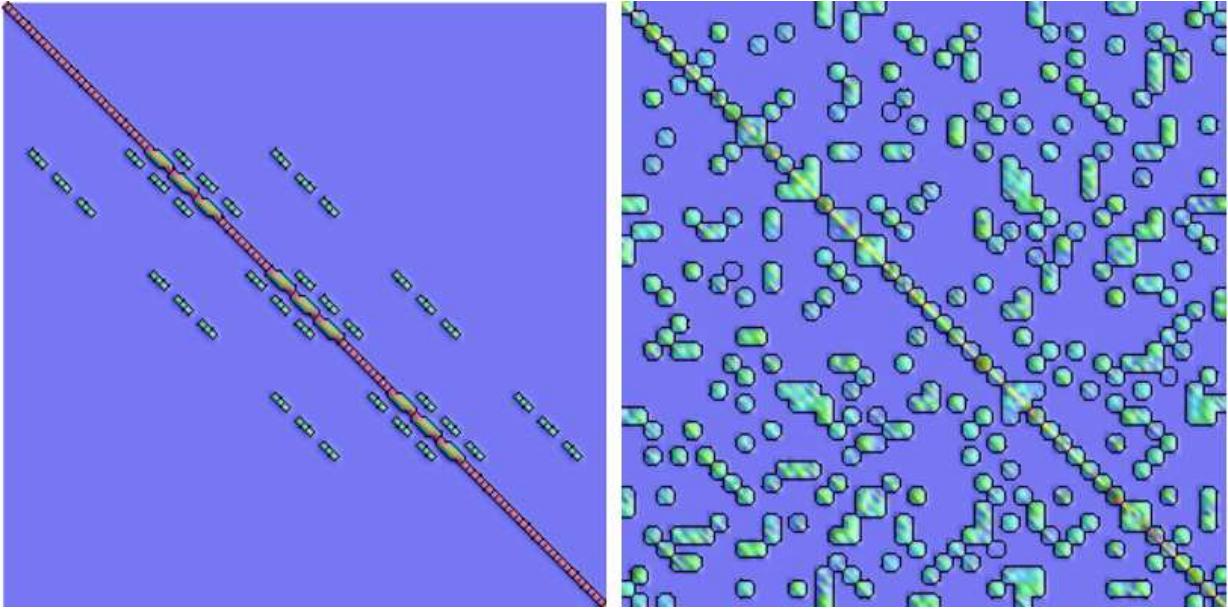
Figure B.1: Distribution of matrix entries for typical linear systems in this thesis. Non-vanishing entries are surrounded by black lines, whereas colours indicate the absolute value of the matrix elements ranging from blue (vanishing) to red (large). Usually, the systems considered are much larger than the examples displayed, which necessitates a sparse storage scheme. **Left:** Typical matrix occupation for a three-dimensional cubic Poissonian problem (here on a $5 \times 5 \times 5$ grid leading to a 125×125 matrix) with Dirichlet boundary conditions. In three dimensions, there are 6 off-diagonal entries for internal grid nodes, compare also equation (2.30). Note that due to the Dirichlet boundary conditions, the boundary nodes do not have off-diagonal entries. **Right:** Typical matrix occupation for equation (2.86) for a system of 46 cells (leading to a 138×138 matrix). The corresponding linear system is symmetric, which enables one to increase the efficiency of storage and calculation further. Since only tangential friction has been considered here ($\gamma_\perp = 0$), the aligned sub-structures in the coloured regions simply reflect the diagonal dominance of the 3×3-dimensional tangential projection operators $\mathcal{P}^{\alpha\beta}_{ij,\parallel}$. Different numbers of off-diagonal blocks correspond to different numbers of neighbouring cells with an overlap, and the different degree of colour saturation in the off-diagonal blocks reflects the varying contact surface. Note that as the system becomes larger (compare figure A.3), the average number of off-diagonal entries will hardly change, such that the degree of sparseness increases.

This storage scheme does have the small overhead of storing vanishing diagonal elements, which is negligible for large systems. The efficient sparse storage scheme has the additional advantage, that matrix-vector multiplications can be performed by using much less operations [68]. For example, the matrix

$$M = \begin{pmatrix} m_{11} & 0 & m_{13} & 0 & 0 \\ 0 & m_{22} & 0 & 0 & 0 \\ m_{31} & m_{32} & m_{33} & m_{34} & m_{35} \\ 0 & 0 & 0 & m_{44} & m_{45} \\ 0 & 0 & 0 & 0 & m_{55} \end{pmatrix}$$

(B.2)

would be stored in the arrays as

index k	0	1	2	3	4	5	6	7	8	9	10	11
IJA[k]	6	7	7	11	12	12	2	0	1	3	4	4
SA[k]	m_{11}	m_{22}	m_{33}	m_{44}	m_{55}	$\times$	m_{13}	m_{31}	m_{32}	m_{34}	m_{35}	m_{45}

.

For symmetric or anti-symmetric matrices this scheme can be made even more efficient by storing only the entries on one side of the diagonal. This must be taken into account when implementing matrix-matrix or matrix-vector multiplication numerically.

B.2 Conjugate Gradient Method

Since the inverse of a sparse matrix is not necessarily sparse itself, the inversion of the $N \times N$ linear system (B.1) is usually not an option. However, if the matrix A is symmetric, the solution of (B.1) is equivalent to minimizing the function

$$f(x) = \frac{1}{2} x^{\mathrm{T}} A x - b^{\mathrm{T}} x .$$

(B.3)

For this problem, A has to be referenced by multiplication only, so there is no need for actual matrix inversion. Therefore, any iterative algorithm can be combined with the sparse storage scheme introduced before in appendix B.1. In addition, it should be noted that since equation (B.3) is a quadratic form, it will have a single global minimum – provided that A is positive definite. Therefore, the possibility of finding local minima does not exist. For sparse matrices, a popular algorithm is the Conjugate Gradient Method, for an introduction see e. g. [68, 178]. The convergence time of the algorithm can be improved by using the following trick: Equation (B.1) can be rewritten as

$$(MA) x = M b ,$$

(B.4)

where $MA \approx \mathbb{1}$. The inverse M^{-1} is then called a preconditioner. If one replaces M by the identity matrix, one reverts to the ordinary method of conjugate gradients. A better ansatz for the matrix M are the diagonal entries of A, if A is diagonally dominated. Being used in combination with preconditioning, the algorithm of conjugate gradients can be summarized as follows:

1: choose a starting point $\boldsymbol{x}^{(0)}$ and set $i = 0$

2: compute $\boldsymbol{r}^{(0)} = \boldsymbol{b} - A\boldsymbol{x}^{(0)}$ {the initial residual}

3: **repeat**

4:     $i = i + 1$ {count iterations}

5:     set $\boldsymbol{z}^{(i-1)} = M^{-1}\boldsymbol{r}^{(i-1)}$ {apply preconditioning}

6:     set $\rho_{i-1} = \boldsymbol{r}^{(i-1)} \cdot \boldsymbol{z}^{(i-1)}$

7:     **if** $i = 1$ **then**

8:         set $\boldsymbol{p}^{(1)} = \boldsymbol{z}^{(0)}$ {the initial direction}

9:     **else**

10:        define $\beta = \rho_{i-1}/\rho_{i-2}$

11:        set $\boldsymbol{p}^{(i)} = \boldsymbol{z}^{(i-1)} + \beta\boldsymbol{p}^{(i-1)}$ {the new direction}

12:    **end if**

13:    set $\boldsymbol{q}^{(i)} = A\boldsymbol{p}^{(i)}$

14:    define $\alpha = \dfrac{\rho_{i-1}}{\boldsymbol{p}^{(i)} \cdot \boldsymbol{q}^{(i)}}$

15:    set $\boldsymbol{x}^{(i)} = \boldsymbol{x}^{(i-1)} + \alpha\boldsymbol{p}^{(i)}$ {the new solution}

16:    set $\boldsymbol{r}^{(i)} = \boldsymbol{r}^{(i-1)} - \alpha\boldsymbol{q}^{(i)}$ {the new residual}

17: **until** convergence reached. {for example $\left\|\boldsymbol{r}^{(i)}\right\| \leq \varepsilon\left\|\boldsymbol{r}^{(0)}\right\|$ or $\left\|\boldsymbol{r}^{(i)}\right\| \leq \varepsilon\|\boldsymbol{b}\|$ for some $\varepsilon < 1$}.

In theory, i. e., when numerical roundoff errors are neglected, the algorithm converges (exactly vanishing residual) after n iterations, with n being the dimension of (B.1) [68, 178]. In practice however, the algorithm might not terminate, since due to numerical roundoff errors an exactly vanishing residual is never reached. Thus, it is appropriate to set up some error criterion above the numerical roundoff threshold which the algorithm should reach. Evidently, if (B.1) describes the temporal evolution of a physical problem, i. e., if $\boldsymbol{x}$ contains the time derivative of a physical quantity, the starting point for computing the solution at time $\boldsymbol{x}(t + \Delta t)$ can be chosen as the solution of the problem at time $\boldsymbol{x}(t)$. This procedure has been applied to equation (2.86). It is visible that for this problem 3×3 blocks occur on the diagonal, i. e.,

$$A = \begin{pmatrix} (A_1) & \dots & \dots \\ \dots & \ddots & \dots \\ \dots & \dots & (A_n) \end{pmatrix}, \tag{B.5}$$

see also figure B.1 right panel. In this case, the inverse of the block-diagonals

$$M^{-1} = \begin{pmatrix} (A_1)^{-1} & \mathbb{O} & \mathbb{O} \\ \mathbb{O} & \ddots & \mathbb{O} \\ \mathbb{O} & \mathbb{O} & (A_n)^{-1} \end{pmatrix} \tag{B.6}$$

can be applied as a preconditioner to improve convergence of the algorithm. For large systems, using a preconditioning matrix becomes contributes significantly to the convergence of the algorithm, compare figure B.2. There it becomes evident that even for large cell numbers, the conjugate gradient algorithm converges in reasonable time. It can be improved by using a good initial guess for the solution $x^{(0)}$, such that the method is suitable for large-scale simulations. The general problem in the computational demands will then rather shift to the globally adaptive timestep that will be forced to small values by only few cells that are subject to strong forces.

The ordinary method of conjugate gradients is only suitable for symmetric and positive definite matrices as occur for example in equation (2.86). For more complicated matrices, the biconjugate gradient algorithm as discussed and provided with the routine **linbcg** in [68] can be used.

B.3 Array referencing

For problems in more than one spatial dimension, it is numerically more favourable to store spatially discretised quantities on a rectangular lattice within a single array that is accessed using an indexing function. Within this thesis, in three dimensions the index function

$$I_{ijk} = \left(kM_y + j\right)M_x + i, \tag{B.7}$$

has been used, where i, j, and k are the indices of a grid node, and $M_{x/y} > 1$ denote the maximum number of grid nodes in x or y direction. Partial differential equations containing derivatives can thus be discretised and thereby reduce to a sparse linear system of the form $Ax = b$, where x contains the unknown quantity that is described by the PDE and the matrix A contains the geometric information of the chosen discretisation. The partial derivatives contribute to the matrix elements of A. Thereby, the order of the matrix elements depends on the chosen index function I_{ijk}. For the index function given above, the derivatives occur in the order as given in table B.1. At the boundaries of the reaction volume however the derivatives cannot be expressed in a centred way: Then, for first order derivatives the corresponding prefactor should be multiplied by two and the matrix element corresponding to the index outside the allowed interval should simply be added to the diagonal of A.
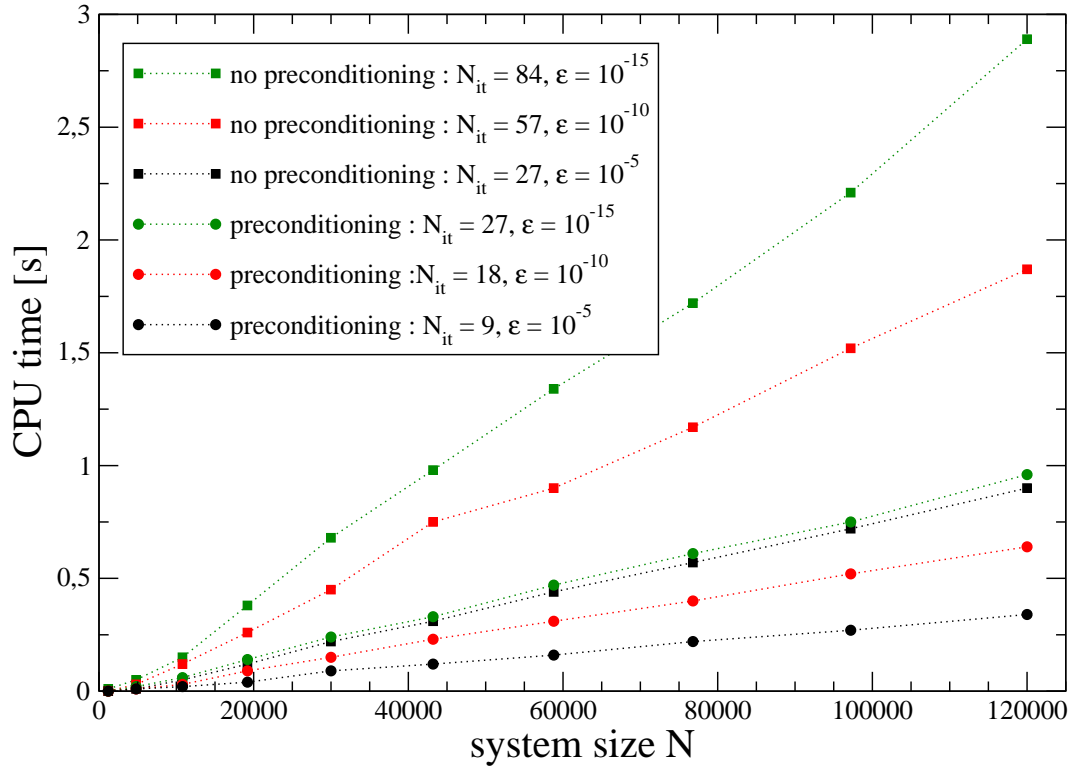
Figure B.2: Performance of the conjugate gradient algorithm. Shown is the CPU time for different sizes N of an $N \times N$ system in equation (2.86). There, a system size of N corresponds to $N/3$ cells. For the displayed regime, the average number of next neighbours per cell becomes independent on the system size, such that the number of iterations (maximum N_{it} displayed) is approximately constant. The linear increase in computing time solely results from the (likewise linearly scaling) number of non-vanishing matrix elements. Note that in this example, preconditioning reduces the number of necessary iterations by about a factor of three, with directly results in the corresponding improvement of the CPU time. To obtain identical conditions, as the initial guess for the solution $x^{(0)} = 0$ and as termination criterion $\left\| r^{(i)} \right\| < \varepsilon \left\| b \right\|$ (Euclidean norm) have been used.

derivative	Δi	Δj	Δk	$I_{i+\Delta i, j+\Delta j, k+\Delta k}$	prefactor
$\partial_y \partial_z$	0	-1	-1	$I_{ijk} - M_x M_y - M_x$	$+(4\Delta y \Delta z)^{-1}$
$\partial_x \partial_z$	-1	0	-1	$I_{ijk} - M_x M_y - 1$	$+(4\Delta x \Delta z)^{-1}$
$\partial_z \quad / \quad \partial_z^2$	0	0	-1	$I_{ijk} - M_x M_y$	$-(2\Delta z)^{-1} \quad / \quad +\Delta z^{-2}$
$\partial_x \partial_z$	+1	0	-1	$I_{ijk} - M_x M_y + 1$	$-(4\Delta x \Delta z)^{-1}$
$\partial_y \partial_z$	0	+1	-1	$I_{ijk} - M_x M_y + M_x$	$-(4\Delta y \Delta z)^{-1}$
$\partial_x \partial_y$	-1	-1	0	$I_{ijk} - M_x - 1$	$+(4\Delta x \Delta y)^{-1}$
$\partial_y \quad / \quad \partial_y^2$	0	-1	0	$I_{ijk} - M_x$	$-(2\Delta y)^{-1} \quad / \quad +\Delta y^{-2}$
$\partial_x \partial_y$	+1	-1	0	$I_{ijk} - M_x + 1$	$-(4\Delta x \Delta y)^{-1}$
$\partial_x \quad / \quad \partial_x^2$	-1	0	0	$I_{ijk} - 1$	$-(2\Delta x)^{-1} \quad / \quad +\Delta x^{-2}$
$\partial_x^2 \quad / \quad \partial_y^2 \quad / \quad \partial_z^2$	0	0	0	I_{ijk}	$-2\Delta x^{-2} \quad / \quad -2\Delta y^{-2} \quad / \quad -2\Delta z^{-2}$
$\partial_x \quad / \quad \partial_x^2$	+1	0	0	$I_{ijk} + 1$	$+(2\Delta x)^{-1} \quad / \quad +\Delta x^{-2}$
$\partial_x \partial_y$	-1	+1	0	$I_{ijk} + M_x - 1$	$-(4\Delta x \Delta y)^{-1}$
$\partial_y \quad / \quad \partial_y^2$	0	+1	0	$I_{ijk} + M_x$	$+(2\Delta y)^{-1} \quad / \quad +\Delta y^{-2}$
$\partial_x \partial_y$	+1	+1	0	$I_{ijk} + M_x + 1$	$+(4\Delta x \Delta y)^{-1}$
$\partial_y \partial_z$	0	-1	+1	$I_{ijk} + M_x M_y - M_x$	$-(4\Delta y \Delta z)^{-1}$
$\partial_x \partial_z$	-1	0	+1	$I_{ijk} + M_x M_y - 1$	$-(4\Delta x \Delta z)^{-1}$
$\partial_z \quad / \quad \partial_z^2$	0	0	+1	$I_{ijk} + M_x M_y$	$+(2\Delta z)^{-1} \quad / \quad +\Delta z^{-2}$
$\partial_x \partial_z$	+1	0	+1	$I_{ijk} + M_x M_y + 1$	$+(4\Delta x \Delta z)^{-1}$
$\partial_y \partial_z$	0	+1	+1	$I_{ijk} + M_x M_y + M_x$	$+(4\Delta y \Delta z)^{-1}$

Table B.1: Array referencing scheme for first and second order spatial derivatives. The table refers to the index function I_{ijk} given in equation (B.7). The first section contains the contributions to matrix elements left of the diagonal of the matrix A, whereas the second section contributes directly to the diagonal. The last section contains contributions to matrix elements right of the diagonal of A. The first column contains all possible spatial derivatives of second order in three dimensions in the order in which they have to occur within a row of the corresponding linear system, and the third column contains the corresponding (increasing) index. All derivatives must be accompanied with the given prefactor. The first and second order derivatives with respect to a single coordinate contribute to the same off-diagonal matrix elements. Note that for volume elements on the boundary, different discretisation rules apply, for more details see the text.

Appendix C

Numerical tests

C.1 Discrete Element Method

All numerical implementations making use of the discrete element method (DEM) have been tested following the scheme below:

1. The module has been put to the test with the memory leak checker **valgrind**.

2. For some sample problem with a given distinct direction, the isotropy of the numerical implementation has been checked by changing the intrinsic direction.

3. When applicable, the numerical solution has been cross-checked with other numerical methods.

4. The numerical solution has been compared with an analytical solution for a sample problem.

The comparisons with analytical solutions of sample problems are discussed in the following subsections.

C.1.1 Constant-Diffusivity problems in a rectangular box

Some of the numerical methods described in section 2.4.2 have been implemented and checked as outlined before, where as a sample problem a rectangular box of dimensions $L_x \times L_y \times L_z$ with constant diffusivity and uniform Dirichlet boundary conditions has been chosen:

$$
\begin{aligned}
\frac{\partial u}{\partial t} - D\nabla^2 u(\boldsymbol{x}, t) &= Q(\boldsymbol{x}, t), \\
u|_{\partial V} &= 0.
\end{aligned}
\tag{C.1}
$$

This problem can be solved by using the eigenfunctions of the Laplacian operator over the box

$$C_{\boldsymbol{n}}(\boldsymbol{x}) = \sqrt{\frac{8}{L_x L_y L_z}} \sin\left(\frac{n_x \pi x}{L_x}\right) \sin\left(\frac{n_y \pi y}{L_y}\right) \sin\left(\frac{n_z \pi z}{L_z}\right), \tag{C.2}$$

with $\boldsymbol{n} = (n_x, n_y, n_z)$ and $n_{x/y/z} \in \{1, 2, \ldots, \infty\}$. By expanding both the solution and the rates into these eigenfunctions with time-dependent coefficients

$$u(\boldsymbol{x}, t) = \sum_{\boldsymbol{n}} u_{\boldsymbol{n}}(t) C_{\boldsymbol{n}}(\boldsymbol{x}), \qquad Q(\boldsymbol{x}, t) = \sum_{\boldsymbol{n}} Q_{\boldsymbol{n}}(t) C_{\boldsymbol{n}}(\boldsymbol{x}), \tag{C.3}$$

one can use the orthonormality relation of the eigenfunctions

$$\int C_{\boldsymbol{n}} C_{\boldsymbol{m}} \, dV = \delta_{\boldsymbol{nm}} \tag{C.4}$$

and the eigenvalue equation

$$\nabla^2 C_{\boldsymbol{n}} = -\lambda_{\boldsymbol{n}} C_{\boldsymbol{n}} = -\left(\frac{n_x^2}{L_x^2} + \frac{n_y^2}{L_y^2} + \frac{n_z^2}{L_z^2}\right) \pi^2 C_{\boldsymbol{n}}, \tag{C.5}$$

to derive ordinary differential equations describing the dynamics of every $u_{\boldsymbol{n}}(t)$. For constant $Q_{\boldsymbol{n}}(t) = Q_{\boldsymbol{n}}^0$ one can obtain their analytic solutions and thus, the full solution can be written as

$$u(\boldsymbol{x}, t) \;=\; \sum_{\boldsymbol{n}} \left\{ u_{\boldsymbol{n}}^0 \exp\left(-D\lambda_{\boldsymbol{n}} t\right) + \frac{Q_{\boldsymbol{n}}^0}{D\lambda_{\boldsymbol{n}}} \left[1 - \exp\left(-D\lambda_{\boldsymbol{n}} t\right)\right] \right\} C_{\boldsymbol{n}}(\boldsymbol{x}). \tag{C.6}$$

The agreement with the numerical implementation has been tested for different values of the timestep (see figure C.1). It turns out that in the observed regime the Crank-Nicholson scheme is stable, whereas for the chosen ADI and the FTCS schemes stability conditions exist. In the limit of $t \to \infty$ the steady-state-solution is obtained

$$u^{\mathrm{SS}}(\boldsymbol{x}) \;=\; \sum_{\boldsymbol{n}} \frac{Q_{\boldsymbol{n}}^0}{D\lambda_{\boldsymbol{n}}} C_{\boldsymbol{n}}(\boldsymbol{x}), \tag{C.7}$$

which enables one to estimate the quality of the often-used steady-state approximation by observing the difference to the full analytical solution

$$\begin{aligned}
\Delta u(\boldsymbol{x}, t) \;=\; & \left| u(\boldsymbol{x}, t) - u^{\mathrm{SS}}(\boldsymbol{x}) \right| = \left| \sum_{\boldsymbol{n}} \left[U_{\boldsymbol{n}}^0 - \frac{Q_{\boldsymbol{n}}^0}{D\lambda_{\boldsymbol{n}}} \right] \exp\left(-D\lambda_{\boldsymbol{n}} t\right) C_{\boldsymbol{n}}(\boldsymbol{x}) \right| \\
\leq \; & \sum_{\boldsymbol{n}} \left| \left(U_{\boldsymbol{n}}^0 - \frac{Q_{\boldsymbol{n}}^0}{D\lambda_{\boldsymbol{n}}} \right) C_{\boldsymbol{n}}(\boldsymbol{x}) \right| \exp\left(-D\lambda_{\boldsymbol{n}} t\right) \\
\leq \; & \exp\left(-D\lambda_{\min} t\right) \sum_{\boldsymbol{n}} \left| \left(U_{\boldsymbol{n}}^0 - \frac{Q_{\boldsymbol{n}}^0}{D\lambda_{\boldsymbol{n}}} \right) C_{\boldsymbol{n}}(\boldsymbol{x}) \right| = \exp\left(-\frac{\lambda_{\min}}{6} 6Dt\right) \Delta u^0(\boldsymbol{x}), \tag{C.8}
\end{aligned}$$
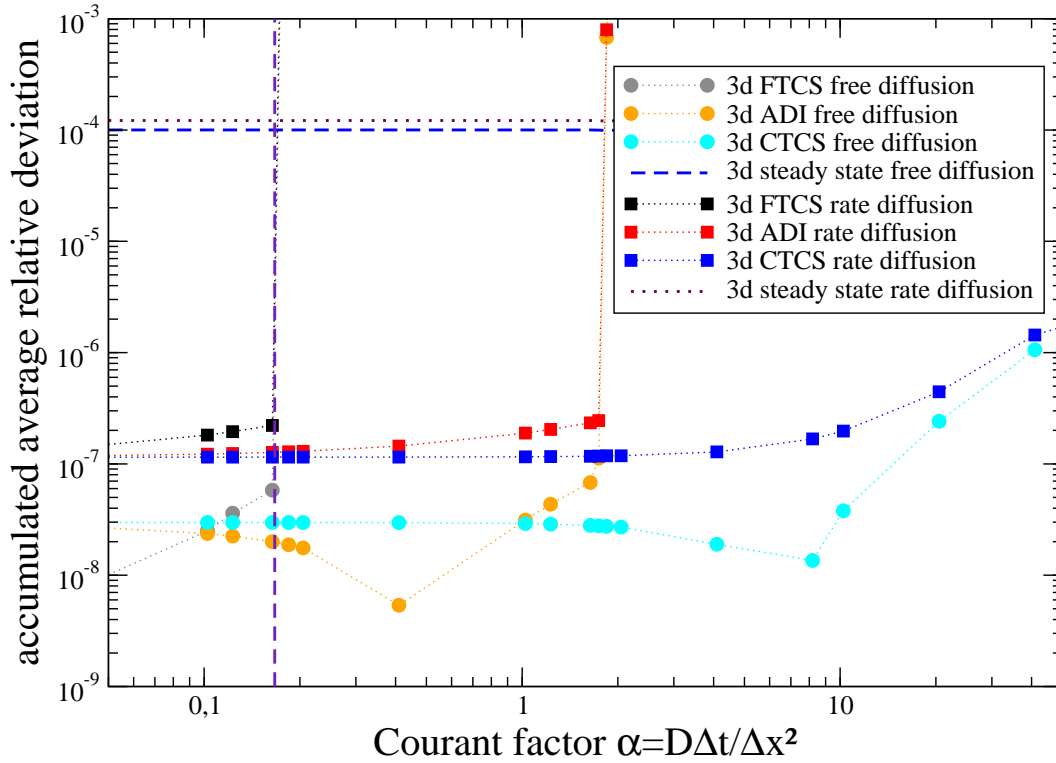
Figure C.1: Analysis of numerical accuracy/stability for a simple test problem. Displayed is the maximum deviation from the analytic solution that has accumulated after evolving the reaction-diffusion equation with different methods for $T = 500$ s using different timesteps – expressed by the Courant factor alpha. The calculations have been performed on a cubic grid with 15.625 μm lattice constant and 65^3 grid nodes. Circle symbols refer to the free diffusion case ($u^0_{1,1,1} = 20$ mM), and the square symbols refer to the reaction-diffusion case ($u^0_{1,1,1} = 20$ mM, $Q^0_{1,1,1} = 0.13$ mM/s), where all coefficients of higher eigenmodes vanish. The FTCS method fails completely at $\alpha = 1/6$ as predicted by equation (2.34), whereas the ADI method has its maximum accuracy at $\alpha = 1/2$ in the free diffusion case, corresponding to the analogous Courant condition in one dimension. Since the error accumulates and the inaccuracy resulting from the chosen numerical approach contributes as well, small timesteps do not necessarily imply small final errors in the case of free diffusion. In addition, the full Crank-Nicholson scheme reaches maximum accuracy at much larger timesteps. For each timestep, the accuracy of the biconjugate gradient method in the Crank-Nicholson scheme had been set to $\varepsilon = 10^{-10}$. Note that the analysed ADI algorithm as given by equation (2.37) is not unconditionally stable in three dimensions as illustrated by the super-polynomial growth of the error at $\alpha = 2$. In the RDE case one can see that the error is now dominated by the reaction terms with the error growing polynomially with the timestep size in the regions of numerical stability. The larger error of the steady-state solutions demonstrates in both cases that after $T = 500$ s the concentration has not yet reached the steady-state.

where $\lambda_{\min}$ is the smallest eigenvalue in equation (C.5) and $\Delta u^0(\boldsymbol{x})$ is the initial difference to the steady-state approximation solution. Thus, it is visible that – besides the initial deviation of the steady-state approximation the lowest eigenvalue of the Laplacian operator in the volume under consideration in comparison with the diffusion length $\sqrt{6Dt}$ determines the quality of the steady-state approximation. Note however, that in above derivation the reaction rates have been kept temporally constant. For physiological values of $t = 500$ s, $D = 105$ μm^2/s (glucose in tissue, [138]), and $V = (1000\ \mu$m$)^3$ one obtains $\exp(-D\lambda_{\min}t) = 0.21$. Therefore, for the validity of the steady-state approximation, the following conditions must be fulfilled

- the initial concentration should be close to the steady-state-concentration,

- the reaction terms should not change much during the observed time interval,

- the time interval should be large enough such that the diffusion length is larger than the typical length scale of the system.

Different methods for obtaining the steady-state concentration from a given distribution of reaction rates have been compared (see figure C.2).

It should be noted that the spatial distribution of the error follows the Laplacian equation as well (see figure C.3 right panel).

In the case of the RDE (2.24) with no-flux von-Neumann boundary conditions and for a given rate term $Q(\boldsymbol{x}, t)$ the total content of the reaction-diffusion volume

$$U(t) = \int_V u(\boldsymbol{x}, t)\, d^3\boldsymbol{x} \tag{C.9}$$

can be obtained via

$$U(t) = U(0) + \int_0^t \left[\int_V Q(\boldsymbol{x}, t')\, d^3\boldsymbol{x} \right] dt', \tag{C.10}$$

which can be calculated analytically for simple choices of $Q(\boldsymbol{x}, t)$. This provides an additional way of testing. Note that above procedure can be applied for small times and Dirichlet boundary conditions as well if there is no interaction with the boundary, i. e., if within a non-vanishing environment of the boundary the cell concentration does not exhibit a gradient.

C.1.2   Steady-state-Solutions for varying-diffusivity problems

By using the formal analogy to electrostatics, where one has [179]

$$\nabla\left[\varepsilon(\boldsymbol{x})\nabla\Phi(\boldsymbol{x})\right] = -4\pi\rho(\boldsymbol{x}), \tag{C.11}$$
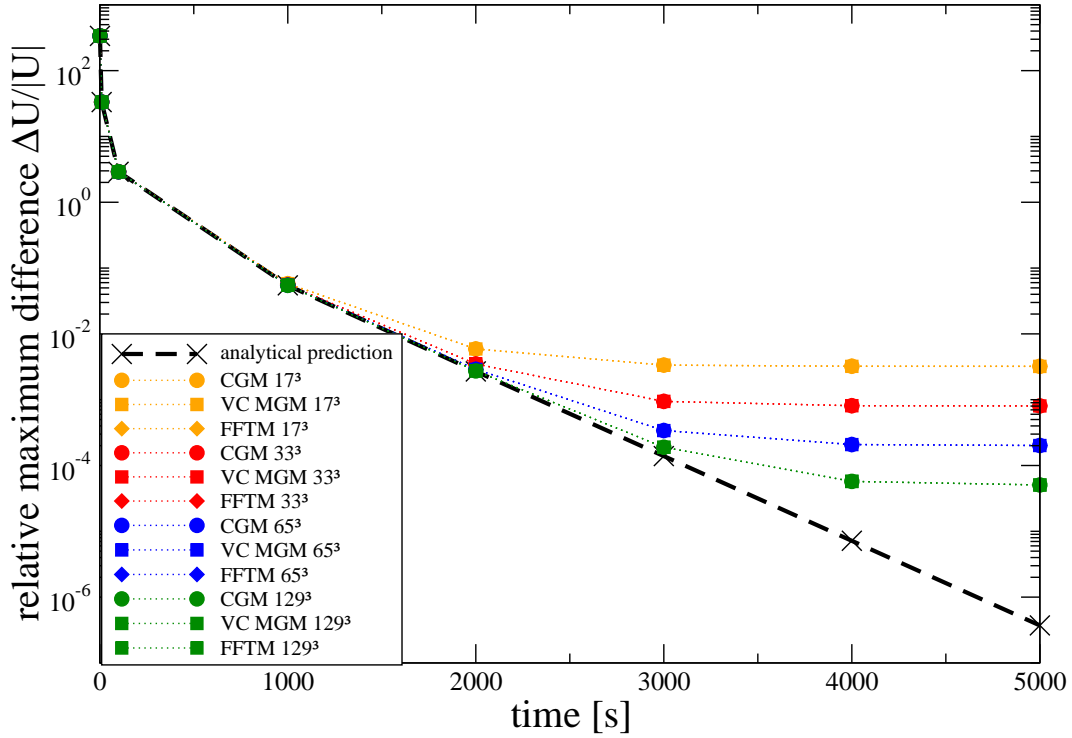
Figure C.2: Deviation of the steady-state approximation from the full analytic solution. The analytical error prediction (dashed line) illustrates the ideal exponential dependence. Three numerical approaches have been compared: the biconjugate gradient method (CGM), a V-cycle-multigrid method (VC MGM), and method based on Fast Fourier transform (FFTM). For equal grid resolutions, all numerical approaches converge to the same result within their desired accuracy (here set to $\varepsilon = 10^{-10}$). For small times, the error must be large due to the invalidity of the steady-state approximation, whereas for large times, the error should decrease as indicated by the dashed line (analytic calculation). Note that the initial nonlinearity does not contradict equation (C.8), since the difference has been divided by the (time-dependent) full solution. The saturation of error in the numerical approaches however indicates that though for large times, the steady-state-approximation becomes valid, the spatial discretisation error will still contribute. Here, it is also demonstrated that the used finite-differencing schemes are of second order in space, as doubled grid resolution reduces the remaining error by a factor of four. Parameters have been chosen as follows: $u^0_{1,1,1} = 0.0$ mM, $Q^0_{1,1,1} = 0.13$ mM/s, $D = 100 \ \mu\text{m}^2/\text{s}$, and $L_x = L_y = L_z = 1000 \ \mu\text{m}$.
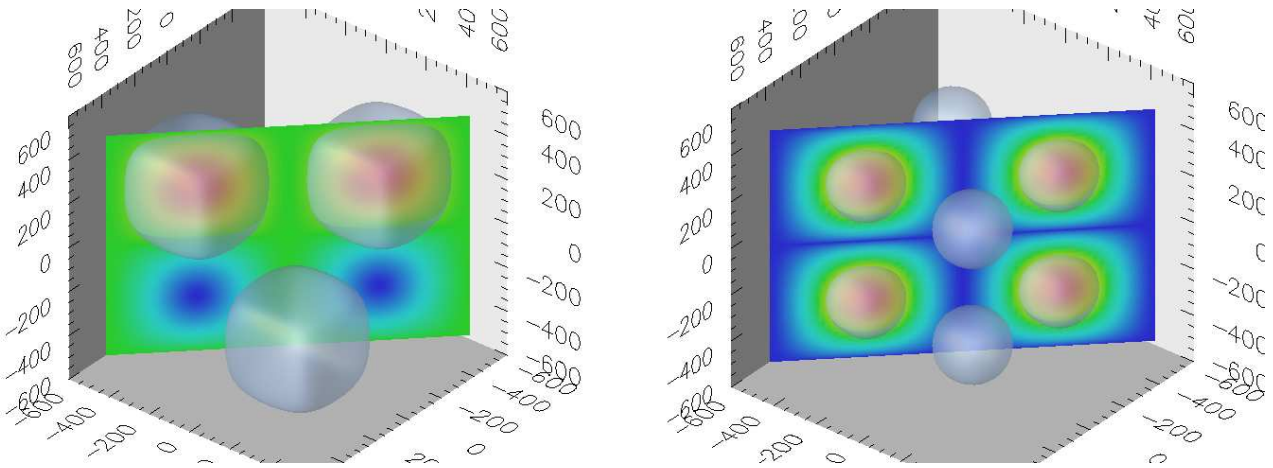
Figure C.3: Density plot of solutions for the 222-eigenmode. The plane of the cross-sections contains the origin and has the normal vector $\boldsymbol{n}_\perp = 1/\sqrt{2}(1,1,0)$ **Left:** Numerical solution of the Poissonian problem with $Q_{222} = 0.13$ a. u., and D = 100 a. u. Red encodes field values of $+9.9 \cdot 10^{-4}$ a. u., whereas blue encodes $-9.9 \cdot 10^{-4}$ a. u. The transparent isosurfaces denote field values of $1.0 \cdot 10^{-4}$ a. u. **Right:** Red encodes absolute error values of $+7.95 \cdot 10^{-7}$ a. u., whereas the transparent isosurfaces denote absolute error values of $5.0 \cdot 10^{-7}$ a. u. Generally, the error follows Laplaces equation as well.

where $\rho(\boldsymbol{x})$ represents the charge distribution and $\varepsilon(\boldsymbol{x})$ the electric permittivity, one can find an analytical solution for simple configurations from the Green's function. For example, if one uses Dirichlet boundary conditions at infinity, the solution can be obtained directly via

$$\Phi(\boldsymbol{x}) = \frac{1}{4\pi\varepsilon_0} \int \frac{\rho(\boldsymbol{x}')}{|\boldsymbol{x} - \boldsymbol{x}'|} d^3\boldsymbol{x}' \,. \tag{C.12}$$

For the special example of a point charge Q located at $\boldsymbol{x}'$ in a half-space with ε_1, whereas the other half-space has permittivity ε_2, a solution can be obtained using the method of images

$$\Phi(\boldsymbol{x}) = \begin{cases} \dfrac{Q}{\varepsilon_1}\left[\dfrac{1}{|\boldsymbol{x} - \boldsymbol{x}'|} + \dfrac{\varepsilon_1 - \varepsilon_2}{\varepsilon_1 + \varepsilon_2}\dfrac{1}{|\boldsymbol{x} - \boldsymbol{x}' + 2\boldsymbol{n}(\boldsymbol{n}\cdot\boldsymbol{x}')|}\right] &: \quad \boldsymbol{x} \in V_1 \\[2ex] \dfrac{2}{\varepsilon_1 + \varepsilon_2}\dfrac{Q}{|\boldsymbol{x} - \boldsymbol{x}'|} &: \quad \boldsymbol{x} \in V_2 \end{cases}, \tag{C.13}$$

where $\boldsymbol{n}$ denotes the normal vector pointing from half-space 1 to half-space 2 (see figure C.4). Obviously, the error is not completely controlled, as in the numerical solution one has additional boundary conditions that are not contained in the analytical solution.

A further test problem with varying diffusion coefficients can be constructed from a one-dimensional example. If both the diffusion coefficient and the reaction rates are isotropic in x and y-directions, and the solution satisfies no-flux von Neumann boundary conditions in these direction, the diffusion
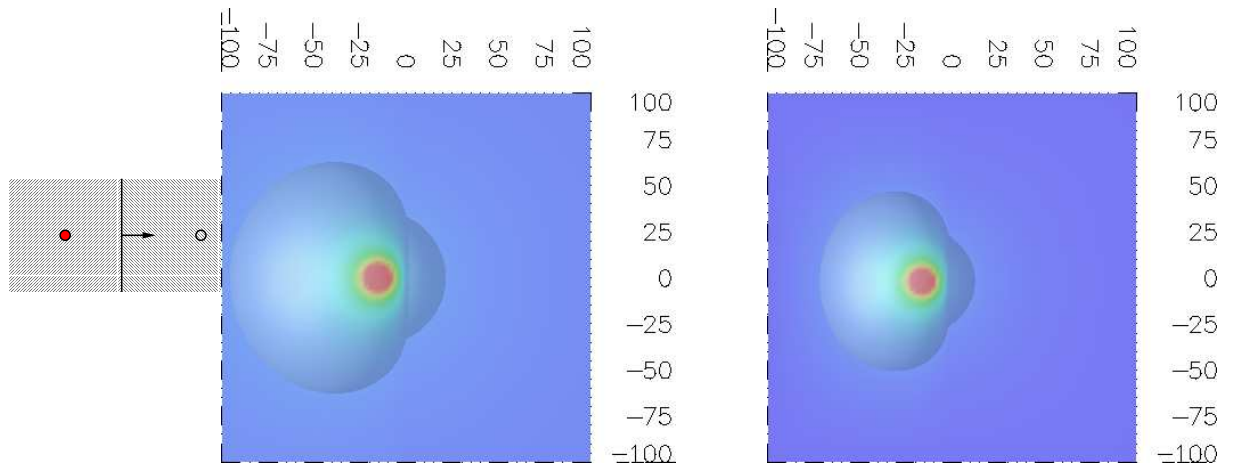
Figure C.4: Approximate solution of an electrostatic test problem. The plane of the cross-sections contains the origin and has normal vector $\boldsymbol{n}_\perp = (1, 0, 0)$. **Left:** Simple test problem for the steady-state-solution of space-dependent diffusion. A point charge (filled point) is placed in the left half-space V_1 with permittivity ε_1, whereas the right half-space V_2 is filled with a medium of permittivity ε_2. The mirror charge (empty point) ensures constant potential at the intermediate boundary. **Middle:** Analytical solution (vanishing potential at infinity) for a point charge with $Q = 1.0$ a. u. placed at (0.0, 0.0, -15.0) inside a cubic box ranging from (-100.0, -100.0, -100.0) to (+100.0, +100.0, +100.0). At $z = 0$ the volume is divided into two half-spaces with $\varepsilon_1 = 1.0$ a. u. and $\varepsilon_2 = 10.0$ a. u. The transparent three-dimensional isosurfaces denote regions with $\Phi = 0.005$ a. u. Blue encodes regions with $\Phi = 0$ a. u., whereas red encodes regions with $\Phi \geq 0.1$ a. u. **Right:** Numerical solution of the same problem with 101 grid nodes in every dimension. In contrast to the analytical solution (middle), the numerical solution underlies $\Phi = 0$ Dirichlet boundary conditions at the box walls (colour coding as in the middle panel). This leads to a faster decreasing potential and to a smaller isosurface of the numerical solution. The associated error can be decreased by enlarging the grid size while keeping the grid resolution constant.

equation will reduce to an effectively one-dimensional problem. For example, in the steady-state approximation one obtains in this case

$$D(z)u''(z) + D'(z)u'(z) + Q(z) = 0 \, . \tag{C.14}$$

Generally, the above one-dimensional problem can for polynomial $D(z)$ and $Q(z)$ be solved with a power-series ansatz

$$u(z) = \sum_{n=0}^{\infty} a_n z^n \, . \tag{C.15}$$

If, for example, the spatial dependence of the diffusion coefficient and reaction rates is given by

$$
\begin{aligned}
D(z) &= D_0 + \alpha z^2 \, , \\
Q(z) &= Q_0 \left(1 + 3 \frac{\alpha}{D_0} z^2 \right) \, ,
\end{aligned}
\tag{C.16}
$$

the solution can be found by inserting ansatz (C.15) into (C.14). With the additional equations for the Dirichlet boundary conditions $u(0) = u_0$ and $u(L_z) = u_L$ the series expansion can be re-summated to

$$u(z) = u_0 - \frac{Q_0}{2D_0} z^2 + \frac{u_L - u_0 + \frac{Q_0}{2D_0} L_z^2}{\arctan\left(\sqrt{\frac{\alpha}{D_0}} L_z\right)} \arctan\left(\sqrt{\frac{\alpha}{D_0}} z\right) \, , \tag{C.17}$$

as can be verified by re-inserting into equation (C.14). The numerical solution of the above example has been compared with the analytical solution (C.17), see figure C.5.

C.1.3 The loaded cuboid

As sample problem the following scenario has been considered: A cuboid of dimensions L_x, L_y and L_z and uniform elastic properties E_0 and ν_0 is pressed with the uniform force density p_x on its left side to the right and is constrained by the half-space situated at $x = L_x$ (see figure C.6 left panel). In this case, the equations decouple

$$U_x(x, y, z) = U_x(x) \, , \qquad U_y(x, y, z) = U_y(y) \, , \qquad U_z(x, y, z) = U_z(z) \, , \tag{C.18}$$

which considerably simplifies equations (2.44) to

$$
\begin{aligned}
U_x''(x) = 0 \, , \qquad U_y''(y) = 0 \, , \qquad U_z''(z) &= 0 \, , \\
n_x \left[f_1 U_x'(x) + f_2 U_y'(y) + f_2 U_z'(z) \right] &= P_x \, , \\
f_1 U_y'(y) + f_2 \left[U_x'(x) + U_z'(z) \right] = 0 \, , \qquad f_1 U_z'(z) + f_2 \left[U_x'(x) + U_y'(y) \right] &= 0 \, .
\end{aligned}
\tag{C.19}
$$
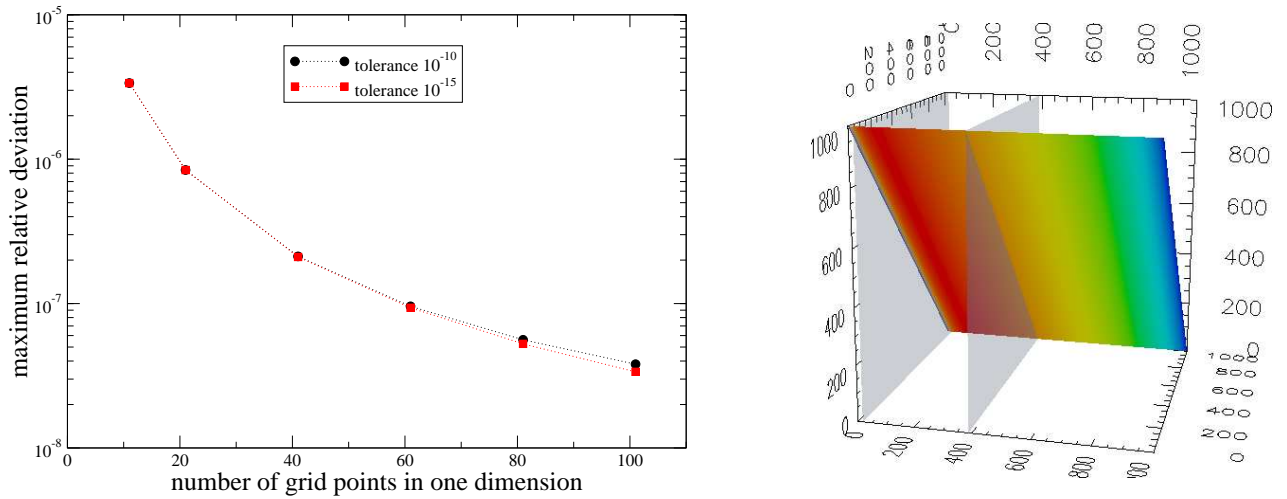
Figure C.5: Steady-state solution of a test problem for varying diffusion coefficients. **Left:** Maximum relative deviation between numerical and analytical solution of C.14 for $D(z) = D_0 + \alpha z^2$ and $Q(z) = Q_0 \left(1 + 3\alpha/D_0 z^2\right)$. The biconjugate gradient algorithm has been used with different values for the error tolerance. For doubled grid resolution, the error decreases by a factor of four. Parameters have been chosen as follows: $D_0 = 1.0$ μm^2/s, $Q_0 = 0.5$ mol/(μm^{3}s), $\alpha = 1.0 \cdot 10^{-9}$/s, $u_0 = 1000.0$ mol/μm^3, $u_L = 100000.0$ mol/μm^3 in a box ranging from $(0, 0, 0)$ μm to $(1000.0, 1000.0, 1000.0)$ μm. **Right:** Density plot of the relative error. The plane of the cross-section contains the centre of the computational domain and has the normal vector $\boldsymbol{n}_\perp = 1/\sqrt{2}(1, 1, 0)$. As in x and y-direction no-flux von-Neumann boundary conditions have been applied, there are no anisotropies in these dimensions, i. e., the isosurfaces (here at $3.0 \cdot 10^{-8}$) are planes. Naturally, at the Dirichlet boundary conditions the error vanishes, as also the numerical solution fulfils the boundary conditions exactly.

In combination with the additional constraints $U_x(L_x) = 0$, $U_y(0) = -U_y(L_y)$, and $U_z(0) = -U_z(L_z)$ this simplified system can be solved analytically. The elastic properties of the plate thus solely enter via the boundary conditions and the solution reads

$$U_x(x) = \frac{p_x}{E}\left[L_x - x\right], \qquad U_y(y) = \nu\frac{p_x}{E}\left[y - \frac{L_y}{2}\right], \qquad U_z(z) = \nu\frac{p_x}{E}\left[z - \frac{L_z}{2}\right]. \qquad (C.20)$$

Here it becomes visible that the elastic parameter E describes the deformation in longitudinal direction, whereas the Poisson number ν quantifies the relative deformation transversally to the acting force, compare also subsection 2.4.3. The total volume is given by

$$V = L_x\left(1 - \frac{p_x}{E}\right)L_y\left(1 + \nu\frac{p_x}{E}\right)L_z\left(1 + \nu\frac{p_x}{E}\right) = V_0\left[1 + (2\nu - 1)\frac{p_x}{E} + O\left(\frac{p_x^2}{E^2}\right)\right], \qquad (C.21)$$

where it is visible that $\nu = 1/2$ corresponds to the case of an incompressible medium.
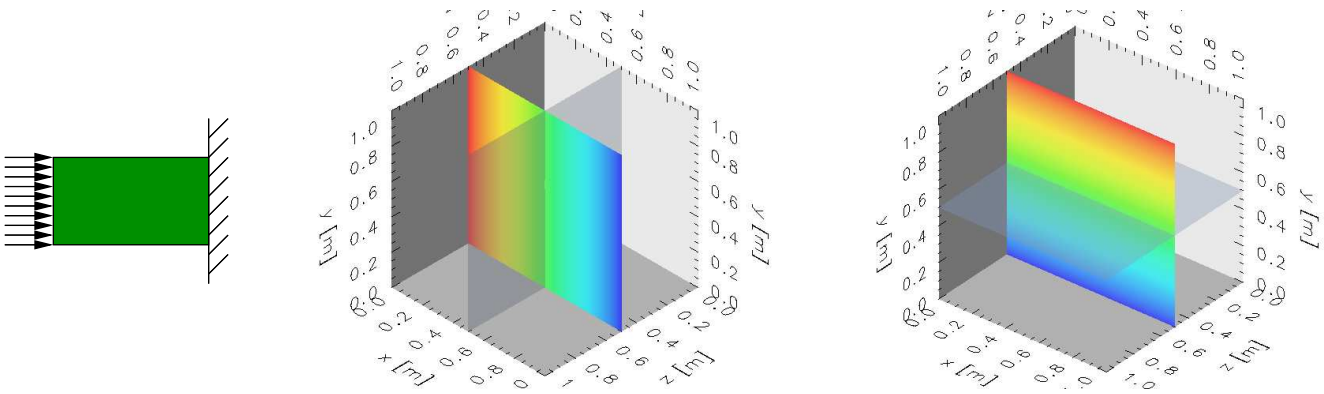
Figure C.6: Illustration of a test problem for strain distribution. **Left:** A plate with dimensions $L_x = L_y = L_z = 1$ m and uniform Poisson and Young moduli $\nu = 0.333$ and $E = 1.0$ kPa, respectively, is pressed with the uniform force density $p_x = 0.1$ Pa as illustrated. **Middle:** This results in a linear dependence of the local deformations: The strain in x direction is largest at the face where the force acts and decreases with x (transparent isosurfaces are planes). **Right:** In contrast, the absolute strain in a perpendicular direction (here y) vanishes at the symmetry plane marked by the transparent isosurface and increases towards the boundaries. As the strain U^α is a linear function of x^α, the resulting strain and stress tensors are spatially constant.

Similarly, for a special case an analytical solution can be found for spatially varying Young modulus. If no transversal deformation is allowed (equivalent to $\nu(\boldsymbol{x}) = 0$) and if the Young modulus varies only in one dimension $E(\boldsymbol{x}) = E(x)$, one has $f_1 = E(x)$, $f_2 = 0$, $g = E(x)/2$ and the same ansatz

$$U_x(\boldsymbol{x}) = U_x(x), \qquad U_y(\boldsymbol{x}) = U_y(y), \qquad U_z(\boldsymbol{x}) = U_z(z) \qquad (C.22)$$

can be used to simplify equations (2.44) to

$$\begin{aligned}
E(x)U_x''(x) + E'(x)U'(x) &= 0, & U_y''(y) &= 0, & U_z''(z) &= 0, \\
n_x E(x)U_x'(x) &= p_x, & U_y'(y) &= 0, & U_z'(z) &= 0,
\end{aligned} \qquad (C.23)$$

which has the solution

$$U_x(x) = p_x \int\limits_{x}^{L_x} \frac{1}{E(x')}\, dx' , \qquad U_y(y) = 0 , \qquad \text{and} \qquad U_z(z) = 0 . \qquad (C.24)$$

Note that for constant $E(x) = E_0$, above equation reduces to the same solution as (C.20) in case of $\nu = 0$.

C.2 Cellular mechanics

The correct calculation of cellular interactions has been tested by the following scheme:

1. The code has been tested with the program **valgrind** for memory leaks.

2. For a sample problem with a given distinct direction, the isotropy of the solution has been checked for by changing the intrinsic direction to all coordinates.

In addition, further comparisons with analytic results as described below have been performed.

C.2.1 Deterministic two-body-problem

The equations of motion for two spheres of radii R_1 and R_2 underlying a JKR-interaction and tangential as well as isotropic friction resulting from (2.86) are given by

$$
\begin{aligned}
m_1 \ddot{\boldsymbol{x}}_1 &= F\boldsymbol{n}_{12} - \gamma_{12}\,(\dot{\boldsymbol{x}}_1 - \dot{\boldsymbol{x}}_2) - \gamma_1 \dot{\boldsymbol{x}}_1 , \\
m_2 \ddot{\boldsymbol{x}}_2 &= F\boldsymbol{n}_{21} - \gamma_{21}\,(\dot{\boldsymbol{x}}_2 - \dot{\boldsymbol{x}}_1) - \gamma_2 \dot{\boldsymbol{x}}_2 ,
\end{aligned}
\qquad (C.25)
$$

where F denotes the JKR-force, $\boldsymbol{n}_{12} = -\boldsymbol{n}_{21}$ the normal vector from cell 1 to cell 2, $\gamma_{12} = \gamma_{21}$ the tangential friction tensor, and $\gamma_i = 6\pi\eta R_i$ the isotropic Stokes friction, where η is the viscosity of the medium. If the friction tensor only incorporates tangential friction, i. e., if only movements tangential to the inter-spherical contact surface contribute to intercellular drag forces, the total drag force will only arise from cell-medium contributions. Mathematically, this reflects in $\gamma_{12}\,(\dot{\boldsymbol{x}}_1 - \dot{\boldsymbol{x}}_2) = 0$, since γ_{12} contains projectors on the tangential part of the velocity difference only. Therefore, one obtains in the over-damped approximation $m_i \ddot{\boldsymbol{x}}_i \approx 0$

$$6\pi\eta R_1 \dot{x}_1 = -Kh^{3/2}R^{1/2}\left[1 - \sqrt{\frac{6\pi\epsilon R^{1/2}}{Kh^{3/2}}}\,\right]\Theta(h) ,$$

$$6\pi\eta R_2 \dot{x}_2 = +Kh^{3/2}R^{1/2}\left[1 - \sqrt{\frac{6\pi\epsilon R^{1/2}}{Kh^{3/2}}}\,\right]\Theta(h) , \qquad (C.26)$$

where $h = R_1 + R_2 - |x_2 - x_1|$ is the total sphere overlap, K denotes the elastic constant defined in equation (2.60), R is the reduced radius defined in (2.58), ϵ stands for the adhesion energy density between the two spheres, and Θ denotes the Heaviside step function. If one assumes – without loss of generality – that $x_2 > x_1$ and that one has an overlap $h > 0$ (otherwise the solution is trivial), the distance between the sphere centers can be calculated by subtracting equations (C.26) from each other and with introducing a normalised distance measure

$$\Delta = \frac{x_2 - x_1}{R_1 + R_2} \tag{C.27}$$

one yields a differential equation

$$\dot{\Delta} = \alpha(1 - \Delta)^{3/2} - \alpha\beta^{1/2}(1 - \Delta)^{3/4}, \qquad \text{with} \tag{C.28}$$

$$\alpha = \frac{K}{6\pi\eta}\left(\sqrt{\frac{R_1}{R_2}} + \sqrt{\frac{R_2}{R_1}}\right) \qquad \text{and} \qquad \beta = \frac{6\pi\epsilon(R_1 + R_2)}{R_1 R_2 K}\left(\frac{\sqrt{R_1 R_2}}{R_1 + R_2}\right)^{3/2}.$$

Via integration of variables and following expansion into partial fractions the above equation leads to the implicit solution

$$\frac{3}{4}\alpha(t - t_0)\beta^{1/3} = \sqrt{3}\left\{\arctan\left[\frac{1}{\sqrt{3}}\left(1 + \frac{2(1 - \Delta)^{1/4}}{\beta^{1/6}}\right)\right] - \arctan\left[\frac{1}{\sqrt{3}}\left(1 + \frac{2(1 - \Delta_0)^{1/4}}{\beta^{1/6}}\right)\right]\right\}$$

$$-\log\left[\frac{\beta^{1/6} - (1 - \Delta)^{1/4}}{\beta^{1/6} - (1 - \Delta_0)^{1/4}}\right] + \frac{1}{2}\log\left[\frac{\beta^{1/3} + \beta^{1/6}(1 - \Delta)^{1/4} + (1 - \Delta)^{1/2}}{\beta^{1/3} + \beta^{1/6}(1 - \Delta_0)^{1/4} + (1 - \Delta_0)^{1/2}}\right], \tag{C.29}$$

that cannot be inverted analytically. Therefore, for testing purposes equation (C.28) has been solved directly with a 4th order Runge-Kutta method [176] using a sufficiently small timestep. As shown in figure C.7, the use of adaptive timestep sizes in the agent-based simulation improves the numeric solution significantly. Note that by using this procedure one has tested the chosen solution scheme with the adaptive timestepping and in addition whether the tangential projection operators have been implemented correctly in the dampening matrix in (2.86).

C.2.2   Deterministic many-body-problem

Since for multi-particle systems an analytical solution is usually impossible to find in the general case, a rather special configuration can serve as a testing problem. A set of N cells of equal and constant radius R being in contact with each other, situated on a plane substrate without any stochastic force will still experience elastic and adhesive cell-cell as well as cell-substrate interactions due to the JKR-model and also the corresponding drag forces. If now in addition every cell crawls with a constant force f^α tangential to the plane, one can expect the cell-cell interaction forces to vanish after some
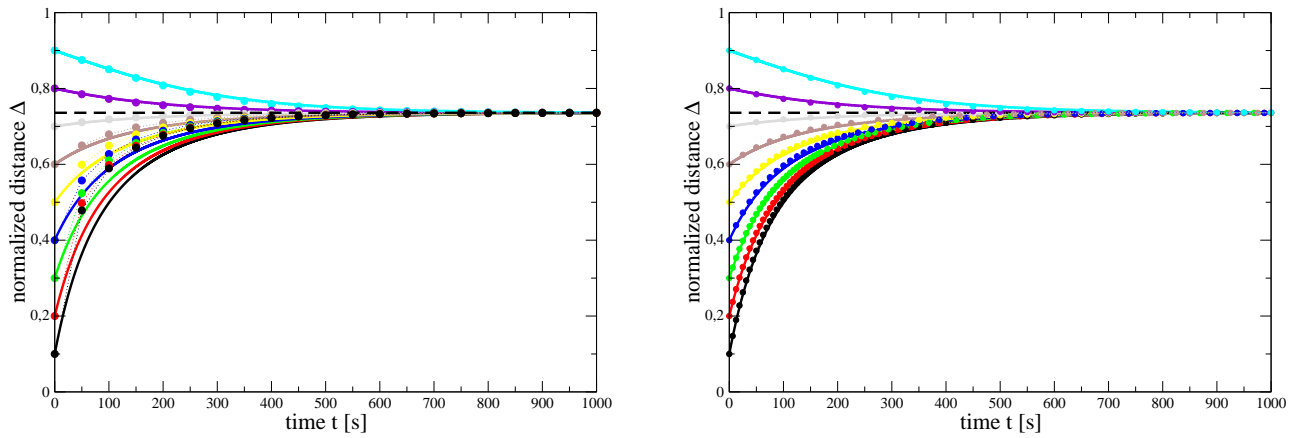
Figure C.7: Numerical solution of the two-body interaction test problem. Temporal evolution of the normalised relative distance $\Delta = (x_2 - x_1)/(R_1 + R_2)$ for constant timestep width (**left**, $\Delta t = 50$ s) and adaptive timestep width (**right**, maximum step-size $\Delta x_{max} = 0.25$ μm). The black dashed line denotes the equilibrium value, for which $\dot{\Delta} = 0$. Solid lines denote pseudo-analytic solutions (4th order Runge-Kutta with sufficiently small timestep and Euler cross-check), whereas symbols denote discretisation by the simulation. For the adaptive scheme, strong slopes automatically enforce smaller timesteps. Parameters have been chosen as follows to correspond with physiological values: $R_1 = R_2 = 5$ μm, $E_1 = E_2 = 1000$ Pa, $\nu_1 = \nu_2 = 0.2$, $\eta = 0.005$ kg/(μm s), $\epsilon = 0.0001$ pJ/μm^2.

time, as the two-body interaction will find its minimum – in particular having the contact surface A^∞ with the boundary. In the limit of large t, all cells will then move as a single rigid body. The equations of motion (2.86) can be written as

$$f^\alpha + \sum_j F_{ij}^\alpha = \sum_{k,\beta} \left\{ \left[\gamma_k^{\alpha\beta} + \sum_j \gamma_{kj}^{\alpha\beta} + \Gamma_k^{\alpha\beta} \right] \delta_{ik} - \gamma_{ik}^{\alpha\beta} \right\} \dot{x}_k^\beta$$
$$= \sum_\beta \left[\gamma_i^{\alpha\beta} + \Gamma_i^{\alpha\beta} \right] \dot{x}_i^\beta + \sum_{j,\beta} \gamma_{ij}^{\alpha\beta} \left(\dot{x}_i^\beta - \dot{x}_j^\beta \right) , \tag{C.30}$$

which simplifies in the large time-limit to

$$f^\alpha \approx \left\{ \gamma_i^{\alpha\beta} + \Gamma_i^{\alpha\beta} \right\} \dot{x}_i^\beta . \tag{C.31}$$

As the force is tangential to the substrate, one has with $\Gamma_i^{\alpha\beta} = A_i^\infty \gamma_\| \mathcal{P}_i^{\alpha\beta}$ and the usual Stokes friction term $\gamma_i^{\alpha\beta} = 6\pi\eta R \delta^{\alpha\beta}$

$$\dot{x}_i^\alpha = \frac{f^\alpha}{6\pi\eta R + \gamma_\| A^\infty} , \tag{C.32}$$

since the cellular velocities are directed tangential to the substrate and are thus unaffected by the projection operator, i. e., $\mathcal{P}_i \dot{x}_i = \dot{x}_i$. Consequently, the observed cellular velocities must approach a common value proportional to the crawling force, compare figure C.8. Note that the large-time limit is independent on the number of cells, whereas the initial conditions and the number of cells determine, how fast this equilibrium is reached.

C.2.3 *Stochastic single-body-problem*

For a single cell of constant radius R and mass m, that is neither subject to cell-cell nor to cell-boundary interaction, the dynamics is described by the Langevin equation of motion

$$\dot{r} = v ,$$
$$\dot{v} = -\frac{\gamma}{m} v(t) + \frac{1}{m} F(t) , \tag{C.33}$$

where $\gamma = 6\pi\eta R$ is the Stokes friction coefficient, η the viscosity of the medium, and $F(t)$ is a stochastic force. Note that for active random cellular dynamics the Einstein relation

$$D = \frac{k_B T}{6\pi\eta R} \tag{C.34}$$

does not directly relate to the physical temperature T, but rather defines an effective temperature T^{eff}, since in this case the cellular movement does not result from physical collisions with particles in the
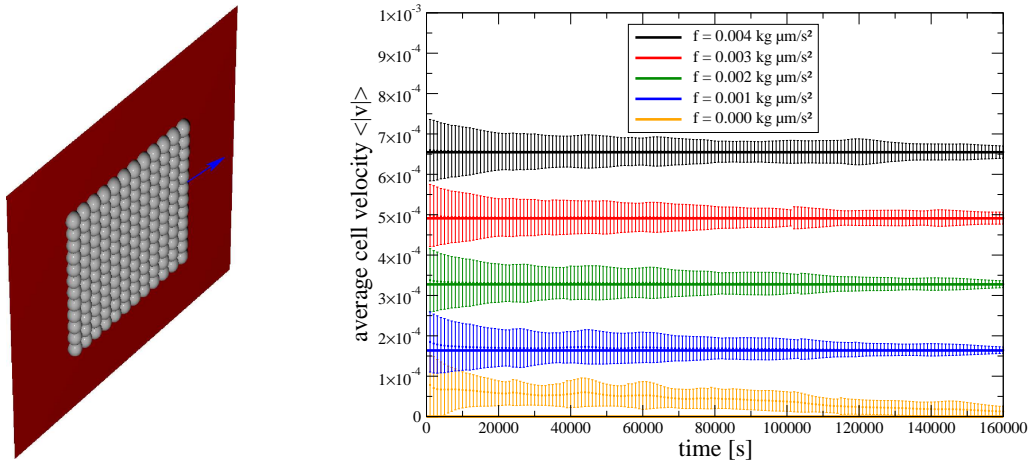
Figure C.8: Deterministic many-body test of the projection operators in the numerical solution. **Left:** A cohort of 144 cells subject to intercellular as well as cell-substrate JKR-forces is moving on the x-y-plane due to a crawling force (arrow) acting on every cell. **Right:** Initially, the intercellular and cell-substrate equilibrium distances have to be found, but for large times all cells move synchronously with a constant velocity, as is indicated by the smaller standard deviations (error bars) of the velocity. For large times, the average absolute value of the velocity matches the theoretical predictions of equation (C.32) (solid horizontal lines). The difference for non-mobile cells (orange) is a result of the tolerance of the conjugate gradient algorithm, that had been set to $\varepsilon = 10^{-5}$ (compare section B.2). Parameters have been chosen as follows: $E_{sub} = E_{cell} = 750.0$ Pa, $\nu_{sub} = \nu_{cell} = 1/3$, $\gamma_\perp = 0$, $\gamma_\parallel = 0.1$ kg/(μm^2 s). $\epsilon_{cell-cell} = \epsilon_{cell-sub} = 0.0001$ pJ/m^2, $\eta = 0.001$ kg/(μm s), $R_{cell} = 5$ μm, $\Delta t = 50$ s, $N = 144$. Note that with the absence of stochastic forces in this example, cells tend to assume a planar equilibrium configuration, which violates the general position assumption and leads to on-going reconstructions in the Delaunay triangulation module.

fluid, but rather from internal cellular actions. The solution of (C.33) can be found by variation of constants and is given by

$$
\boldsymbol{r}(t) \;=\; \boldsymbol{r}_0 + \frac{m}{\gamma}\left[1 - \exp\left(-\frac{\gamma t}{m}\right)\right]\boldsymbol{v}_0 + \frac{1}{\gamma}\int_0^t\left[1 - \exp\left(-\frac{\gamma(t-\tau)}{m}\right)\right]\boldsymbol{F}(\tau)\,d\tau\,. \tag{C.35}
$$

In the large-time limit (over-damped approximation), i. e., with $\gamma t/m \gg 1$, this reduces to

$$
\boldsymbol{r}(t) \;=\; \boldsymbol{r}_0 + \frac{m}{\gamma}\boldsymbol{v}_0 + \frac{1}{\gamma}\int_0^t \boldsymbol{F}(\tau)\,d\tau\,. \tag{C.36}
$$

By using the two assumptions on the stochastic force

$$
\langle \boldsymbol{F} \rangle \;=\; \boldsymbol{0}\,,
$$
$$
\langle \boldsymbol{F}(t_1)\cdot \boldsymbol{F}(t_2)\rangle \;=\; 3\xi^2\delta(t_1 - t_2)\,, \tag{C.37}
$$

where ξ is a parameter that describes the strength of the stochastic forces, the mean square displacement can be calculated in the large-time limit as

$$
\langle r^2(t) - r_0^2\rangle = \left(\frac{m}{\gamma}\right)^2\langle v_0^2\rangle + 3\frac{\xi^2}{\gamma^2}t \approx +3\frac{\xi^2}{\gamma^2}t\,. \tag{C.38}
$$

Note that the constant term can be safely neglected, as $(m_{\text{cell}}/\gamma_{\text{cell}})^2 = O\left(10^{-22}\text{s}^2\right)$ for realistic systems. The above identity is known as the fluctuation-dissipation theorem, where the diffusion coefficient is sometimes defined as $D = \xi^2/(2\gamma^2)$.

A numerical emulation of a stochastic force fulfilling the conditions (C.37) can be derived as follows: The first condition is met by using any random number distribution with a vanishing mean. In numerical calculations, the smallest time unit within which the stochastic forces can differ is given by the time step Δt. This can be used to derive the amplitude of the stochastic force from the correlation condition in (C.37):

$$
\int_{t-\Delta t/2}^{t+\Delta t/2}\langle \boldsymbol{F}(t)\cdot \boldsymbol{F}(\tau)\rangle\,d\tau = 3\xi^2 \approx \boldsymbol{F}^2(t)\Delta t\,. \tag{C.39}
$$

Thus, every component of the stochastic force must be renormalised with the timestep width

$$
F_i(t) \;=\; \frac{\xi}{\sqrt{\Delta t}}\,\chi_{0,1}^{\text{GAUSS}}\,, \tag{C.40}
$$

where $\chi_{0,1}^{\text{GAUSS}}$ is a random number drawn from a normalised normal distribution with mean 0 and width 1. Consequently, the spread of the random forces becomes larger for smaller timesteps. The fluctuation-dissipation theorem is reproduced by the numerical implementation (see figure C.9). For the simulations within this thesis, the random number generator **Ran800** – as provided in the Matpack package [97] – has been used.
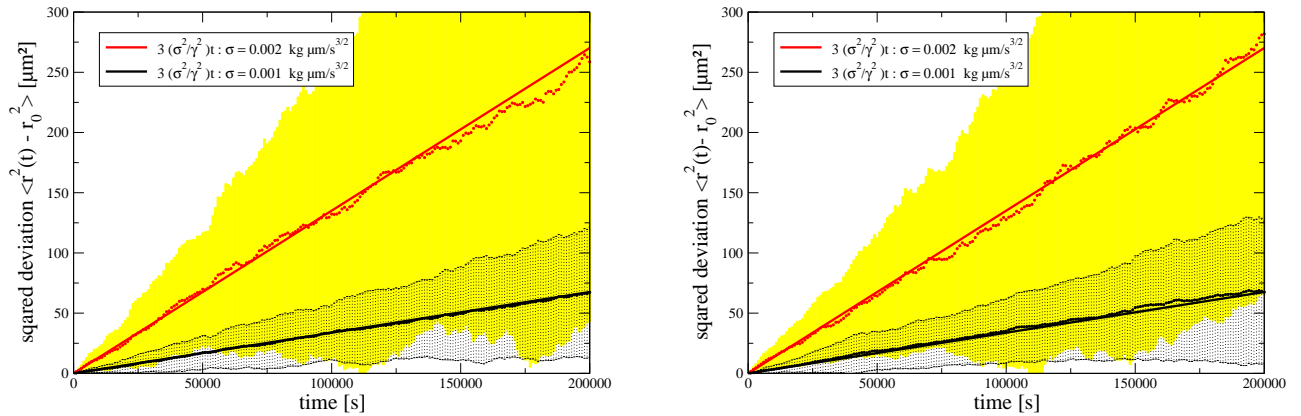
Figure C.9: Test of the random force calculations. Solid lines indicate the prediction by the fluctuation-dissipation theorem, whereas the symbols indicate the mean out of 100 test runs with different seed values of the random number generator. The corresponding standard deviation is indicated by the yellow or black-dotted region, respectively. **Left:** For constant timestep width ($\Delta t = 50$ s), the fluctuation-dissipation theorem is well-reproduced. **Right:** If spatial step-sizes are constrained to $0.05\ \mu$m $\leq \Delta x_i \leq 0.5\ \mu$m by using a variable timestep width Δt, this appearance is not changed: As the random forces are normalised by $\sqrt{\Delta t}$ in every timestep, the fluctuation-dissipation-theorem is recovered. The remaining parameters have been chosen as $R_{\text{cell}} = 5\ \mu$m and $\eta = 10^{-3}$ kg/(μm s). Mean square displacements have been recorded every 1000 seconds. If this was not possible due to the variable timestep width, linear interpolation between the two closest successive time points has been used.

C.3   *Fitting Experimental Data*

In order to fit theoretical results to experimental data, a χ^2-fit has been performed (compare e. g. sub-section 3.3.2). Thereby, one considers a minimization problem on the function

$$\chi^2[p_1,\ldots,p_n] = \sum_{i:\text{experiments}} \sum_{j:\text{datapoints}} \frac{\left(y_{ij}^{\text{exp}}(t_{ij}) - y_{ij}^{\text{sim}}[p_1,\ldots,p_n](t_{ij})\right)^2}{\sigma_{ij}^2}\,, \tag{C.41}$$

which expresses a measure for the differences between experimental data points y_{ij}^{exp} and the simulation results y_{ij}^{sim} – weighted by the experimental uncertainties σ_{ij} of y_{ij}^{exp}. Note that generally an error in t_{ij} will contribute to σ_{ij} as well, but for most measurements on growth experiments its contribution can safely be neglected. Since the simulation results will depend on the parameters $\{p_1,\ldots,p_n\}$, the quantity $\chi^2[p_1,\ldots,p_n]$ can be minimized by varying the parameters $\{p_1,\ldots,p_n\}$ by specified protocols such as e. g. systematic rastering of the parameter space, Monte-Carlo methods such as simulated annealing or genetic algorithms, and geometric algorithms such as simplex walk and Powell's method [68, 176]. Note however, that due to numerical reasons equation (C.41) may not be favourable for minimization problem, as – especially having the initial exponential growth of cell populations in mind – the cell numbers $y_{ij}^{\text{sim}}[p_1,\ldots,p_n]$ may fluctuate strongly. This problem can be alleviated by reducing the differences between the cell numbers, i. e., by setting $y_{ij}^{\text{exp/sim}} = \ln\left(N_{ij}^{\text{exp/sim}}\right)$ and likewise for the other quantities [66].

In this thesis, Powell's algorithm as provided in [68] has been used as minimization protocol. It is a purely deterministic algorithm, which opens the possibility that it will terminate within a local minimum. Therefore, different test runs (starting from different initial parameter sets) should be performed to check whether these terminate within the same minimum.

At a local minimum $\boldsymbol{p}$, any function f can be expressed as

$$f(\boldsymbol{p} + \boldsymbol{x}) = f_0 + \frac{1}{2}\left.\frac{\partial^2 f}{\partial p_i \partial p_j}\right|_{\boldsymbol{p}} x_i x_j + \ldots = f_0 + \frac{1}{2}\boldsymbol{x}^{\mathrm{T}}A\boldsymbol{x} + \ldots\,, \tag{C.42}$$

where A is the symmetric Hessian matrix at the minimum that can be determined using finite-differencing. At a local minimum, the Hessian matrix must be positive definite. With $f = \chi^2$, the isosurfaces of the quadratic form $\boldsymbol{x}^{\mathrm{T}}A\boldsymbol{x} = 2\Delta\chi^2$ define n-dimensional hyper-ellipsoids that can generally be rotated against the parameters axes. By a fixed $\Delta\chi^2$, an ellipsoid of confidence is defined and consequently, error estimates for single parameters can then be obtained from perpendicular projection of the hyperellipsoid on the parameter axes. Such a projection is obtained from the inverse of the Hessian matrix at the minimum, i. e., for parameter P_i one can derive an error estimate via

$$\Delta p_i = \sqrt{\boldsymbol{e}_i A^{-1}\boldsymbol{e}_i 2\Delta\chi^2}\,, \tag{C.43}$$

where $\boldsymbol{e}_i$ denote the Cartesian unit vectors and $\Delta\chi^2$ defines the confidence region. Technically, $\boldsymbol{x} = A^{-1}\boldsymbol{e}_i$ can be determined using the method of conjugate gradients, compare appendix B.2. Note that $2\boldsymbol{e}_i A^{-1}\boldsymbol{e}_i$ is identical with the ith diagonal element of the covariance matrix [68].

The algorithm has been tested using the logistic growth equation $\dot{N} = \alpha N - \beta N^2$ – compare equation (2.1), which has the solution

$$N(t) = \frac{\alpha N_0}{(\alpha - \beta N_0)\, e^{-\alpha t} + \beta N_0} \tag{C.44}$$

with the three parameters N_0, α, and β. By adding normally-distributed random deviations to above equation, an artificial data set has been created with the parameters $N_0 = 4$ cells, $\alpha = 1.0$/day, and $\beta = 0.005$/(day cell), compare figure C.10. The fit yielded the parameter estimates $N_0 = (3.94\pm0.17)$ cells, $\alpha = (1.01\pm0.02)$/day, and $\beta = (5.1\pm0.1)\cdot10^{-3}$/(cell day) at a confidence level of 99%. Consequently, provided with sufficient quantitative data, Powell's method can be used to extract model parameters with acceptable accuracy.

The implemented method has the advantage that the function to be minimized can be defined in a non-analytic form.
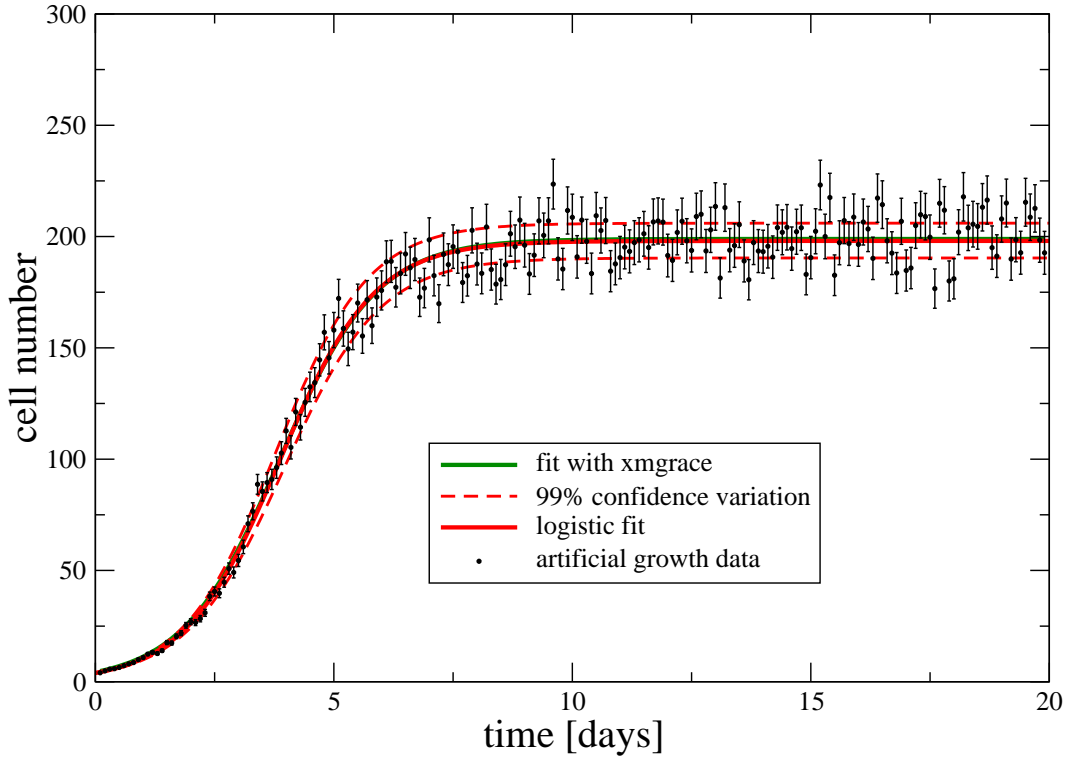
Figure C.10: Test of Powell's minimization method with an artificial data set. Using the parameters $N_0 = 4$ cells, $\alpha = 1.0$/day, and $\beta = 0.005$/(day cell) in equation (C.44) with assumed normally-distributed relative errors of $\Delta N/N = 0.05$, 200 artificial data points have been created (symbols, error bars correspond to one standard deviation). Powell's method [68] has been used to minimize χ^2 in equation (C.41) (red line). Using confidence ellipsoids of $\Delta\chi^2 \approx 6.63$ (corresponding to a confidence level for single parameters of 99% [68] in case of normally-distributed errors), the algorithm yielded the parameter estimates $N_0 = (3.94 \pm 0.17)$ cells, $\alpha = (1.01 \pm 0.02)$/day, and $\beta = (5.1 \pm 0.1) \cdot 10^{-3}$/(cell day) (dashed lines mark extremal fits). The green line represents a fit performed with **xmgrace**, which uses a Levenberg-Marquard algorithm [68] for χ^2-minimization and yields $N_0 = 4.36$ cells, $\alpha = 0.98$/day, and $\beta = 4.9 \cdot 10^{-3}$/(cell day). The discrepancy in N_0 results from the fact that the interface provided in xmgrace ignores the error bars and thereby weights all points equally, as can be verified by applying Powell's method to a χ^2 with $\sigma_{ij} = 1 \forall i, j$ in equation (C.41).

Appendix D

Source Code

The source code has been written in the programming language C++. Generally, the paradigm of object-oriented programming [42] has been followed.

The following modules have been implemented as separate (documented) classes, such that they can be included in independent applications:

- a parameter parser (`parameter.h, parameter.cc`, approx. 350 lines) that processes parameter files, command line options, and provides parameter values upon request,

- a structure class (`structs3D.h, structs3D.cc`, approx. 2000 lines), within which fundamental data structures such as vertex and simplex and the corresponding necessary operations are defined,

- a triangulation class (`triangulator3D.h, triangulator3D.cc`, approx. 4000 lines) that provides the functionality to construct and maintain weighted kinetic and dynamic Delaunay triangulations in three dimensions as described in section 2.3,

- a series of classes (`soluble.h, soluble.cc`, approx. 4200 lines) with similar interface member functions all intended for the solution of RDE with different methods:

  - a class providing the multigrid method on a rectangular grid for the steady-state solution of RDE,

  - a class providing the FFT method for the steady-state solution of RDE,

  - a class providing the ADI algorithm for the full solution of RDE,

  - a class providing the Crank-Nicholson algorithm for the full solution of RDE with the method of biconjugate gradients.

Note however that owing to technical necessities, these separate implementations differ in some aspects, which are described in the respective documentations.

The source code will be available upon request from July 2006 from Gernot Schaller, Tilo Beyer, and Dr. Michael Meyer-Hermann.

Appendix E

Used Symbols and Acronyms

Used symbols:

symbol	meaning	unit/comment
∇	Nabla operator	μm^{-1}
$\mathbb{R}$	the set of real numbers	-
$\hat{\boldsymbol{r}}$	weighted vertex associated with a vector $\boldsymbol{r}$	-
$\boldsymbol{r}^+$	lifted vertex $\hat{\boldsymbol{r}}$	-
$\mathcal{F}_{14}$	flip replacing one by four simplices	-
$\mathcal{F}_{41}$	flip replacing four simplices by one	-
$\mathcal{F}_{23}$	flip replacing two by three simplices	-
$\mathcal{F}_{32}$	flip replacing three by two simplices	-
$\pi(\hat{\boldsymbol{r}}_i, \hat{\boldsymbol{r}}_j)$	orthogonal sphere distance	-
$u(\boldsymbol{r}, t)$	concentration of a substance	$mM = amol\ \mu m^{-3}$
$D(\boldsymbol{r}, t)$	diffusion coefficient	$\mu m^2\ s^{-1}$
∇^2, Δ	Laplacian operator	μm^{-2}
$Q(\boldsymbol{r}, t)$	reaction term	$mM\ s^{-1}$
$u_I(t)$	spatially discretised concentration	mM
$D_I(t)$	spatially discretised diffusion coefficient	$\mu m^2\ s^{-1}$
$Q_I(t)$	spatially discretised reaction term	$mM\ s^{-1}$
u_I^n	spatially and temporally discretised concentration	mM
D_I^n	spatially and temporally discretised diffusion coefficient	$\mu m^2\ s^{-1}$
Q_I^n	spatially and temporally discretised reaction term	$mM\ s^{-1}$
A_{IJ}	contact surface between I and J	μm^2

symbol	meaning	unit/comment
$\mathcal{L}$	lattice discretisation operator	s^{-1}
$\mathbb{1}$	identity operator	1
Δt	timestep width	s
$\Delta x, \Delta y, \Delta z$	lattice constants	$\mu\mathrm{m}$
$O(\ldots)$	order of $\ldots$	-
∂^α	partial derivative with respect to $\boldsymbol{x}_\alpha$	$\mu\mathrm{m}^{-1}$
$\sigma_{\alpha\beta}$	stress tensor	MPa
E	Young modulus	MPa
ν	Poisson modulus	1
$U_{\alpha\beta}$	strain tensor	1
F_{ij}^{JKR}	JKR interaction force	$\mu\mathrm{N}$
R_{ij}	reduced radius	$\mu\mathrm{m}$
K_{ij}	elastic coefficient	MPa
h_{ij}	virtual overlap between spheres i and j	$\mu\mathrm{m}$
ϵ_{ij}	adhesive energy density between spheres i and j	$\mathrm{J\,m}^{-2}$
$\Theta(x)$	Heaviside step function	1
V_{ij}^{JKR}	JKR interaction potential between cells i and j	pJ
$C_i^{\mathrm{rec}}(t)$	receptor density of cell i	1
$C_i^{\mathrm{lig}}(t)$	ligand density of cell j	1
$F_i(t)$	force acting on cell i	$\mu\mathrm{N}$
$F_{ij}(t)$	force acting between cells i and j	$\mu\mathrm{N}$
$\gamma_i^{\alpha\beta}$	cell-medium friction coefficients	$\mathrm{kg\,s}^{-1}$
$\Gamma_{iJ}^{\alpha\beta}$	cell-boundary friction coefficients	$\mathrm{kg\,s}^{-1}$
$\gamma_{ij}^{\alpha\beta}$	cell-cell friction coefficients	$\mathrm{kg\,s}^{-1}$
η	medium viscosity	$\mathrm{kg\,\mu m}^{-1}\,\mathrm{s}^{-1}$
$\delta^{\alpha\beta}, \delta_{ij}$	Kronecker symbol	1
$\gamma_\parallel$	friction coefficient for tangential movement	$\mathrm{kg\,s}^{-1}\,\mu\mathrm{m}^{-2}$
$\gamma_\perp$	friction coefficient for perpendicular movement	$\mathrm{kg\,s}^{-1}\,\mu\mathrm{m}^{-2}$
$\mathcal{P}_{ij,\parallel}^{\alpha\beta}$	tangential projection operator for cells i and j	1
$\mathcal{P}_{ij,\perp}^{\alpha\beta}$	perpendicular projection operator for cells i and j	1
$\mathbb{O}$	zero operator	1
$R^{(\mathrm{m})}$	(pre-mitotic) mother cell radius	$\mu\mathrm{m}$
$R^{(\mathrm{d})}$	(post-mitotic) daughter cell radius	$\mu\mathrm{m}$

symbol	meaning	unit/comment
γ^{max}	maximum cell-cell friction contribution	kg s^{-1} μm^{-2}
f^{ad}	maximum adhesive force	μN μm^{-2}
T^{crit}	critical cell tension	MPa
k_{B}	Boltzmann constant	J K^{-1}
T	temperature	K
$C_{\text{ox}}(\boldsymbol{r}, t)$	oxygen concentration	mM
$C_{\text{gl}}(\boldsymbol{r}, t)$	glucose concentration	mM
$C_{\text{vb}}(\boldsymbol{r}, t)$	viable cell density	μm^{-3}
$C_{\text{nc}}(\boldsymbol{r}, t)$	necrotic cell density	μm^{-3}
$\alpha[C_{\text{vb}}, C_{\text{nc}}]$	proliferation rate	s^{-1}
$\beta[C_{\text{ox}}, C_{\text{gl}}]$	death rate	s^{-1}
γ	necrotic removal rate	s^{-1}
C^{thresh}	cell threshold density	μm^{-3}
C^{crit}	maximum cell density	μm^{-3}
K^{crit}	cell compression factor	1
P^{crit}	minimum nutrient product	mM^2
m	diffusion exponent	1
L_{D}	diffusion length	μm
$\tau^{(\text{m})}$	mean M-phase time	s
$\tau^{(\text{S/G}_2)}$	mean S/G$_2$-phase time	s
τ^{min}	minimum observed cycle time	s
λ_{ox}	cellular oxygen uptake rate	amol cell^{-1} s^{-1}
λ_{gl}	cellular glucose uptake rate	amol cell^{-1} s^{-1}
ε_i	cellular anchorage	pJ
ε^{min}	minimum anchorage	pJ
τ^{mel}	melanocyte cycle time	s
ξ	fluctuation force parameter	kg m^{-1} s$^{-3/2}$
$\delta(x)$	Dirichlet δ-distribution function	1

Table E.1: Symbols used throughout this thesis. If units are given, these correspond to the units chosen in this thesis, unless noted otherwise. Symbols are in order of their first occurrence in the text.

Used acronyms:

abbreviation	full phrase
ADI	Alternating-Direction Implicit
BTCS	Backward-Time-Centred Space
CGM	Conjugate Gradient Method
CNS	Crank-Nicholson Scheme
DEM	Discrete Element Method
DNA	Deoxyribose Nucleic Acid
FFT	Fast Fourier Transform
FTCS	Forward-Time-Centred Space
JKR	Johnson-Kendall-Roberts
MTS	Multicellular Tumour Spheroid
ODE	Ordinary Differential Equation
PDE	Partial Differential Equation
RDE	Reaction-Diffusion Equation
VCMGM	V-Cycle Multigrid Method

Table E.2: Abbreviations used throughout this thesis.

List of Figures

The figures in this thesis have been created on a Linux operating system using the programs **xfig** [180] for drawings, **xmgrace** [181] for graphs, **IBM Data Explorer** [182] for the colour-coded visualisation of density plots and the calculation of isosurfaces, and **povray** [183] or **VRMLview** [184] for rendering colour-coded cross-sections of cell distributions.

List of Tables

Acknowledgements

Bibliography

[1] R. A. Gatenby and P. K. Maini. *Cancer summed up*. Nature **421**, 321–322, 2003.

[2] S. Schirra, R. Veltkamp, and M. Yvinec. The CGAL Reference Manual, 1999.

[3] S. Wolfram. Cellular Automata and Complexity: Collected Papers. Wolfram Research, 1994.

[4] A. Deutsch. *Zelluläre Automaten als Modelle von Musterbildungsprozessen in biologischen Systemen*. Informatik in den Biowissenschaften 181–192, 1993.

[5] F. Graner and J. A. Glazier. *Simulation of Biological Cell Sorting Using a Two-Dimensional Extended Potts Model*. Physical Review Letters **69**(13), 2013–2016, 1992.

[6] M. Weliky and G. Oster. *The mechanical basis of cell rearrangement*. Development **109**, 373–386, 1990.

[7] S. Dormann and A. Deutsch. *Modeling of self-organized avascular tumor growth with a hybrid cellular automaton*. In Silico Biology **2**(3), 393–406, 2002.

[8] D. Drasdo, R. Kree, and J. S. McCaskill. *Monte Carlo approach to tissue-cell populations*. Physical Review E **52**(6), 6635–6657, 1995.

[9] J. D. Murray. Mathematical Biology I, volume 17 of *Interdisciplinary Applied Mathematics*. Springer, Berlin Heidelberg, 3$^{\text{rd}}$ edition, 2002.

[10] J. D. Murray. Mathematical Biology II, volume 17 of *Interdisciplinary Applied Mathematics*. Springer, Berlin Heidelberg, 3$^{\text{rd}}$ edition, 2002.

[11] B. Gompertz. *On the Nature of the Function Expressive of the Law of Human Mortality, and on a New Mode of Determining the Value of Life Contingencies*. Philosophical Transactions of the Royal Society of London **123**, 513–585, 1825.

[12] Y. Ling and B. He. *Entropic Analysis of Biological Growth Models*. IEEE Transactions on Biomedical Engineering **40**(12), 1193–1200, 1993.

[13] C. L. Frenzen and J. D. Murray. *A Cell Kinetics Justification for Gompertz Equation*. SIAM Journal on Applied Mathematics **46**(4), 614–629, 1986.

[14] W. Mueller-Klieser, W. Schreiber-Klais, S. Walenta, and M. H. Kreuter. *Bioactivity of well-defined green tea extracts in multicellular tumor spheroids*. International Journal of Oncology **21**, 1307–1315, 2002.

[15] R. P. Araujo and D. L. S. McElwain. *A History of the Study of Solid Tumour Growth: The Contribution of Mathematical Modelling*. Bulletin of Mathematical Biology **66**, 1039–1091, 2004.

[16] R. A. Fisher. *The wave of advance of advantageous genes*. Annals of Eugenics **7**, 355–369, 1937.

[17] A. Kolmogoroff, I. Petrovsky, and N. Piscounoff. *Edude de l'equation de la diffusion avec croissance de la quantite de matiere et son application a un probleme biologique*. Moscow University Mathematics Bulletin **1**, 1–25, 1937.

[18] J. von Neumann. Theory of Self-Reproducing Automata. University of Illinois Press, 1st edition, 1966.

[19] A. Deutsch and S. Dormann. Cellular automaton modeling of biological pattern formation. Modeling and simulation in science, engineering and technology. Birkhäuser-Verlag, Berlin, 1st edition, 2005.

[20] M. Gardner. *Mathematical Games*. Scientific American 120–123, 1970. John Horton Conway.

[21] D. Drasdo. Polymer and cell dynamics, chapter On selected individual-based approaches to the dynamics in multicellular systems, 169–204. Birkhäuser, Basel, 2003.

[22] F. Meineke, C. Potten, and M. Loeffler. *Cell migration and organization in the intestinal crypt using a lattice-free model*. Cell Proliferation **34**, 253–266, 2001.

[23] H. Honda, M. Tanemura, and A. Yoshida. *Differentiation of wing epidermal scale cells in a butterfly under the lateral inhibition model – appearance of large cells in a polygonal pattern*. Acta Biotheoretica **48**, 121–136, 2000.

[24] M. Weliky, G. Oster, S. Minsuk, and R. Keller. *Notochord morphogenesis in Xenopus laevis: Simulation of cell behavior underlying tissue convergence and extension*. Development **113**, 1231–1244, 1991.

[25] G. D. Fabritiis and P. V. Coveney. *Dynamical geometry for multiscale dissipative particle dynamics*. Computer Physics Communications **153**(2), 209–226, 2003.

[26] G. Schaller and M. Meyer-Hermann. *Kinetic and dynamic Delaunay tetrahedralizations in three dimensions*. Computer Physics Communications **162**, 9–23, 2004.

[27] J.-A. Ferrez. Dynamic triangulations for efficient 3d simulations of granular materials. Ph.D. thesis, EPFL, thesis 2432, 2001.

[28] A. Okabe, B. Boots, K. Sugihara, and S. N. Chiu. Spatial tessellations: Concepts and applications of Voronoi diagrams. Probability and Statistics. Wiley, New York, 2nd edition, 2000.

[29] H. Edelsbrunner and N. Shah. *Incremental Topological Flipping Works for Regular Triangulations*. Algorithmica **15**, 223–241, 1996.

[30] E. Mücke. *A Robust Implementation for Three-Dimensional Delaunay Triangulations*. International Journal of Computational Geometry and Applications **2**(8), 255–276, 1998.

[31] X. Xinjian, R. Franco, T. Hubert, T. Liebling, and A. Mocellin. *The Laguerre model for grain growth in three dimensions*. Philosophical Magazine B **75**(4), 567–585, 1997.

[32] J. Goodman and J. O'Rourke. Handbook of Discrete and Computational Geometry. CRC Press, New York, 1st edition, 1997.

[33] S. Fortune. *Voronoi diagrams and Delaunay triangulations*. Computing in Euclidean Geometry **1**, 1992.

[34] E. Schönhardt. *Über die Zerlegung von Dreieckspolyedern in Tetraeder*. Mathematische Annalen **98**, 309–312, 1928.

[35] A. Below, U. Brehm, J. D. Loera, and J. Richter-Gebert. *Minimal Simplicial Dissections and Triangulations of Convex 3-Polytopes*. Discrete and Computational Geometry **24**, 35–48, 2000.

[36] J. R. Shewchuk. *Constrained Delaunay Tetrahedralizations and Provably Good Boundary Recovery*. In Eleventh International Meshing Roundtable, 193–204. Sandia National Laboratories, 2002.

[37] J. Sauer. Allgemeine Kollisionserkennung und Formrekonstruktion basierend auf Zellkomplexen. Ph.D. thesis, Universität des Saarlandes, Fachbereich 14 Informatik, 1995.

[38] F. Aurenhammer and H. Imai. *Geometric relations among Voronoi diagrams*. Geometriae Dedicata **27**, 65–75, 1988.

[39] J. R. Shewchuk. *Adaptive Precision Floating-Point Arithmetic and Fast Robust Geometric Predicates*. In Discrete and Computational Geometry, volume 18, 305–363. 1997.

[40] T. Beyer, G. Schaller, A. Deutsch, and M. Meyer-Hermann. *Parallel dynamic and kinetic regular triangulation in three dimensions*. to appear in Computer Physics Communications 2005.

[41] L. Devroye, E. P. Mücke, and B. Zhu. *A Note on Point Location in Delaunay Triangulations of Random Points*. Algorithmica **22**, 477–482, 1998.

[42] B. Stroustrup. Die $C++$ Programmiersprache. Addison-Wesley, München, 2000.

[43] K. B. Lauritsen, H. Puhl, and H.-J. Tillemans. *Performance of Random Lattice Algorithms*. International Journal of Modern Physics C **5**(6), 909–922, 1994.

[44] J.-D. Boissonnat and M. Teillaud. *On the randomized construction of the Delaunay tree*. Theoretical Computer Science **112**(2), 339–354, 1993.

[45] T. J. Choi. *Generating Optimal Computational Grids: Overview and Review*. http : //www.me.cmu.edu/faculty1/shimada/cg97/taek/, 1997.

[46] O. Devillers, S. Pion, and M. Teillaud. *Walking in a triangulation*. In Proceedings of the 17th Annual ACM Symposium on Computational Geometry, 106–114. 2001.

[47] M. A. Facello. Constructing Delaunay and regular triangulations in three dimensions. Ph.D. thesis, University of Illinois at Urbana-Champaign, 1993.

[48] A. Bowyer. *Computing Dirichlet tessellations*. The Computer Journal **24**(2), 162–166, 1981.

[49] O. Devillers. *Improved incremental randomized Delaunay triangulation*. In Proceedings of the 14th Annual ACM Symposium on Computational Geometry, 106–115. 1998.

[50] E. P. Mücke, I. Saias, and B. Zhu. *Fast Randomized Point Location Without Preprocessing in Two- and Three-Dimensional Delaunay Triangulations*. In Proceedings of the 12th Annual ACM Symposium on Computational Geometry, 274–283. 1996.

[51] G. Brouns, A. D. Wulf, and D. Constales. *Multibeam data processing: Adding and deleting vertices in a Delaunay triangulation.* The Hydrographic Journal **101**, 2001.

[52] O. Devillers. *On Deletion in Delaunay Triangulation.* International Journal of Computational Geometry and Applications **12**, 193–205, 2002.

[53] M. A. Mostafavi, C. Gold, and M. Dakowicz. *Delete and insert operations in Voronoi/Delaunay methods and applications.* Computers and Geosciences **29**, 523–530, 2003.

[54] J.-D. Boissonnat and M. Yvinec. Algorithmic Geometry. Cambridge University Press, Cambridge, 1st edition, 1998.

[55] J. R. Shewchuk. *A Condition Guaranteeing the Existence of Higher-Dimensional Constrained Delaunay Triangulations.* In Proceedings of the 14th Annual Symposium on Computational Geometry, 76–85. 1998.

[56] M. Vigo and N. Pla. *Regular Triangulations of Dynamic Sets of Points*, 2000.

[57] O. Devillers and S. Pion. *Efficient Exact Geometric Predicates for Delaunay Triangulations.* In Proceedings of the 5th Workshop on Algorithm Engineering and Experiments, 37–44. 2003.

[58] Y. A. Teng, F. Sullivan, I. Beichl, and E. Puppo. *A data-parallel algorithm for three-dimensional Delaunay triangulation and its implementation.* In Conference on High Performance Networking and Computing, 112–121. Proceedings of the 1993 ACM/IEEE conference on Supercomputing, 1993.

[59] C. Kittel. Introduction to Solid State Physics. John Wiley and Sons, 7th edition, 1996.

[60] S. Sastry, D. S. Corti, P. G. Debenedetti, and F. H. Stillinger. *Statistical geometry of particle packings. I. Algorithm for exact determination of connectivity, volume, and surface areas of void space in monodisperse and polydisperse sphere packings.* Physical Review E **56**(5), 5524–5532, 1997.

[61] F. Aurenhammer. *Voronoi diagrams – A survey of fundamental geometric data structure.* ACM Computing Surveys **23**(3), 345–405, 1991.

[62] H. Honda, M. Tanemura, and T. Nagai. *A three-dimensional vertex dynamics cell model of space-filling polyhedra simulating cell behavior in a cell aggregate.* Journal of Theoretical Biology **226**, 439–453, 2004.

[63] G. L. Miller, D. Talmor, S.-H. Teng, and N. Walkington. *A Delaunay Based Numerical Method for Three Dimensions: generation, formulation, and partition.* Proceedings of the 27th Annual ACM Symposium on Theory of Computing 683–692, 1995.

[64] D. C. Bottino. *Computer simulations of mechanochemical coupling in a deforming domain: applications to cell motion.* IMA Volumes in Mathematics and its Applications, Frontiers in Applied Mathematics Series **121**, 295–314, 2000.

[65] C. J. Roussel and M. R. Roussel. *Reaction-diffusion models of development with state-dependent chemical diffusion coefficients.* Progress in Biophysics and Molecular Biology **86**, 113–160, 2004.

[66] G. Schaller and M. Meyer-Hermann. *Continuum versus Discrete model: A Comparison for Multicellular Tumour Spheroids.* to appear in Philosophical Transactions of the Royal Society Series A 2005.

[67] I. N. Bronstein, K. A. Semendjajew, G. Musiol, and H. Mühlig. Taschenbuch der Mathematik. Harri Deutsch, Frankfurt am Main, Thun, 3rd edition, 1997.

[68] W. H. Press, S. A. Teukolsky, W. T. Vetterling, and B. P. Flannery. Numerical Recipes in C. Cambridge University Press, 2nd edition, 1994.

[69] W. L. Briggs, V. E. Henson, and S. F. McCormick. A multigrid tutorial. Society for Industrial and Applied Mathematics, 2nd edition, 2000.

[70] L. D. Landau and E. M. Lifshitz. Theory of Elasticity. Pergamon Press, London, 1959.

[71] M. A. Stülpner, B. D. Reddy, G. R. Starke, and A. Spirakis. *A three-dimensional finite analysis of adaptive remodelling in the proximal femur.* Journal of Biomechanics **30**(10), 1063–1066, 1997.

[72] M. Stülpner. Various Continuum Bone Remodelling Algorithms applied to the Proximal Femur in Two and Three Dimensions. Master's thesis, University of Cape Town, Department of Mechanical Engineering Rondebosch, 1995.

[73] P. Bongrand. *Ligand-receptor interactions.* Reports on Progress in Physics **62**, 921–968, 1999.

[74] U. S. Schwarz and S. A. Safran. *Elastic Interactions of Cells.* Physical Review Letters **88**(4), 0481021–0481024, 2002.

[75] C. Verdier. *Rheological Properties of Living Materials. From Cells to Tissues*. Journal of Theoretical Medicine **5**(2), 67–91, 2003.

[76] J. Galle, M. Loeffler, and D. Drasdo. *Modeling the Effect of Deregulated Proliferation and Apoptosis on the Growth Dynamics of Epithelial Cell Populations In Vitro*. Biophysical Journal **88**, 62–75, 2005.

[77] G. Schaller and M. Meyer-Hermann. *Multicellular Tumor Spheroid in an off-lattice Voronoi/Delaunay cell model*. Physical Review E **71**, 051910–16, 2005.

[78] A. Rahman. *Correlations in the Motion of Atoms in Liquid Argon*. Physical Review **136**, A405–A411, 1964.

[79] E. Palsson and H. G. Othmer. *A model for individual and collective cell movement in Dictyostelium discoideum*. Proceedings of the National Academy of Sciences **97**(19), 10448–10453, 2000.

[80] E. Palsson. *A three-dimensional model of cell movement in multicellular systems*. Future Generation Computer Systems **17**, 835–852, 2001.

[81] D. E. Ingber. *Tensegrity I: Cell structure and hierarchical systems biology*. Journal of Cell Science **116**(7), 1157–1173, 2003.

[82] D. E. Ingber. *Tensegrity II: How structural networks influence cellular information processing networks*. Journal of Cell Science **116**(8), 1397–1408, 2003.

[83] N. N. Brilliantov and T. Pöschel. The Physics of Granular Media, chapter Collision of viscoelastic particles with adhesion. Wiley-VCH, Berlin, 2004.

[84] H. Hertz. *Über die Berührung fester elastischer Körper*. Journal für die reine und angewandte Mathematik **92**, 156–171, 1882.

[85] K. L. Johnson, K. Kendall, and A. D. Roberts. *Surface Energy and the Contact of Elastic Solids*. Proceedings of the Royal Society of London A **324**(1558), 301–313, 1971.

[86] F. Yang. *Load-displacement relation in adhesion measurement*. Journal of Physics D: Applied Physics **36**, 2417–2420, 2003.

[87] M. Benoit, D. Gabriel, G. Gerisch, and H. E. Gaub. *Discrete interactions in cell adhesion measured by single-molecule force spectroscopy*. Nature Cell Biology **2**, 313–317, 2000.

[88] Y.-S. Chu, W. A. Thomas, O. Eder, F. Pincet, E. Perez, J. P. Thiery, *et al. Force measurements in E-cadherin-mediated cell doublets reveal rapid adhesion strenghtened by actin cytoskeleton remodeling through Rac and Cdc42*. Journal of Cell Biology **167**(6), 1183–1194, 2004.

[89] J. Galle, G. Aust, G. Schaller, T. Beyer, and D. Drasdo. *Individual cell-based models of the spatio-temporal organisation of multicellular systems – achievements and limitations*. submitted 2005.

[90] P. Attard. *Interaction and deformation of viscoelastic particles: Nonadhesive particles*. Physical Review E **63**, 061604–9, 2001.

[91] P. Attard. *Interaction and Deformation of Viscoelastic Particles. 2. Adhesive Particles*. Langmuir **17**(14), 4322–4328, 2001.

[92] J. Dallon and H. G. Othmer. *How cellular movement determines the collective force generated by the Dictyostelium discoideum slug*. Journal of Theoretical Biology **231**(2), 203–222, 2004.

[93] A. Dziugys and B. Peters. *An approach to simulate the motion of spherical and non-spherical fuel particles in combustion chambers*. Granular Matter **3**, 231–265, 2001.

[94] G. Joos. Lehrbuch der Theoretischen Physik. AULA-Verlag, Wiesbaden, 15$^{\text{th}}$ edition, 1989.

[95] J. Howard. Mechanics of Motor Proteins and the Cytoskeleton. Sinauer Associates, Inc., 23 Plumtree Road Sunderland MA 01375 U.S.A., 2001.

[96] D. A. Fletcher and J. A. Theriot. *An introduction to cell motility for the physical scientist*. Physical Biology **1**, T1–T10, 2004.

[97] B. M. Gammel. Matpack C++ Numerics and Graphics Library 1.7.3, 2003. http : //www.matpack.de/.

[98] H. S. Bell, I. R. Whittle, M. Walker, H. A. Leaver, and S. B. Wharton. *The development of necrosis and apoptosis in glioma: Experimental findings using spheroid culture systems*. Neuropathology and Applied Neurobiology **27**, 291–304, 2001.

[99] J.-U. Kreft, G. Booth, and J. W. T. Wimpenny. *BacSim, a simulator for individual-based modelling of bacterial colony growth*. Microbiology **144**, 3275–3287, 1998.

[100] J. Landry, J. P. Freyer, and R. M. Sutherland. *Shedding of mitotic cells from the surface of multicell spheroids during growth*. Journal of Cellular Physiology **106**(1), 23–32, 1981.

[101] G. I. Evan and K. H. Vousden. *Proliferation, cell cycle and apoptosis in cancer*. Nature **411**, 342–348, 2001.

[102] S. S. Ferreira, M. L. Martins, and M. J. Vilela. *Reaction-diffusion model for the growth of avascular tumor*. Physical Review E **65**, 021907–021915, 2002.

[103] D. Drasdo and S. Höhme. *Individual-Based Approaches to Birth and Death in Avascular Tumors*. Mathematical and Computer Modelling **37**, 1163–1175, 2003.

[104] K. Groebe and W. Mueller-Klieser. *On The Relation between Size of Necrosis and Diameter of Tumor Spheroids*. International Journal of Radiation Oncology Biology Physics **34**(2), 395–401, 1996.

[105] H. P. Greenspan. *Models for the Growth of a Solid Tumor by Diffusion*. Studies in Applied Mathematics **51**, 317–340, 1972.

[106] G. Helmlinger, P. A. Netti, H. C. Lichtenbeld, R. J. Melder, and R. K. Jain. *Solid stress inhibits the growth of multicellular tumor spheroids*. Nature Biotechnology **15**, 778–783, 1997.

[107] J. P. Freyer and R. M. Sutherland. *Regulation of Growth Saturation and Development of Necrosis in EMT6/Ro Multicellular Spheroids by the Glucose and Oxygen Supply*. Cancer Research **46**(7), 3504–3512, 1986.

[108] J. Folkman and M. Hochberg. *Self-Regulation of Growth in Three Dimensions*. The Journal of Experimental Medicine **138**(4), 745–753, 1973.

[109] G. Hamilton. *Multicellular spheroids as an in vitro tumor model*. Cancer Letters **131**, 29–34, 1998.

[110] M. T. Santini and G. Rainaldi. *Three-Dimensional Spheroid Model in Tumor Biology*. Pathobiology **67**, 148–157, 1999.

[111] J. P. Ward and J. R. King. *Mathematical modelling of avascular-tumour growth*. IMA Journal of Mathematics Applied in Medicine and Biology **14**, 39–69, 1997.

[112] L. A. Kunz-Schughart, J. Doetsch, W. Mueller-Klieser, and K. Groebe. *Proliferative activity and tumorigenic conversion: Impact on cellular metabolism in 3-D culture*. American Journal of Physiology: Cell Physiology **278**, 765–780, 2000.

[113] J. J. Casciari, S. V. Sotirchos, and R. M. Sutherland. *Variations in Tumor Cell Growth Rates and Metabolism With Oxygen Concentration, Glucose Concentration, and Extracellular pH*. Journal of Cellular Physiology **151**, 386–394, 1992.

[114] E. E. Beuling, J. C. van den Heuvel, and S. P. P. Ottengraf. *Diffusion Coefficients of Metabolites in Active Biofilms*. Biotechnology and Bioengineering **67**(1), 53–60, 2000.

[115] H. M. Byrne, J. R. King, D. L. S. McElwain, and L. Preziosi. *A Two-Phase Model of Solid Tumour Growth*. Applied Mathematics Letters **16**, 567–573, 2003.

[116] T. Roose, P. A. Netti, L. L. Munn, Y. Boucher, and R. K. Jain. *Solid stress generated by spheroid growth estimated using a linear poroelasticity model*. Microvascular Research **66**, 204–212, 2003.

[117] B. Noble. *Bone Microdamage and Cell Apoptosis*. European Cells and Materials **6**, 46–56, 2003.

[118] K. Groebe and W. Mueller-Klieser. *Distributions of oxygen, nutrient and metabolic waste concentrations in multicellular spheroids and their dependence on spheroid parameters*. European Biophysics Journal **19**, 169–181, 1991.

[119] M. Castro, C. Molina-Paris, and T. S. Deisboeck. *Tumor growth instability and the onset of invasion*. arXiv physics/0503127, 2005.

[120] A. Matzavinos, M. A. J. Chaplain, and V. A. Kuznetsov. *Mathematical modelling of the spatio-temporal response of cytotoxic T-lymphocytes to a solid tumour*. Mathematical Medicine and Biology **21**, 1–34, 2004.

[121] C. A. Parent and P. N. Devreotes. *A Cell's Sense of Direction*. Science **284**, 765–770, 1999.

[122] M. Iijima, Y. E. Huang, and P. Devreotes. *Temporal and Spatial Regulation of Chemotaxis*. Developmental Cell **3**, 469–478, 2002.

[123] L. L. Latour, K. Svoboda, P. P. Mitra, and C. H. Sotak. *Time-dependent diffusion of water in a biological model system*. Proceedings of the National Academy of Sciences of the USA **91**, 1229–1233, 1994.

[124] J. Alvarez-Ramirez, S. Nieves-Mendoza, and J. Gonzalez-Trejo. *Calculation of the effective diffusivity of heterogenous media using the lattice-Boltzmann method*. Physical Review E **53**(3), 2298–2303, 1996.

[125] K. A. Landman and C. P. Please. *Tumour dynamics and necrosis: Surface tension and stability*. IMA Journal of Mathematics Applied in Medicine and Biology **18**, 131–158, 2001.

[126] H. Byrne and L. Preziosi. *Modelling solid tumour growth using the theory of mixtures*. Mathematical Medicine and Biology **20**, 341–366, 2003.

[127] C. J. W. Breward, H. M. Byrne, and C. E. Lewis. *The role of cell-cell interactions in a two-phase model for avascular tumour growth*. Journal of Mathematical Biology **45**(2), 125–152, 2002.

[128] C. Y. Chen, H. M. Byrne, and J. R. King. *The influence of growth-induced stress from the surrounding medium on the development of multicell spheroids*. Journal of Mathematical Biology **43**, 191–220, 2001.

[129] D. R. Sengelaub and B. L. Finlay. *Cell death in the mammalian visual system during normal development: I. Retinal ganglion cells*. The Journal of Comparative Neurology **204**, 311–317, 1982.

[130] S. Walenta, J. Doetsch, W. Mueller-Klieser, and L. A. Kunz-Schughart. *Metabolic Imaging in Multicellular Spheroids of Oncogene-transfected Fibroblasts*. The Journal of Histochemistry and Cytochemistry **48**(4), 509–522, 2000.

[131] J. P. Ward and J. R. King. *Mathematical modelling of avascular-tumour growth II: Modelling growth saturation*. IMA Journal of Mathematics Applied in Medicine and Biology **16**, 171–211, 1999.

[132] E. I. Zacharaki, G. S. Stamatakos, K. S. Nikita, and N. K. Uzunoglu. *Simulating growth dynamics and radiation response of avascular tumour spheroids – model validation in the case of an EMT6/Ro multicellular spheroid*. Computer Methods and Programs in Biomedicine **76**, 193–206, 2004.

[133] J. Guck, R. Ananthakrishnan, H. Mahmood, T. J. Moon, C. C. Cunningham, and J. Käs. *The Optical Stretcher: A Novel Laser Tool to Micromanipulate Cells*. Biophysical Journal **81**, 767–784, 2001.

[134] A. J. Maniotis, C. S. Chen, and D. E. Ingber. *Demonstration of mechanical connections between integrins, cytoskeletal filaments, and nucleoplasm that stabilize nuclear structure*. Proceedings of the National Academy of Sciences USA **94**, 849–854, 1997.

[135] V. I. Baranov, V. M. Belichenko, and C. A. Shoshenko. *Oxygen Diffusion Coefficient in Isolated Chicken Red and White Skeletal Muscle Fibers in Ontogenesis*. Microvascular Research **60**(2), 168–176, 2000.

[136] J. Grote, R. Susskind, and P. Vaupel. *Oxygen diffusivity in tumor tissue (DS-carcinosarcoma) under temperature conditions within the range of 20–40 degrees C*. Pflugers Archiv - European Journal of Physiology **372**(1), 37–42, 1977.

[137] E. K. Rofstad, K. Eide, R. Skøyum, M. E. Hystad, and H. Lyng. *Apoptosis, energy metabolism, and fraction of radiobiologically hypoxic cells: A study of human melanoma multicellular spheroids*. International Journal of Radiation Biology **70**(3), 241–249, 1996.

[138] J. J. Casciari, S. V. Sotirchos, and R. M. Sutherland. *Glucose Diffusivity in Multicellular Tumor Spheroids*. Cancer Research **48**(14), 3905–3909, 1988.

[139] J. P. Wehrle, C. E. Ng, K. A. McGovern, N. R. Aiken, D. C. Shungu, E. M. Chance, *et al. Metabolism of alternative substrates and the bioenergetic status of EMT6 tumor cell spheroids*. NMR in Biomedicine **13**, 349–460, 2000.

[140] R. E. Mahaffy, C. K. Shih, F. C. MacKintosh, and J. Käs. *Scanning Probe-Based Frequency-Dependent Microrheology of Polymer Gels and Biological Cells*. Physical Review Letters **85**(4), 880–883, 2000.

[141] D. A. Beysens, G. Forgacs, and J. A. Glazier. *Cell sorting is analogous to phase ordering in fluids*. Proceedings of the National Academy of Sciences of the USA **97**(17), 9467–9471, 2000.

[142] J. P. Freyer and R. M. Sutherland. *A reduction in the in situ rates of oxygen and glucose consumption of cells in EMT6/Ro spheroids during growth*. Journal of Cellular Physiology **124**, 516–524, 1985.

[143] M. R. Riley, F. J. Muzzio, H. M. Buettner, and S. C. Reyes. *Monte Carlo calculation of effective diffusivities in two- and three-dimensional heterogeneous materials of variable structure*. Physical Review E **49**(4), 3500–3503, 1994.

[144] J. Landry, J. P. Freyer, and R. M. Sutherland. *A model for the growth of multicellular spheroids*. Cell Tissue Kinetics **15**(6), 585–594, 1982.

[145] J. P. Ward and J. R. King. *Modelling the effects of cell shedding on avascular tumour growth.* Journal of Theoretical Medicine **2**, 155–174, 2000.

[146] L. Preziosi. Cancer Modelling and Simulation. Mathematical Biology and Medicine. Chapman and Hall/CRC, London, UK, 2003.

[147] N. L. Komarova and V. Mironov. *On the role of endothelial progenitor cells in tumor neovascularization.* Journal of Theoretical Biology **235**, 338–349, 2005.

[148] E. Sahai and C. J. Marshall. *Differing modes of tumour cell invasion have distinct requirements for Rho/ROCK signalling and extracellular proteolysis.* Nature Cell Biology **5**(8), 711–720, 2003.

[149] L. A. Liotta and E. C. Kohn. *The microenvironment of the tumour-host interface.* Nature **411**, 375–379, 2001.

[150] S. Turner and J. A. Sherratt. *Intercellular Adhesion and Cancer Invasion: A Discrete Simulation Using the Extended Potts Model.* Journal of Theoretical Biology **216**, 85–100, 2002.

[151] J. Smolle, R. Hofmann-Wellenhof, and R. Fink-Puches. *Cellular invasion without cellular motility in a stochastic growth model.* Analytical Cellular Pathology **10**, 37–43, 1996.

[152] S. D. Webb, J. A. Sherratt, and R. G. Fish. *Mathematical Modelling of Tumour Acidity: Regulation if Intracellular pH.* Journal of Theoretical Biology **196**, 237–250, 1999.

[153] J. Smolle. *Cellular automaton simulation of tumour growth – equivocal relationships between simulation parameters and morphologic pattern features.* Analytical Cellular Pathology **17**, 71–82, 1998.

[154] W. Montagna, A. M. Kligman, and K. S. Charlisle. Atlas of Normal Human Skin. Springer Verlag, New York, 1992.

[155] S. B. Hoath and D. G. Leahy. *The organization of Human epidermis: Functional Epidermal Units and Phi Proportionality.* The Journal of Investigative Dermatology **121**(6), 1440–1446, 2003.

[156] J. Bauer, F. A. Bahmer, J. Wörl, W. Neuhuber, G. Schuler, and M. Fartasch. *A Strikingly Constant Ratio Exists Between Langerhans Cells and Other Epidermal Cells in Human Skin. A Stereologic Study Using the Optical Disector Method and the Confocal Laser Scanning Microscope.* The Journal of Investigative Dermatology **116**(2), 313–318, 2001.

[157] E. A. Hsieh, C. M. Chai, B. O. de Lumen, R. A. Neese, and M. K. Hellerstein. *Dynamics of Keratinocytes in vivo using* ^2H_2O *Labeling: A Sensitive Marker of Epidermal Proliferation State*. The Journal of Investigative Dermatology **123**, 530–536, 2004.

[158] M. Moncrieff. The clinical application of spectrophotometric intracutaneous analysis for the diagnosis of cutaneous malignant melanoma. Ph.D. thesis, University of East Anglia, 2001.

[159] P. Boderke, K. Schittkowski, M. Wolf, and H. P. Merkle. *Modeling of Diffusion and Concurrent Metabolism in Cutaneous Tissue*. Journal of Theoretical Biology **204**, 393–407, 2000.

[160] G. Schaller and M. Meyer-Hermann. *Epidermal homeostasis control in an off-lattice agent-based model*. arXiv physics/0507059, 2005.

[161] C. S. Potten, Y. Q. Li, R. Ohlrich, B. Matthe, and M. Loeffler. *Proliferation in murine epidermis after minor mechanical stimulation. Part 1. Sustained increase in keratinocyte production and migration*. Cell Proliferation **33**, 231–246, 2000.

[162] D. Barthel, B. Matthe, C. S. Potten, G. Owen, and M. Loeffler. *Proliferation in murine epidermis after minor mechanical stimulation. Part 2. Alterations in keratinocyte cell cycle fluxes*. Cell Proliferation **33**, 247–259, 2000.

[163] G. B. Kasting, N. D. Barai, T.-F. Wang, and J. M. Nitsche. *Mobility of Water in Human Stratum Corneum*. Journal of Pharmaceutical Sciences **92**(11), 2326–2340, 2003.

[164] A. Tang, M. S. Eller, M. Hara, M. Yaar, S. Hirohashi, and B. A. Gilchrest. *E-cadherin is the major mediator of human melanocyte adhesion to keratinocytes in vitro*. Journal of Cell Science **107**, 983–992, 1994.

[165] L. Norlen and A. Al-Amoudi. *Stratum Corneum Keratin Structure, Function, and Formation: The Cubic Rod-Packing and Membrane Templating Model*. The Journal of Investigative Dermatology **123**, 715–732, 2004.

[166] T. L. Chenevert, J. G. Pipe, D. M. Williams, and J. A. Brunberg. *Quantitative measurement of tissue perfusion and diffusion in vivo*. Magnetic Resonance in Medicine **17**(1), 197–212, 1991.

[167] E. H. Livingston and E. Engel. *Modeling of the gastric gel mucus layer: application to the measured pH gradient*. Journal of Clinical Gastroenterology **21**, S120–S124, 1995. Suppl. 1.

[168] D. A. Schwindt, K. P. Wilhelm, and H. I. Maibach. *Water Diffusion Characteristics of Human Stratum Corneum at Different Anatomical Sites in vivo*. The Journal of Investigative Dermatology **111**(3), 385–389, 1998.

[169] S. J. Bashir, A.-L. Chew, A. Anigbogu, F. Dreher, and H. I. Maibach. *Physical and phsiological effects of stratum corneum tape stripping*. Skin Research and Technology **7**, 40–48, 2001.

[170] V. V. Tuchin, A. N. Bashkatov, E. A. Genina, Y. P. Sinichkin, and N. A. Lakodina. *In vivo Investigation of the immersion-liquid-induced human skin clearing dynamics*. Technical Physics Letters **27**(6), 489–490, 2001.

[171] G. Carvalho, A. Moore, B. Qizilbash, K. Lachapelle, and T. Schricker. *Maintenance of normoglycemia during cardiac surgery*. Anesthesia and Analgesia **99**(2), 319–324, 2004.

[172] J. P. Freyer and R. M. Sutherland. *Proliferative and Clonogenic Heterogeneity of Cells from EMT6/Ro Multicellular Spheroids Induced by the Glucose and Oxygen Supply*. Cancer Research **46**(7), 3513–3520, 1986.

[173] N. J. Savill and J. A. Sherratt. *Control of epidermal stem cell clusters by Notch-mediated lateral induction*. Developmental Biology **258**, 141–153, 2003.

[174] D. Morel, R. Marcelpoil, and G. Brugal. *A Proliferation Control Network Model: The Simulation of Two-Dimensional Epithelial Homeostasis*. Acta Biotheoretica **49**, 219–234, 2001.

[175] G. Fenteany, P. A. Janmey, and T. P. Stossel. *Signaling pathways and cell mechanics involved in wound closure by epithelial cell sheets*. Current Biology **10**, 831–838, 2000.

[176] N. Gershenfeld. The Nature of Mathematical Modeling. Cambridge University Press, Cambridge, 2000.

[177] H. Hesse. Das Glasperlenspiel. Suhrkamp, Frankfurt/Main, 1996.

[178] J. R. Shewchuk. *An Introduction to the Conjugate Gradient Method Without the Agonizing Pain*. Technical report, Carnegie Mellon University, Pittsburgh, PA, USA, 1994.

[179] J. D. Jackson. Classical Electrodynamics. John Wiley and Sons, New York, 3rd edition, 1998.

[180] T. Sato and B. V. Smith. Xfig User Manual 3.2.4, 2002.
http : //www.xfig.org/userman/.

[181] the Grace Team. Grace User's Guide 5.1.18, 2004.
      http : //plasma−gate.weizmann.ac.il/Grace/doc/UsersGuide.html#ss1.2.

[182] IBM Corporation. IBM Visualization Data Explorer User's Guide 3.1.4., 1997.
      http : //opendx.npaci.edu/docs/pdf/userref.pdf.

[183] Persistence of Vision Raytracer Pty. Ltd. POV-Ray Documentation 3.6.1, 2005.
      http : //www.povray.org/documentation/.

[184] SIM Corporation. SIM VRMLview 3.0.
      http : //www.sim.no/products/SIM_VRMLview/.

Publications

articles:

- G. Schaller, R. Schützhold, G. Plunien, and G. Soff, *Dynamical Casimir effect in a designed leaky cavity*, Physics Letters A **297**, 81–86, 2002.

- G. Schaller, R. Schützhold, G. Plunien, and G. Soff, *Dynamical Casimir effect in a leaky cavity at finite temperature*, Physical Review A **66**, 023812–19, 2002.

- G. Schaller and M. Meyer-Hermann, *Kinetic and dynamic Delaunay tetrahedralizations in three dimensions*, Computer Physics Communications **162**, 9–23, 2004, [26].

- G. Schaller and M. Meyer-Hermann, *Multicellular Tumor Spheroid in an off-lattice Voronoi/Delaunay cell model*, Physical Review E **71**, 051910–16, 2005, [77].

- G. Schaller and M. Meyer-Hermann, *Continuum versus Discrete model: A Comparison for Multicellular Tumour Spheroids*, to appear in Philosophical Transactions of the Royal Society Series A, 2005, [66].

- G. Schaller and M. Meyer-Hermann, *Epidermal homeostasis control in an off-lattice agent-based model*, arXiV, physics/0507059, 2005, [160].

- T. Beyer, G. Schaller, A. Deutsch, and M. Meyer-Hermann, *Parallel dynamic and kinetic regular triangulation in three dimensions*, to appear Computer Physics Communications, 2005, [40].

- J. Galle, G. Aust, G. Schaller, T. Beyer, and D. Drasdo, *Individual cell-based models of the spatio-temporal organisation of multicellular systems – achievements and limitations*, submitted, 2005, [89].

talks, posters, and proceedings:

- G. Schaller, G. Plunien, and G. Soff, *The Dynamical Casimir Effect in Leaky Cavities*, EAS conference, Riezlern, Austria, presented talk, 2002.

- G. Schaller, R. Schützhold, G. Plunien, and G. Soff, *Dynamischer Casimir Effekt in nichtidealen Kavitäten*, EAS-Tagung Riezlern, Austria, proceeding, 2002.

- G. Schaller, *Dynamic and weighted Delaunay triangulations: An application to Tumor growth modelling*, Bonn, Germany, presented talk, 2003.

- G. Schaller, T. Beyer, and M. Meyer-Hermann, *Weighted dynamic and kinetic Delaunay triangulations in tumor growth modelling*, Linking mathematical and biological models in cancer research, Magdeburg, Germany, presented talk, 2003.

- G. Schaller and M. Meyer-Hermann, *An off-lattice agent-based model for multicellular tumor spheroid growth (work in progress)*, DPG Frühjahrstagung, Regensburg, Germany, poster presentation, 2004.

Curriculum Vitae

address:

Gernot Schaller,

Rabenauer Straße 29,

01159 Dresden, Germany,

g.schaller@figss.uni-frankfurt.de

personal details:

name: Gernot Schaller

marital status: single

nationality: German

date of birth: 28.03.1977

place of birth: Wismar

previous occupations:

1995 - 1996	civilian service
1997 - 2001	occasional employment as student assistant at TU Dresden
10/2001 - 12/2004	scientific assistant at TU Dresden
01/2005 - 06/2005	scholarship holder at FIAS

Development:

1983 - 1991	primary school in Wismar and Zingst (Grundschule)
1991 - 1995	grammar school in Barth (Gymnasium)
1995	general qualification for university entrance (Abitur, overall average grade 1.2)
1995 - 1996	civilian service at the Reha-Klinik Ahrenshoop GmbH
1996 - 2001	studies in physics at the TU Dresden
1998	intermediate diploma (Vordiplom)
1999	fellow of the German National Academic Foundation
08/1999 - 06/2000	studies in physics at Duke University, Durham (NC), USA with a DAAD-scholarship
09/2001	graduation under the supervision of Prof. Dr. Soff at TU Dresden (Diplom, overall average grade 1.0)
10/2001	beginning of PhD studies with Dr. Meyer-Hermann at TU Dresden
2002	award of the Lohrmann medal of TU Dresden
01/2005 -	graduate student at FIAS under the supervision of Prof. Dr. Stöcker